Ballistic Limit Velocity For Continuous Fiber Polymeric Composite Materials and Polymers Through Experimental and Numerical Methods

by

Jonathan Scott Grupp

A thesis submitted to the Graduate Faculty of
Auburn University
in partial fulfillment of the
requirements for the Degree of
Doctorate of Philosophy

Auburn, Alabama
May 10, 2015

Keywords: ballistic impact, LS-DYNA, composites, viscoplastic, finite element

Approved by

David Beale, Chair, Professor of Mechanical Engineering
Royall Broughton, Professor Emeritus of Polymer Fiber Engineering
Pradeep Lall, Thomas Walter Professor of Mechanical Engineering
Jeffrey Suhling, Department Head of Mechanical Engineering

Abstract

Composite materials are often subject to harsh operating environments which may include impact from errant projectiles of various geometries traveling at specific velocities and trajectories. Experimentalists seek to establish the ballistic limit velocity of the composite material where the composite absorbs all of the energy of the projectile traveling at an initial velocity. An analytical approach for the impact event can be difficult to reliably establish the ballistic limit of a particular composite material due to the nonlinear response including rate dependency and post-failure behavior. The finite element method has shown to be capable of modeling the impact event. However many available material models require calibration from the experimental impact tests.

The goal of the present research is to develop and implement an efficient finite element simulation of the composite material under impact which does not require calibration. A general orthotropic viscoplastic material model will be presented. The viscoplastic model utilizes a more generalized form of plastic potential than previous works in that it allows plasticity to occur in the fiber direction. The model represents the nonlinear post-failure behavior through the Continuum Damage Mechanics framework by utilizing an energy balance approach. Additionally a smeared crack model algorithm is utilized to reduce the mesh dependency inherent to finite element solutions. The material model was implemented for the explicit integration solver in LS-DYNA. An implicit return mapping algorithm was utilized to integrate the material model response for each load step. The material model was validated using data from published impact testing and material characterization. The finite element simulations show that the material model is able to predict the ballistic limit velocity within a reasonable margin.

Impact experiments were performed using a single-stage light gas gun. The response of standard aerospace-grade satin weave T300 carbon fiber panels using thermoplastic and thermoset matrices were compared. The ballistic limit velocities for the aforementioned composites were determined using a high speed video camera.

Ballistic testing was also performed on polycarbonate panels towards the development of standardized test methods for ‘chainshot’ hazards present in the operation of the timber harvesting operations. The experimental impact results were also simulated using finite element analysis. The numerical results were compared to the experiment.

Table of Contents

List of Figures

Chapter 1 : Introduction

Composite materials are often utilized in harsh environments where the composite structure can be subject to high velocity impact. It is therefore of the utmost importance for the designer to understand the behavior of the composite structure resulting from the impact event. The composite designer can use experimental testing, analytical models, and/or numerical methods to determine the ballistic performance of the composite material. Experimental testing is the most reliable method to determine the ballistic performance. However, experimental methods are expensive and time-consuming. Analytical models typically rely on an energy balance and several factors or empirical relationships to determine the ballistic performance. Although some analytical methods have shown to be able to predict ballistic performance reasonably, very little additional insight regarding the impact of the composite material can be garnered. Numerical methods such as the Finite Element Method (FEM) can readily predict ballistic performance while also providing the analyst with additional insight to the composite behavior due to the impact. However numerical methods require a significant understanding of the composite behavior beforehand. This includes experimental material characterization test data and a corresponding material model that can accurately represent the composite. As such, numerical methods can be difficult to implement effectively. Given the aforementioned strengths and weaknesses for each of the approaches, the pursuant research will utilize both experimental and numerical methods to determine the ballistic performance of composites.

Composite materials are becoming more prevalent in a wider range of applications due to the inherent advantages afforded by their strength to weight ratio over more traditional engineering materials such as metals. However in recent years designers have placed an increased emphasis on optimum structural performance. Through more advanced design tools and analysis, the optimum composite design includes more focus on the specific constituents, underlying structure, and layup pattern selected. The aforementioned factors are among the many that affect the stress distribution within the composite structure. Fibrous composites take advantage of both the high axially-aligned strength of the fibers with the improved shear response of the matrix material. Due to the underlying geometry and interactions of the constituent materials, composites are generally anisotropic and exhibit nonlinear behavior which can include yielding, strain softening, and strain hardening. In addition, composites also are rate-dependent and exhibit nonlinear post-failure behavior. Post-failure nonlinearity is often due to fiber breakage, fiber kink, matrix cracking, and delamination. In order to accurately represent the composite behavior, the model must take into account the aforementioned phenomena. Typically material models describing composite behavior can be classified within three major classifications: micromechanical, Continuum Damage Mechanics (CDM), and plasticity. Composite material models natively available in commercial Finite Element codes often make many assumptions to simplify the derivation and also implementation of the model. This can severely limit the ability of the model to accurately represent the composite behavior. The available models can be difficult for the analyst to utilize due to either the difficulty of required testing or specialized test fixtures required for material characterization. Additionally some models require calibration in order to accurately represent the post-failure nonlinear behavior of composite materials. It is therefore desired to develop a material model which can accurately describe the composite behavior for highly dynamic events such as ballistic impact using common material characterization testing data without the necessity of calibration parameters. The foregoing research couples an orthotropic viscoplastic model with a progressive damage model to represent the aforementioned behavior of composites under ballistic load conditions. The model was developed for implementation in the commercial Finite Element code, LS-DYNA. The derivation, development, and validation of the composite material model are outlined. An example is presented for a common aerospace-grade composite to validate the model using a series of simulations. Techniques for determining model parameters are presented and demonstrated for the example case using published literature data. The validated material model was used to simulate the ballistic impact event for the example case. The ballistic simulation results were compared to published ballistic data. The model capability for the ballistic simulation is also discussed.

Experimental test methodologies were developed throughout the course of the research to evaluate the ballistic performance of composites. A single stage gas gun was developed to accelerate projectiles to the desired energy levels for the ballistic impact testing. The development and validation of the experimental setup is described in detail. Early testing indicated that thermoplastic based composite materials held an advantage in the ballistic performance observed over epoxy based composites. As such a formal study was performed to better quantify the observed performance differential. Four matrix materials were compared at obliquity angles of 0° and 45° consisting of two thermoplastics and epoxies. An additional test requirement for a falling object hazard necessitated the modification of the gas gun setup to handle larger projectiles. The modified setup development is also outlined. An initial test program for the falling object hazard considered the performance of a two different composites with aluminum as a reference.

Additionally the experimental gas gun was used to replicate the 'chainshot' event that occurs in timber harvesting applications resulting from chain failure and fragmentation. 'Chainshot' is the impact of a chain fragment against the protective polycarbonate glazing which can penetrate and/or perforate the glazing. The polycarbonate glazing serves to project the harvester equipment operator from the 'chainshot' event among other hazards. Experimental testing was performed to determine the ballistic performance of polycarbonate commonly used in timber harvesting applications. A representative chain fragment was selected for the testing. Numerical analysis was performed to simulate the 'chainshot' impact in the commercial Finite Element code, LS-DYNA. Published experimental data was used to determine the model parameters for the rate-dependent plasticity material model selected for the simulations. The simulation results are compared to the experimental testing results.

1.1 : Research Outline

Chapter 2 covers the design and construction of the single-stage gas gun used in the experimental testing. The design and manufacture of the sabot, or projectile carrier, used during the research is also highlighted. The performance of the gas gun and sabot are also examined.

Chapter 3 outlines the methodology for the use of the high speed camera in velocity measurements. The graphical user interface developed to perform the velocity calculations is demonstrated through several examples.

Chapter 4 summarizes the experimental testing performed during the research. The performance of the thermoplastic and thermoset based composites are compared. The initial validation testing for a large diameter falling object hazard is also considered.

Chapter 5 shows the derivation of the viscoplastic composite material model. The return mapping algorithm used to integrate the viscoplastic model equations is detailed. A methodology is presented to determine the parameters necessary for the model from experimental characterization data. An algorithm is developed to find an optimum combination of model parameters. An example of a unidirectional IM7/8552 carbon fiber epoxy composite is shown to demonstrate the parameter calibration procedure. The resulting model fit is compared to the experimental characterization data.

Chapter 6 presents the methodology to couple the Continuum Damage Mechanics framework to the viscoplastic model presented in Chapter 5. The energy-based damage progression is covered which controls the post-failure behavior. The selection of a strain-based failure criterion is discussed. The algorithm for a three dimensional smeared crack model is presented. The resulting LS-DYNA model implementation is validated through a series of simple loading conditions to explore the features of the material model.

Chapter 7 presents an example simulation using published experimental impact results for a unidirectional IM7/8552 composite with the material model presented in Chapter 6. The predicted panel deflection and ballistic limit velocity are discussed. The damage progression is also considered.

Chapter 8 outlines the ‘chainshot’ operator hazard present in forestry operations. An experimental method is developed utilizing the gas gun to recreate the chainshot event in a repeatable manner. The results of the impact of both monolithic and laminate polycarbonate panels are summarized.

Chapter 9 highlights the LS-DYNA simulation to model the impact of the monolithic polycarbonate panel. The simulation results are compared to the experimental results.

Chapter 10 concludes the research with comments on the results and suggested improvements for future works.

Chapter 2 : Experimental Setup

A single-stage gas gun system has been developed for the ballistic testing in the current research. The design process is highlighted with the design choices selected based on the desired performance targets. The projectile carrier design and manufacturing processes are detailed along with the validation of the design through high speed video recordings. During the course of the research the system was adapted to handle larger projectiles. The overall gun system performance is evaluated in terms of accuracy and projectile velocity obtained.

2.1 : Gas Gun Design

Several different types of projectile accelerators are utilized in high velocity impact studies which include electromagnetic, plasma, and propellant-based or pressurized gas guns (1). Gas guns are the most typically utilized mode of projectile acceleration since a wider range of projectile geometries, materials, and masses can be accommodated. For gas guns the projectile acceleration is provided through the rapid expansion of gas. As the gas is transferred down the gun barrel, a pressure wave is exerted on the projectile or the projectile carrier which accelerates it down the gun barrel to the desired velocity or energy level. There are three main configurations for gas guns which include propellant-based gas and single and multiple stage pressurized gas guns (3). The underlying operating principles and control mechanisms for each type of gas gun are different. Pressurized gas guns have a reservoir of compressed gas at a given pressure for a particular volume. The gas pressure, in addition to the speed of the firing mechanism and the flow rate of the gas, impact the resulting projectile velocity in pressurized gas guns. For single-stage gas guns, a burst diaphragm (1) or fast-acting valve release the pressurized gas from the single gas reservoir to the barrel to accelerate the projectile. The burst diaphragm is designed to burst at a specific pressure. Multiple stage guns often use a series of pressure reservoirs separated by burst diaphragms (1) (2). Typically the first stage is propellant-based. In each stage a piston is displaced which increases the pressure from the previous stage. After the final stage, the pressurized gas accelerates the projectile. Propellant-based guns utilize a chemical compound, typically in powder form, whereupon through controlled ignition, the rapid expansion of gases pressurizes the reservoir and finally accelerates the projectile. Generally single-stage gas guns offer more control of the impact velocity for high velocity events up to approximately 900 meters per second, while multiple stage gas and propellant-based guns are capable of hypervelocity projectile speeds above 1500 meters per second.

Based on the energy absorption capabilities of similar composites reported in the literature, a single-stage gas gun has been developed for the experimental ballistic testing. For simplicity in use and design, a high speed valve will be used to regulate the delivery of the pressurized gas. In order to ensure the effectiveness of the gas gun, the response time of the high speed valve must be as close to instantaneous. In addition the flow rate must be sufficiently high to prevent a bottleneck in the gun system. For pressurized gas guns the muzzle velocity can be controlled through the following factors: selection of driving gas, gas pressure and temperature, length of the gun barrel, and cross-sectional areas of the pressure reservoir and barrel. One of the most critical considerations in obtaining a desired range of muzzle velocities is the choice of the driving gas. Driving gases of different densities or molecular weight, and thus different speeds of sound, have a major impact on the range of muzzle velocities. The most common driving gases used in pressurized gas guns are air, nitrogen or nitrogen blends, helium, and hydrogen. The speed at which a projectile can move in a given gas medium is related to its compressibility and inertia, commonly represented as the Mach number:

$$Mach = \frac{V}{c} \tag{1.1}$$

where V if the gas flow speed and c is the speed of sound in the gas (3) (4). The gas flow over the projectile is often divided into several regimes based on the Mach number (3). For large guns where the length of the barrel may be significant, air can be evacuated from the barrel and filled with a particular gas to ensure the desired muzzle velocity. The driving gas pressure and temperature also have a significant influence on the muzzle velocity obtained. The initial pressure of the gas reservoir dictates the mechanisms that affect the projectile acceleration. Since the driving gas, initial pressure, and valve speed can be controlled, pressurized gas guns offer a good level of control to the experimentalist in obtaining the desired impact velocity and energy.

2.2: Barrel Design

The barrel is another critical component to the gas gun. The barrel is typically constructed from high strength steel with a sufficient wall thickness to handle the operating pressures. The interaction of the barrel geometry, cross-sectional area and length, with the driving gas pressure affects the gun performance. Based on Newton's Law of Motion, Seigel developed a basic relationship to calculate the theoretical maximum muzzle speed, v_0, for a given gas gun:

$$v_O = \sqrt{\frac{2 p_O A L}{m}} \tag{1.2}$$

where p_O is the base pressure, A is the cross-sectional area of the barrel, L is the length of the barrel, and m is the mass of the projectile (4). This relationship is considered an approximation because it does not include friction effects against the interior barrel wall or the compressibility effects of the gas in front of the projectile and the base pressure is considered to remain constant during projectile acceleration. As a guideline, the muzzle velocity of an actual gun will not be more than half the theoretical prediction (4). Generally a longer barrel is used for higher muzzle velocities. Depending on the type of projectile, the barrel can utilize either a rifled or smooth bore (1). Rifling is a common machining technique that adds helical grooves to the bore wall. As the projectile moves through the barrel, the rifling induces spin onto the projectile which provides for a much straighter trajectory. However, depending on the test requirements, induced spin may not be desirable for the impact event since orientation to the impact surface may need to be controlled in the experiment. There are several machining or manufacturing processes used to create a high precision barrel. Generally a barrel is machined by honing the interior surface to the desired diameter (1). For extremely long barrels, several tube sections have to be attached due to the limitation of the depth the honing process can occur on a given section (1).

2.3 : Sabot Design

A carrier is usually required to house the projectile and is typically referred to as a sabot which is the French word for ‘shoe’ (3). The functions of the sabot are pressure sealing, and projectile protection and alignment (1). One of the top functions of the sabot is to properly seal against the barrel wall so that the driving gas pressure is not lost thus reducing the effectiveness of the gun. The sabot also provides protection to both the projectile and the barrel wall which prevents mass loss and deformation to the projectile and barrel scoring. Finally the sabot ensures that the desired projectile trajectory is obtained without itself affecting it. This requires that the sabot can separate easily from the projectile. Typically the sabot design takes advantage of the aerodynamic effects to promote sabot separation (1). Depending on the projectile dimensions and geometry, there are two main sabot carrier strategies: push and pull sabots (1). Push and pull sabots are illustrated in Figure 2.1. Based on the three primary functions, the sabot design is a critical component of the gas gun. In order to achieve the design functions, the sabot needs to be constructed of a durable material that is light weight and can withstand the large stresses present in the gun without considerable deformation or fracture. Common materials used are polycarbonate, polyimide, fiber-reinforced plastics, polyethylene, and various other plastics (1). There are several different manufacturing methods currently in use such as injection molding and rapid prototyping.

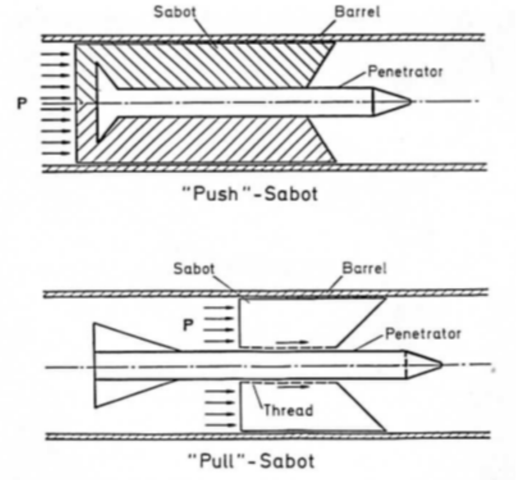

Figure 2.1: Push And Pull Sabots (Stilp et al, 1990)

2.4 : Gas Gun Implementation

During the course of the research, an experimental accelerator for projectile impact was co-developed with several Mechanical Engineering undergraduate design project groups. Based on current design practices and the aforementioned design and safety requirements, a single stage pressurized-gas gun design was selected. The gun design objectives and performance requirements have evolved during the research to accommodate testing of various materials with a range of projectiles of different geometries and masses. As such the gun design underwent several iterations to improve both the gun performance, such as achievable velocity range and accuracy, and to extend the range of projectile geometries. The resulting gun is capable of accelerating projectile ranging in size from 1/8” to 1-3/8” diameter to velocities ranging from 100 to 900 meters per second.

The original primary design directives included true trajectory, high accuracy and precision for impact location, and controllable projectile speed up to 500 meters per second for a 1/2” diameter steel sphere. Based on the aforementioned design targets, a single stage pressurized-gas gun design was selected. Since the composite panels were not expected to require energy levels beyond the aforementioned design requirements, air pressurized by a compressor is used as the driving gas. The original system consisted of a high pressure compressor, high pressure scuba tank, piping manifold, high speed valve, and a smooth bore barrel as shown in Figure 2.2. Since ballistic testing can sometimes lead to unpredictable behavior, safety enclosures were utilized as in Figure 2.3. The enclosures are made from a wood frame with steel sheeting and Lexan windows. Depending on the testing performed either of the enclosures can be utilized.

Figure 2.2: Experimental Gas Gun

Figure 2.3: Experimental Safety Enclosures

The gun system is designed around a minimum safety factor of 2 by using a maximum operating pressure of 1500 psi. Based on the gas gun theory presented by Seigel and the size of the projectiles originally desired, a DOM steel tube measuring 10’ long with a 5/8” bore and 3/16” wall thickness was utilized for the barrel. The nominal barrel outer diameter of 1” was chosen since it allows for the use of 3/4” NPT threading to mate with of a standard scuba tank as the pressure reservoir. In order to determine the safety factor for the barrel under normal operating pressures, the barrel yield stress was calculated. The hoop and radial stresses for the barrel are determined through the Lamé equations for a thick-walled cylinder under pressure as shown in equation 1.3 with definitions illustrated in Figure 2.4. Since the external pressure for the barrel can be considered to be zero, equation 1.3 can be reduced to the form shown in equation 1.4 (5). The maximum shear stress can be determined through the definition in equation 1.5. The yield pressure, p_{yield}, can be determined through Tresca yield criteria by setting $\tau_{\max} = \sigma_{yield}/2$ and substituting into equation 1.5 which after simplification can be expressed as shown in equation 1.6 (5). The maximum hoop stress according to equation 1.4 occurs at r=a and therefore can be further simplified to the form expressed in equation 1.7. The resulting factor of safety for the barrel is 5.84 which is the ratio of the yield stress of the material considered to the yield pressure, $S.\mathrm{F}. = \sigma_{yield}/p_{yield}$. A summary of the calculations is outlined in Table 2.1.

$$\sigma_\theta = \frac{a^2 p_i - b^2 p_o}{b^2 - a^2} + \frac{(p_i - p_o)a^2 b^2}{(b^2 - a^2)r^2} \quad \sigma_r = \frac{a^2 p_i - b^2 p_o}{b^2 - a^2} - \frac{(p_i - p_o)a^2 b^2}{(b^2 - a^2)r^2} \qquad \mathbf{1.3}$$

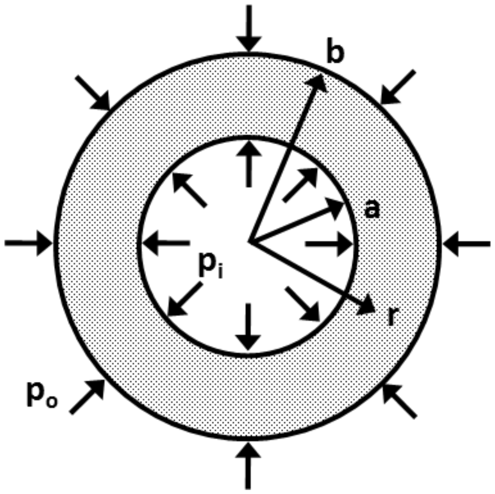

Figure 2.4: Lamé Equation Definitions; Thick-walled Cylinder Under Pressure

$$\sigma_\theta = \frac{a^2 p_i}{b^2 - a^2}\left(1 + \frac{b^2}{r^2}\right) \quad \sigma_r = \frac{a^2 p_i}{b^2 - a^2}\left(1 - \frac{b^2}{r^2}\right) \tag{1.4}$$

$$\tau_{\max} = \frac{(\sigma_\theta - \sigma_r)}{2} = \frac{p_i b^2}{b^2 - a^2} \tag{1.5}$$

$$p_{yield} = \frac{(b^2 - a^2)\sigma_{yield}}{2b^2} \tag{1.6}$$

$$\sigma_{\theta,\max} = p_i \frac{b^2 + a^2}{b^2 - a^2} \quad where \;\; r = a \tag{1.7}$$

Barrel Nominal Dimension (in)	NPT Pipe Size (in)	a, Inner Diameter (in)	b, Outer Diameter (in)	p_i , Internal Pressure (psi)	p_o , Outer Pressure (psi)	$\sigma_{\theta,max}$, Max. Hoop Stress (psi)	σ_{yield} , Steel, Yield Stress (psi)	p_{yield} , Yield Stress (psi)	Safety Factor
5/8	0.75	0.620	1.050	1500	0	3105.90	55700	18139.76	5.84
1-1/2	2.00	1.5	2.375	1500	0	3490.78	55700	16740.86	4.80

Table 2.1: Barrel Safety Factor Calculations Summary

The DOM manufacturing process results in a seamless, smooth bore without any surface preparation or machining. The dimensional variability for DOM tube in the cross-section is minimal. The smooth bore surface reduces the amount of friction between the sabot and barrel bore which allows the use of a tighter fitting sabot without degradation in performance. The use of tighter fitting sabots has been shown in preliminary gun testing to result in more reliable velocity control and also more controlled projectile trajectory and attitude (pitch, yaw, and roll). Using compressed air as the driving gas, a velocity range of 100 to 315 meters per second was obtained. Control of the velocity is provided through the initial pressure in the system. Since air was chosen as the driving gas, the system performance was limited to the speed of sound which at room temperature is approximately 345 meters per second.

Although good accuracy was obtained using the configuration shown in Figure 2.2, the gun support structure originally utilized was subject to drift in impact location which affected the accuracy of the gun for the duration of a long series of experimental tests. The sources of the drift included the flexure of the wooden “A” frame support and the barrel support movement. In order to resolve the drift issues, a rigid steel structure was designed with a recoil mechanism as shown in Figure 2.5. The recoil mechanism facilitates the barrel translational motion due to the significant thrust forces from high air pressure. A center support with a linear bearing and end support were constructed as shown in Figures 2.6 and 2.7. The center and end supports also reduce the amount of barrel deflection and bending during gun operation which affect the gun accuracy. The recoil system was developed in response to the significant amount of thrust observed during high pressure gun operation using compressed air. In order to properly size the recoil spring, the proposed gun system was created in the Solid Edge CAD program and modeled in the rigid body dynamics solver Dynamic Designer Motion. Dynamic Designer allows the analyst to make use of the advanced geometry tools present in a dedicated CAD program and perform rigid body dynamics simulations within the CAD environment. The simulation for the CAD model is shown in Figure 2.8. During the same design iteration as the recoil rigid support system, the velocity performance objective increased to approximately 900 meters per second. In order to facilitate this objective without a radical change in the gun design, compressed ultra-high purity helium was incorporated as a driving gas. Slight changes in the gun manifold were made to allow use of either compressed air or helium. The speed of sound of helium is approximately 1011 meters per second at room temperature and atmospheric pressure. The maximum observed velocity for 1/4” diameter steel spherical projectile during testing was 780 meters per second at a pressure of 1300 psi. Although this velocity does not quite meet the updated velocity performance target, the change of driving gas to helium is a cost effective measure to increase gun performance. Further development of the gun will be needed to increase the performance further which can include the change of design to include multiple pressure stages.

Figure 2.5: Experimental Gas Gun Support System Upgrade

Figure 2.6: Barrel Center Support With Linear Bearing

Figure 2.7: Barrel End Support

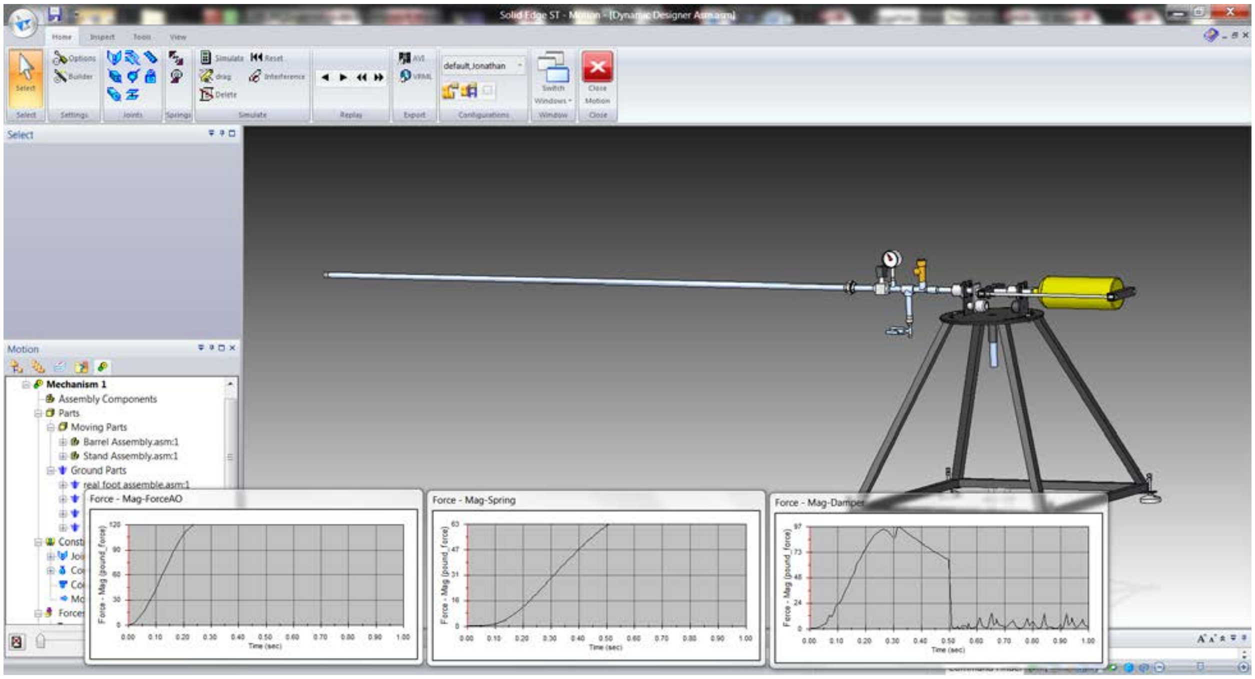

Figure 2.8: CAD Gas Gun Model Recoil Simulation

For the final design iteration, a testing program required a spherical steel projectile measuring 1-3/8” in diameter. In order to house the projectile, a larger barrel was necessary. Due to time and budget constraints, it was determined that the optimum solution was to utilize the basic gun configuration developed thus far. Therefore the existing gun structure and barrel supports were adapted to accept the upsized barrel. The upsized barrel configuration was designed such that the experimentalist could change between the 5/8” bore diameter barrel configuration and the upsized barrel configuration within one man-hour. The gun in the upsized barrel configuration is shown in Figure 2.9. The nominal inner diameter of the barrel is 1-1/2” and the factor of safety calculated to be 4.80 as outlined in Table 2.1. The existing barrel supports were also reused. For the larger barrel size, suitable linear bearings for barrel supports were cost prohibitive. As such bushings were made using Delrin with DOM steel tube as the bushing housing. The Delrin bushings were manufactured using a lathe and then press fit into DOM housings. The Delrin bushing assemblies are shown in Figures 2.10 and 2.11 for the center and end supports, respectively.

Figure 2.9: Experimental Gas Gun Upsized Barrel Configuration

Figure 2.10: Upsized Barrel Delrin Bushing; Center Support

Figure 2.11: Upsized Barrel Delrin Bushing; End Support

2.5 : Gas Gun Design Performance

The gas gun developed during the course of the research is currently capable of impact velocities ranging from 100 to 800 meters per second. As mentioned in previous sections, the main impact velocity control mechanisms for the current gun design are the choice of the driving gas and the initial pressure of the reservoir. As such for each driving gas, air and helium, a performance relationship can be established for a particular projectile. In order to establish the pressure versus impact velocity relationship, 1/4” diameter spherical steel projectiles were accelerated using a range of pressures. The velocities were measured using a high speed video camera as outlined in Chapter 3. As shown in Figure 2.12, a logarithmic regression was used to establish the pressure-velocity relationship for air. Beyond approximately 600 psi the impact velocity does not increase significantly and plateaus. In addition it is also apparent that the speed of sound is the limiting factor for the single stage gun design.

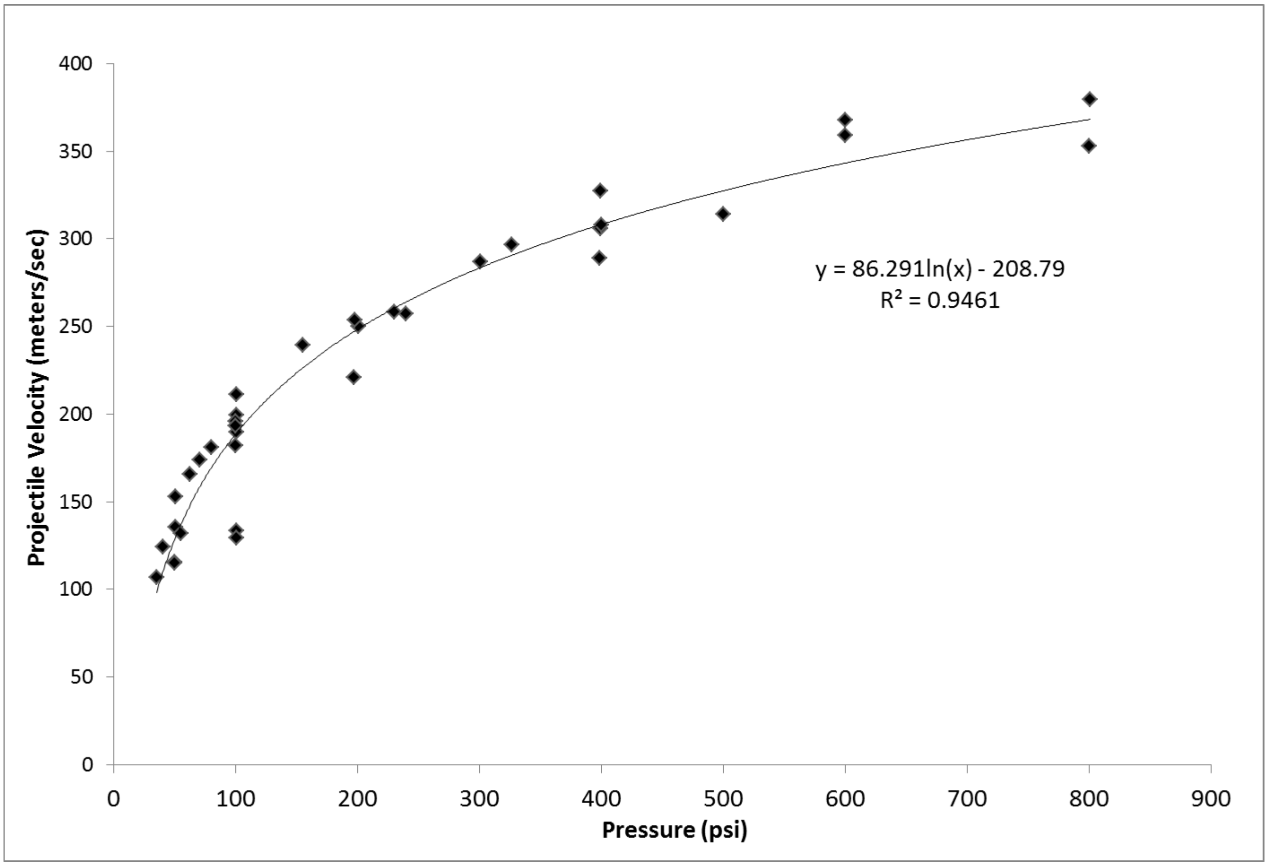

Figure 2.12: Projectile Velocity As A Function Of Pressure For Air

Performing the same tests using helium as the driving gas resulted in the logarithmic pressure-velocity relationship illustrated in Figure 2.13. It is easily noticed that the helium easily outperforms air but unlike air the gas gun was not able to approach the speed sound for helium as closely as in the case of air. This is likely due to the fact that the barrel is initially filled with ambient air prior to projectile acceleration. Immediately after the fast-acting valve releases the pressurized helium, the barrel becomes filled with a mixture of helium and air where the density and thus the speed of sound is somewhere between that of helium and air. This mixture negatively affects the resulting velocity. As mentioned in a previous section, a typical countermeasure to increase the velocity obtained at a given initial pressure of helium is to evacuate the barrel and fill it with helium. Since additional equipment would need to be implemented and the performance obtained is satisfactory, this countermeasure is left for future improvement efforts.

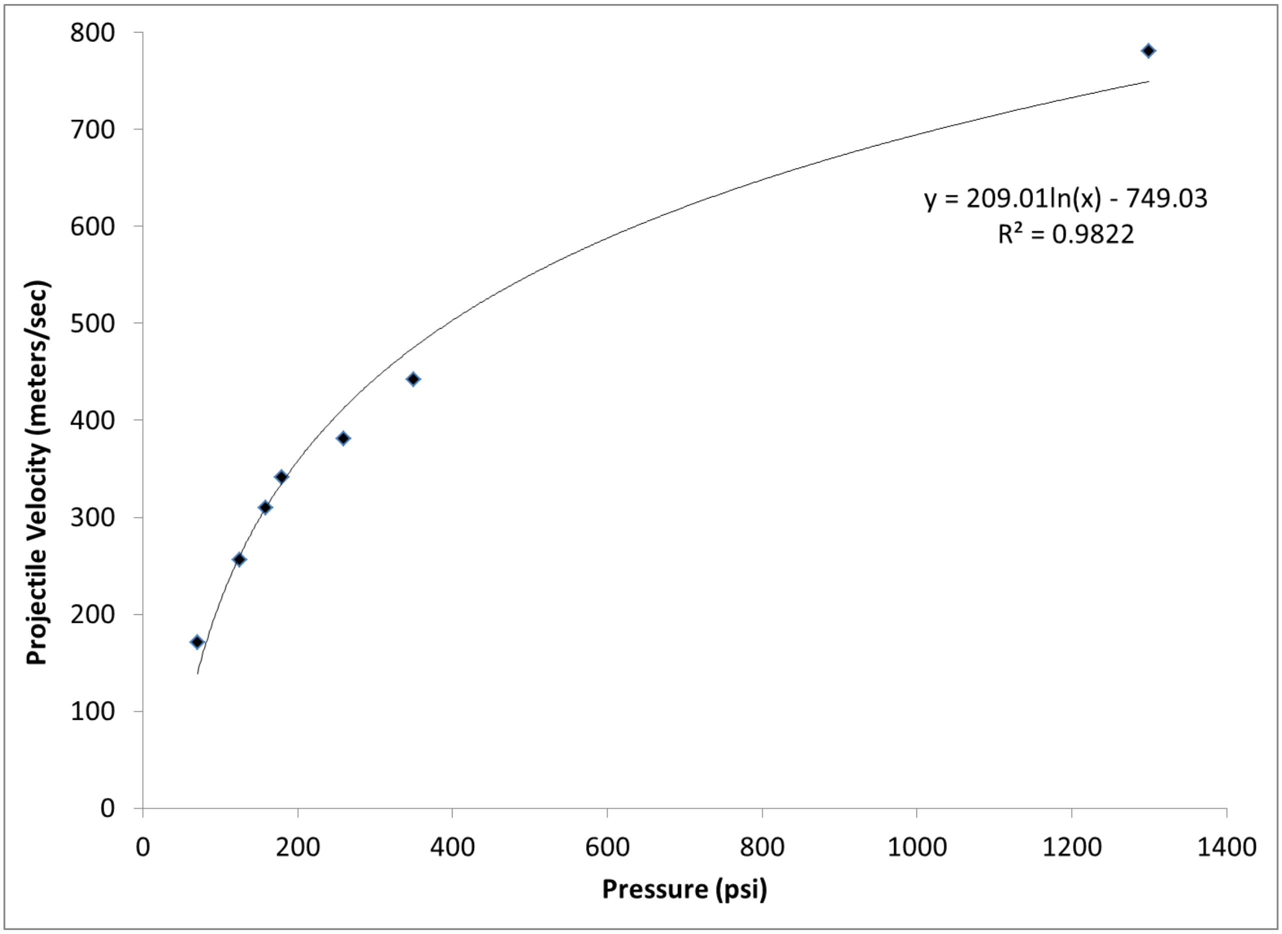

Figure 2.13: Projectile Velocity As A Function Of Pressure For Helium

Impact location accuracy and precision are part of the design parameters for the gun and also are highly important in ballistic experiments. By striking in the center of the target for each of the test shots, the experimentalist can ensure that the effect of the boundary conditions are comparable between each test and minimizes the chance the boundary conditions affect the resulting data. In Figure 2.14, a location plot of the impact is provided for a test consisting of 13 samples at various velocities in order to simulate an actual test matrix. The center of the target is at the x and y coordinates of 2.5” and 2.5”, respectively. From visual inspection, both the precision and accuracy of the gun is high. The standard deviation for the impact locations in both the x and y coordinates are 0.027” and 0.145” respectively. Reviewing the standard deviations the y coordinate location is less precise but is expected as the amount the projectile drops is related to the velocity at which it is traveling. The impact locations are no greater than a 0.14” radius from center for a maximum striking zone area of $0.062\ in^2$. Based on this analysis, the interaction effects between the impact location and the boundary conditions can be considered constant in experimental testing.

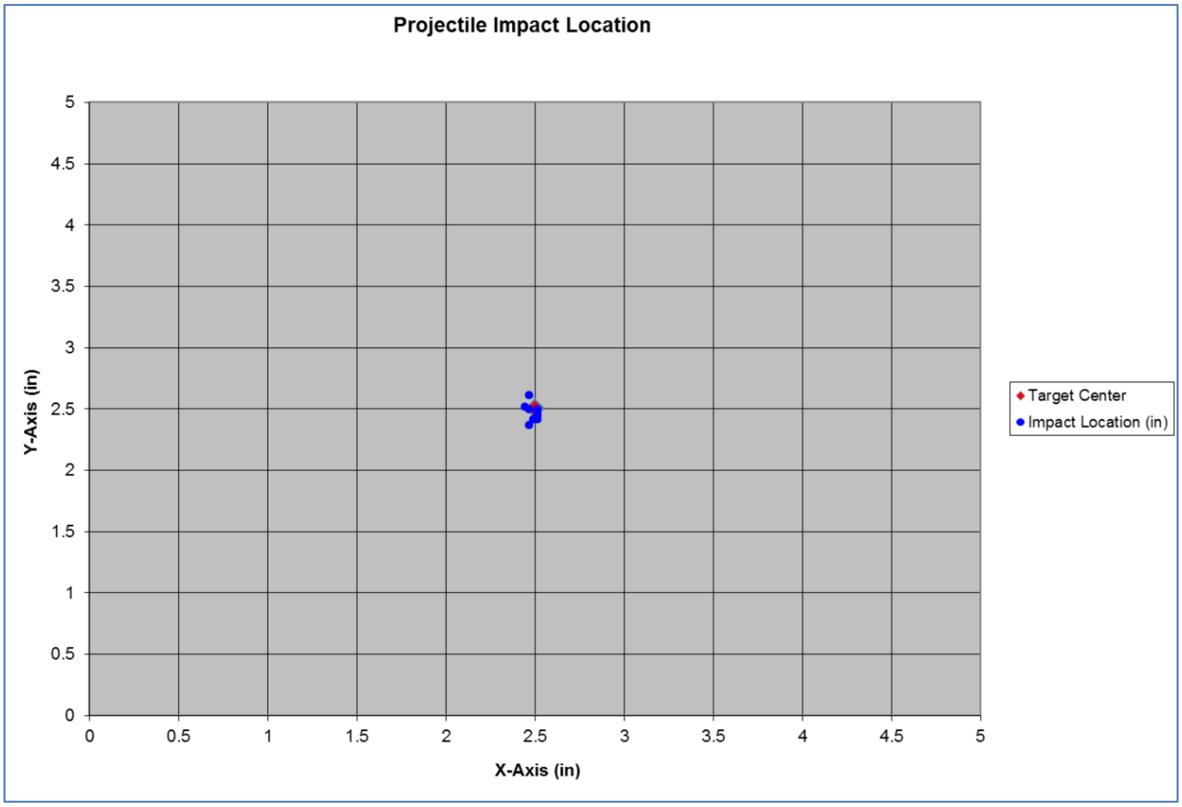

Figure 2.14: Projectile Impact Location

2.6 : Sabot Design Implementation

The sabot developed is a three piece push design consisting of three main parts: the two sabot halves and the interlocking rod. The design can readily handle solids of revolution such as spheres or cylinders having various impact geometries such as blunt, conical, parabolic, and hemispherical. Additionally the design can also house asymmetrical geometries effectively. An acetal plastic, known by the trade name Delrin, was selected as the sabot material based on its strength characteristics, low friction, and machinability. As can be seen in Figures 2.15 and 2.16, an angled ramp is added to promote sabot separation through aerodynamic forces. The interlocking rod maintains the positioning of the two halves by preventing relative translation and also provides a pivot point for sabot separation from the projectile.

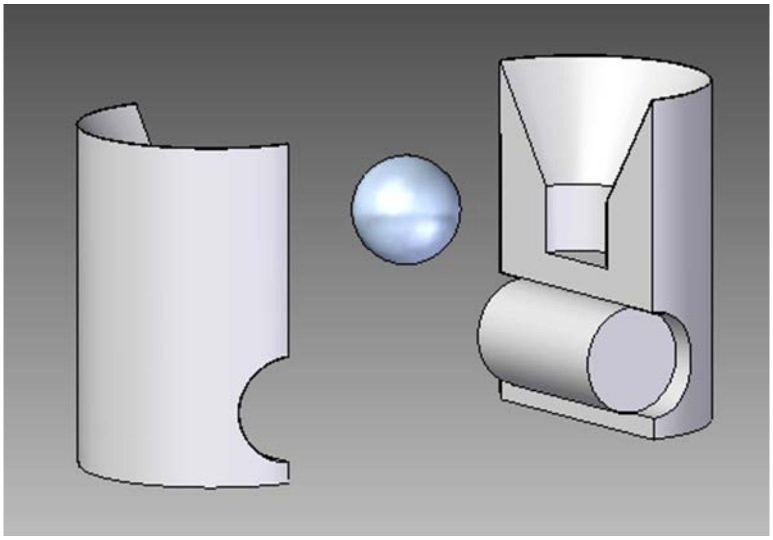

Figure 2.15: CAD Representation of Sabot Design With Spherical Projectile

A low cost method, developed by the author, utilizes common machine shop equipment to create the sabots' design features. The manufacturing method consists of seven main operations listed by equipment used and operation description:

1) Lathe - turn down a cylindrical rod of Delrin stock to the appropriate outer diameter
2) Lathe - drill to create the channel to house the projectile
3) Lathe - countersink aerodynamic ramp feature to aid in sabot separation
4) Drill press - drill channel for interlocking rod
5) Miter Saw - precut the sabot to allow for better sabot separation
6) Custom Shear Press - initiate a crack and create two sabot halves
7) Assemble three sabot pieces

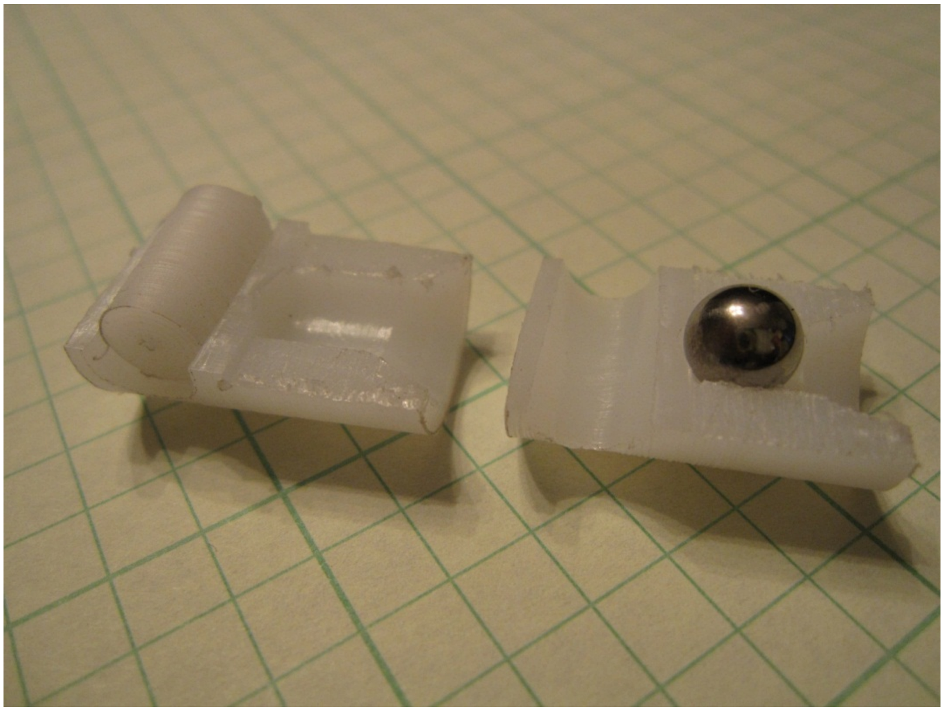

Figure 2.16: Completed Sabot With Spherical Projectile

The sawing and shear operations are highlighted in Figure 2.17. A custom shear jig was created that utilizes the mechanical advantage of a drill press to initiate a crack in the Delrin sabot as shown in Figures 2.18 and 2.19. Additionally the shear jig guides the motion of the cutting blade through the shearing process. By using a shearing process, no material is lost and the sabot retains its cylindrical cross section which ensures that proper sealing can be achieved against the barrel bore.

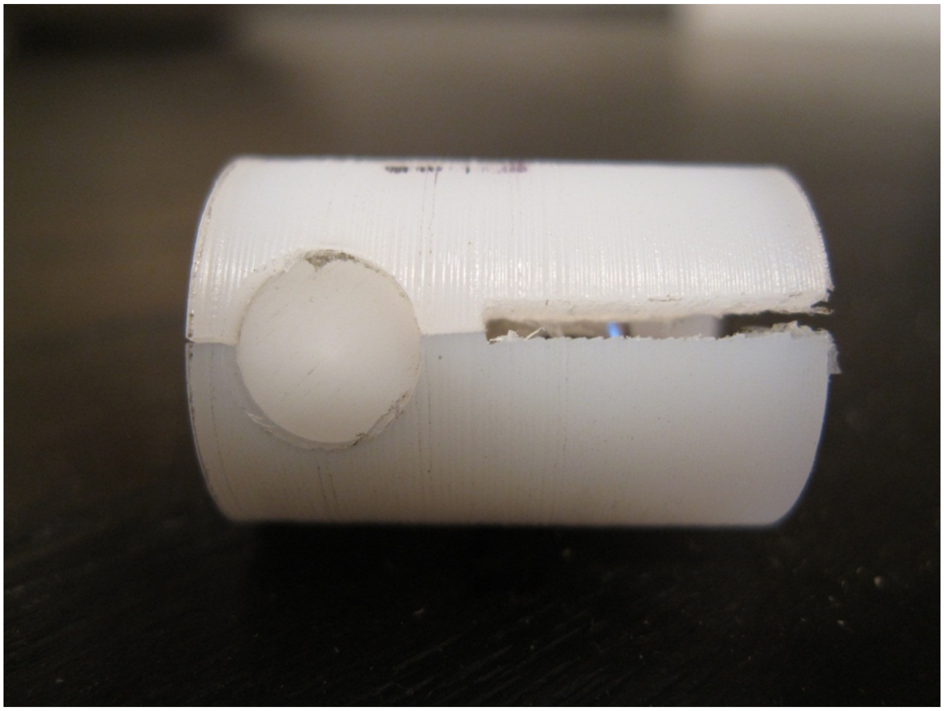

Figure 2.17: Assembled Sabot

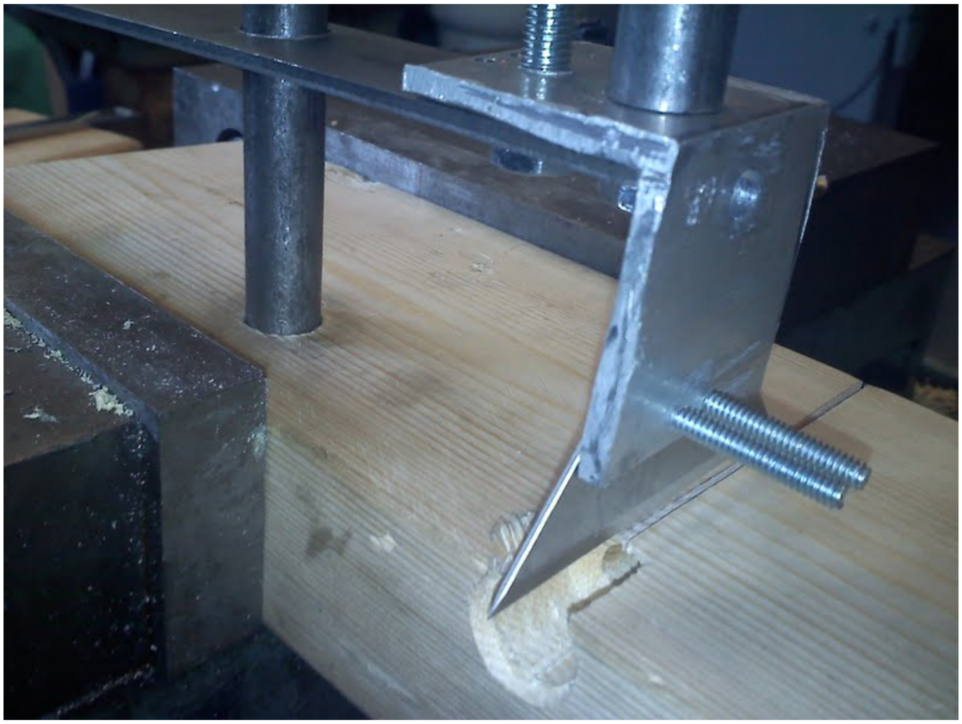

Figure 2.18: Prototype Shear Jig

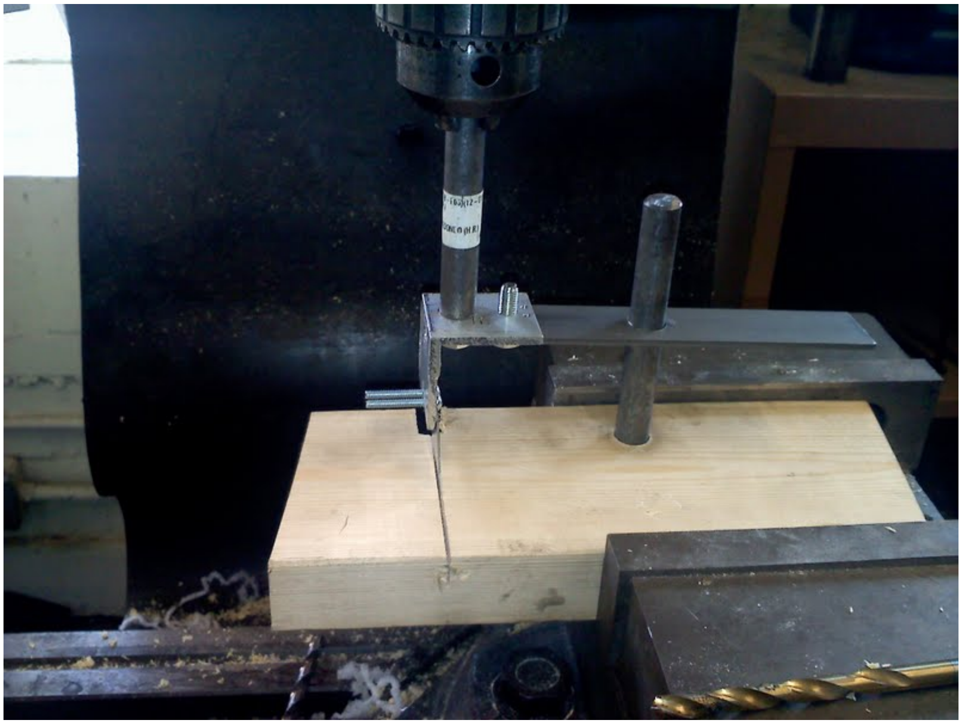

Figure 2.19: Prototype Shear Jig Mounted In Drill Press

The main benefit to the outlined manufacturing method is that it is readily modified to produce sabots that can house a wide range of size and geometries. Some of the sabots created for different testing projects are shown in Figure 2.20.

Figure 2.20: Sample Of Sabots Manufactured

2.7 : Sabot Design Validation

A high speed video camera was utilized to validate the performance of the sabot. As mentioned previously, an effective sabot design will accelerate and then separate from the projectile without affecting the trajectory or inducing trajectory deviations or attitude as illustrated in Figure 2.21. In order to validate the sabot design, cylindrical rods were shot at approximately 200 meters per second. High speed video was used to track the sabot and projectile trajectories to evaluate the sabot design. Cylindrical rods were selected as the evaluation projectile since it is prone to pitch and yaw. Since the single high speed video camera limits observation to one plane, only projectile pitch will be considered.

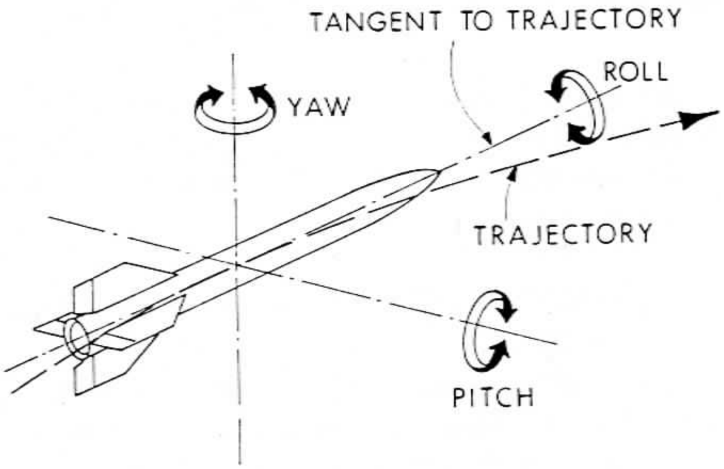

Figure 2.21: Projectile Trajectory Deviations, Attitude (Zukas, 1990)

As can be seen in the video stills of Figure 2.22, the sabot starts to separate from the projectile at 3 feet from the muzzle and is fully separated from the projectile at 4 feet. Through several rounds of experimentation, the sabot design demonstrated consistent separation from the projectile without affecting the trajectory or inducing pitch. Also evident from the video stills is that although the sabot separates from the projectile, the sabot maintains the same general trajectory as the projectile and thus additional protection is needed to protect the test sample from impact with the sabot. As illustrated in Figure 2.23, two sabot stripper plates were placed in front of the impact location to ‘strip’ or separate the sabot from the projectile. The first stripper plate is constructed of 12 gauge sheet steel and the second plate is a 0.5” thick Lexan plate. Lexan was selected for the second stripper plate to allow for light to illuminate the impact location. Each stripper plate has a hole cut to allow only the projectile to pass through the plate. The first stripper plate blocks most of the sabot but causes a particle field due to the fracture of the Delrin upon impact. The second stripper plate blocks the sabot particle field from impacting the test sample.

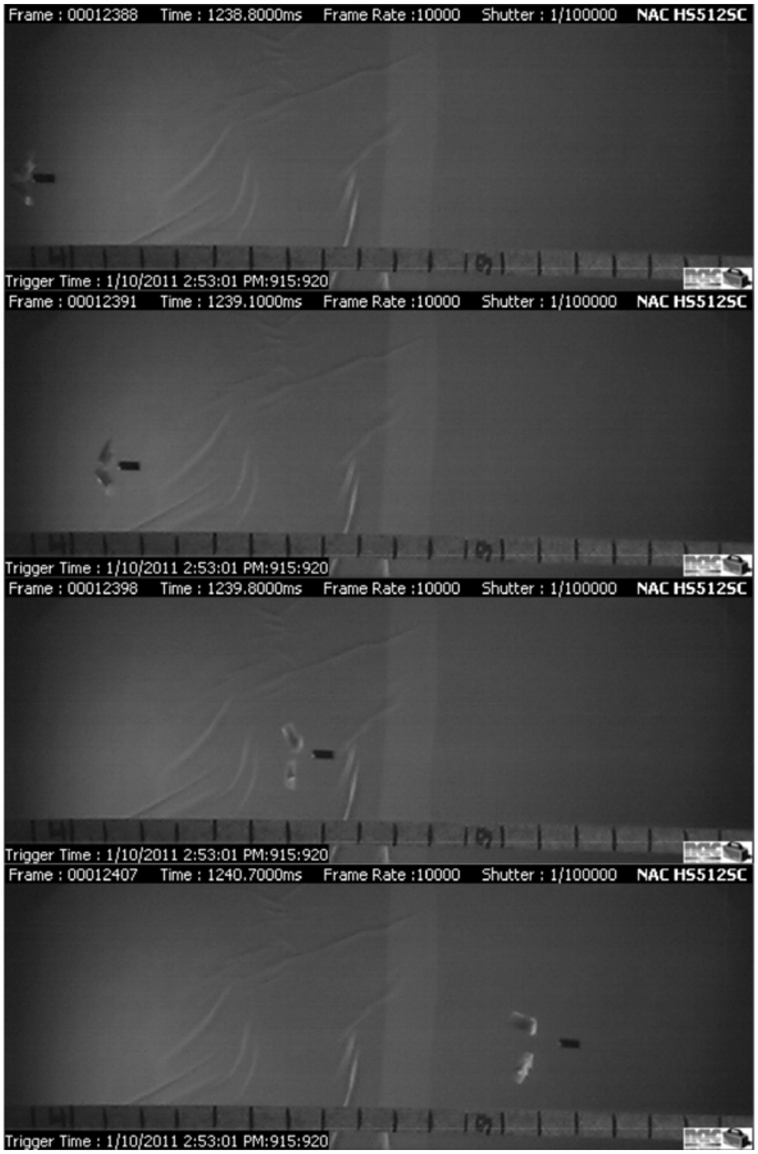

Figure 2.22: High Speed Video Stills Of Sabot Design Validation

Figure 2.23: Sabot Stripper Plates

Chapter 3 : Velocity Measurement

In order to establish the energy absorption capabilities of the composite, the velocity of the projectile both pre- and post-impact must be measured. There are several different methodologies available which include chronographs, laser array fields, and high speed video cameras. Chronographs and laser field arrays typically have two gates that are a predetermined distance apart at each point where velocity needs to be measured. As an object breaks the gate, a timer is started and stopped. The average velocity over the gate distance is calculated using the elapsed time and the gate distance. Similarly for a high speed video camera the elapsed time between each of the frames is known and using a reference distance the instantaneous velocities can be calculated for each frame. Each of the methods has its advantages and disadvantages. Chronographs and laser arrays calculate the velocity very close to real time. Thus a near instantaneous velocity readout is obtained. The main problem with chronographs and laser arrays is that the gates may not sense the object passing and no velocity calculation will be recorded. High speed cameras not only provide the velocity measurements but may also provide additional information such as the deflection of the composite panel during impact or the amount of particulate created due to impact and the particulate dispersion. However high speed video will result in many frames and require post-processing the images to calculate the velocities. So the velocity measurement is not produced in real time. All of the aforementioned methods require that lighting in the area of interest be controlled. For this study, a high speed camera was selected since it is possible to gain further insight regarding the impact event.

3.1 : High Speed Camera

The camera used for the present study is a NAC HotShot 512c shown in Figure 3.1. Its capabilities include resolutions of 512 x 512 pixels with frame rates up to 200,000 frames per second (6). The camera can record full resolution frames up to 5,000 frames per second and beyond which the resolution is reduced to maintain within the camera’s data throughput limitations (6). For the velocities and recording environment in this study, a frame rate of 10,000 frames per second and a shutter speed of 1/100,000 were found to provide suitable video quality. As mentioned earlier, lighting is a very important consideration to the video quality possible given a particular recording environment. Since the safety enclosures do not allow for much ambient lighting to enter, an array of halogen lights were utilized to illuminate the impact event. Note that special care must be taken to mitigate the level of heat gain in the composite samples when using halogen lighting due to the heat output. In addition to the halogen lighting, the interior walls of the safety enclosure were either painted or coated white to take advantage of the reflectivity provided by the white paint. An example of the resulting images is depicted in Figure 3.2. It is apparent from the image stills that additional information such as the particulate distribution can be observed.

Figure 3.1: High Speed Video Camera Used For Velocity Measurements

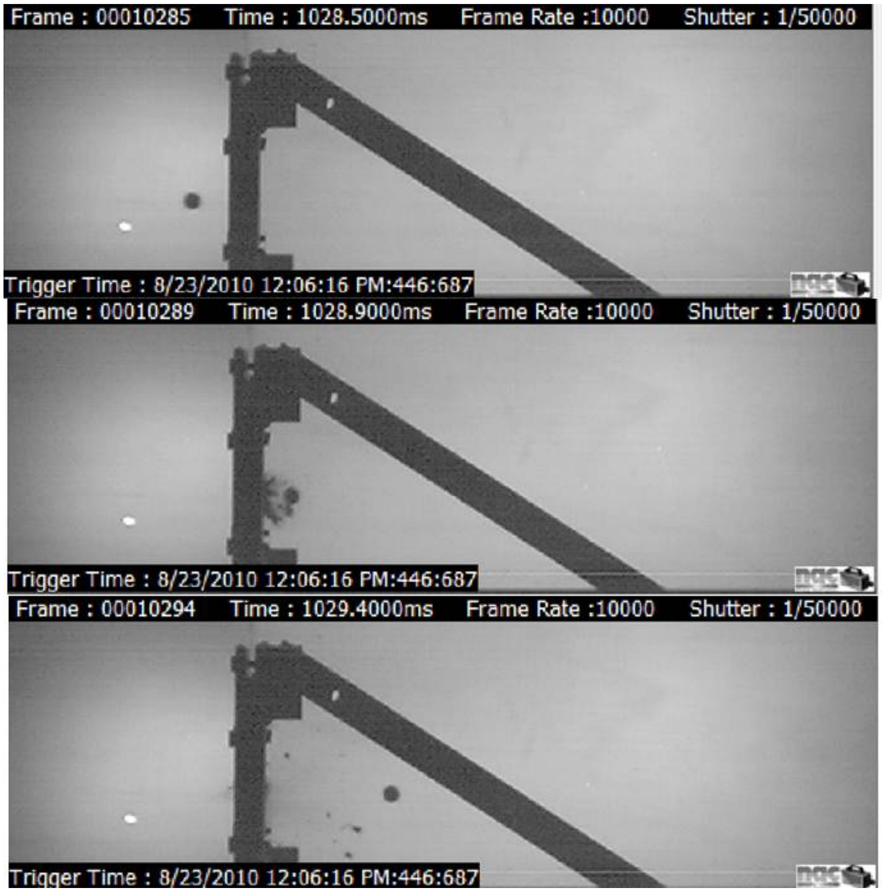

Figure 3.2: High Speed Video Frames From Composite Panel Ballistic Impact

3.2 : Velocity Calculations Using Image Processing

As mentioned earlier, velocity calculations using high speed video images requires a reference distance. Since a digital high speed camera was utilized the cameras' pixel grid array can be calibrated to an object. A common technique to obtain calibration is the use of a metric board as pictured in Figure 3.3. The metric board used in the study is a translucent plastic board with gridlines measuring 2” x 1”, vertically and horizontally, respectively. During calibration, the metric board is placed in the trajectory path of the projectile and a scaling factor is obtained from the cameras pixel grid array. The camera software provided by the manufacturer has a built-in feature to facilitate determining the scaling factor.

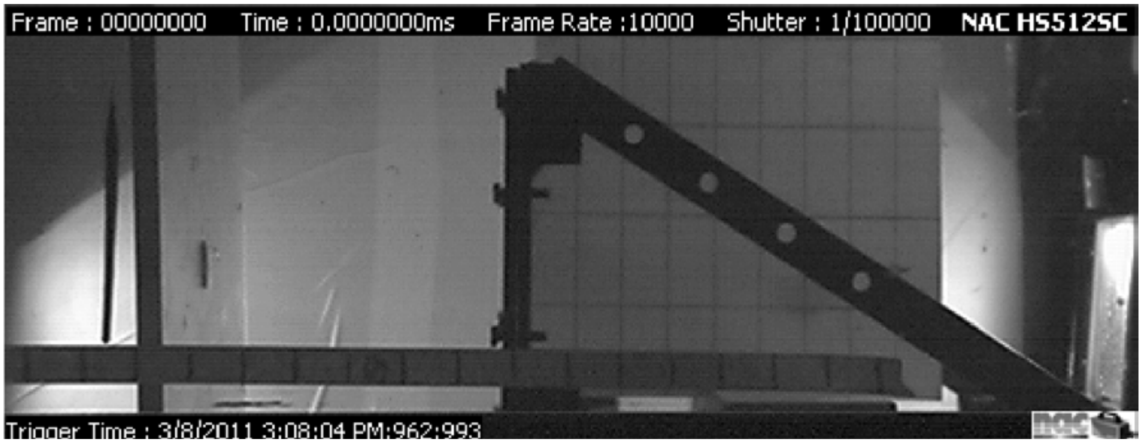

Figure 3.3: Metric Board During Calibration Of High Speed Video Camera

Since the frame rate selected for this research produces a large number of frames to postprocess for the velocity measurements, the author developed a stand-alone program to better facilitate velocity calculations of the projectile. The graphical user interface, GUI, of the velocity calculation program is shown in Figure 3.4.

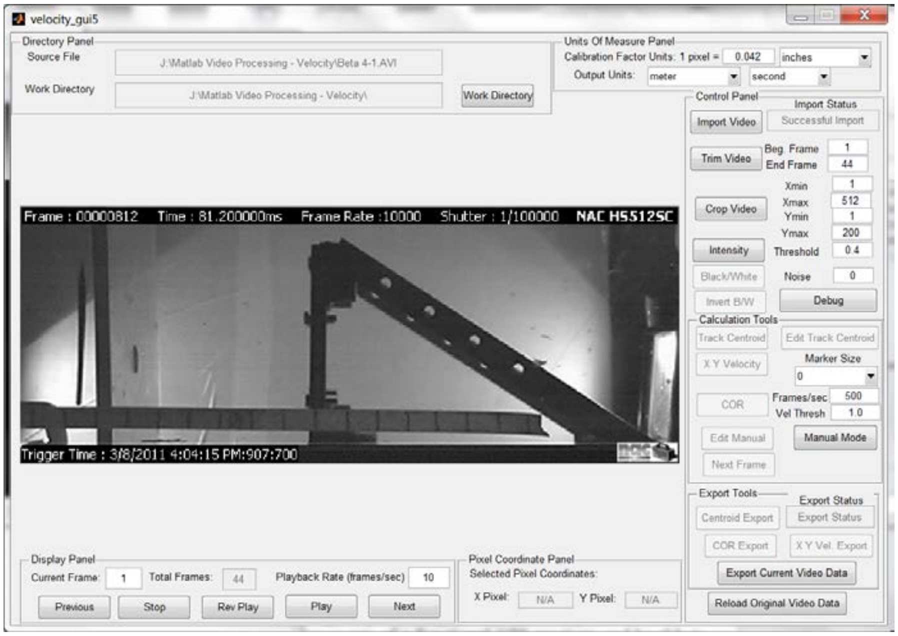
velocity_gui5

Directory Panel
Source File: J:\Matlab Video Processing - Velocity\Beta 4-1.AVI
Work Directory: J:\Matlab Video Processing - Velocity\

Units Of Measure Panel
Calibration Factor Units: 1 pixel = 0.042 inches
Output Units: meter second

Control Panel
Import Status: Successful Import
Beg. Frame: 1
End Frame: 44
Xmin: 1
Xmax: 512
Ymin: 1
Ymax: 200
Threshold: 0.4
Noise: 0

Calculation Tools
Marker Size: 0
Frames/sec: 500
Vel Thresh: 1.0

Export Tools
Export Status: Export Status

Display Panel
Current Frame: 1
Total Frames: 44
Playback Rate (frames/sec): 10

Pixel Coordinate Panel
Selected Pixel Coordinates:
X Pixel: N/A
Y Pixel: N/A

Figure 3.4: Velocity Calculation Program GUI

The program was written and compiled using the deployment compiler in MATLAB. MATLAB was chosen since the existing image processing functions could be leveraged in order to expedite the development of the program. The program can calculate the x- and y-coordinate velocities of the projectile, calculate

Coefficient of Restitution or COR, and export the resulting velocity data and processed video files. The user can select the units of measure for both time and distance.

In order to demonstrate the program flow, an example of a 1/4” steel ball impacting the composites from the research study will be given. To start the velocity calculation process, the user first imports the desired video file and trims out unnecessary frames. Next the video frames can be cropped to eliminate unnecessary pixel data as shown in Figure 3.5. The user can then adjust the pixel contrast by adjusting the pixel intensity as illustrated in Figure 3.6. The RGB data of the frames are then converted into black and white data while simultaneously removing image noise. The resulting black and white images should show the projectile as a white entity. In this case an optional function allows the user to invert the image as shown in Figure 3.7. Next the image tracking algorithm can be requested by the user. The algorithm identifies the centroid pixel coordinates of the white entity in each of the video frame images and the program marks the centroid calculated with an orange-colored marker as shown in Figure 3.8. Now, depending on the calculations desired, the user can select the x- and y-velocities or COR to be calculated. Figure 3.9 shows the plot that is outputted from the velocity calculations which in this example shows an average velocity of 154.5685 meters per second. At this point the user can choose to export the data used to calculate the velocities. For the majority of the research, the velocity data was processed in this fashion. However in the case where no perforation occurred and the projectile deflected back, the COR algorithm could be utilized. In order to demonstrate the COR calculation algorithm, an example of a baseball impacting a steel plate is analyzed. The COR can be defined as the ratio of the residual projectile velocity to the initial velocity as shown in equation 2.1.

$$COR = \frac{\mathrm{Re}\,sidual\ Velocity}{Initial\ Velocity} \qquad \textbf{2.1}$$

Figure 3.10 shows the unprocessed video file image. After processing the image in the same manner as described for the previous example, the resulting video file appears as illustrated in Figure 3.11. The plot results from the COR calculation algorithm is shown in Figure 3.12 where a COR of 0.5089 is obtained for an impact velocity of 53.616 miles per hour. The plot also shows the velocities that are averaged to compute the initial and final velocities. The COR algorithm identifies the minimum acceleration where the ball bounces back and uses a velocity threshold value inputted by the user to determine the pre- and post-impact velocities to calculate the COR as shown in Figure 3.13

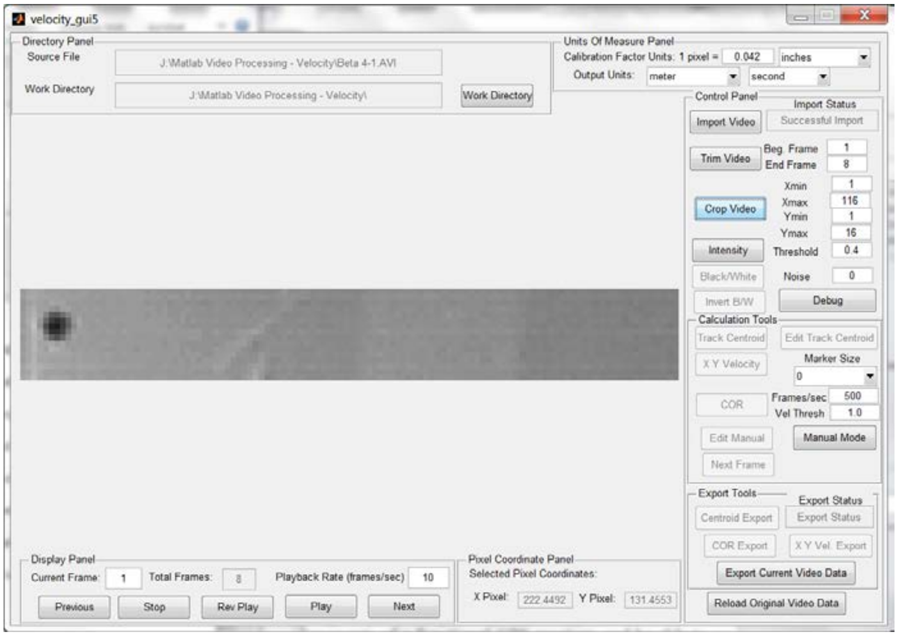

Source File: J:\Matlab Video Processing - Velocity\Beta 4-1.AVI
Work Directory: J:\Matlab Video Processing - Velocity\
Calibration Factor Units: 1 pixel = 0.042 inches
Output Units: meter second
Import Status: Successful Import
Beg. Frame: 1
End Frame: 8
Xmin: 1
Xmax: 116
Ymin: 1
Ymax: 16
Threshold: 0.4
Noise: 0
Marker Size: 0
Frames/sec: 500
Vel Thresh: 1.0
Export Status: Export Status
Current Frame: 1
Total Frames: 8
Playback Rate (frames/sec): 10
Selected Pixel Coordinates:
X Pixel: 222.4492
Y Pixel: 131.4553

Figure 3.5: Video Data Trimmed And Cropped

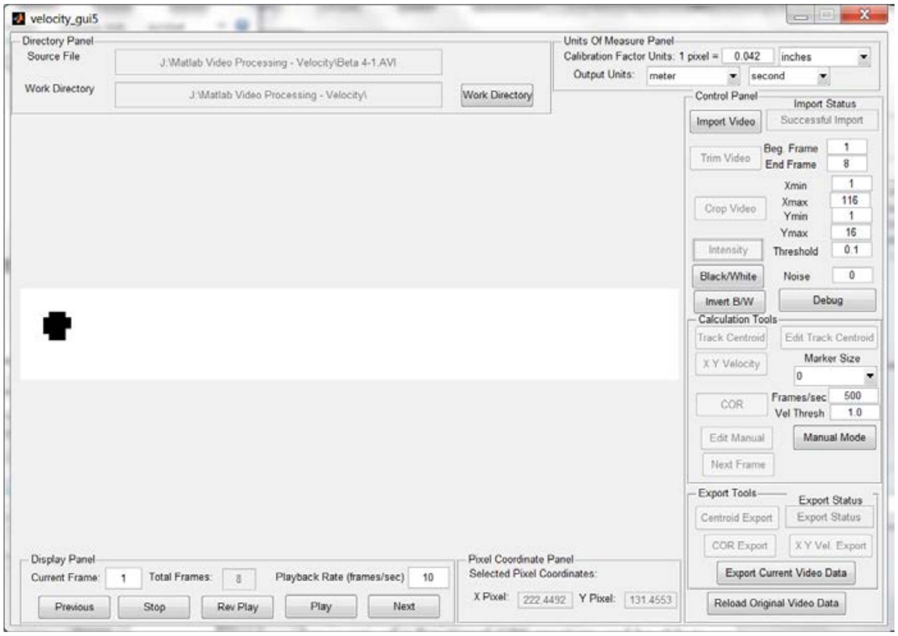

Source File: J:\Matlab Video Processing - Velocity\Beta 4-1.AVI
Work Directory: J:\Matlab Video Processing - Velocity\
Calibration Factor Units: 1 pixel = 0.042 inches
Output Units: meter second
Import Status: Successful Import
Beg. Frame: 1
End Frame: 8
Xmin: 1
Xmax: 116
Ymin: 1
Ymax: 16
Threshold: 0.1
Noise: 0
Marker Size: 0
Frames/sec: 500
Vel Thresh: 1.0
Export Status: Export Status
Current Frame: 1
Total Frames: 8
Playback Rate (frames/sec): 10
X Pixel: 222.4492
Y Pixel: 131.4553

Figure 3.6: Pixel Intensity Adjusted

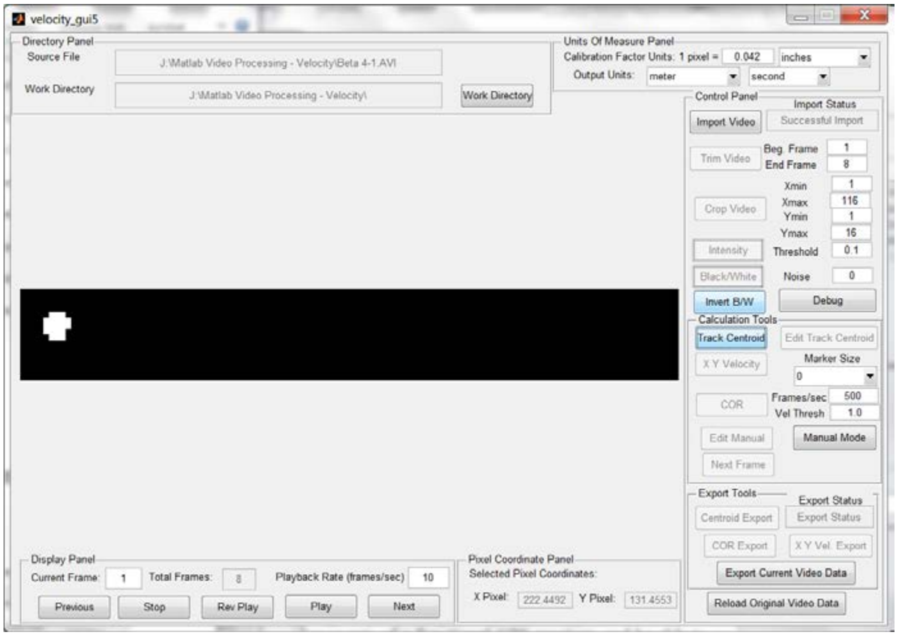

Source File: J:\Matlab Video Processing - Velocity\Beta 4-1.AVI
Work Directory: J:\Matlab Video Processing - Velocity\
Calibration Factor Units: 1 pixel = 0.042 inches
Output Units: meter second
Import Status: Successful Import
Beg. Frame: 1
End Frame: 8
Xmin: 1
Xmax: 116
Ymin: 1
Ymax: 16
Threshold: 0.1
Noise: 0
Marker Size: 0
Frames/sec: 500
Vel Thresh: 1.0
Export Status: Export Status
Current Frame: 1
Total Frames: 8
Playback Rate (frames/sec): 10
X Pixel: 222.4492
Y Pixel: 131.4553

Figure 3.7: Image Inversion

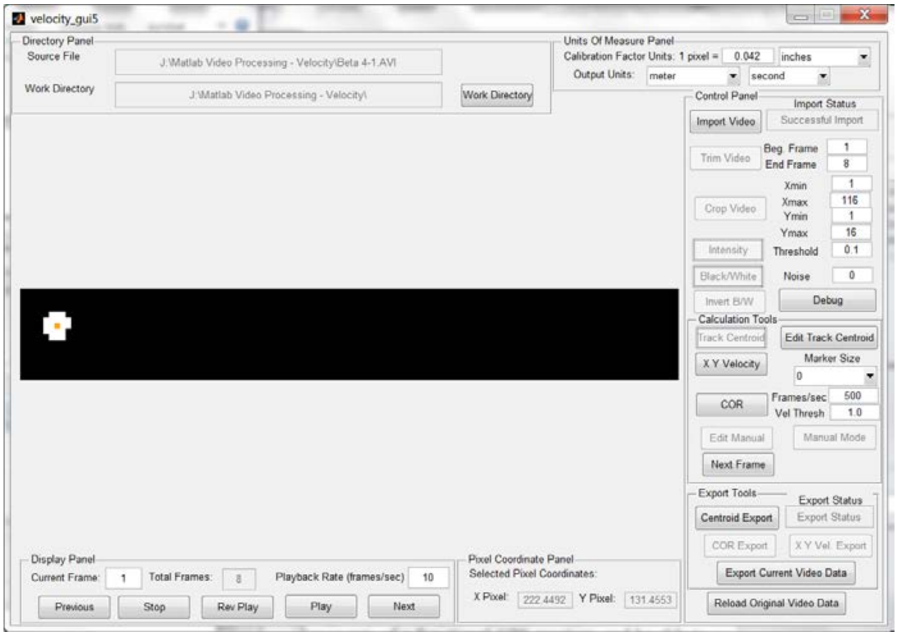

Source File: J:\Matlab Video Processing - Velocity\Beta 4-1.AVI
Work Directory: J:\Matlab Video Processing - Velocity\
Calibration Factor Units: 1 pixel = 0.042 inches
Output Units: meter second
Import Status: Successful Import
Beg. Frame: 1
End Frame: 8
Xmin: 1
Xmax: 116
Ymin: 1
Ymax: 16
Threshold: 0.1
Noise: 0
Marker Size: 0
Frames/sec: 500
Vel Thresh: 1.0
Export Status: Export Status
Current Frame: 1
Total Frames: 8
Playback Rate (frames/sec): 10
Selected Pixel Coordinates:
X Pixel: 222.4492
Y Pixel: 131.4553

Figure 3.8: Centroid Data Calculated For Video Frame Images

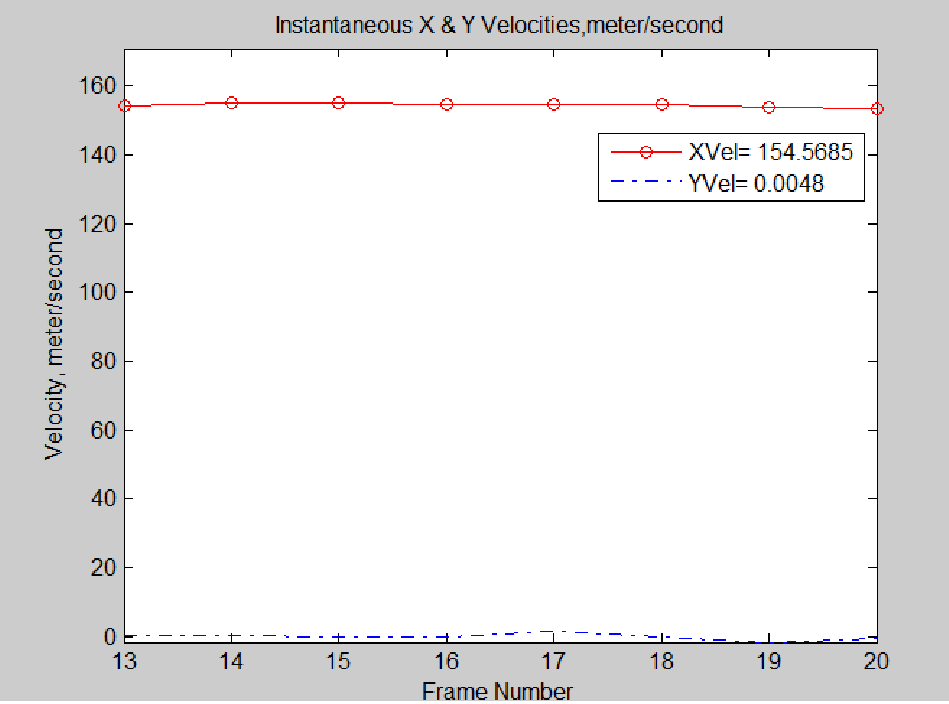

Figure 3.9: X- And Y-Velocity Plot Output

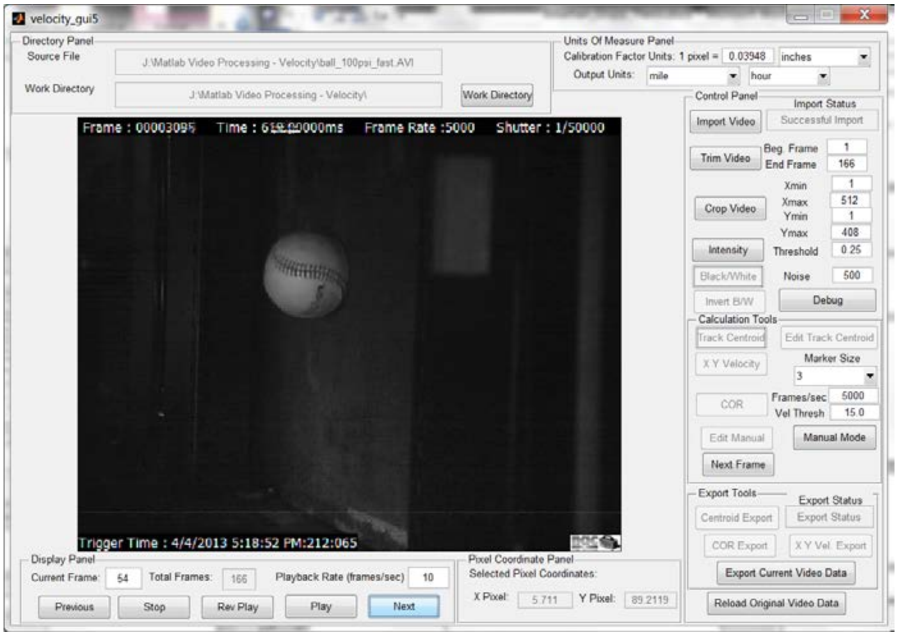
velocity_gui5

Directory Panel

Source File: J:\Matlab Video Processing - Velocity\ball_100psi_fast.AVI

Work Directory: J:\Matlab Video Processing - Velocity\

Units Of Measure Panel

Calibration Factor Units: 1 pixel = 0.03948 inches

Output Units: mile hour

Frame : 00003095 Time : 619.00000ms Frame Rate :5000 Shutter : 1/50000

Trigger Time : 4/4/2013 5:18:52 PM:212:065

Control Panel

Import Status: Successful Import

Beg. Frame: 1

End Frame: 166

Xmin: 1

Xmax: 512

Ymin: 1

Ymax: 408

Threshold: 0.25

Noise: 500

Calculation Tools

Marker Size: 3

Frames/sec: 5000

Vel Thresh: 15.0

Export Tools

Export Status: Export Status

Display Panel

Current Frame: 54

Total Frames: 166

Playback Rate (frames/sec): 10

Pixel Coordinate Panel

Selected Pixel Coordinates:

X Pixel: 5.711

Y Pixel: 89.2119

Figure 3.10: Unprocessed Baseball Impact Video

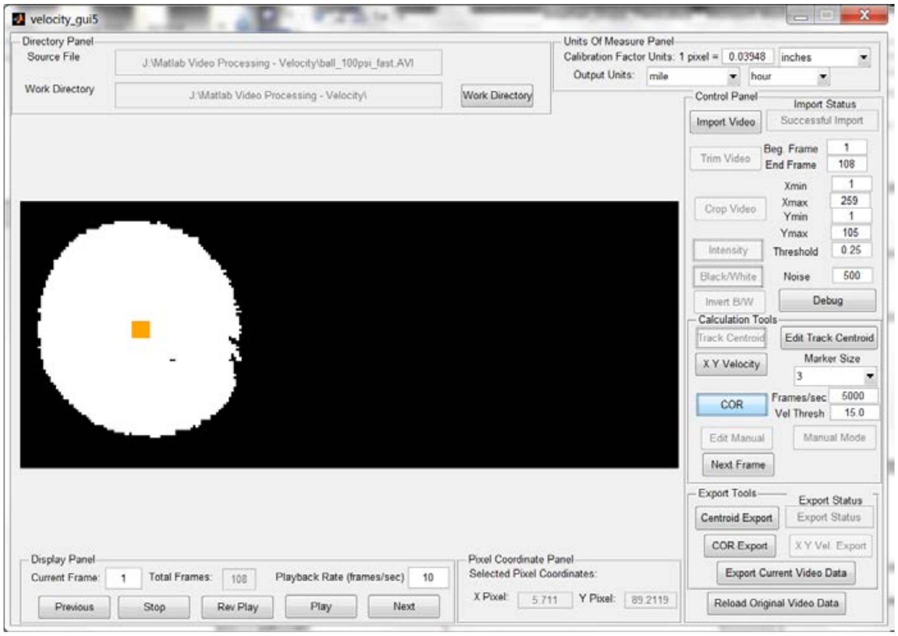
velocity_gui5

Directory Panel

Source File: J:\Matlab Video Processing - Velocity\ball_100psi_fast.AVI

Work Directory: J:\Matlab Video Processing - Velocity\

Units Of Measure Panel

Calibration Factor Units: 1 pixel = 0.03948 inches

Output Units: mile hour

Control Panel

Import Status: Successful Import

Beg. Frame: 1

End Frame: 108

Xmin: 1

Xmax: 259

Ymin: 1

Ymax: 105

Threshold: 0.25

Noise: 500

Calculation Tools

Marker Size: 3

Frames/sec: 5000

Vel Thresh: 15.0

Export Tools

Export Status: Export Status

Display Panel

Current Frame: 1

Total Frames: 108

Playback Rate (frames/sec): 10

Pixel Coordinate Panel

Selected Pixel Coordinates:

X Pixel: 5.711

Y Pixel: 89.2119

Figure 3.11: Processed Baseball Impact Video

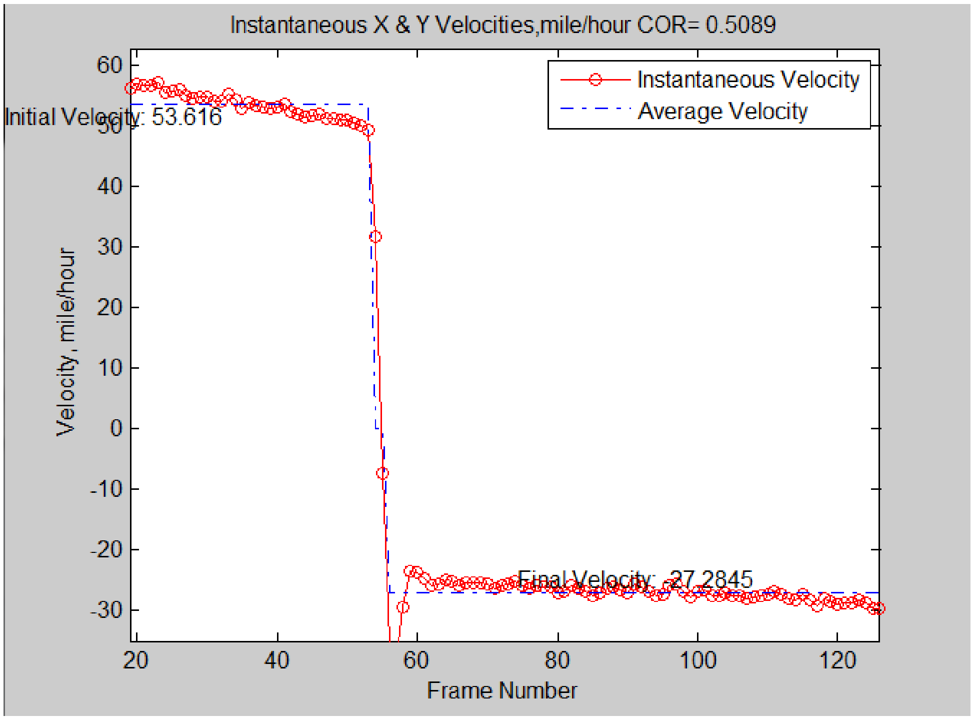

Figure 3.12: COR Output Results

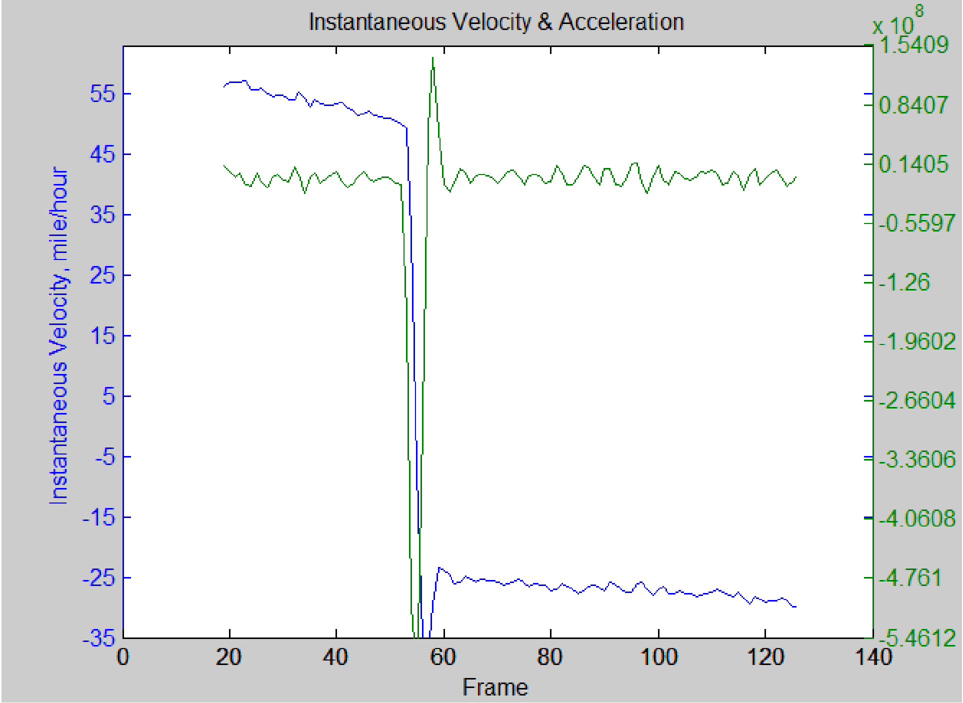

Figure 3.13: COR Algorithm; Determination of Minimum Acceleration

Chapter 4 : Composite Panel Ballistic Impact Testing Results

Experimental ballistic testing was performed for two different research projects studying composite material behavior. Previous testing has suggested that a performance differential exists between thermoplastic and epoxy composites with the same fiber structure and or layup orientation. Since the data was very limited in those preliminary observations, a more detailed study is needed to better quantify the performance differential. A formal study comparing the performance differential of thermoplastic and epoxy based composites subject to ballistic impact was performed. Additionally a new performance requirement to establish the energy absorption capability for composite structures subject to a specific falling object hazard requires an experimental test procedure. The test setup is developed and a preliminary test matrix is tested. The results from the falling object hazard test are examined for the composite behavior. Areas where improvements can be made in the initial test setup are identified.

4.1: Introduction

Carbon fiber composites are currently being adopted into applications where a combination of light weight and strength are needed. In many applications such as those in the aerospace sector, the response to errant fragments and the resulting particle debris field is pertinent to evaluate a potentially critical failure mode such as the hypervelocity impact of the Columbus module shielding (7) (8). The kinetic energy of the resulting debris field can also cause further damage to internal components such as structural elements and control systems. However experimental testing is an expensive process to incur on several possible designs. In order to reduce the amount of experimental testing needed, considerable effort is going towards a better understanding of the underlying mechanics involved in terminal ballistics and accurately modeling the response using numerical methods such as Finite Element methods (9).

In order to properly apply a numerical approach to model the impact event, experimental testing is needed for model evaluation and validation. One of the common performance characteristics in impact dynamics is the V_{50} or ballistic limit velocity (10) (11). V_{50} is defined as the velocity at which perforation of the target occurs 50% of the time and as such is considered to be the threshold for the energy absorption capabilities. There are several different methodologies to develop V_{50} experimentally. The most referenced are the Jonas-Lambert correlation and Recht-Ipson formula as shown in equations 4.1 and 4.2, respectively (12) (13).

$$V_{RES} = a\left(V_{IMP}^{2} - V_{50}^{2}\right)^{1/2}, \ a = \left(M / M + m\right) \tag{4.1}$$

$$V_{RES} = a\left(V_{IMP}^{P} - V_{50}^{P}\right)^{1/P} \tag{4.2}$$

Both are based on the conservation of energy but the Jonas-Lambert correlation utilizes a semi-empirical approach through two correlation factors: a and p (14). A minimum of three experimental data points are needed in the Jonas- Lambert correlation to solve for the three variables (15). As has been demonstrated by others, these techniques have difficulty due to the fact that as the V_{50} is approached, there is a 'zone of mixed results' where perforation predictability varies as shown in Figure 4.1 (10) (15) (16).

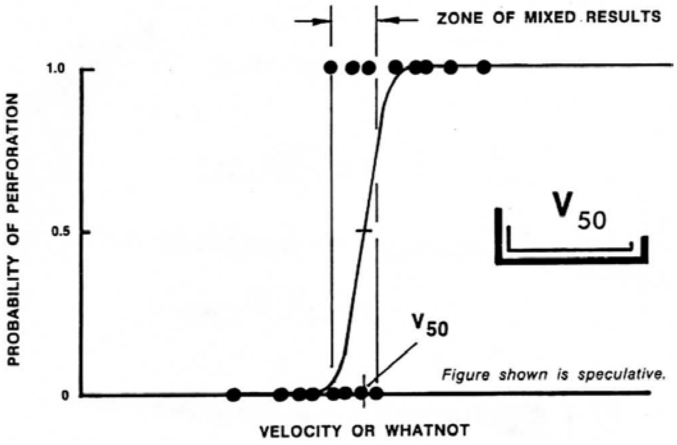

Figure 4.1: V50 And The Zone Of Mixed Results (Solsby, 1987)

The methodology used in this research is a variation on the bisection method or also known as bracketing. Generally the bisection method is the most efficient but can be still problematic in the 'zone of mixed results' (15). The operating principle starts with an initial velocity bracket based on available ballistic data for both composite construction and projectile impact geometry. The first experimental test is performed at the midpoint value of the initial velocity bracket. If perforation occurs, then a slower impact velocity will be chosen for the next shot based on the residual velocity, whereas, if perforation does not occur, then a higher impact velocity will be chosen. A velocity bracket is created in this manner where the next impact velocity is at the midpoint between the initial estimate and the initial bracket range. The testing continues until the resulting V_{50} converges within a desired range of error.

4.2 : Ballistic Impact Comparison of Thermoplastic and Epoxy Based Composites

As mentioned earlier the development of the gas gun was performed in conjunction with Mechanical Engineering undergraduate design teams. In parallel, Polymer Fiber Engineering undergraduate design teams designed, manufactured, and experimentally tested composites panels. Part of the experimental testing included high velocity ballistic testing utilizing the developed experimental gas gun system outlined previously. Several design teams created a range of composite panels using various constituent materials and layup orientations. During the course of the testing of the student-produced panels, it was observed that there was a significant performance differential between epoxy and thermoplastic based composite panels using a 4 x 4 twill woven carbon fiber fabric. Since the students produced the composites in a manual press where the pressure and temperature had to be controlled manually during the curing cycle, some of the panels were suspected to be of various levels of quality in terms of matrix infusion and void presence. This could lead to a higher variation in panel performance. Also the student teams produced very few panels for each of the experimental tests in their study which limited the significance of the performance differential observed. As such a more in-depth analysis was deemed necessary.

A common aerospace grade carbon fiber, T300 five harness satin with a 3k fiber count (T300 5HS 3k), was used as the basis of the comparison. The test matrix proposed for the testing included four different matrix constituents. These included a standard and toughened epoxy, RM2002 and RM2005 respectively, and two thermoplastics, polyphenylene sulfide (PPS) and polyethylenimine (PEI). RM2002 and RM2005 are manufactured by Renegade Materials. The epoxies are similar in formulation to Hexcell 8552 epoxy (17) (18). The thermoplastics were manufactured by Tencate (19) (20). The panels were 12 plies thick or 4.1 millimeters nominally. The layup was orientated in the 0° direction such that the warp and weft fabric orientations were the same between each ply. In previous rounds of testing, typically a minimum of five tests were needed to experimentally determine the ballistic limit velocity. For each of the four constructions, obliquity angles of 0° and 45° were tested. It is well known that the obliquity angle or angle of the trajectory path to the normal direction of the panel plane will have an effect due to both geometry considerations and also the resulting asymmetrical stress wave propagation. The test fixture, as in Figure 4.2, was adjusted appropriately to obtain the desired obliquity angles. Additionally it should be noted that a standard torque sequence was utilized on the fixture to obtain a uniform clamping pressure along the boundary condition. The torque sequence moved in a clockwise fashion where bolts across from each other are tightened. Uneven clamping pressure along the boundary condition could lead to test panel slippage and also localized crushing which can both have a significant influence on the test results.

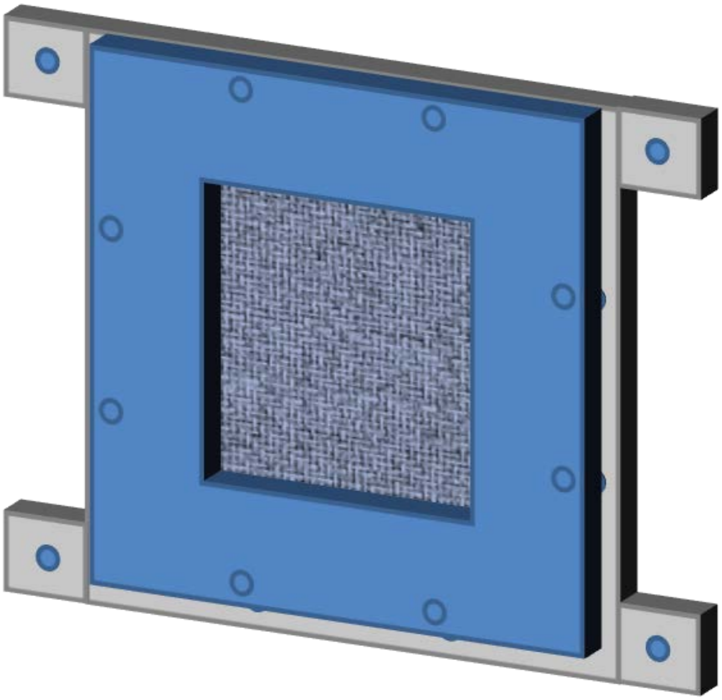

Figure 4.2: CAD Representation Of Test Sample Fixture (AMRDEC, 2010)

A total of 48 tests were performed where six panels were tested for each construction/obliquity angle combination. No replication was used in this study as this would increase the amount of experimental testing necessary considerably. Thus statistical significance cannot be reported to establish the variance of the panels tested. Each of the panels measured 6” x 6” (LW) and was constrained by a 0.5”overlap clamped condition on the perimeter such that the unconstrained portion of the panel measured 5” x 5 (LW). A CAD representation of the test fixture used in experimental testing is shown in Figure 4.2. The projectile selected for the testing was a 1/4” diameter steel spherical ball bearings. The projectile is shown with the sabot in Figure 4.3. The testing was performed using the gas gun configuration shown in Figure 2.5 with the 5/8” bore diameter. Both helium and air were used as driving gases in the experimental testing.

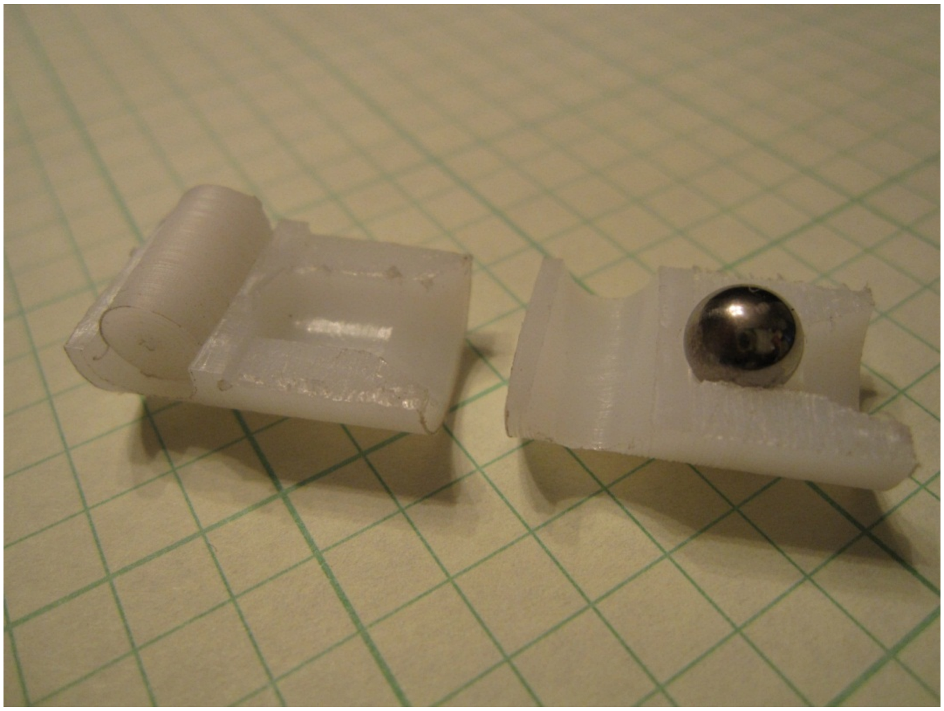

Figure 4.3: 1/4" Diameter Spherical Projectile With Sabot

The summaries of the ballistic results for the RM2005, RM2002, PPS and PEI constructions are in Tables 4.1, 4.2, 4.3, and 4.4, respectively. The entrance and exit velocities have been normalized relative to the maximum velocity in each dataset. For each of the constructions and obliquity angles, pre- and post-impact panel weights and projectile velocities were recorded. The panel weights were used to quantify the level of mass loss for each of the impact events. The digital weigh scale used has a resolution of 0.05 grams. The initial and residual velocities were measured using the high speed video camera as outlined in Section 3.2. The ballistic limit velocities or V_{50} are calculated by estimating the intercept of the initial and residual velocities.

From Tables 4.1 and 4.2, the toughened and standard epoxies performance can be compared. Initially in the testing, it was anticipated that the panels would require velocities well beyond 300 meters per second, thus helium was selected as the driving gas. However from the RM2005 epoxy test matrix in Table 4.1, helium provided too much energy for the composite panels and projectile considered. For the remainder of tests, air was used for the driving gas. The calculated ballistic limit velocities suggest that the standard epoxy, RM2002, has performance advantage in the 0° case over RM2005. However this difference is likely due to the fact the V_{50} had to be calculated based on an extrapolation of the RM2005 0° case. Therefore the performance difference between the toughened and standard epoxies is considered to be nearly negligible. This corroborates previous research findings (21).

T300 RM2005								
Matrix	ID	Obliquity	Pre Impact Wt (g)	Post Impact Wt (g)	Wt Loss (g)	Entrance Velocity	Exit Velocity	Vel Loss (%)
2005	1	0	136.15	135.70	0.45	1.00	1.00	18.0%
2005	2	0	133.65	133.25	0.40	0.86	0.80	23.9%
2005	3	0	135.85	135.35	0.50	0.77	0.69	27.2%
2005	4	0	141.85	141.45	0.40	0.58	0.42	40.3%
2005	5	0	143.15	142.95	0.20			
2005	6	0	146.25	146.10	0.15	0.51	0.32	49.6%
2005	7	0	134.95	134.85	0.10	0.48	0.29	51.2%
2005	8	45	140.15					
2005	9	45	143.85	143.85	0.00	0.62	-0.31	127.8%
2005	10	45	130.20	129.75	0.45	0.81	0.70	51.5%
2005	11	45	137.50	137.05	0.45	1.00	1.00	43.9%
2005	12	45	148.40	148.35	0.05	0.48	-0.18	121.5%

Table 4.1: T300 RM2005 Ballistic Testing Summary

T300 RM2002								
Matrix	Obliquity	ID	Pre Impact Wt (g)	Post Impact Wt (g)	Wt Loss (g)	Entrance Velocity	Exit Velocity	Vel Loss (%)
2002	0	1	122.95	123.00	-0.05	0.54	0.02	97.0%
2002	0	2	124.85	124.55	0.30	1.00	1.00	24.9%
2002	0	3	123.75	123.45	0.30	0.75	0.64	36.0%
2002	0	4	126.15	126.10	0.05	0.53	-0.10	114.1%
2002	0	5	125.40	125.30	0.10	0.66	0.47	47.0%
2002	0	6	125.45	125.25	0.20	0.61	0.41	49.6%
2002	45	7	127.65	127.25	0.40	0.81	0.75	40.5%
2002	45	8	127.75	127.25	0.50	0.68	0.44	58.3%
2002	45	9	124.45	124.25	0.20	0.58	0.13	85.5%
2002	45	10	129.80	130.75	-0.95	0.57	0.00	100.0%
2002	45	11	130.90	130.50	0.40	1.00	1.00	35.6%
2002	45	12	132.35	131.95	0.40	0.85	0.80	39.7%

Table 4.2: T300 RM2002 Ballistic Testing Summary

From Tables 4.3 and 4.4, the two thermoplastics, PPS and PEI, ballistic performance can be compared. For both the 0° and 45° obliquity angles, similar ballistic limits were observed for each thermoplastic. Since replication was not considered, error ranges were not established. Thus for the purpose of the study, the difference in ballistic performance between PPS and PEI will be considered small to negligible. A larger study will be needed to better quantify the difference between the two thermoplastics.

T300 PPS								
Matrix	Obliquity	ID	Pre Impact Wt (g)	Post Impact Wt (g)	Wt Loss (g)	Entrance Velocity	Exit Velocity	Vel Loss (%)
PPS	0	1	160.00	159.85	0.15	1.00	1.00	35.5%
PPS	0	2	159.50	159.55	-0.05	0.70	0.00	100.0%
PPS	0	3	160.45	160.45	0.00	0.51	-0.15	118.9%
PPS	0	4	160.15	160.15	0.00	0.83	0.51	60.4%
PPS	0	5	160.05	159.95	0.10	0.62	-0.17	117.5%
PPS	0	6	160.40	160.35	0.05	0.83	0.52	59.9%
PPS	45	7	160.95	160.85	0.10	0.91	0.25	85.3%
PPS	45	8	158.40	158.35	0.05	0.86	0.31	80.8%
PPS	45	9	158.75	158.45	0.30	1.00	1.00	45.6%
PPS	45	10	158.65	158.45	0.20	0.94	0.77	55.2%
PPS	45	11	160.25	161.35	-1.10	0.82	0.00	100.0%
PPS	45	12	159.65	159.55	0.10	0.78	-0.28	119.1%

Table 4.3: T300 PPS Ballistic Testing Summary

T300 PEI								
Matrix	ID	Obliquity	Pre Impact Wt (g)	Post Impact Wt (g)	Wt Loss (g)	Entrance Velocity	Exit Velocity	Vel Loss (%)
PEI	1	0	159.30	158.85	0.45	1.00	1.00	37.4%
PEI	2	0	159.75	159.55	0.20	0.74	0.09	92.8%
PEI	3	0	157.25	157.25	0.00	0.60	-0.14	114.5%
PEI	4	0	159.35	158.95	0.40	0.90	0.78	45.9%
PEI	5	0	160.05	159.80	0.25			
PEI	6	0	160.15	160.25	-0.10	0.71	-0.12	110.5%
PEI	7	45	159.65	159.15	0.50	0.84	0.59	57.6%
PEI	8	45	160.05	159.45	0.60	0.76	0.36	71.3%
PEI	9	45	159.95	159.85	0.10	0.66	-0.05	105.0%
PEI	10	45	159.95	159.55	0.40	0.85	0.58	58.2%
PEI	11	45	157.35	156.80	0.55	1.00	1.00	39.3%
PEI	12	45	157.05	156.60	0.45	0.79	0.56	57.4%

Table 4.4: T300 PEI Ballistic Testing Summary

The ballistic data for the epoxies and thermoplastics in Tables 4.1, 4.2, 4.3, and 4.4 can be reorganized for graphical plot comparison. Based on the results obtained previously, a negligible performance difference is assumed within each matrix class: epoxies and thermoplastics. Therefore the data and plots are organized to compare the matrix classes. The 0° and 45° obliquity cases are illustrated in Figures 4.4 and 4.5, respectively, using the normalized velocity data. It is readily apparent that the ballistic limit velocity is noticeably different between the thermoplastic and epoxy matrices. Regardless of the obliquity angle used, the thermoplastics outperform the epoxies by approximately 10%.

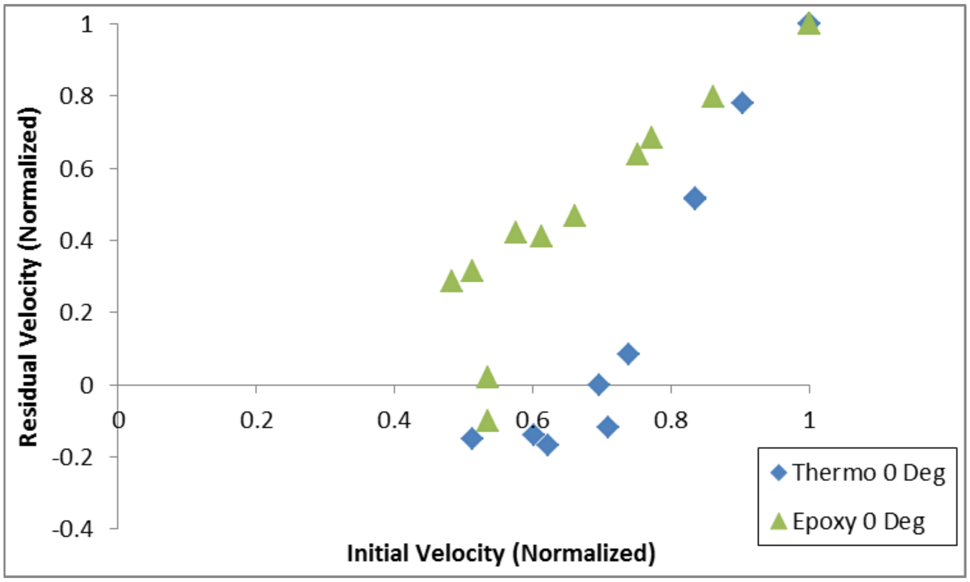

Figure 4.4: 0° Obliquity Ballistic Performance Thermoplastic And Epoxy Comparison

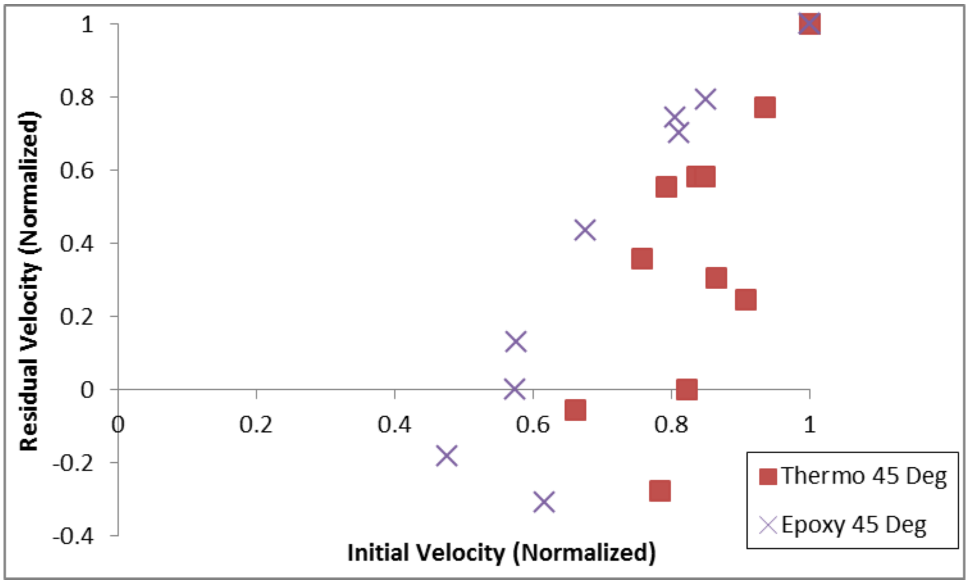

Figure 4.5: 45° Obliquity Ballistic Performance Thermoplastic And Epoxy Comparison

4.3 : Falling Object Hazard, Ballistic Impact With Large Diameter Projectiles

Up to this point the majority of the testing has been performed with emphasis on examining the perforation of composite panels with small projectiles. A new test requirement was needed to establish the energy absorption of composite panels to an impact of a 6 ounce, 1-3/8” diameter steel sphere traveling at an initial velocity of 150 feet per second. The test is intended to simulate a falling object hazard for composite structures. In the test, penetration and indentation may occur but it is expected that the composites will not be perforated. In order to facilitate testing, the gun was modified to handle the larger projectile as outlined in Figure 2.9. The sabot design and manufacturing process defined in Section 2.6 were modified in order to handle the larger projectile. The resulting sabot with the projectile is shown in Figure 4.6. The assembled sabot with the 1-3/8” diameter projectile is shown in Figure 4.7. In order to keep testing costs low and to avoid special machining, a standard ball bearing was used for the experimental testing. Figure 4.9 shows early sabot development while testing a composite sample at approximately 658 feet per second. The video demonstrates that the operating principles of the sabot translate to the larger design to provide a controlled trajectory. Machining for the large sabot was slightly more difficult and thus made obtaining a good fit in the barrel bore more challenging. In order to compensate for the machining difficulties, layers of masking tape were applied on the sabot interior. The layered tape, as shown in Figure 4.6, provided the additional gauge to ensure good sealing in the barrel bore and therefore provide repeatable gun performance in both projectile velocity and trajectory.

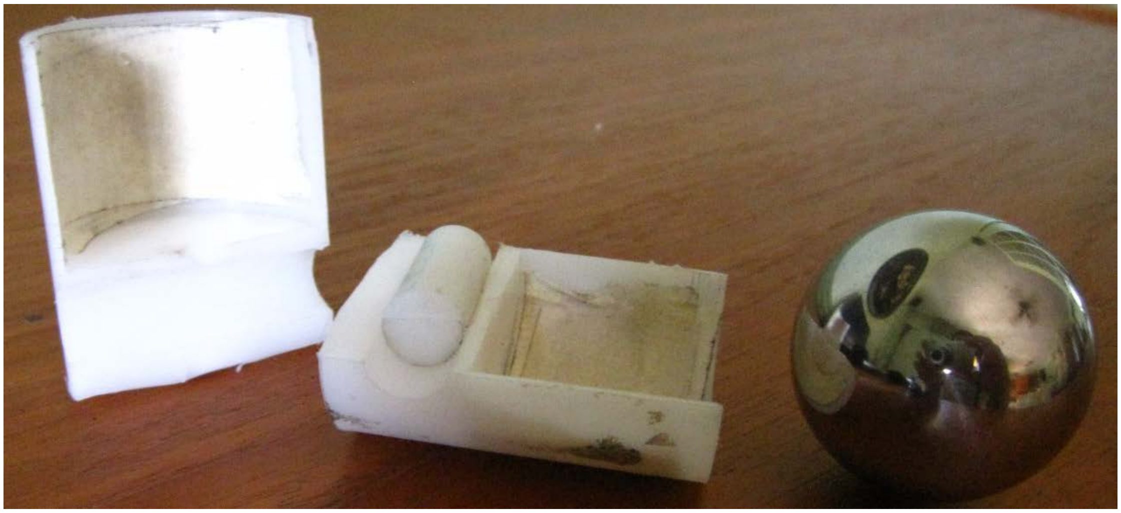

Figure 4.6: 1-3/8" Spherical Sabot

Figure 4.7: Assembled 1-3/8" Spherical Sabot With Projectile

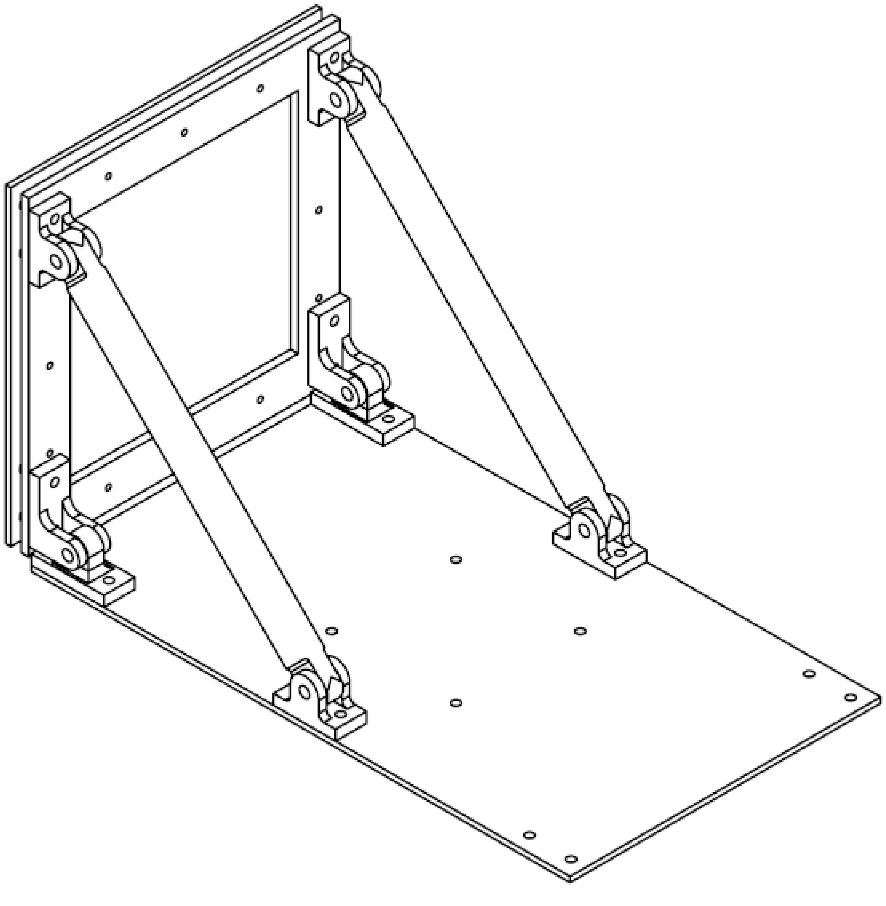

Figure 4.8: CAD Representation Of Large Projectile Test Fixture (AMRDEC, 2012)

Figure 4.9: High Speed Video Stills Of Large Projectile Sabot Development; 658 fps

Since the test fixture for previous testing would place the boundary condition too close to the impact area, a larger test fixture was developed. Figure 4.8 shows the CAD representation of the large test fixture. The fixture is a larger version of the previous design. It also allows for obliquity angles of 0° and 45°. The intended panel size for the fixture is 12” x 12” (LW) with the same 0.5” overlap clamped condition along the perimeter. The free portion of the panel measures 11” x 11” (LW). The same standard torque sequence mentioned previously is utilized for the large test fixture to ensure even clamping pressure. The floor of the safety enclosures were further reinforced to minimize the amount of deflection anticipated from the larger mass of the projectile and the mechanical advantage from the larger test fixture.

A limited test matrix was performed to compare quasi-isotropic layup carbon fiber/epoxy and carbon fiber/nylon composite panels to a reference of aluminum (AL6061). Since the testing is currently in the preliminary phases, this round of testing is performed with the intent of establishing the baseline material performance in addition to evaluation of the test itself. For each of the three materials, four tests were performed where different thickness samples were tested to an impact of approximately 150 feet per second with the large projectile. In order to consistently obtain an initial projectile velocity of 150 feet per second, air was chosen as the driving gas. Additionally the assembled sabot, as in Figure 4.7, was fitted prior to each test and gauge was adjusted using the layers of tape mentioned previously. A summary of the results for the considered materials is outlined in Table 4.5.

Test #	Panel	Thickness, in	Initial Velocity, fps	Residual Velocity, fps	COR	Initial Weight, gr	Residual Weight, gr
1	Aluminum	0.10	178.14	-58.35	0.328		
2	Aluminum	0.10	171.76	-54.29	0.316		
3	Aluminum	0.09	150.20	-51.45	0.343		
4	Q-I-Epoxy	0.51	158.52	-31.48	0.199		
5	Q-I-Epoxy	0.39	156.38	-44.54	0.285	1359.20	1359.20
6	Q-I-Epoxy	0.26	157.99	-65.29	0.413	912.45	912.45
7	Q-I-Epoxy	0.13	159.88	-81.80	0.512	461.65	461.65
8	Carbon/Nylon	0.42	157.51	-24.72	0.157	1354.05	1354.05
9	Carbon/Nylon	0.30	161.12	-32.24	0.200	939.90	938.96
10	Carbon/Nylon	0.20	162.73	-44.43	0.273	591.55	591.35
11	Carbon/Nylon	0.10	155.81	-60.20	0.386	336.45	336.35
12	Aluminum	0.09	160.33	-52.59	0.328		

Table 4.5: Large Projectile Impact Test Summary

Velocities were measured using the methods outlined in Section 3.2. The coefficient of restitution (COR) for each of the test cases were also calculated using the analysis software developed. As expected, the COR for the composites have an inverse relationship with respect to the thickness of the composites such that the COR increases as the thickness decreases. This phenomenon is mainly due to what is commonly referred to as the ‘trampoline’ effect. As the material becomes thinner, the material starts to behave more like a trampoline and will more readily deform and deflect impact. As the thickness increases, the panel becomes stiffer and deforms less. Therefore more energy is absorbed through the increased stiffness and mass and also internal damage mechanisms such as delamination and matrix cracking. Figure 4.10 compares the relationship of COR with respect to the sample thickness. For the samples considered the quasi-isotropic carbon fiber composite mechanically dissipates more of the projectile energy evident by the higher COR values for comparable sample thicknesses. Meanwhile the carbon/nylon composite absorbs more of the projectile energy.

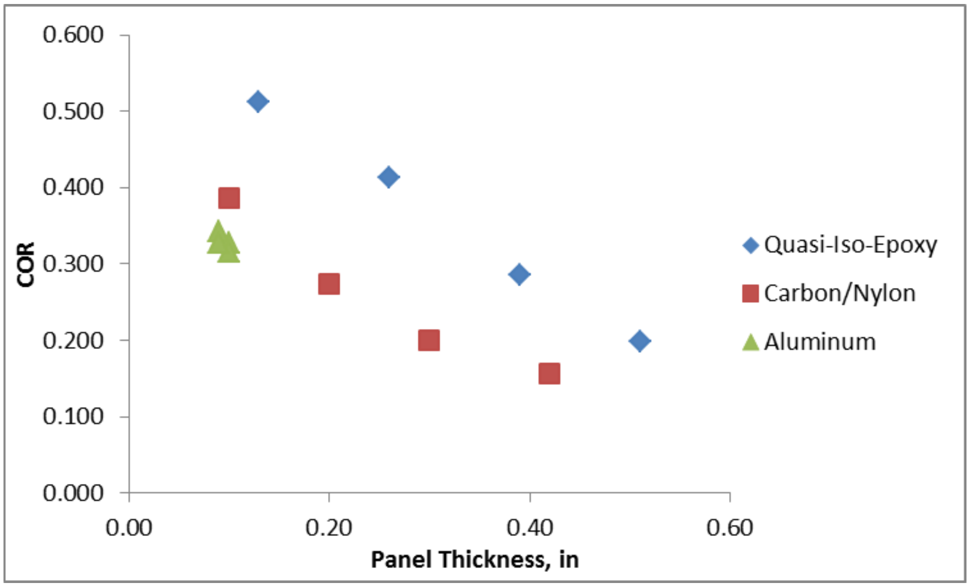

Figure 4.10: COR As Function Of Sample Thickness

The modifications made to the gun configuration allowed for simulation of the falling object hazard. However some issues were noticed with the test fixture developed. During testing at the prescribed impact velocity, noticeable deflection was observed in the test fixture. The majority of the deflection of the test fixture resulted from the mid-span flexure. The progression of the flexure during impact for test 6 is shown in Figure 4.11. The arrows highlight the flexure where both bending and twisting is observed. Additionally the test fixture deflected due to flexure in the safety enclosure despite the reinforcements installed prior to testing. It is unclear the level of influence the test fixture flexure has on the composite response. A formal study could be performed to quantify the influence of the test fixture flexure has on the composite response. Based on the observed performance of the test setup, several improvements are suggested for future falling object hazard testing. The test fixture needs a higher level of rigidity which can be obtained by using thicker plates for clamping the plate or by switching to steel from the aluminum currently used. Also further reinforcement is needed for the safety enclosure floor.

Figure 4.11: Test Fixture Mid-span Deflection

Chapter 5 : Viscoplastic Composite Model

The plasticity framework can effectively be used to describe the nonlinear, rate-dependent behavior observed in composites. A viscoplastic material model is presented that is suitable for a wide range of composites under various loading conditions. The model makes no assumption regarding whether plasticity can form in the fiber axial direction. A return mapping integration scheme is presented suitable for the viscoplastic material model. Since the model requires more parameters than the models typically used in the literature, an optimization algorithm has been developed to determine the parameters for the viscoplastic model. Finally the model is considered for a unidirectional carbon fiber composite presented in the literature. The model results are compared to the published experimental data.

5.1 : Development of Sun's Plastic Potential

The associated flow rule is stated as shown in equation 5.1 where f is the plastic potential function and $d\lambda$ is the proportionality factor (22). The associated flow or normality flow rule implies that the plastic strain formation is in normal direction from the yield surface (23). The term associated is due to the fact that the flow rule and yield criterion are the same functions (23).

$$d\varepsilon_{ij}^{p} = \frac{\partial f}{\partial \sigma_{ij}} d\lambda \qquad \textbf{5.1}$$

Hill proposed a generalized orthotropic plastic potential based on the von Mises' J2 plasticity theory where the Baushinger effect was ignored and that the addition of hydrostatic loading has no influence on yielding, the plastic potential, or yield criterion (24). The form of Hill's plastic potential takes the form shown in equation 5.2. The expression is equivalent to von Mises' criterion when $F = G = H$ and $L = M = N = 3F$ (24).

$$2f(\sigma_{ij}) = F\left(\sigma_{22} - \sigma_{33}\right)^2 + G\left(\sigma_{33} - \sigma_{11}\right)^2 + H\left(\sigma_{11} - \sigma_{22}\right)^2 + 2L\sigma_{23}^2 + 2M\sigma_{31}^2 + 2N\sigma_{12}^2 \qquad \textbf{5.2}$$

Based on Hill's plastic potential, Sun and Chen proposed a more generalized form of the orthotropic plastic potential shown in equation 5.3 which did not have the restriction of no plasticity due to hydrostatic loading (22).

$$\begin{aligned} 2f(\sigma_{ij}) &= a_{11}\sigma_{11}^2 + a_{22}\sigma_{22}^2 + a_{33}\sigma_{33}^2 \\ &+2a_{12}\sigma_{11}\sigma_{22} + 2a_{23}\sigma_{22}\sigma_{33} + 2a_{13}\sigma_{11}\sigma_{33} \\ &+2a_{44}\sigma_{23}^2 + 2a_{55}\sigma_{13}^2 + 2a_{66}\sigma_{12}^2 \end{aligned} \qquad \mathbf{5.3}$$

Sun and Chen originally formed a 2-D viscoplastic model where the simplifying assumptions were that no plastic strain occurred along the fiber direction, no plasticity forms due to dilatation, and transverse isotropic behavior (22). Equation 5.4 is the form derived for the plastic potential where $a_{22} = 1$ (22).

$$2f(\sigma_{ij}) = a_{22}\sigma_{22}^2 + 2a_{66}\sigma_{12}^2 \qquad \mathbf{5.4}$$

Chen et al observed that in effect by making the aforementioned simplifications the derived plastic potential for the special case of transverse isotropy is equivalent to Hill's (25). Chen et al further illustrated that for some cases, such as the example of Boron-Aluminum examined, exhibit plasticity under uniform dilatation (25). Thiruppuzhi and Sun applied the form of the Sun and Chen's 2-D viscoplasticity model shown in equation 5.4 to an Abaqus Finite Element material model for strain rates from 0.0001 to 1.0 per second (26). Using the recommendations made by Ninan et al, Tsai and Sun performed a comprehensive analysis on the model by performing off-axis compressive Split Hopkinson Bar testing at various angles and compared the determined plastic potential coefficients and parameters for low strain rate and those determined from strain rates ranging from 400 to 1000/s (27) (28). Tsai and Sun found that the low strain rate parameters could be applied to higher strain rate loadings and produce good model results (28). Weeks and Sun proposed a 3-D viscoplastic model using the same assumptions made by Sun and Chen where the plastic potential takes the form shown in equation 5.5 and compared the model to experimental data for strain rates ranging from 10e-6 to 1000 per second from servo-hydraulic and Split Hopkinson testing (29). The Split Hopkinson testing was performed from

100 to 1000 per second on balanced angle ply composites (29). Weeks and Sun obtained good results from the 3-D viscoplasticity model and posited that the model could also be applied to determine the off-axis behavior (29).

$$2f(\sigma_{ij}) = \left(\sigma_{22} - \sigma_{33}\right)^2 + 4\sigma_{23}^2 + 2a_{66}\left(\sigma_{13}^2 + \sigma_{12}^2\right) \quad 5.5$$

Recently Flesher et al applied the aforementioned 3-D viscoplastic model to carbon fiber triaxial braided composites tubes for dynamic crush simulations (30) (31) (32). A simple micromechanical model was implemented where the axial tows were assumed to have no undulation and took into account the 'scissoring' effect of triaxial composites. Flesher also developed a new procedure to determine the a_{66} parameters through the use of rail-shear test data (31). Janapala et al also have recently have expanded upon Flesher's work by developing a more generalized form of the plastic potential to model the behavior of Kevlar braided tubes to dynamic crush, although the actual form of the adopted plastic potential was not reported (33). As noted by Janapala et al, the original assumptions that plastic strain did not occur in the tow direction is no longer applicable due to both the rate dependency and plastic behavior of Kevlar (33). This is readily apparent in the tensile Split Hopkinson testing from the work of Wang et al for Kevlar fiber bundles reproduced in Figure 5.1 (34). From the positive initial results, Janapala et al posited that the model was suitable and could be applied to impact analysis (33).

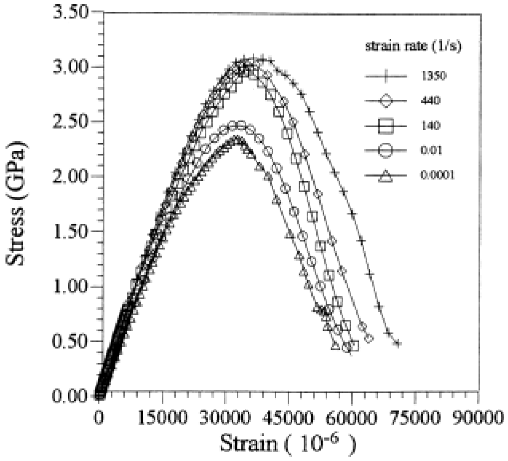

Figure 5.1: Stress-strain curves of Kevlar 49 fiber bundles, Wang et al (34)

5.2: Derivation of Viscoplastic Model

In the scope of the present work, a more generalized version is desired to represent behavior of a wider range of composites constituents. In order to be suitable for more fiber types, some of the plasticity potential constraints such as the lack of plasticity forming along the axis of the tow are removed.

Chen and Sun later revisited the Hill type plastic potential and derived a new form based on the finite element results from a representative volume element (RVE) of a square packed array composite fiber (35). Based on the RVE study, the following observations were made:

a) 'Plastic strains are compressible and plastic behavior occurs due to hydrostatic stresses'

b) 'Uniform dilatation does not have an impact on plastic behavior'

c) 'Behavior along the fiber direction is essentially linear elastic.'

Chen et al noted that to enforce observation 'b' the following relation in equation 5.6 results due to the fact that under uniform dilation $\varepsilon_{11} = \varepsilon_{22} = \varepsilon_{33} = \varepsilon$.

$$\begin{gathered}
\sigma_{11} = \left(C_{11} + C_{12} + C_{13}\right)\varepsilon \\
\sigma_{22} = \left(C_{12} + C_{22} + C_{23}\right)\varepsilon \\
\sigma_{33} = \left(C_{13} + C_{23} + C_{33}\right)\varepsilon \\
\frac{\sigma_{11}}{C_{11} + C_{12} + C_{13}} = \frac{\sigma_{22}}{C_{12} + C_{22} + C_{23}} = \frac{\sigma_{33}}{C_{13} + C_{23} + C_{33}} \\
\text{where } C_{ij} \text{ are components of the elastic stiffness matrix}
\end{gathered} \qquad \textbf{5.6}$$

From the original form of the plastic potential in equation 5.3 and applying the relation in equation 5.6, a new form of the plastic potential was derived as presented in equation 5.7 (35). This form of the plastic potential will be utilized in the development of the viscoplastic model since it is a more generalized form. Additionally the α_{ij} terms can be defined explicitly without the definitions in equation 5.7 to allow for more anisotropic plastic behavior.

$$
\begin{gathered}
2f(\sigma_{ij}) = A_{12}\left(\sigma_{11}-\alpha_{12}\sigma_{22}\right)^2 + A_{23}\left(\sigma_{22}-\alpha_{23}\sigma_{33}\right)^2 + A_{31}\left(\sigma_{33}-\alpha_{31}\sigma_{11}\right)^2 \\
+2a_{44}\sigma_{23}^2 + 2a_{55}\sigma_{13}^2 + 2a_{66}\sigma_{12}^2 \\
where \\
\alpha_{12} = \frac{C_{11}+C_{12}+C_{13}}{C_{12}+C_{22}+C_{23}} \; \alpha_{23} = \frac{C_{12}+C_{22}+C_{23}}{C_{13}+C_{23}+C_{33}} \; \alpha_{31} = \frac{C_{13}+C_{23}+C_{33}}{C_{11}+C_{12}+C_{13}}
\end{gathered}
\tag{5.7}
$$

Chen and Sun observed that although the α_{ij} terms do not equal, Hill's original plasticity potential can be obtained by setting the α_{ij} terms equal to unity (35). Also implicit to this plastic potential is the fact that the initial plasticity is related to the elastic behavior through the α_{ij} terms. As will be demonstrated in the following section, this feature will be important for modeling highly anisotropic behavior such as that present in carbon fiber composites when the simplification of linear elastic axial behavior is not enforced.

Although the form of the plastic potential in equation 5.7 will be used throughout the research, it is instructive to show that the plastic potential can be simplified for transversely isotropic behavior present in unidirectional composites. As Hill originally stated, for the case of transversely isotropic behavior, the plastic potential must remain invariant for an arbitrary rotation about the normal direction of the isotropic plane (24). Considering the 1-direction to be the direction of the tows, it can be shown that the following relations in equation 5.8 result from an arbitrary rotation about the 1-axis.

$$
A_{12} = A_{13}\alpha_{31}^2 \quad A_{13} = A_{12}\alpha_{12}^2 \quad a_{55} = a_{66}
\tag{5.8}
$$

Additionally for transversely isotropic materials the following stiffness matrix components relations can be applied, $C_{12} = C_{13} \quad C_{22} = C_{33}$, resulting in the simplifications to the α_{ij} terms as shown in equation 5.9.

$$
\alpha_{12} = \frac{C_{11}+2C_{12}}{C_{12}+C_{22}+C_{23}} \quad \alpha_{23} = \frac{C_{12}+C_{22}+C_{23}}{C_{12}+C_{22}+C_{23}} = 1 \quad \alpha_{31} = \frac{C_{12}+C_{22}+C_{23}}{C_{11}+2C_{12}} = \frac{1}{\alpha_{12}}
\tag{5.9}
$$

Applying the simplifications from equations 5.8 and 5.9 with further algebraic manipulation, the plastic potential simplifies to the following simplified form.

$$\begin{aligned} 2f(\sigma_{ij}) = A_{12}\left(\sigma_{11}-\alpha_{12}\sigma_{22}\right)^2 + A_{23}\left(\sigma_{22}-\sigma_{33}\right)^2 + A_{12}\left(\sigma_{11}-\alpha_{12}\sigma_{33}\right)^2 \\ +2a_{44}\sigma_{23}^2 + 2a_{66}\left(\sigma_{13}^2+\sigma_{12}^2\right) \end{aligned} \tag{5.10}$$

The anisotropic terms control the level of anisotropic plastic behavior exhibited by the material.

Through work equivalence, the increment of plastic work per unit volume, dW^P, can be expressed in terms of the stress and plastic strain increment tensors (22). By substituting the associated flow rule from equation 5.1 into 5.11, the incremental plastic work takes the form shown in equation 5.12. Additionally dW^P can also be expressed in terms of the effective stress, $\overline{\sigma}$, and the effective plastic strain increment, $\overline{d\varepsilon^p}$ (22).

$$dW^P = \sigma_{ij} d\varepsilon_{ij}^p \tag{5.11}$$

$$dW^P = \sigma_{ij}\frac{\partial f}{\partial \sigma_{ij}} d\lambda \tag{5.12}$$

$$dW^P = \overline{\sigma}\,\overline{d\varepsilon^p} \tag{5.13}$$

From expansion of equation 5.12, it is apparent that the incremental plastic work is equal to the plastic potential as shown in equation 5.14.

$$dW^P = \sigma_{ij} d\varepsilon_{ij}^p = \sigma_{ij}\frac{\partial f}{\partial \sigma_{ij}} d\lambda = 2f\left(\sigma_{ij}\right) \tag{5.14}$$

After further manipulation of equation 5.14, the proportionality factor can be expressed in terms of $\overline{\sigma}$ and $\overline{d\varepsilon^p}$ (22). Also the incremental plastic strain can be expressed as shown in equation 5.16. Upon evaluation of the aforementioned expression, the effective plastic strain increment for the generalized model, equation 5.7 takes the form shown in 5.17

$$d\lambda = \frac{\sqrt{3f\left(\sigma_{ij}\right)}}{2f\left(\sigma_{ij}\right)}\overline{d\varepsilon^{p}} = \frac{3}{2}\frac{\overline{d\varepsilon^{p}}}{\overline{\sigma}} \tag{5.15}$$

$$\overline{d\varepsilon^{p}} = \frac{2}{3}\frac{d\varepsilon_{ij}^{p}}{\partial f / \partial\sigma_{ij}} \tag{5.16}$$

$$\overline{d\varepsilon^{p}} = \sqrt{\frac{2}{3}}\left[\frac{\left(d\varepsilon_{2}^{p} - \alpha_{12}d\varepsilon_{1}^{p}\right)^{2}}{A_{12}\alpha_{12}^{2}} + \frac{\left(d\varepsilon_{3}^{p} - \alpha_{23}d\varepsilon_{2}^{p}\right)^{2}}{A_{23}\alpha_{23}^{2}} + \frac{\left(d\varepsilon_{1}^{p} - \alpha_{31}d\varepsilon_{3}^{p}\right)^{2}}{A_{31}\alpha_{31}^{2}} + \frac{d\varepsilon_{12}^{p^{2}}}{2a_{66}} + \frac{d\varepsilon_{23}^{p^{2}}}{2a_{44}} + \frac{d\varepsilon_{13}^{p^{2}}}{2a_{55}}\right]^{1/} \tag{5.17}$$

In a similar fashion as the derivation by Thiruppukuzhi, the rate forms of the proportionality factor and effective plastic strain, equations 5.15 and 5.17 respectively, are expressed as follows. Also, the viscoplastic modulus term is introduced at this point, H_{P} (26) .

$$\dot{\lambda} = \frac{3}{2}\frac{\overline{\dot{\varepsilon}}^{p}}{\overline{\sigma}} = \frac{3}{2}\frac{\dot{\overline{\sigma}}}{\mathrm{H}_{P}\overline{\sigma}} \quad where\ \mathrm{H}_{P} = \frac{\dot{\overline{\sigma}}}{\overline{\dot{\varepsilon}}^{p}} \tag{5.18}$$

$$\overline{\dot{\varepsilon}}^{p} = \sqrt{\frac{2}{3}}\left[\frac{\left(\dot{\varepsilon}_{2}^{p} - \alpha_{12}\dot{\varepsilon}_{1}^{p}\right)^{2}}{A_{12}\alpha_{12}^{2}} + \frac{\left(\dot{\varepsilon}_{3}^{p} - \alpha_{22}\dot{\varepsilon}_{2}^{p}\right)^{2}}{A_{23}\alpha_{23}^{2}} + \frac{\left(\dot{\varepsilon}_{1}^{p} - \alpha_{31}\dot{\varepsilon}_{3}^{p}\right)^{2}}{A_{31}\alpha_{31}^{2}} + \frac{\dot{\varepsilon}_{12}^{p^{2}}}{2a_{66}} + \frac{\dot{\varepsilon}_{23}^{p^{2}}}{2a_{44}} + \frac{\dot{\varepsilon}_{13}^{p^{2}}}{2a_{55}}\right]^{1/2} \tag{5.19}$$

As Hill and Sun stated, the effective stress can be expressed as the following form (22) (24).

$$\overline{\sigma} = \sqrt{3f} \tag{5.20}$$

Evaluating the expression in equation 5.20 with the plastic potential from equation 5.10, the effective stress for the two parameter model takes the form shown in equation 5.21.

$$\overline{\sigma} = \sqrt{\frac{3}{2}\left[\begin{matrix} \mathrm{A}_{12}\left(\sigma_{11} - \alpha_{12}\sigma_{22}\right)^{2} + \mathrm{A}_{23}\left(\sigma_{22} - \alpha_{23}\sigma_{33}\right)^{2} + \mathrm{A}_{31}\left(\sigma_{33} - \alpha_{31}\sigma_{11}\right)^{2} \\ +2a_{66}\sigma_{12}^{2} + 2a_{44}\sigma_{23}^{2} + 2a_{55}\sigma_{13}^{2} \end{matrix}\right]^{1/2}} \tag{5.21}$$

The effective stress rate is found by taking the derivative of equation 5.21 with respect to time. After simplification and reordering the effective stress rate equation can be represented as shown in 5.22.

$$\dot{\bar{\sigma}} = \frac{d(\bar{\sigma})}{dt} = \frac{3}{2\bar{\sigma}} \begin{bmatrix} \left(\mathrm{A}_{12}\left(\sigma_{11} - \alpha_{12}\sigma_{22}\right) - \mathrm{A}_{31}\alpha_{31}\left(\sigma_{33} - \alpha_{31}\sigma_{11}\right)\right)\dot{\sigma}_{11} \\ +\left(\mathrm{A}_{23}\left(\sigma_{22} - \alpha_{23}\sigma_{33}\right) - \mathrm{A}_{12}\alpha_{12}\left(\sigma_{11} - \alpha_{12}\sigma_{22}\right)\right)\dot{\sigma}_{22} \\ +\left(\mathrm{A}_{31}\left(\sigma_{33} - \alpha_{31}\sigma_{11}\right) - \mathrm{A}_{23}\alpha_{23}\left(\sigma_{22} - \alpha_{23}\sigma_{33}\right)\right)\dot{\sigma}_{33} \\ +2a_{66}\sigma_{12}\dot{\sigma}_{12} + 2a_{44}\sigma_{23}\dot{\sigma}_{23} + 2a_{55}\sigma_{13}\dot{\sigma}_{13} \end{bmatrix} \qquad \mathbf{5.22}$$

As noted from Sun, fiber composites experimentally do not exhibit a definite yield point so a simple power law was used to fit the master effective stress - effective strain curve as shown in equation 5.23. The master effective stress- effective strain curve is developed from off-axis testing. Thiruppukuzhi expanded the power law such that the coefficient A is a power law of the effective plastic strain rate as shown in equation 5.24. Applying the aforementioned power laws, the viscoplastic modulus can be expressed as shown in equation 5.25. As noted by Flesher there can be several suitable $\mathrm{A},\ n$ pairs and thusly proposed and implemented a relationship established from the monotonic loading conditions present in a rail-shear test (31). The terms χ and m are denoted the viscoplasticity terms (26). χ and m are determined by plotting the log-log relation of A and the effective plastic strain rate where they are the intercept and slope, respectively (26). As evidenced by the power law, χ has a linear effect on the material behavior (31). m controls the rate sensitivity of the material (26). Negative values of m correspond to stiffening behavior as load rate increases which is often observed in polymeric composites (31). The n term controls the shape of the power law curve fit (31).

$$\bar{\varepsilon}^{p} = \mathrm{A}\bar{\sigma}^{n} \qquad \mathbf{5.23}$$

$$A = \chi\left(\dot{\bar{\varepsilon}}^{p}\right)^{m} \quad \bar{\varepsilon}^{p} = \chi\left(\dot{\bar{\varepsilon}}^{p}\right)^{m}\bar{\sigma}^{n} \qquad \mathbf{5.24}$$

$$\mathrm{H}_{P} = \frac{\dot{\bar{\sigma}}}{\dot{\bar{\varepsilon}}^{p}} = \frac{1}{n\chi\left(\dot{\bar{\varepsilon}}^{p}\right)^{m}\left(\bar{\sigma}\right)^{n-1}} \qquad \mathbf{5.25}$$

Since this material model will be implemented into an explicit integration Finite Element code where many small time steps are made, the small strain assumption can be made and the strain rate can be additively decomposed into elastic and plastic contributions (36). By evaluating the additive decomposition strain rates, and likewise strain, in equation 5.26, the strain rate-stress rate relationship can be considered to be a function of the elastic and viscoplastic compliance matrices, S^E and S^{VP} respectively, shown in equation 5.27.

$$\left\{\dot{\varepsilon}\right\} = \left\{\dot{\varepsilon}^e\right\} + \left\{\dot{\varepsilon}^p\right\} \tag{5.26}$$

$$\left\{\dot{\varepsilon}\right\} = \left[S^{TOT}\right]\left\{\dot{\sigma}\right\}, \;\; where \left[S^{TOT}\right] = \left[S^E\right] + \left[S^{VP}\right] \tag{5.27}$$

The elastic compliance matrix for transversely isotropic materials can be expressed as shown in equation 5.28 (37). Note that the order of the compliance matrix is the nonstandard order utilized by LS-DYNA and this order will be used throughout the present study.

$$\left[S^E\right] = \begin{bmatrix} S_{11}^E & S_{12}^E & S_{13}^E & 0 & 0 & 0 \\ S_{12}^E & S_{22}^E & S_{23}^E & 0 & 0 & 0 \\ S_{13}^E & S_{23}^E & S_{33}^E & 0 & 0 & 0 \\ 0 & 0 & 0 & S_{44}^E & 0 & 0 \\ 0 & 0 & 0 & 0 & S_{55}^E & 0 \\ 0 & 0 & 0 & 0 & 0 & S_{66}^E \end{bmatrix} \tag{5.28}$$

$$where$$

$$S_{11}^E = \frac{1}{E_1} \quad S_{12}^E = \frac{-\nu_{12}}{E_1} \quad S_{13}^E = \frac{-\nu_{13}}{E_1}$$

$$S_{22}^E = \frac{1}{E_2} \quad S_{23}^E = \frac{-\nu_{23}}{E_2} \quad S_{33}^E = \frac{1}{E_3}$$

$$S_{44}^E = \frac{1}{G_{12}} \quad S_{55}^E = \frac{1}{G_{23}} \quad S_{66}^E = \frac{1}{G_{13}}$$

Considering the rate form of the associated flow rule in equation 5.29 and applying equations 5.18, and 5.25, the viscoplastic compliance matrix can be determined as defined explicitly in equations 5.30-5.32.

$$\dot{\varepsilon}_{ij}^p = \frac{\partial f}{\partial \sigma_{ij}} \dot{\lambda} \tag{5.29}$$

$$\begin{Bmatrix} \dot{\varepsilon}_{11}^{p} \\ \dot{\varepsilon}_{22}^{p} \\ \dot{\varepsilon}_{33}^{p} \\ \dot{\gamma}_{12}^{p} \\ \dot{\gamma}_{23}^{p} \\ \dot{\gamma}_{13}^{p} \end{Bmatrix} = \left[S_{ij}^{VP} \right] \begin{Bmatrix} \dot{\sigma}_{11} \\ \dot{\sigma}_{22} \\ \dot{\sigma}_{33} \\ \dot{\tau}_{12} \\ \dot{\tau}_{23} \\ \dot{\tau}_{13} \end{Bmatrix} \tag{5.30}$$

$$\left[S^{VP} \right] = \frac{9n\chi\left(\bar{\varepsilon}^{p}\right)^{m}\left(\bar{\sigma}\right)^{n-3}}{4} \begin{bmatrix} S_{11}^{VP} & S_{12}^{VP} & S_{13}^{VP} & S_{14}^{VP} & S_{15}^{VP} & S_{16}^{VP} \\ S_{12}^{VP} & S_{22}^{VP} & S_{23}^{VP} & S_{24}^{VP} & S_{25}^{VP} & S_{26}^{VP} \\ S_{13}^{VP} & S_{23}^{VP} & S_{33}^{VP} & S_{34}^{VP} & S_{35}^{VP} & S_{36}^{VP} \\ S_{14}^{VP} & S_{24}^{VP} & S_{34}^{VP} & S_{44}^{VP} & S_{45}^{VP} & S_{46}^{VP} \\ S_{15}^{VP} & S_{25}^{VP} & S_{35}^{VP} & S_{45}^{VP} & S_{55}^{VP} & S_{56}^{VP} \\ S_{16}^{VP} & S_{26}^{VP} & S_{36}^{VP} & S_{46}^{VP} & S_{56}^{VP} & S_{66}^{VP} \end{bmatrix} \tag{5.31}$$

$$\begin{array}{lllllll} S_{11}^{VP} = A^2 & S_{12}^{VP} = AB & S_{13}^{VP} = AC & S_{14}^{VP} = AD & S_{15}^{VP} = AE & S_{16}^{VP} = AF & S_{22}^{VP} = B^2 \\ S_{23}^{VP} = BC & S_{24}^{VP} = BD & S_{25}^{VP} = BE & S_{26}^{VP} = BF & S_{33}^{VP} = C^2 & S_{34}^{VP} = CD & S_{35}^{VP} = CE \\ S_{36}^{VP} = CF & S_{44}^{VP} = D^2 & S_{45}^{VP} = DE & S_{46}^{VP} = DF & S_{55}^{VP} = E^2 & S_{56}^{VP} = EF & S_{66}^{VP} = F^2 \end{array}$$
$$\textit{where}$$
$$\begin{array}{ll} A = \left(\mathrm{A}_{12} + \mathrm{A}_{31}\alpha_{31}^{2}\right)\sigma_{11} - \mathrm{A}_{12}\alpha_{12}\sigma_{22} - \mathrm{A}_{31}\alpha_{31}\sigma_{33} & D = 2a_{66}\sigma_{12} \\ B = -\mathrm{A}_{12}\alpha_{12}\sigma_{22} + \left(\mathrm{A}_{23} + \mathrm{A}_{12}\alpha_{12}^{2}\right)\sigma_{22} - \mathrm{A}_{23}\alpha_{23}\sigma_{33} & E = 2a_{44}\sigma_{23} \\ C = -\mathrm{A}_{31}\alpha_{31}\sigma_{11} - \mathrm{A}_{23}\alpha_{23}\sigma_{22} + \left(\mathrm{A}_{31} + \mathrm{A}_{23}\alpha_{23}^{2}\right)\sigma_{33} & F = 2a_{55}\sigma_{13} \end{array} \tag{5.32}$$

5.3 : Return Mapping Algorithm

In general solving the 1st order ordinary differential equations represented by equations 5.29 through 5.32 explicitly will result in a conditionally stable solution which requires a sufficiently small step to maintain numerical stability. Since it is expected that large strain increments may occur in the ballistic impact simulations, a return mapping algorithm based on a 1st order backward Euler integration algorithm will be utilized to obtain unconditional stability (38). Additionally, as pointed out by Simo et al, the return mapping algorithm transforms the differential equations into an algebraically constrained optimization problem (38). An example of the general class of return mapping algorithms is the well-known radial return integration scheme for J2-plasticity proposed by Key and Krieg (39). Return mapping integration schemes are based on the split operator methodology where the elastic and plastic components of the material response are split into a predictor-corrector scheme (38) (39). The most common split is the elastic predictor/plastic corrector but Fotiu et al have also proposed a plastic predictor/elastic corrector scheme (40). For the elastic predictor/plastic corrector split, the elastic prediction is returned to the plastic yield surface which is convex due to the associated flow rule utilized. Ortiz and Simo formulated the generalized algorithm for rate-independent elastoplastic material behavior (41). Return mapping algorithms have also been extended to viscoplastic constitutive behavior using overstress functions such as the Duvaut-Lions and Perzyna models and also rate tangent modulus method (38) (39). Wang et al have proposed a consistency model for rate-dependent elastoplastic models that uses the consistency condition that results from the Kuhn-Tucker or loading/unloading conditions, equation 5.33 (42), where F denotes the plastic yield function.

$$\begin{gathered}\dot{\lambda} \geq 0 \quad F \leq 0 \quad \dot{\lambda} F \leq 0 \\ \textit{where} \\ F(\sigma, \lambda, \dot{\lambda}) = 0\end{gathered} \tag{5.33}$$

Since the associated flow rule and hardening rule have been implemented, the algorithm outlined by Wang et al is applicable and will be utilized for the present research. From equation 5.33, the consistency condition can be expressed as shown in 5.34. The summarization of the general algorithm is shown in Figure 5.2 where n and k refer to the global and the local solution steps, respectively (42). It should also be noted that a slight modification was made to the algorithm to be able to use the dual power law hardening rule shown in equation 5.24. In order to obtain a continuous solution the power law requires that the instantaneous viscoplastic scaling factor rate, $\dot{\lambda}$, must be initialized to the value at the previous time step. This relaxes the split operator definition which states that the plastic evolution is frozen during the elastic predictor.

$$\dot{F}(\sigma,\lambda,\dot{\lambda}) = \frac{\partial F}{\partial \sigma} : \dot{\sigma} + \frac{\partial F}{\partial \lambda}\dot{\lambda} + \frac{\partial F}{\partial \dot{\lambda}}\ddot{\lambda} = 0 \tag{5.34}$$

```
Calculate Elastic Predictor
$\Delta\varepsilon_{n+1} \quad \sigma_{tr} = \sigma_n + C^E \Delta\varepsilon_{n+1}$
if $F\left(\sigma_{tr}, \dot{\lambda}_{n+1}\right) \geq 0$; plastic state
Initialize
$\Delta\lambda_{n+1}^{k=0} = 0 \quad \dot{\lambda}_{n+1}^{k=0} = \dot{\lambda}_n \quad \sigma^{k=0} = \sigma_{tr} \quad F^{k=0} = F\left(\sigma_{tr}, \lambda_{n+1}^{k=0}, \dot{\lambda}_{n+1}^{k=0}\right)$
Begin $k^{th}$ iteration
$H^k = \left[ S^E + \Delta\lambda^k \frac{\partial^2 F}{\partial \sigma^2} \right]^{-1}$
$\beta^k = \left(\frac{\partial F}{\partial \sigma}\right)^T H^k \left[ \frac{\partial F}{\partial \sigma} + \Delta\lambda^k \frac{\partial^2 F}{\partial \sigma \partial \lambda} + \frac{\Delta\lambda^k}{\Delta t} \frac{\partial^2 F}{\partial \sigma \partial \dot{\lambda}} \right] - \frac{\partial F}{\partial \lambda} - \frac{1}{\Delta t}\frac{\partial F}{\partial \dot{\lambda}}$
$\Delta\lambda^{k+1} = \Delta\lambda^k + \frac{F^k}{\beta^k}$
$\sigma_{n+1}^{k+1} = \sigma_n + C^E \left( \Delta\varepsilon_{n+1} - \Delta\lambda^{k+1} \frac{\partial F}{\partial \sigma} \right)$
$F^{k+1} = F\left( \sigma_{tr}, \lambda_n + \Delta\lambda^{k+1}, \frac{\Delta\lambda^{k+1}}{\Delta t} \right)$
if $F^{k+1} > tol$, perform next iteration
else elastic state; $\sigma_{n+1} = \sigma_{tr}$
```

Figure 5.2: 3-D General Return Mapping Algorithm

Up to this point the general orthotropic model presented in the previous section has been stated in the quadratic form, equation 5.7. For the return mapping algorithm, the yield function, F, can be stated in terms of the effective stress as shown in equations 5.35 since $\lambda = \bar{\varepsilon}^p$ through work equivalence. The 1st partial derivatives and 2nd partial derivatives, or Hessian matrix, of the yield function, F, for the return mapping algorithm can be defined explicitly as shown in equations 5.36 and 5.37. It can be observed that the Hessian matrix defined in equation 5.37 is symmetric.

$$F(\sigma,\bar{\varepsilon}^p,\dot{\bar{\varepsilon}}^p)=\bar{\sigma}-\bar{\sigma}\left(\bar{\varepsilon}^p,\dot{\bar{\varepsilon}}^p\right)=0$$

where

$$\bar{\sigma}=\sqrt{\frac{3}{2}}\begin{bmatrix}\mathrm{A}_{12}\left(\sigma_{11}-\alpha_{12}\sigma_{22}\right)^2+\mathrm{A}_{23}\left(\sigma_{22}-\alpha_{23}\sigma_{33}\right)^2+\mathrm{A}_{31}\left(\sigma_{33}-\alpha_{31}\sigma_{11}\right)^2\\ +2a_{66}\sigma_{12}^2+2a_{44}\sigma_{23}^2+2a_{55}\sigma_{13}^2\end{bmatrix}^{1/2} \tag{5.35}$$

$$\bar{\sigma}\left(\bar{\varepsilon}^p,\dot{\bar{\varepsilon}}^p\right)=\left(\frac{\bar{\varepsilon}^p}{\chi\left(\dot{\bar{\varepsilon}}^p\right)^m}\right)^{1/n}$$

$$\frac{\partial F}{\partial\sigma}=\frac{3}{2\bar{\sigma}}\{A\,B\,C\,D\,E\,F\}^T$$

$$\frac{\partial F}{\partial\bar{\varepsilon}^p}=-\frac{1}{\bar{\varepsilon}^p n}\left(\frac{\bar{\varepsilon}^p}{\chi\left(\dot{\bar{\varepsilon}}^p\right)^m}\right)^{1/n}$$

$$\frac{\partial F}{\partial\dot{\bar{\varepsilon}}^p}=\frac{m}{\dot{\bar{\varepsilon}}^p n}\left(\frac{\bar{\varepsilon}^p}{\chi\left(\dot{\bar{\varepsilon}}^p\right)^m}\right)^{1/n} \tag{5.36}$$

where

$$A=\left(\mathrm{A}_{12}+\mathrm{A}_{31}\alpha_{31}^2\right)\sigma_{11}-\mathrm{A}_{12}\alpha_{12}\sigma_{22}-\mathrm{A}_{31}\alpha_{31}\sigma_{33}\qquad D=2a_{66}\sigma_{12}$$

$$B=-\mathrm{A}_{12}\alpha_{12}\sigma_{22}+\left(\mathrm{A}_{23}+\mathrm{A}_{12}\alpha_{12}^2\right)\sigma_{22}-\mathrm{A}_{23}\alpha_{23}\sigma_{33}\qquad E=2a_{44}\sigma_{23}$$

$$C=-\mathrm{A}_{31}\alpha_{31}\sigma_{11}-\mathrm{A}_{23}\alpha_{23}\sigma_{22}+\left(\mathrm{A}_{31}+\mathrm{A}_{23}\alpha_{23}^2\right)\sigma_{33}\qquad F=2a_{55}\sigma_{13}$$

$$\frac{\partial^2 F}{\partial \sigma^2}=\begin{bmatrix}
\dfrac{\partial^2 F}{\partial \sigma_1^2} & \dfrac{\partial^2 F}{\partial \sigma_2 \partial \sigma_1} & \dfrac{\partial^2 F}{\partial \sigma_3 \partial \sigma_1} & \dfrac{\partial^2 F}{\partial \sigma_{12} \partial \sigma_1} & \dfrac{\partial^2 F}{\partial \sigma_{23} \partial \sigma_1} & \dfrac{\partial^2 F}{\partial \sigma_{13} \partial \sigma_1} \\
\dfrac{\partial^2 F}{\partial \sigma_2 \partial \sigma_1} & \dfrac{\partial^2 F}{\partial \sigma_2^2} & \dfrac{\partial^2 F}{\partial \sigma_3 \partial \sigma_2} & \dfrac{\partial^2 F}{\partial \sigma_{12} \partial \sigma_2} & \dfrac{\partial^2 F}{\partial \sigma_{23} \partial \sigma_2} & \dfrac{\partial^2 F}{\partial \sigma_{13} \partial \sigma_2} \\
\dfrac{\partial^2 F}{\partial \sigma_3 \partial \sigma_1} & \dfrac{\partial^2 F}{\partial \sigma_3 \partial \sigma_2} & \dfrac{\partial^2 F}{\partial \sigma_3^2} & \dfrac{\partial^2 F}{\partial \sigma_{12} \partial \sigma_3} & \dfrac{\partial^2 F}{\partial \sigma_{23} \partial \sigma_3} & \dfrac{\partial^2 F}{\partial \sigma_{13} \partial \sigma_3} \\
\dfrac{\partial^2 F}{\partial \sigma_{12} \partial \sigma_1} & \dfrac{\partial^2 F}{\partial \sigma_{12} \partial \sigma_2} & \dfrac{\partial^2 F}{\partial \sigma_{12} \partial \sigma_3} & \dfrac{\partial^2 F}{\partial \sigma_{12}^2} & \dfrac{\partial^2 F}{\partial \sigma_{23} \partial \sigma_{12}} & \dfrac{\partial^2 F}{\partial \sigma_{13} \partial \sigma_{12}} \\
\dfrac{\partial^2 F}{\partial \sigma_{23} \partial \sigma_1} & \dfrac{\partial^2 F}{\partial \sigma_{23} \partial \sigma_2} & \dfrac{\partial^2 F}{\partial \sigma_{23} \partial \sigma_3} & \dfrac{\partial^2 F}{\partial \sigma_{23} \partial \sigma_{12}} & \dfrac{\partial^2 F}{\partial \sigma_{23}^2} & \dfrac{\partial^2 F}{\partial \sigma_{13} \partial \sigma_{23}} \\
\dfrac{\partial^2 F}{\partial \sigma_{13} \partial \sigma_1} & \dfrac{\partial^2 F}{\partial \sigma_{13} \partial \sigma_2} & \dfrac{\partial^2 F}{\partial \sigma_{13} \partial \sigma_3} & \dfrac{\partial^2 F}{\partial \sigma_{13} \partial \sigma_{12}} & \dfrac{\partial^2 F}{\partial \sigma_{13} \partial \sigma_{23}} & \dfrac{\partial^2 F}{\partial \sigma_{13}^2}
\end{bmatrix}$$

where

$$\begin{aligned}
&\frac{\partial^2 F}{\partial \sigma_1^2}=\frac{3}{2\bar{\sigma}^2}\left[\left(\mathrm{A}_{12}+\mathrm{A}_{31}\alpha_{31}^2\right)\bar{\sigma}-A\frac{\partial F}{\partial \sigma_1}\right] && \frac{\partial^2 F}{\partial \sigma_2 \partial \sigma_1}=\frac{3}{2\bar{\sigma}^2}\left[-\mathrm{A}_{12}\alpha_{12}\bar{\sigma}-A\frac{\partial F}{\partial \sigma_2}\right] \\
&\frac{\partial^2 F}{\partial \sigma_3 \partial \sigma_1}=\frac{3}{2\bar{\sigma}^2}\left[-\mathrm{A}_{31}\alpha_{31}\bar{\sigma}-A\frac{\partial F}{\partial \sigma_3}\right] && \frac{\partial^2 F}{\partial \sigma_{12} \partial \sigma_1}=\frac{3}{2\bar{\sigma}^2}\left[-A\frac{\partial F}{\partial \sigma_{12}}\right] \\
&\frac{\partial^2 F}{\partial \sigma_{23} \partial \sigma_1}=\frac{3}{2\bar{\sigma}^2}\left[-A\frac{\partial F}{\partial \sigma_{23}}\right] && \frac{\partial^2 F}{\partial \sigma_{13} \partial \sigma_1}=\frac{3}{2\bar{\sigma}^2}\left[-A\frac{\partial F}{\partial \sigma_{13}}\right] \\
&\frac{\partial^2 F}{\partial \sigma_2^2}=\frac{3}{2\bar{\sigma}^2}\left[\left(\mathrm{A}_{23}+\mathrm{A}_{12}\alpha_{12}^2\right)\bar{\sigma}-B\frac{\partial F}{\partial \sigma_2}\right] && \frac{\partial^2 F}{\partial \sigma_3 \partial \sigma_2}=\frac{3}{2\bar{\sigma}^2}\left[-\mathrm{A}_{23}\alpha_{23}\bar{\sigma}-B\frac{\partial F}{\partial \sigma_2}\right] \\
&\frac{\partial^2 F}{\partial \sigma_{12} \partial \sigma_2}=\frac{3}{2\bar{\sigma}^2}\left[-B\frac{\partial F}{\partial \sigma_{12}}\right] && \frac{\partial^2 F}{\partial \sigma_{23} \partial \sigma_2}=\frac{3}{2\bar{\sigma}^2}\left[-B\frac{\partial F}{\partial \sigma_{23}}\right] \\
&\frac{\partial^2 F}{\partial \sigma_{13} \partial \sigma_2}=\frac{3}{2\bar{\sigma}^2}\left[-B\frac{\partial F}{\partial \sigma_{13}}\right] && \frac{\partial^2 F}{\partial \sigma_3^2}=\frac{3}{2\bar{\sigma}^2}\left[\left(\mathrm{A}_{31}+\mathrm{A}_{23}\alpha_{23}^2\right)\bar{\sigma}-C\frac{\partial F}{\partial \sigma_3}\right] \\
&\frac{\partial^2 F}{\partial \sigma_{12} \partial \sigma_3}=\frac{3}{2\bar{\sigma}^2}\left[-C\frac{\partial F}{\partial \sigma_{12}}\right] && \frac{\partial^2 F}{\partial \sigma_{23} \partial \sigma_3}=\frac{3}{2\bar{\sigma}^2}\left[-C\frac{\partial F}{\partial \sigma_{23}}\right] \\
&\frac{\partial^2 F}{\partial \sigma_{13} \partial \sigma_3}=\frac{3}{2\bar{\sigma}^2}\left[-C\frac{\partial F}{\partial \sigma_{13}}\right] && \frac{\partial^2 F}{\partial \sigma_{12}^2}=\frac{3}{2\bar{\sigma}^2}\left[2a_{66}\left(\bar{\sigma}-\sigma_{12}\frac{\partial F}{\partial \sigma_{12}}\right)\right] \\
&\frac{\partial^2 F}{\partial \sigma_{23} \partial \sigma_{12}}=\frac{3}{2\bar{\sigma}^2}\left[-D\frac{\partial F}{\partial \sigma_{23}}\right] && \frac{\partial^2 F}{\partial \sigma_{13} \partial \sigma_{12}}=\frac{3}{2\bar{\sigma}^2}\left[-D\frac{\partial F}{\partial \sigma_{13}}\right] \\
&\frac{\partial^2 F}{\partial \sigma_{23}^2}=\frac{3}{2\bar{\sigma}^2}\left[2a_{44}\left(\bar{\sigma}-\sigma_{23}\frac{\partial F}{\partial \sigma_{23}}\right)\right] && \frac{\partial^2 F}{\partial \sigma_{13} \partial \sigma_{23}}=\frac{3}{2\bar{\sigma}^2}\left[-E\frac{\partial F}{\partial \sigma_{13}}\right] \\
&\frac{\partial^2 F}{\partial \sigma_{13}^2}=\frac{3}{2\bar{\sigma}^2}\left[2a_{55}\left(\bar{\sigma}-\sigma_{13}\frac{\partial F}{\partial \sigma_{13}}\right)\right]
\end{aligned}\tag{5.37}$$

5.4 : Material Parameter Determination Procedure

In order to develop the material parameters for the tow model, a 1-D simplification to off-axis tensile loads was utilized as originally outlined by Sun et al for their 2-D model (22). Assuming an arbitrary rotation θ about the 3-axis, the stress transformation equations can be expressed as shown in equations 5.38.

$$\begin{aligned}
\sigma_{11} &= \cos^2\theta\,\sigma_x + \sin^2\theta\,\sigma_y + 2\sin\theta\cos\theta\,\tau_{xy} \\
\sigma_{22} &= \sin^2\theta\,\sigma_x + \cos^2\theta\,\sigma_y - 2\sin\theta\cos\theta\,\tau_{xy} \\
\sigma_{33} &= \sigma_z \\
\tau_{12} &= -\sin\theta\cos\theta\,\sigma_x + \sin\theta\cos\theta\,\sigma_y + \left(\cos^2\theta - \sin^2\theta\right)\tau_{xy} \\
\tau_{23} &= \cos\theta\,\tau_{yz} - \sin\theta\,\tau_{xz} \\
\tau_{13} &= \sin\theta\,\tau_{yz} + \cos\theta\,\tau_{xz}
\end{aligned} \tag{5.38}$$

For an axis tensile test where the loading direction is along the x-axis, the following relations hold true: $\sigma_x \neq 0; \sigma_y = \sigma_z = \tau_{xy} = \tau_{yz} = \tau_{xz} = 0$. Thus, equations 5.38 reduces to those shown in 5.39.

$$\begin{aligned}
\sigma_{11} &= \cos^2\theta\,\sigma_x \\
\sigma_{22} &= \sin^2\theta\,\sigma_x \\
\sigma_{33} &= 0 \\
\tau_{12} &= -\sin\theta\cos\theta\,\sigma_x \\
\tau_{23} &= 0 \\
\tau_{13} &= 0
\end{aligned} \tag{5.39}$$

Applying the aforementioned relations to the effective stress equation in 5.21, yields the following simplification in equations 5.40 where $h(\theta)$ is an off-axis function that contains the anisotropy parameters.

$$\bar{\sigma}=\sqrt{\frac{3}{2}}\begin{bmatrix}\left(\mathrm{A}_{12}+\mathrm{A}_{31}\alpha_{31}^{2}\right)\cos^{4}\theta+\left(\mathrm{A}_{23}+\mathrm{A}_{12}\alpha_{12}^{2}\right)\sin^{4}\theta\\+2\left(a_{66}-\mathrm{A}_{12}\alpha_{12}\right)\cos^{2}\theta\sin^{2}\theta\end{bmatrix}^{1/2}\sigma_{x}$$

$$or\quad \bar{\sigma}=h(\theta)\,\sigma_{x}$$

$$where: \tag{5.40}$$

$$h(\theta)=\sqrt{\frac{3}{2}}\begin{bmatrix}\left(\mathrm{A}_{12}+\mathrm{A}_{31}\alpha_{31}^{2}\right)\cos^{4}\theta+\left(\mathrm{A}_{23}+\mathrm{A}_{12}\alpha_{12}^{2}\right)\sin^{4}\theta\\+2\left(a_{66}-\mathrm{A}_{12}\alpha_{12}\right)\cos^{2}\theta\sin^{2}\theta\end{bmatrix}^{1/2}$$

Rearranging equation 5.15 and substituting the relation in equation 5.40, the effective plastic strain increment can be expressed as shown in 5.41.

$$\begin{gathered}\overline{d\varepsilon^{p}}=\frac{2}{3}\bar{\sigma}\,d\lambda\\\overline{d\varepsilon^{p}}=\frac{2}{3}h(\theta)\,\sigma_{x}\,d\lambda\end{gathered}\tag{5.41}$$

From coordinate transformation, the off-axis plastic strain increment can be expressed in terms of composite coordinate system's strains as shown in equation 5.42.

$$d\varepsilon_{x}^{p}=\cos^{2}\theta\,d\varepsilon_{11}^{p}+\sin^{2}\theta\,d\varepsilon_{22}^{p}-\cos\theta\sin\theta\,d\gamma_{12}^{p}\tag{5.42}$$

From the associated flow rule and the plastic potential, equations 5.1 and 5.10, the incremental plastic strains are found to be the following in 5.43.

$$\begin{gathered}d\varepsilon_{11}^{p}=\frac{3}{2\overline{\sigma}}\left(\left(\mathrm{A}_{12}+\mathrm{A}_{31}\alpha_{31}^{2}\right)\sigma_{11}-\mathrm{A}_{12}\alpha_{12}\sigma_{22}-\mathrm{A}_{31}\alpha_{31}\sigma_{33}\right)d\lambda\\d\varepsilon_{22}^{p}=\frac{3}{2\overline{\sigma}}\left(-\mathrm{A}_{12}\alpha_{12}\sigma_{22}+\left(\mathrm{A}_{23}+\mathrm{A}_{12}\alpha_{12}^{2}\right)\sigma_{22}-\mathrm{A}_{23}\alpha_{23}\sigma_{33}\right)d\lambda\\d\gamma_{12}^{p}=\frac{3}{2\overline{\sigma}}\left(2a_{66}\sigma_{12}\right)d\lambda\end{gathered}\tag{5.43}$$

Substituting equations 5.39 and 5.43 into 5.42 and simplifying yields the off-axis plastic strain increment in terms of the off-axis function as shown in equation 5.44.

$$d\varepsilon_x^p = \frac{3}{2\bar{\sigma}}\begin{bmatrix}\left(\mathrm{A}_{12}+\mathrm{A}_{31}\alpha_{31}^2\right)\cos^4\theta+\left(\mathrm{A}_{23}+\mathrm{A}_{12}\alpha_{12}^2\right)\sin^4\theta \\ +2\left(a_{66}-\mathrm{A}_{12}\alpha_{12}\right)\cos^2\theta\sin^2\theta\end{bmatrix}\sigma_x\, d\lambda$$
$$d\varepsilon_x^p = h(\theta)\, d\lambda \qquad \textbf{5.44}$$

Comparing equations 5.41 and 5.44, the effective plastic strain increment can be expressed as shown in equation 5.45.

$$\overline{d\varepsilon^p} = \frac{d\varepsilon_x^p}{h(\theta)} \qquad \textbf{5.45}$$

Since equation 5.45 is well-defined, integration yields equation 5.46 for the plastic strain in the loading direction.

$$\varepsilon_x^p = h(\theta)\overline{\varepsilon^p} \qquad \textbf{5.46}$$

Recalling the power law, $\bar{\varepsilon}^p = \mathrm{A}\bar{\sigma}^n$, and effective stress simplification, $\bar{\sigma} = h(\theta)\,\sigma_x$, plastic strain in the loading direction can be expressed in terms of the power law, loading stress, and off axis function $h(\theta)$ as shown in 5.47

$$\varepsilon_x^p = \left[h(\theta)\right]^{n+1} A\,\sigma_x^n \qquad \textbf{5.47}$$

Using the additive decomposition of the total strain, $\varepsilon_x = \varepsilon_x^e + \varepsilon_x^p$, and the total strain is defined as equation 5.48 using the apparent elastic modulus E_x.

$$\varepsilon_x^p = \frac{\sigma_x}{E_x} + \left[h(\theta)\right]^{n+1} A\,\sigma_x^n$$
$$where:$$
$$\frac{1}{E_x} = \frac{1}{E_1}\cos^4\theta + \left(\frac{1}{G_{12}} - \frac{2\nu_{12}}{E_1}\right)\sin^2\theta\cos^2\theta + \frac{1}{E_2}\sin^4\theta \qquad \textbf{5.48}$$

The power law relates the effective plastic strain to the effective stress and as such a master curve can be created from the off-axis data at a particular strain rate relating the two using equations 5.40 and 5.46. Suitable anisotropic parameters are determined by adjusting the parameter values to collapse the master effective plastic strain vs. effective stress curve data into a single curve. Notably additional loading condition data can also be utilized into the master curve data. Next a linear regression through a log-log transformation can be used to calculate a suitable A and n pair for that particular strain rate. As mentioned by Flesher, there are several A and n pairs that are suitable to model the yielding of the tow (31). This procedure can be repeated at several strain rates while keeping the n parameter constant to find the A parameter at each strain rate. Again performing another log-log transformation and using the relations in equation 5.24, the χ and m parameters can be determined to allow the model response be interpolated and extrapolated to other strain rates.

5.5 : Material Parameter Determination Algorithm

Since a more complex plastic potential is being utilized in the pursuant research, equation 5.7, a more systematic methodology is needed to determine the optimum anisotropic and hardening law parameters. In the majority of the literature, simpler forms of the plastic potential often only involving a single anisotropic term such as the form in equation 5.5. As such simple trial and error is adequate to determine the parameters for the single term model but becomes cumbersome for the more generalized model under consideration, equation 5.7. It is proposed that a simple optimization algorithm can easily be implemented to calculate the parameters for more complex viscoplastic models. To facilitate this, the 1-D uniaxial off-axis simplification presented in the preceding section will be used to calculate the parameters. It should be noted that this method could be extended to other loading conditions. Since the algorithm needs to be able to handle any strain/time history, a 1-D simplification of the general 3-D return mapping algorithm shown in Figure 5.2 can be used to solve for the uniaxial stress for the off-axis tension/compression loading condition. A summary of the 1-D return mapping algorithm is presented in Figure 5.3

Consistency Condition

$$\dot{F}(\sigma,\bar{\varepsilon}^{p},\dot{\bar{\varepsilon}}^{p})=\frac{\partial F}{\partial\sigma_x}:\dot{\sigma}_x+\frac{\partial F}{\partial\bar{\varepsilon}^{p}}\dot{\bar{\varepsilon}}^{p}+\frac{\partial F}{\partial\dot{\bar{\varepsilon}}^{p}}\ddot{\bar{\varepsilon}}^{p}$$

Yield Function

$$F(\sigma,\bar{\varepsilon}^{p},\dot{\bar{\varepsilon}}^{p})=\bar{\sigma}-\bar{\sigma}\left(\bar{\varepsilon}^{p},\dot{\bar{\varepsilon}}^{p}\right)=0;\quad \bar{\sigma}=h(\theta)\sigma_x$$

Calculate Elastic Predictor

$$\Delta\varepsilon_{n+1}\quad \sigma_{tr}=\sigma_n+E_x\Delta\varepsilon_{n+1}$$

$$\textit{if}\ F\left(\sigma_{tr},\bar{\varepsilon}^{p}_{n+1},\dot{\bar{\varepsilon}}^{p}_{n+1}\right)\geq 0;\ \textit{plastic state}$$

Initialize

$$\Delta\bar{\varepsilon}^{p,k=0}_{n+1}=0\quad \dot{\bar{\varepsilon}}^{p,k=0}_{n+1}=\dot{\bar{\varepsilon}}^{p}_{n}\quad \sigma^{k=0}=\sigma_{tr}\quad F^{k=0}=F\left(\sigma_{tr},\bar{\varepsilon}^{p,k=0}_{n+1},\dot{\bar{\varepsilon}}^{p,k=0}_{n+1}\right)$$

Begin k^{th} *iteration*

$$H^k=\left[\frac{1}{E_x}+\Delta\lambda^k\frac{\partial^2F}{\partial\sigma_x^2}\right]^{-1}=E_x$$

$$\beta^k=\left(\frac{\partial F}{\partial\sigma_x}\right)H^k\left[\frac{\partial F}{\partial\sigma_x}\right]-\frac{\partial F}{\partial\bar{\varepsilon}^{p}}-\frac{1}{\Delta t}\frac{\partial F}{\partial\dot{\bar{\varepsilon}}^{p}}=h^2\left(\theta\right)E_x-\frac{\partial F}{\partial\bar{\varepsilon}^{p}}-\frac{1}{\Delta t}\frac{\partial F}{\partial\dot{\bar{\varepsilon}}^{p}}$$

$$\Delta\lambda^{k+1}=\Delta\lambda^k+\frac{F^k}{\beta^k}$$

$$\sigma^{k+1}_{n+1}=\sigma_n+E_x\left(\Delta\varepsilon_{n+1}-\Delta\bar{\varepsilon}^{p,k+1}\frac{\partial F}{\partial\sigma_x}\right)$$

$$F^{k+1}=F\left(\sigma_{tr},\bar{\varepsilon}^{p}_{n}+\Delta\bar{\varepsilon}^{p,k+1},\frac{\Delta\bar{\varepsilon}^{p,k+1}}{\Delta t}\right)$$

$$\textit{if}\ F^{k+1}>tol,\ \textit{perform next iteration}$$

$$\textit{else elastic state};\ \sigma_{n+1}=\sigma_{tr}$$

Figure 5.3: 1-D Uniaxial Off-Axis Return Mapping Algorithm

Although advanced search algorithms could be utilized to identify potential optimum solutions, for the sake of simplicity the algorithm searches over the entire range of suitable permutations designated by the analyst. For each of these permutations the algorithm performs the following operations:

1) Form the master effective stress – effective plastic strain curve from the reference off-axis stress-strain data using equations 5.40 and 5.46. A minimum of two angles is required to form

the master curve. Additionally the best results will be obtained by using the lowest strain rate as the reference data to form the master curve.

2) Linearize the master curve data from step 1 using a log-log transformation and perform linear regression on the transformed data. Record the coefficient of determination or R^2 to use as a threshold value. From the linear regression analysis, calculate the resulting A, n pair.

3) While holding the n parameter constant, calculate the A parameter using the off-axis data at strain rates different from the reference state using the same method from step 1. Repeat this for each strain rate to be considered. During the step the effective plastic strain rate is also calculated.

4) Perform a linear regression on the log-log transformation of the A parameter and corresponding effective plastic strain rate data. Calculate the resulting χ and m viscoplasticity terms.

5) If the R^2 exceeds the minimum threshold value designated by the analyst, the 1-D return mapping algorithm can be used. Since the return mapping algorithm is unconditionally stable the exact strain-time history can be used to calculate the 1-D model response. The 1-D model response can now be compared for all off axis input data. Since this process is akin to non-linear regression analysis, the standard error of regression value, or SER, can used as means to evaluate how well each curve fits. SER was chosen since R^2, in general, is not an appropriate measure to evaluate a nonlinear regression analysis (43). SER is defined by equation 5.49 (43). The SER calculates how closely the fitted curve represents the original data. Therefore from equation 5.49, the smaller the SER value the better the fit with a value of zero being an exact fit. For all of the curves the average SER value calculated and recorded. Although in the present work an equal weighting is given to each curve's SER value a different weighting scheme can be chosen by the analyst.

6) Repeat above steps for all response curves designated by the analyst.

$$SER = \sqrt{\frac{\sum\left(y_{data} - y_{fit}\right)^2}{D.O.F.}} \quad where\ D.O.F. = \#\,data\ points - \#\text{parameters} \qquad \textbf{5.49}$$

Once the above algorithm has completed evaluation of all anisotropic parameter permutations, the optimum solution is simply chosen by one of the permutations that meets the R^2 threshold requirement with the minimum average SER value. During the development of the algorithm these simple criteria have been shown to be effective indicators of suitable parameters. The benefit to using this methodology to determine the optimum solution is it provides a structured procedure that can more quickly determine suitable parameters. A potential downside to this method is that many permutations need to be performed. The number of permutations can be reduced by careful consideration by the analyst. Although the method requires many permutations to be performed, it is relatively efficient in that tens of thousands of permutations can be performed within minutes using a high level language as MATLAB in this case. If implemented into a lower level language such as C or Fortran, it is likely that this execution time could be reduced further. Also more advanced search algorithms could be implemented to predetermine suitable ranges of permutations. The major downside to the algorithm is that although the SER value is convenient in both its ease of calculation and the fact that it provides a singular numerical evaluation of the fit of the model, it does not indicate where the model differs from the data. This deficiency can be mitigated by manually reviewing the algorithm output.

5.6: IM7/8552 Parameter Determination

The material parameters for the unidirectional IM7/8552 carbon fiber epoxy laminate reported by Koerber et al will be determined using the procedure outlined in Section 5.5 (44). Koerber et al performed split Hopkinson pressure bar experiments at different angle orientations from 15° to 90° in

15° increments. Each experiment was replicated at least three times for each angle. Although the strain rate varies in SPHB throughout the duration of the test, constant strain rates were assumed since Koerber et al did not publish the strain-time histories. The constant strain rate values are listed in Table 6.2. Compression experiments were also performed at quasi-static loading conditions with a strain rate of 4.0 E-4 per second. The reported graphical data from Koerber was digitized to obtain numerical data. Since each of the experiments' graphical data contained multiple datasets, a 4th order nonlinear polynomial regression analysis was performed on all datasets to reduce the variability in the data to help improve the performance of both the 1-D return mapping and parameter determination algorithms. The 15°, 30°, and 60° datasets were considered in the parameter determination and are summarized below in Figures 5.4, 5.5, and 5.6.

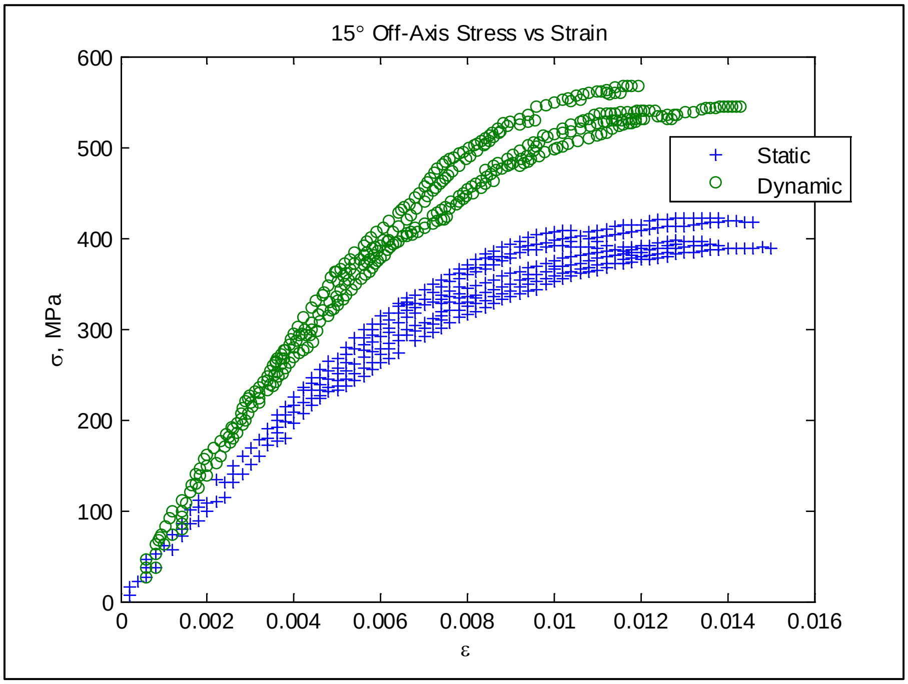

Figure 5.4: IM7/8552 15° Off-Axis

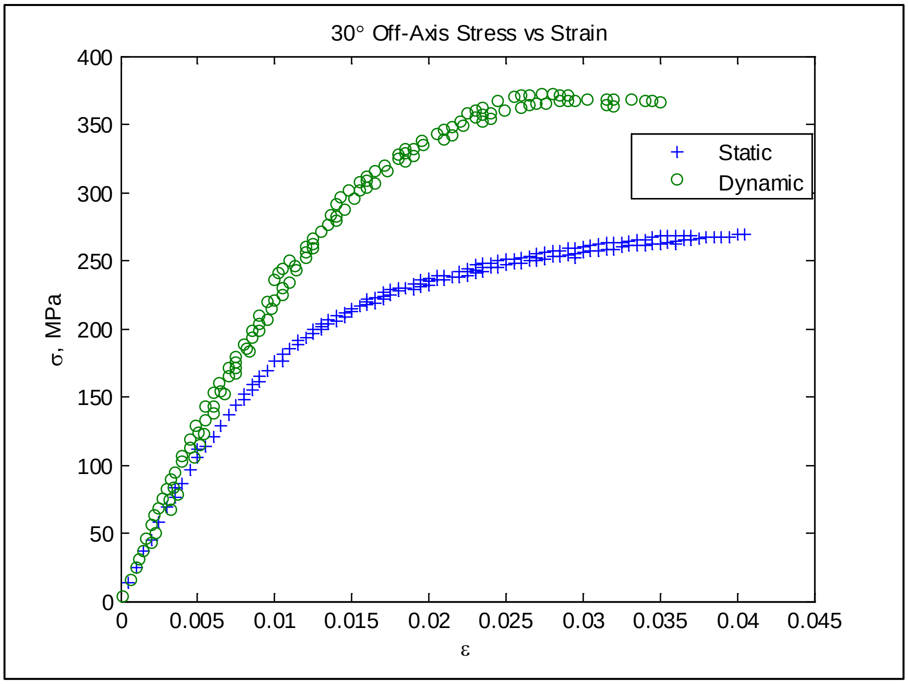

Figure 5.5: IM7/8552 30° Off-Axis

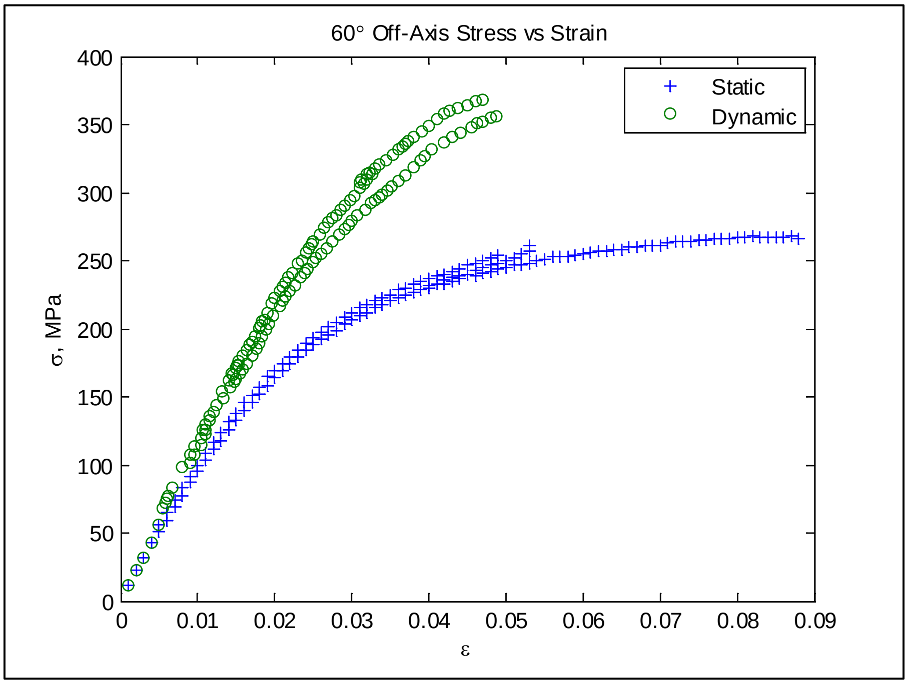

Figure 5.6: IM7/8552 60° Off-Axis

The elastic constants used for the composite were reported from Camanho et al since the fiber volume fractions were similar (45). The elastic constants are summarized in Table 5.1.

Moduli, GPa			Poisson's Ratio
E_1	E_2	G_{12}	ν_{12}
171.420	9.080	5.068	0.32

Table 5.1: IM7/8552 Elastic Constants; 1D Model

The resulting parameters for the anisotropic and hardening rule parameters calculated by the optimization algorithm are summarized in Tables 5.2 and 5.3, respectively.

A_{12}	A_{23}	a_{66}	α_{12}	α_{31}
0.1	0.1	48.0	10.4964	0.0953

Table 5.2: IM7/8552 Anisotropic Parameters; 1D Model

A, $(MPa)^{-n}$	n	χ, $(MPa)^{-n}$	m
4.9756E-17	4.3930861	1.0010E-17	-0.16103

Table 5.3: IM7/8552 Hardening Law Parameters; 1D Model

The master curve of the effective stress against the effective plastic strain was formed from the 30° and 60° datasets at quasi-static loading conditions as shown in Figure 5.7. The master curve data is used to form a single dataset from which the power law as expressed in equation 5.23 can be fitted.

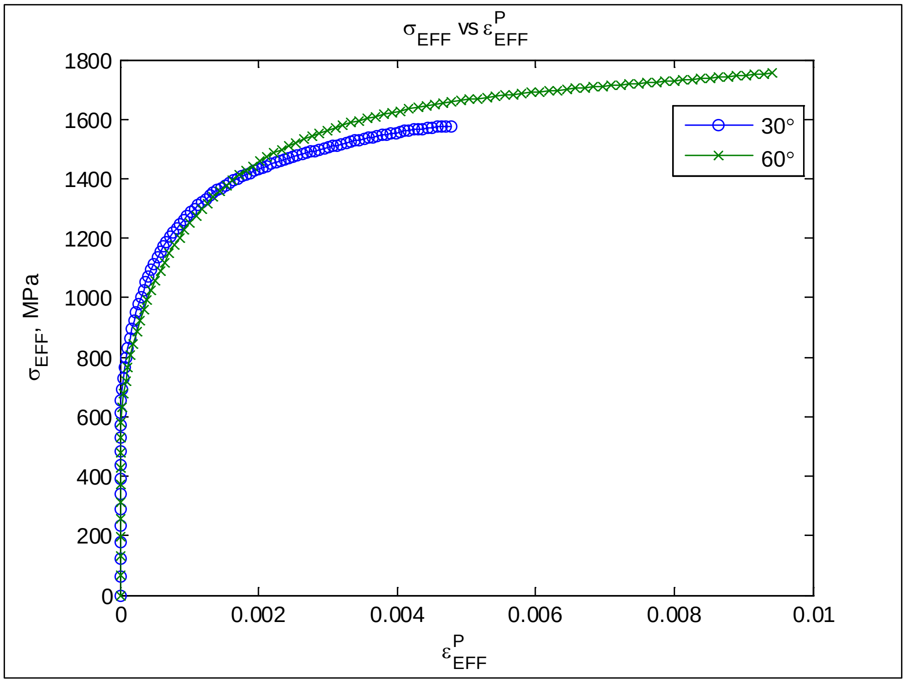

Figure 5.7: Master Curve Effective Stress vs. Effective Plastic Strain for IM7/8552

A linear regression is next performed on the log-log transformation data of the master curve as shown in Figure 5.8. The resulting power law fit for equation 5.23 is shown in Figure 5.9.

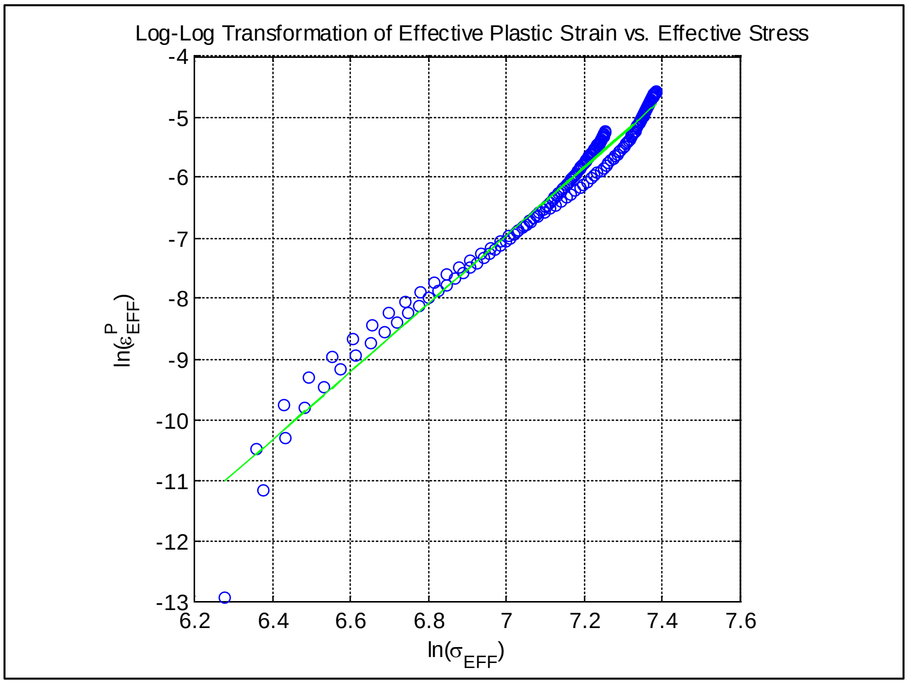

Figure 5.8: Log-Log Transformation of Master Curve IM7/8552 Data

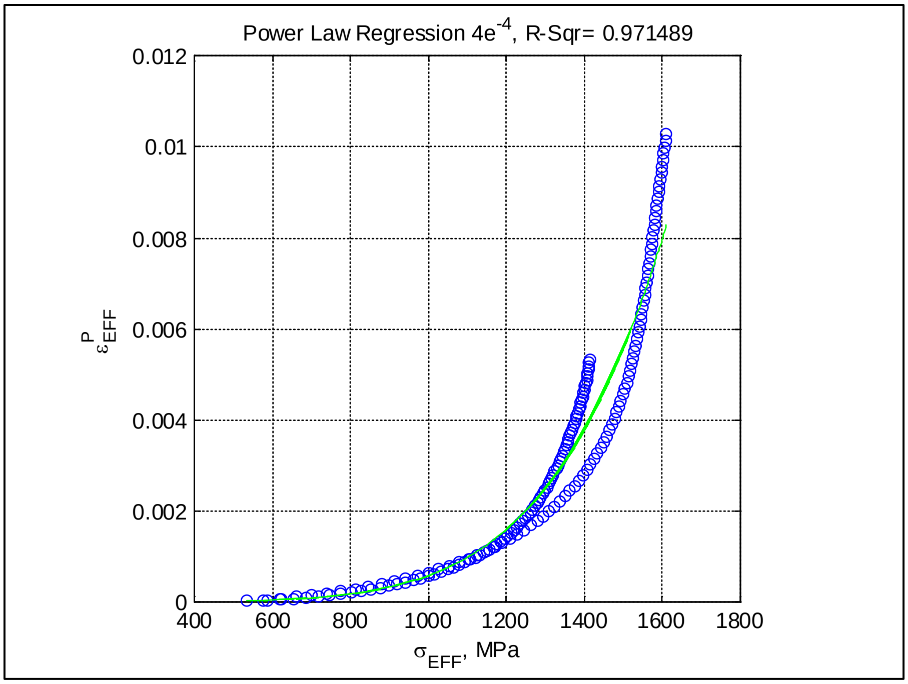

Figure 5.9: IM7/8552 Power Law Hardening Rule Fit

Holding the n parameter constant in equation 5.23, the A parameter is calculated for the SPHB dynamic loading cases for the 30° and 60° angles. A linear regression is performed on the log-log transformed data of the relationship of the A parameter against the effective plastic strain rate. From the linear regression shown in Figure 5.10 the χ and m parameters for the dual power law hardening rule in equation 5.24 can be determined.

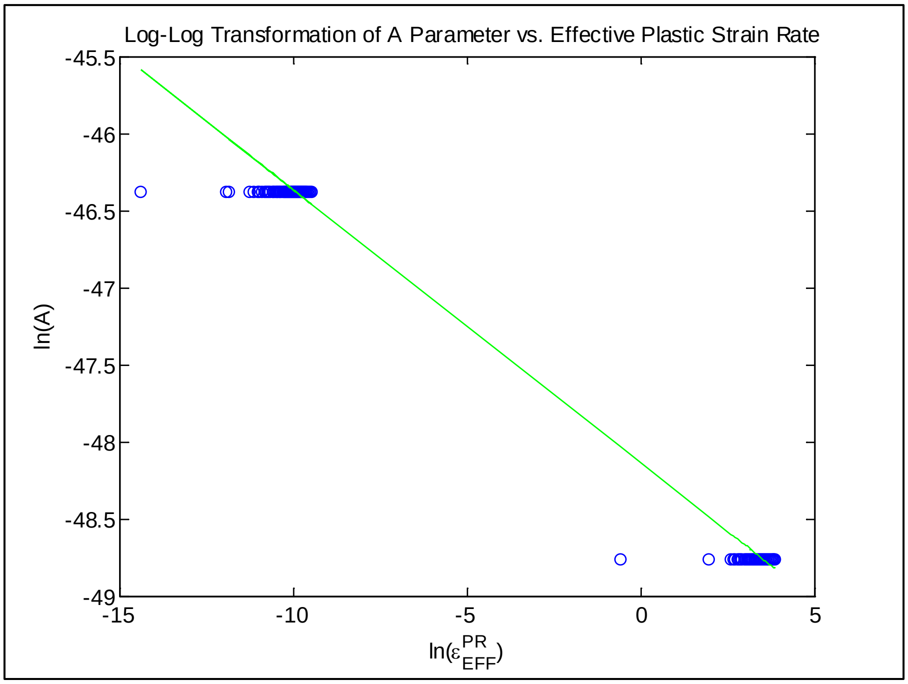

Figure 5.10: Linear Regression Calculation for χ and m Parameters

Comparing the 4th order polynomial fitted data to the viscoplastic model, the static and dynamic cases are considered. Recall that the polynomial fits were used to average the variation from the test replications. For the static case illustrated in Figure 5.11 an excellent agreement is observed between the fitted data. For the dynamic case in Figure 5.12 a reasonable fit is obtained for the 15° and 30° cases. Although the viscoplastic model under-predicts in the 60° case, the overall model response for the dynamic cases is still acceptable. Figures 5.13 and 5.14 compare the viscoplastic model response to the experimental data for the static and dynamic cases, respectively.

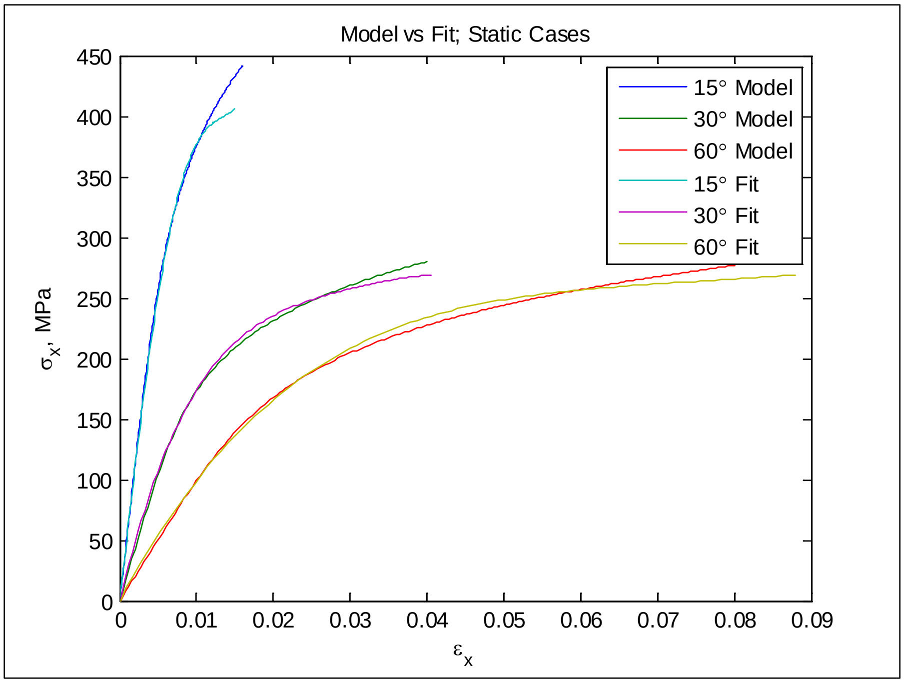

Figure 5.11: IM7/8552 Stress vs Strain; Comparison of Model to Fitted Data; Static Cases

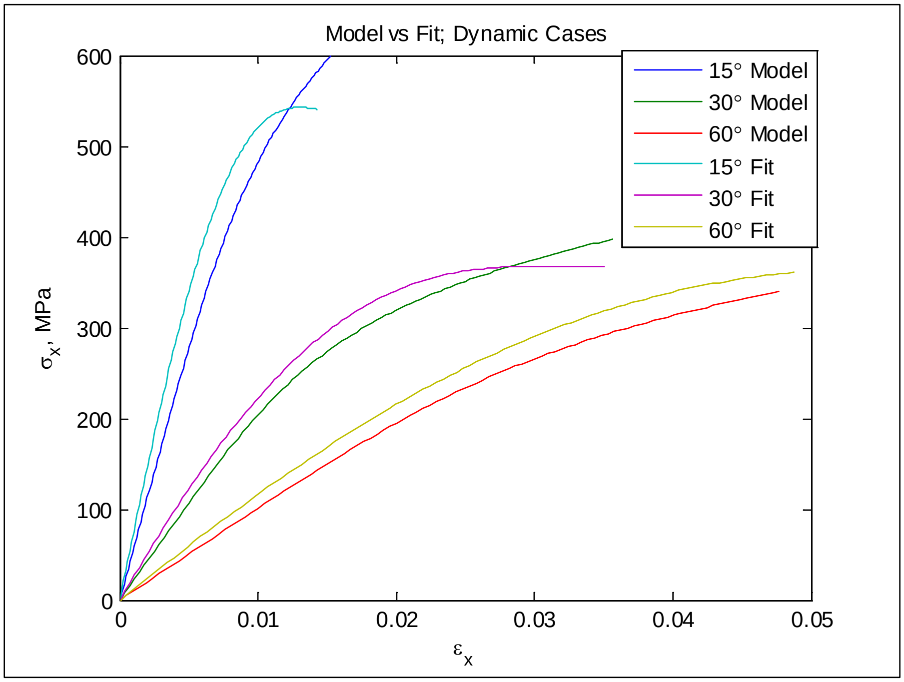

Figure 5.12: IM7/8552 Stress vs Strain; Comparison of Model to Fitted Data; Dynamic Cases

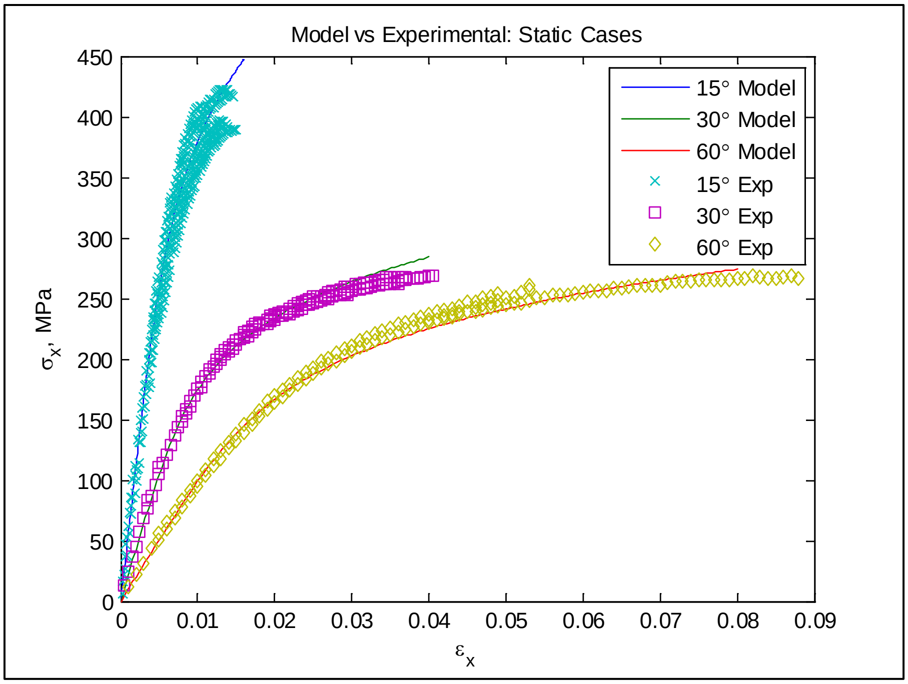

Figure 5.13: IM7/8552 Stress vs Strain; Comparison of Model to Experimental Data; Static Cases

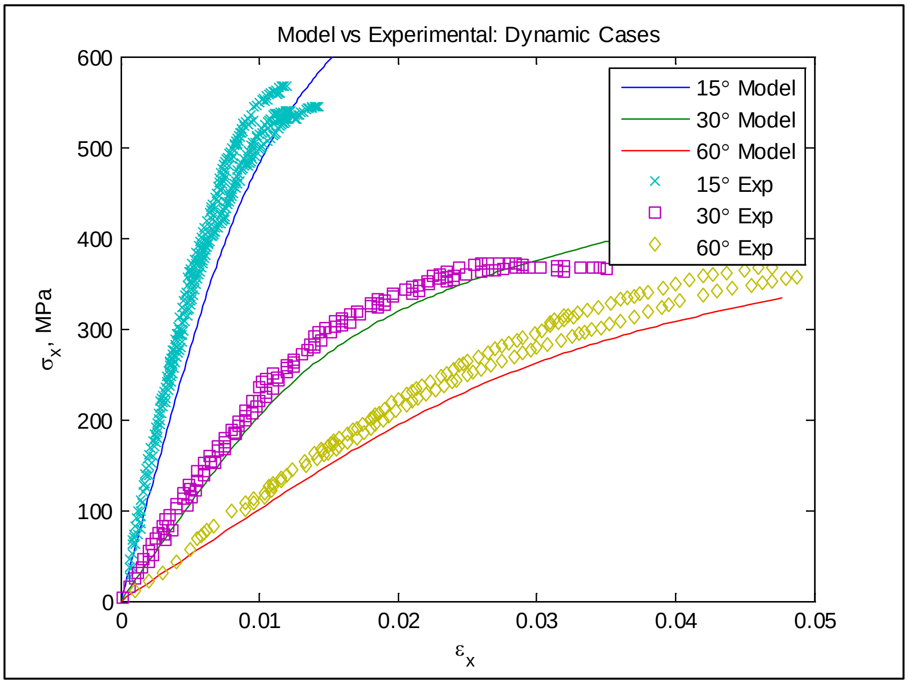

Figure 5.14: IM7/8552 Stress vs Strain; Comparison of Model to Experimental Data; Dynamic Cases

Chapter 6 : Coupled Viscoplastic Progressive Damage Model

The viscoplastic material model presented in Chapter 5 is algorithmically coupled to an energy-based progressive damage model in the on-going chapter. As such the viscoplastic model is restated in terms of the Continuum Damage Mechanics (CDM) framework. The energy-based progressive damage model is derived (46) (47). Intralaminar and interlaminar fracture energies are dissipated through the damage model. Based on the experimental data for composite behavior, a strain-based failure criteria is selected as the initiation criteria for the damage model. A 3-D smeared crack model is presented that links the fracture mechanics and continuum damage mechanics frameworks through characteristic lengths. The material model is implemented into the commercial Finite Element code LS-DYNA as a user defined material model subroutine. The required material model parameters are developed based on experimental data presented in the literature, the results from the optimization algorithm presented in Section 5.6, and estimations. LS-DYNA simulations are then performed to examine and evaluate the model response to various loading conditions.

6.1: Continuum Damage Mechanics Approach

Using the classical definitions, the nominal Cauchy stresses, $\boldsymbol{\sigma}$, is based on the undamaged material while the effective stresses, $\bar{\boldsymbol{\sigma}}$, is based on the damaged material (48). Note that hereafter boldface denotes a tensor. The nominal and effective stresses can be related through a damage variable, d_{ij}, which represents a ratio between the initial undamaged cross-sectional area and the damaged cross-sectional area as shown in equation 6.1. Alternatively equation 6.1 can be expressed in matrix form as shown in equation 6.2. The value of the damage variable ranges from 0 for undamaged material to 1 for fully damaged.

$$\begin{gathered} \sigma_{ij} = (1 - d_{ij})\,\bar{\sigma}_{ij} \\ where\ \ d = \frac{A}{A_{initial}} \end{gathered} \qquad \textbf{6.1}$$

$$\{\boldsymbol{\sigma}\}=\begin{bmatrix}(1-d_{11}) & 0 & 0 & 0 & 0 & 0\\ 0 & (1-d_{22}) & 0 & 0 & 0 & 0\\ 0 & 0 & (1-d_{33}) & 0 & 0 & 0\\ 0 & 0 & 0 & (1-d_{12}) & 0 & 0\\ 0 & 0 & 0 & 0 & (1-d_{23}) & 0\\ 0 & 0 & 0 & 0 & 0 & (1-d_{13})\end{bmatrix}\{\bar{\boldsymbol{\sigma}}\} \qquad 6.2$$

$$or \quad \boldsymbol{\sigma}=D\bar{\boldsymbol{\sigma}}$$

Composite materials damaged in tension can still bear a load under compressive loading. The damage variables for the normal stresses and thus the damage due to tension and compression are maintained separately. The damage for the shear stresses are the same regardless of the shear direction. Since the damage criteria for this model will be strain based, the material loading state is determined by the total strain. Equation 6.3 explicitly defines the damage variables for the normal stresses under tensile or compressive loading.

$$d_{11}=\begin{matrix} d_{11t} & if\ \varepsilon_{11}\geq 0\\ d_{11c} & if\ \varepsilon_{11}\leq 0\end{matrix} \quad d_{22}=\begin{matrix} d_{22t} & if\ \varepsilon_{22}\geq 0\\ d_{22c} & if\ \varepsilon_{22}\leq 0\end{matrix} \quad d_{33}=\begin{matrix} d_{33t} & if\ \varepsilon_{33}\geq 0\\ d_{33c} & if\ \varepsilon_{33}\leq 0\end{matrix} \qquad 6.3$$

6.2: Viscoplastic Model Within Damage Mechanics Framework

The viscoplastic material model presented in Chapter 5 can be restated in terms consistent with the traditional terminology present in the CDM approach. Based on equation 6.1 effective stresses will be considered as the Cauchy stresses in terms of the undamaged cross-sectional area. In order to remain consistent, the effective stress, effective plastic strain, and effective plastic strain rate in the plasticity framework will from this point forward be referred to as the equivalent stress, equivalent plastic strain, equivalent plastic strain rate in the CDM framework, respectively (49). The notation for the effective stress, effective plastic strain, and effective plastic strain rate will accordingly be updated for the CDM framework as shown in equation 6.4.

$$\begin{gathered}\bar{\boldsymbol{\sigma}}\rightarrow\tilde{\sigma}\\ \bar{\varepsilon}^{p}\rightarrow\tilde{\varepsilon}^{p}\\ \bar{\dot{\varepsilon}}^{p}\rightarrow\tilde{\dot{\varepsilon}}^{p}\end{gathered} \qquad 6.4$$

The plastic potential from equation 5.7 is simply reframed as shown in equation 6.5 using the effective stress definition from the CDM framework:

$$\begin{gathered}2f(\bar{\boldsymbol{\sigma}}_{ij}) = A_{12}\left(\bar{\sigma}_{11} - \alpha_{12}\bar{\sigma}_{22}\right)^2 + A_{23}\left(\bar{\sigma}_{22} - \alpha_{23}\bar{\sigma}_{33}\right)^2 + A_{31}\left(\bar{\sigma}_{33} - \alpha_{31}\bar{\sigma}_{11}\right)^2 \\ +2a_{44}\bar{\sigma}_{23}^2 + 2a_{55}\bar{\sigma}_{13}^2 + 2a_{66}\bar{\sigma}_{12}^2 \\ where \\ \alpha_{12} = \frac{C_{11} + C_{12} + C_{13}}{C_{12} + C_{22} + C_{23}} \quad \alpha_{23} = \frac{C_{12} + C_{22} + C_{23}}{C_{13} + C_{23} + C_{33}} \quad \alpha_{31} = \frac{C_{13} + C_{23} + C_{33}}{C_{11} + C_{12} + C_{13}}\end{gathered} \tag{6.5}$$

Likewise, the equivalent stress can be expressed as shown in equations 6.6 and 6.7.

$$\tilde{\sigma} = \sqrt{3f} \tag{6.6}$$

$$\tilde{\sigma} = \sqrt{\frac{3}{2}}\left[\begin{gathered}A_{12}\left(\bar{\sigma}_{11} - \alpha_{12}\bar{\sigma}_{22}\right)^2 + A_{23}\left(\bar{\sigma}_{22} - \alpha_{23}\bar{\sigma}_{33}\right)^2 + A_{31}\left(\bar{\sigma}_{33} - \alpha_{31}\bar{\sigma}_{11}\right)^2 \\ +2a_{44}\bar{\sigma}_{23}^2 + 2a_{55}\bar{\sigma}_{13}^2 + 2a_{66}\bar{\sigma}_{12}^2\end{gathered}\right]^{1/2} \tag{6.7}$$

The rate-independent and rate-dependent hardening rules from equation 5.24 are restated as shown in equations 6.8 and 6.9, respectively.

$$\tilde{\sigma}\left(\tilde{\varepsilon}^p\right) = \left(\frac{\tilde{\varepsilon}^p}{A}\right)^{1/n} \tag{6.8}$$

$$\tilde{\sigma}\left(\tilde{\varepsilon}^p, \dot{\tilde{\varepsilon}}^p\right) = \left(\frac{\tilde{\varepsilon}^p}{\chi\left(\dot{\tilde{\varepsilon}}^p\right)^m}\right)^{1/n} \tag{6.9}$$

The plastic yield function from equation 5.35 is reframed as shown in equation 6.10.

$$\begin{gathered}F\left(\bar{\boldsymbol{\sigma}}, \tilde{\varepsilon}^p, \dot{\tilde{\varepsilon}}^p\right) = \tilde{\sigma}\left(\bar{\boldsymbol{\sigma}}\right) - \tilde{\sigma}\left(\tilde{\varepsilon}^p, \dot{\tilde{\varepsilon}}^p\right) = 0 \\ or \\ F\left(\bar{\boldsymbol{\sigma}}, \tilde{\varepsilon}^p, \dot{\tilde{\varepsilon}}^p\right) = \sqrt{\frac{3}{2}}\left[\begin{gathered}A_{12}\left(\bar{\sigma}_{11} - \alpha_{12}\bar{\sigma}_{22}\right)^2 + A_{23}\left(\bar{\sigma}_{22} - \alpha_{23}\bar{\sigma}_{33}\right)^2 \\ +A_{31}\left(\bar{\sigma}_{33} - \alpha_{31}\bar{\sigma}_{11}\right)^2 + 2a_{44}\bar{\sigma}_{23}^2 \\ +2a_{55}\bar{\sigma}_{13}^2 + 2a_{66}\bar{\sigma}_{12}^2\end{gathered}\right]^{1/2} - \left(\frac{\tilde{\varepsilon}^p}{\chi\left(\dot{\tilde{\varepsilon}}^p\right)^m}\right)^{1/n} = 0\end{gathered} \tag{6.10}$$

From the associated flow rule, the plastic strain rates can be defined explicitly as in equation 6.11.

$$\dot{\varepsilon}_{ij}^{p}=\frac{3}{2\tilde{\sigma}}\left\{\begin{matrix}\left(\mathrm{A}_{12}+\mathrm{A}_{31}\alpha_{31}^{2}\right)\bar{\sigma}_{11}-\mathrm{A}_{12}\alpha_{12}\bar{\sigma}_{22}-\mathrm{A}_{31}\alpha_{31}\bar{\sigma}_{33}\\-\mathrm{A}_{12}\alpha_{12}\bar{\sigma}_{11}+\left(\mathrm{A}_{23}+\mathrm{A}_{12}\alpha_{12}^{2}\right)\bar{\sigma}_{22}-\mathrm{A}_{23}\alpha_{23}\bar{\sigma}_{33}\\-\mathrm{A}_{31}\alpha_{31}\bar{\sigma}_{11}-\mathrm{A}_{23}\alpha_{23}\bar{\sigma}_{22}+\left(\mathrm{A}_{31}+\mathrm{A}_{23}\alpha_{23}^{2}\right)\bar{\sigma}_{33}\\2a_{66}\bar{\sigma}_{12}\\2a_{44}\bar{\sigma}_{23}\\2a_{55}\bar{\sigma}_{13}\end{matrix}\right\}\dot{\lambda} \qquad \mathbf{6.11}$$

6.3: Energy-Based Damage Progression

As suggested by Zheng et al, it can be argued that a strain-based failure criteria is more appropriate for rate-dependent composite materials subject to dynamic loading conditions such as ballistic impact (50). Koerber et al performed off-axis compressive testing for unidirectional IM7/8552 carbon fiber/epoxy composite panels for various fiber angles relative to the loading direction at both quasi-static and dynamic loading conditions (44) (51). The experimental results for the failure stress and strain from Koerber et al are summarized in Tables 6.1 and 6.2 for quasi-static and dynamic compressive loading conditions, respectively. The results show that the strength is rate-dependent for all of the cases tested while the failure strain varied less for the majority of the off-axis angles considered. Additionally, stress-based failure criteria can be difficult to implement for a composite model in that the stress at failure will change with the loading rate. In order to facilitate the change of failure stress, Yen utilized a Johnson-Cook type relationship to represent the current failure stress in terms of the current strain rate and the failure stress at a reference strain rate [3] [4]. Thus strain-based failure criteria will be utilized for the damage model in the present research.

Fiber Angle	Ultimate Strength (MPa)	Ultimate Strain (%)	Strain Rate (1/second)
15°	399	1.27	4.0E-04
30°	266	3.68	4.0E-04
45°	254	8.38	4.0E-04
60°	263	6.16	4.0E-04
75°	252	4.20	4.0E-04
90°	255	4.26	4.0E-04

Table 6.1: IM7/8552 Unidirectional Strength Off-Axis Compression Quasi-static Loading

Fiber Angle	Ultimate Strength (MPa)	Ultimate Strain (%)	Strain Rate (1/second)
15°	549	1.27	122
30°	370	3.14	246
45°	354	6.00	321
60°	365	4.81	367
75°	363	4.38	317
90°	371	4.58	271

Table 6.2: IM7/8552 Unidirectional Strength Off-Axis Compression Dynamic Loading

In order to maintain simplicity, the maximum strain failure criteria will be utilized since there are no assumptions regarding the preform structure (i.e. unidirectional or woven) and also there are no interactions between the strains. The lack of interactions will make attributing damage to particular failure criteria easier. Although the maximum strain criteria do not directly have interactions defined, due to Poisson's effect there are indirect interactions between the normal strains. The maximum strain failure criteria for the damage model can be defined as shown in equation 6.12.

$$F_{ii}(\varepsilon_{ii}) = \frac{\varepsilon_{ii}}{\varepsilon_{ii}^{fail,t}} - 1 \geq 0 \;\; if \;\; \varepsilon_{ii} \geq 0 \quad F_{ii}(\varepsilon_{ii}) = \frac{\varepsilon_{ii}}{\varepsilon_{ii}^{fail,c}} - 1 \geq 0 \;\; if \;\; \varepsilon_{ii} < 0$$
$$F_{ij}(\gamma_{ij}) = \frac{\gamma_{ij}}{\gamma_{ij}^{fail}} - 1 \geq 0 \qquad \textbf{6.12}$$

Iannucci et al have presented an energy-based damage mechanics model that assumes linear energy dissipation post-failure using a smeared crack methodology [27] [28] [29] [30]. A representative volume element was assumed and therefore the energy dissipation and crack growth are defined in terms of the energy needed to expand the fracture area [28]. Iannucci et al linked the damage mechanics model with fracture mechanics to reduce the level of mesh sensitivity present in the solution. The specific fracture energy can be written in terms of the stress and strain relationship as in equation 6.13.

$$E_F = \int_0^\infty \sigma_{ij} d\varepsilon_{ij} \qquad \textbf{6.13}$$

Assuming a largely bi-linear stress strain damage relationship, Iannucci demonstrated that the specific fracture energy, E_F, can be decomposed into the elastic, E_E, and plastic, E_P, energy contributions as defined in equation 6.14 and illustrated in Figure 6.1.

$$E_F = E_E + E_P \tag{6.14}$$

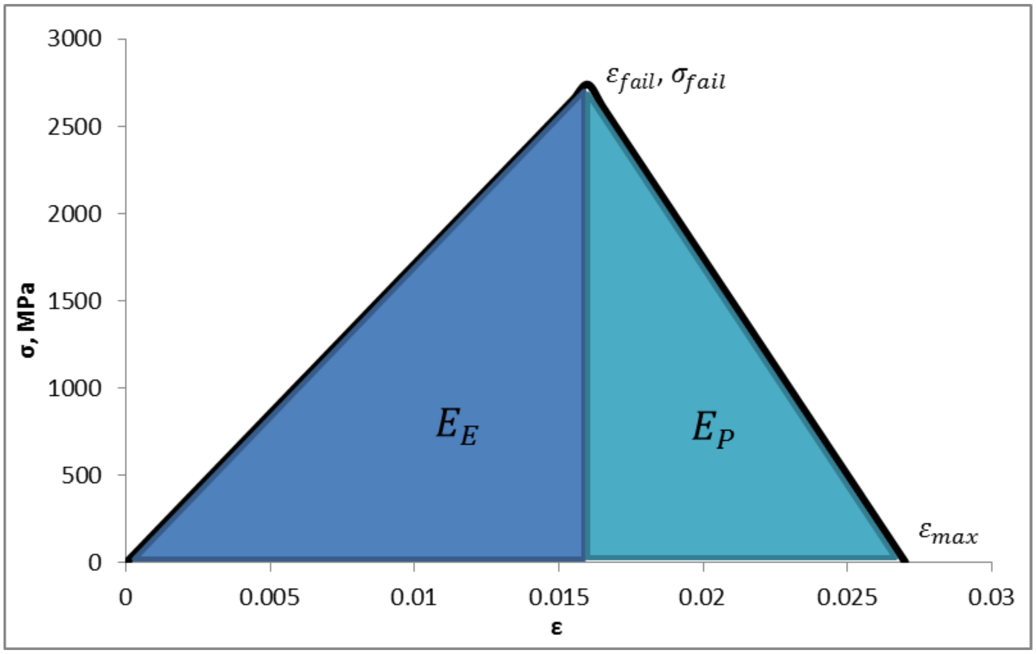

Figure 6.1: Energy Contributions to Total Fracture Energy

The fracture energy per unit area, often referred to as either the intralaminar or interlaminar fracture energy depending on direction, can be expressed as shown in equation 6.15 where δ is the increase in crack length. The intralaminar and interlaminar fracture energies are determined experimentally using different methodologies depending on the direction and the underlying structure [31] [32] [33] [34] [35] [36].

$$G_{fr} = \int_0^\infty \sigma_{ij} d\delta_{ij} \tag{6.15}$$

Using equations 6.13 through 6.15 and defining the characteristic length, l_{el}, and fracture area in the element, A_{el}, the energy released is defined as in equation 6.16.

$$\left(E_E + E_P\right) A_{el} l_{el} = G_{fr} A_{el} \qquad \textbf{6.16}$$

Simplifying equation 6.16 and rearranging in terms of the plastic energy contribution gives the relationship in equation 6.17.

$$E_P = \frac{G_{fr}}{l_{el}} - E_E \qquad \textbf{6.17}$$

Based on the assumption that the energy dissipated can be described by a bi-linear relationship, the specific fracture energy and the elastic and plastic contributions can be defined as in equations 6.18 and 6.19, respectively.

$$E_F = \frac{1}{2}\sigma_{fail}\varepsilon_{\max} \qquad \textbf{6.18}$$

$$E_E = \frac{1}{2}\sigma_{fail}\varepsilon_{fail} \quad E_P = \frac{1}{2}\sigma_{fail}\left(\varepsilon_{\max} - \varepsilon_{fail}\right) \qquad \textbf{6.19}$$

Using equations 6.17 and 6.18, the maximum strain, $\varepsilon_{\max}$, can be defined explicitly for the bilinear assumption as defined in equation 6.20.

$$\varepsilon_{\max} = \frac{2G_{fr}}{\sigma_{fail}\, l_{el}} \qquad \textbf{6.20}$$

Additionally Iannucci et al noted that the representative volume element should not exceed a particular size in order to prevent negative E_P (46). Using equations 6.16 and 6.18, an inequality for the maximum characteristic length results.

$$l_{el} < \frac{2G_{fr}}{\sigma_{fail}\, \varepsilon_{fail}} \qquad \textbf{6.21}$$

The linear damage progression for different directions can be defined in terms of the strain and maximum strain defined in equation 6.20.

$$d_{ij}(\varepsilon_{ij}) = \left(\frac{\varepsilon_{\max,\mathrm{ij}}}{\varepsilon_{\max,\mathrm{ij}} - \varepsilon_{fail,\mathrm{ij}}}\right)\left(1 - \frac{\varepsilon_{fail,\mathrm{ij}}}{\varepsilon_{ij}}\right) \qquad \textbf{6.22}$$

Donadon et al presented an interpolation polynomial damage progression function based on the linear relationship assumed by Iannucci et al as shown in equation 6.23 (47).

$$d_{ij}(\varepsilon_{ij}) = 1 - \frac{\varepsilon_{fail,\mathrm{ij}}}{\varepsilon_{ij}}\left(1+\kappa_{ij}^2\left(\varepsilon_{ij}\right)\left(2\kappa_{ij}\left(\varepsilon_{ij}\right)-3\right)\right)$$

$$where\ \ \kappa_{ij}\left(\varepsilon_{ij}\right) = \frac{\varepsilon_{ij}-\varepsilon_{fail,\mathrm{ij}}}{\varepsilon_{\max,\mathrm{ij}}-\varepsilon_{fail,\mathrm{ij}}} \qquad \mathbf{6.23}$$

Figure 6.2 compares the polynomial and linear damage progression for a 1-D uniaxial tensile loading case. The interpolation polynomial proposed by Donadon et al allows for a smoother transition from damage initiation to a fully damaged material as evidenced by the post failure stress. As such the interpolation polynomial will be utilized in the present research.

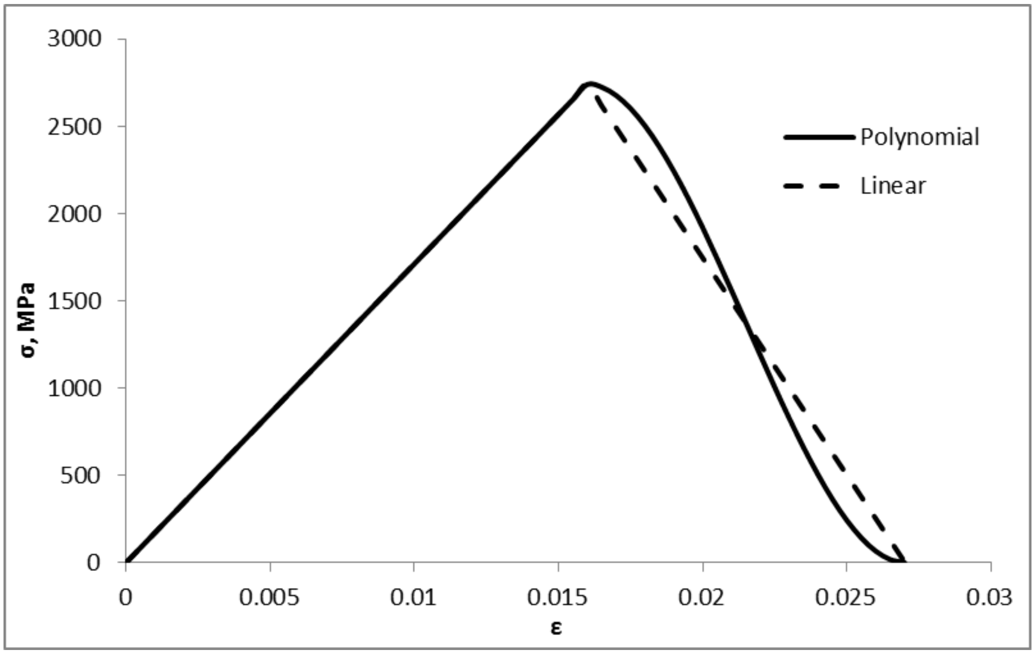

Figure 6.2: Comparison of Energy Dissipation for Polynomial and Linear Damage Progression

Figure 6.3 examines a 1-D uniaxial tensile loading case in terms of the element size and the damage variable progression. As the element size increases, and correspondingly the characteristic length, the maximum strain obtained reduces. This ensures that regardless of the element size, the energy released for the structure will remain the same for different mesh discretizations.

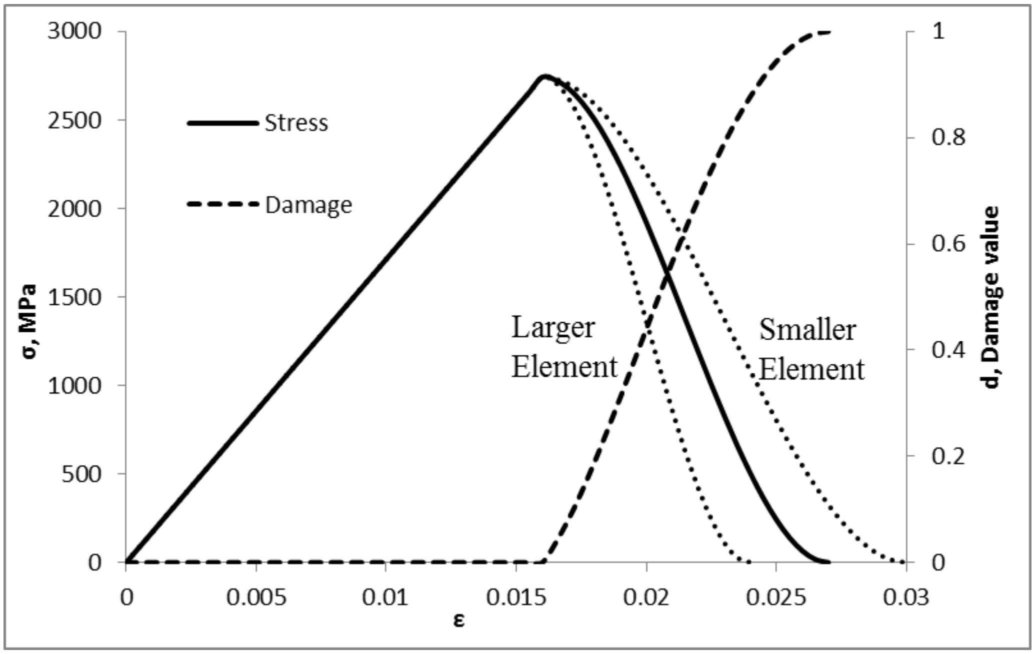

Figure 6.3: 1-D Uniaxial Tensile Damage Progression

6.4: Smeared Crack Model

As mentioned in the previous section the damage progression model is coupled to the fracture mechanics framework though the smeared crack methodology. A large discontinuity such as fracture violates the continuum assumption inherent to the finite element method. The smeared crack model is a methodology to treat this discontinuity by representing the fracture as a dense distribution of micro-cracks (52) (53). The fracture energy dissipated is maintained for different element sizes by the characteristic length of the element. The characteristic length depends on the crack direction in addition to the element size. For 2-D models, the crack band model proposed by Bazant et al (52) has been used by several authors effectively (54) (55) (49) (56).

However, for 3-D composite models, the crack propagation can also occur through the thickness direction in addition to within the composite plane. Donadon et al extended the 2-D smeared crack model proposed by Oliver (53) for 3-D composite models (57) (58) (47). Oliver assumed a curvilinear singularity band formed by a pair of singular lines. By enforcing equilibrium across the singularity band, Oliver established the relationship between the specific energy and fracture energy, equation 6.24, where ϕ is a continuous, derivable function and the characteristic length, l_{el}, is a function of the crack direction in an auxiliary x'-y'coordinate system.

$$E_F = G_{fr}\frac{\partial\phi}{\partial x'} = \frac{G_{fr}}{l_{el}}$$
$$where\ \ l_{el}\left(x',y'\right) = \left(\frac{\partial\phi}{\partial x'}\right)^{-1} \tag{6.24}$$

Oliver considered the single integration point quadrilateral or Q4 element. The isoparametric coordinate relationships to the global coordinate system for the Q4 element are shown in equation 6.25. Thus the function ϕ can be expressed as shown in equation 6.26 and meets the requirement that the function equals +1 if the node position is ahead of the crack and 0 if the node position is behind the crack (53).

$$x = \sum_{i=1}^{4} x_i\, N_i\left(\xi,\eta\right) \quad y = \sum_{i=1}^{4} y_i\, N_i\left(\xi,\eta\right)$$
$$where\ \ N_i\left(\xi,\eta\right) = \frac{1}{4}\left(1+\xi_i\,\xi\right)\left(1+\eta_i\,\eta\right) \tag{6.25}$$

$$\phi\left(\xi,\eta\right) = \sum_{i=1}^{4} N_i\left(\xi,\eta\right)\phi_i \tag{6.26}$$

Donadon et al considered a single integration point hexahedral or ‘brick’ element. In order to consider failure modes both in-plane and out-of-plane, virtual Q4 elements are formed in the mid-planes as shown in Figure 6.4. An auxiliary coordinate system (x'-y'-z') for the virtual mid-plane elements, Figure 6.5, is formed for each integration point j. The direction of the local x' axis is defined by the normal to the fracture plane which is also the fiber direction. The local auxiliary coordinate transformation is given by equation 6.27.

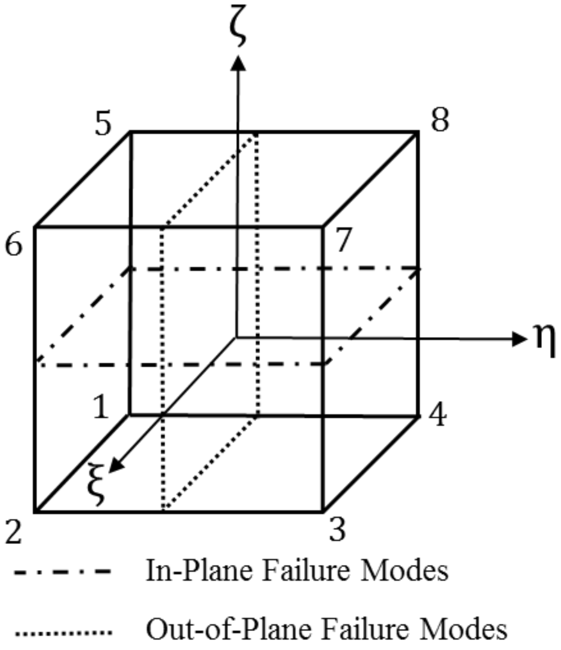

Figure 6.4: Isoparametric Coordinate System and Element Node Numbering for Hexahedral Element

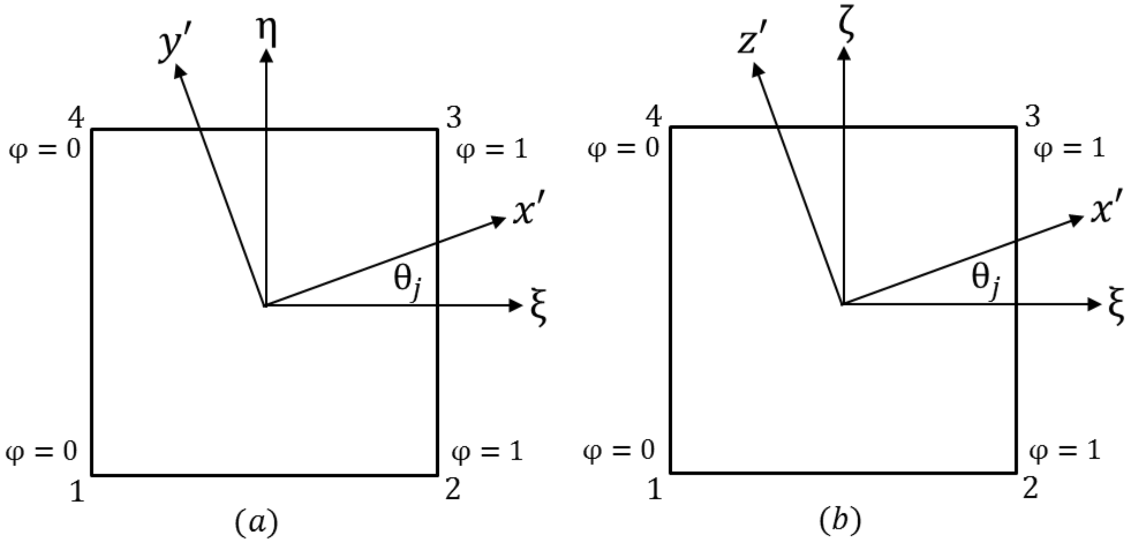

Figure 6.5: Virtual Mid-planes of Hexahedral Element (a) in-plane failure modes (b) out-of-plane failure modes

$$\begin{Bmatrix} x_i' \\ y_i' \end{Bmatrix} = \begin{bmatrix} \cos\theta_j & \sin\theta_j \\ -\sin\theta_j & \cos\theta_j \end{bmatrix} \begin{Bmatrix} x_i \\ y_i \end{Bmatrix} \qquad \textbf{6.27}$$

Using equations 6.24, 6.26, and 6.27 the characteristic length for fiber failure under tension or compression is defined as in equation 6.28. As pointed out by Donadon et al, in-plane shear cracking is strongly dependent on the fiber orientation and as such the associated characteristic length is equal to the fiber failure characteristic length, $l_{12} = l_{11}$.

$$l_{11} = l_{12} = \left(\frac{\partial \phi(\xi_j, \eta_j)}{\partial x'} \right)^{-1} = \left(\sum_{i=1}^{4} \left[\frac{\partial N_i(\xi_j, \eta_j)}{\partial x} \cos\theta_j + \frac{\partial N_i(\xi_j, \eta_j)}{\partial y} \sin\theta_j \right] \phi_i \right)^{-1} \qquad \textbf{6.28}$$

Similarly, the characteristic length for tensile matrix failure or weft tow failure can be defined as shown in equation 6.29.

$$l_{22}^{t} = \left(\frac{\partial \phi(\xi_j, \eta_j)}{\partial y'} \right)^{-1} = \left(\sum_{i=1}^{4} \left[-\frac{\partial N_i(\xi_j, \eta_j)}{\partial x} \sin\theta_j + \frac{\partial N_i(\xi_j, \eta_j)}{\partial y} \cos\theta_j \right] \phi_i \right)^{-1} \qquad \textbf{6.29}$$

The partial derivatives in equations 6.28 and 6.29 can be defined explicitly as in equation 6.30 where the element Jacobian, J_{xy} , is defined as in equation 6.31. The equations have been derived to match the node numbering convention in LS-DYNA.

$$\begin{Bmatrix} \frac{\partial N_i}{\partial x} \\ \frac{\partial N_i}{\partial y} \end{Bmatrix} = J_{xy}^{-1} \begin{Bmatrix} \frac{\partial N_i}{\partial \xi} \\ \frac{\partial N_i}{\partial \eta} \end{Bmatrix} \qquad \textbf{6.30}$$

$$J_{xy} = \begin{bmatrix} \frac{\partial N_1}{\partial \xi} & \frac{\partial N_2}{\partial \xi} & \frac{\partial N_3}{\partial \xi} & \frac{\partial N_4}{\partial \xi} \\ \frac{\partial N_1}{\partial \eta} & \frac{\partial N_2}{\partial \eta} & \frac{\partial N_3}{\partial \eta} & \frac{\partial N_4}{\partial \eta} \end{bmatrix} \begin{bmatrix} x_1 & y_1 \\ x_2 & y_2 \\ x_3 & y_3 \\ x_4 & y_4 \end{bmatrix}$$

$$where$$

$$\left\{ \frac{\partial N_i}{\partial \xi} \right\} = \begin{Bmatrix} \frac{\partial N_1}{\partial \xi} \\ \frac{\partial N_2}{\partial \xi} \\ \frac{\partial N_3}{\partial \xi} \\ \frac{\partial N_4}{\partial \xi} \end{Bmatrix} = \frac{1}{4} \begin{Bmatrix} -(1-\eta) \\ (1-\eta) \\ (1+\eta) \\ -(1+\eta) \end{Bmatrix} \quad \left\{ \frac{\partial N_i}{\partial \eta} \right\} = \begin{Bmatrix} \frac{\partial N_1}{\partial \eta} \\ \frac{\partial N_2}{\partial \eta} \\ \frac{\partial N_3}{\partial \eta} \\ \frac{\partial N_4}{\partial \eta} \end{Bmatrix} = \frac{1}{4} \begin{Bmatrix} -(1-\xi) \\ -(1+\xi) \\ (1+\xi) \\ (1-\xi) \end{Bmatrix} \qquad \textbf{6.31}$$

Donadon et al then utilized the out-of-plane mid-plane to define the characteristic length for the out-of-plane failure modes including transverse compression failure and out-of-plane shear failure (58). In a similar fashion, transverse compression characteristic length, l_{22}^c, is defined by equations 6.32, 6.33, and 6.34.

$$l_{22}^c = \left(\frac{\partial\phi\left(\xi_j,\varsigma_j\right)}{\partial x'}\right)^{-1} = \left(\sum_{i=1}^{4}\left[\frac{\partial N_i\left(\xi_j,\varsigma_j\right)}{\partial x}\cos\theta_j + \frac{\partial N_i\left(\xi_j,\varsigma_j\right)}{\partial z}\sin\theta_j\right]\phi_i\right)^{-1} \qquad \textbf{6.32}$$

$$\begin{Bmatrix}\dfrac{\partial N_i}{\partial x}\\ \dfrac{\partial N_i}{\partial z}\end{Bmatrix} = J_{xz}^{-1}\begin{Bmatrix}\dfrac{\partial N_i}{\partial \xi}\\ \dfrac{\partial N_i}{\partial \varsigma}\end{Bmatrix} \qquad \textbf{6.33}$$

$$J_{xz} = \begin{bmatrix}\dfrac{\partial N_1}{\partial\xi} & \dfrac{\partial N_2}{\partial\xi} & \dfrac{\partial N_3}{\partial\xi} & \dfrac{\partial N_4}{\partial\xi}\\ \dfrac{\partial N_1}{\partial\varsigma} & \dfrac{\partial N_2}{\partial\varsigma} & \dfrac{\partial N_3}{\partial\varsigma} & \dfrac{\partial N_4}{\partial\varsigma}\end{bmatrix}\begin{bmatrix}x_1 & z_1\\ x_2 & z_2\\ x_3 & z_3\\ x_4 & z_4\end{bmatrix}$$

$$\textit{where}$$

$$\begin{Bmatrix}\dfrac{\partial N_i}{\partial\xi}\end{Bmatrix} = \begin{Bmatrix}\dfrac{\partial N_1}{\partial\xi}\\ \dfrac{\partial N_2}{\partial\xi}\\ \dfrac{\partial N_3}{\partial\xi}\\ \dfrac{\partial N_4}{\partial\xi}\end{Bmatrix} = \frac{1}{4}\begin{Bmatrix}-(1-\varsigma)\\ (1-\varsigma)\\ (1+\varsigma)\\ -(1+\varsigma)\end{Bmatrix} \quad \begin{Bmatrix}\dfrac{\partial N_i}{\partial\varsigma}\end{Bmatrix} = \begin{Bmatrix}\dfrac{\partial N_1}{\partial\varsigma}\\ \dfrac{\partial N_2}{\partial\varsigma}\\ \dfrac{\partial N_3}{\partial\varsigma}\\ \dfrac{\partial N_4}{\partial\varsigma}\end{Bmatrix} = \frac{1}{4}\begin{Bmatrix}-(1-\xi)\\ -(1+\xi)\\ (1+\xi)\\ (1-\xi)\end{Bmatrix} \qquad \textbf{6.34}$$

For the remaining out-of-plane failure modes, the micro-cracks are assumed to be smeared over thickness of the ‘brick’ element which corresponds to $\theta_j = 90^\circ$ (58). Thus the characteristic length for the out-of-plane failure modes is defined as in equation 6.35.

$$l_{33} = l_{13} = l_{23} = \left(\sum_{i=1}^{4}\left[\frac{\partial N_i\left(\xi_j,\varsigma_j\right)}{\partial z}\right]\phi_i\right)^{-1} \qquad \textbf{6.35}$$

6.5: Erosion Algorithm

During ballistic impact simulations, elements can become overly distorted which can lead to numerical instabilities and premature termination of the simulation. In order to avoid overly distorted elements, several different techniques can be utilized such as adaptive Lagrangian-Eulerian meshing

(ALE) and element erosion. ALE remeshing involves switching from the distorted Lagrangian elements to an Eulerian definition and back to a Lagrangian defined element mesh. ALE is quite effective in simulations where large deformations are present however it can add significant computational cost. Element erosion instead simply maintains the original Lagrangian mesh and deletes elements once given criteria are met. The downside to erosion algorithms is that the element deletion can lead to unrealistic mass loss and thus energy imbalances in the presence of large deformations. For the impact velocities in the present research the deformations are not expected to lead to many distorted elements, thus the element erosion algorithm will be utilized. Several different criteria can used for the erosion algorithm such as different combinations of the damage variables, d_{ij} . However it is desired to have criteria that are not directly involved in the progressive model in order to avoid premature deletion of elements that could affect the results of the simulation. Yen utilized three simple criteria for the proposed progressive damage composite model (59) (60). As such, for the present research the same criteria will be utilized. The first two criteria define the limit compressive and expansive relative element volumes, ECRSH and EEXPN, as shown in equation 6.36.

$$ECRSH \geq \frac{V_{el}}{V_{el}^{initial}} \quad EEXPN \leq \frac{V_{el}}{V_{el}^{initial}} \tag{6.36}$$

The relative element volume can readily be calculated using the element Jacobian which is simply the determinant of the deformation gradient, F^{DEF} (61). The deformation gradient is readily obtained by the material model from the main LS-DYNA program.

$$V_{REL} = \frac{V_{el}}{V_{el}^{initial}} = \det\left(F^{DEF}\right) \tag{6.37}$$

The remaining criteria is simply a limit on the normal strain, E_LIMT, for the 1-direction for unidirectional composites and both the 1-/2-directions for plain-weave composites. The aforementioned criteria were incorporated into the user-defined material model.

6.6: Material Model Assumptions And Limitations

Throughout the development of the material model several assumptions have been made regarding the material behavior to simplify either the implementation of the model or the material behavior itself. These implied assumptions will be explicitly defined and explored at this time. It is well known that composite materials exhibit a differential in both stiffness and strength when under either compression or tension. This is due to both the residual stresses from manufacturing processes and the various mechanisms between the constituents such as adhesion. Although some CDM-based models such as those for concrete include this differential (62), the present model assumes that there is no difference in stiffness between compressive and tensile loads. However the model does take into account the difference in strength through the maximum strain failure criteria for the normal strains. The failure strains are assumed to be rate-independent based on the experimental data presented in Tables 6.1 and 6.2 (44). Since strain-based failure criteria are desired, the maximum strain criteria have been selected as the failure criteria for the present model. Additionally the damage model also takes into account the strength differential through the characteristic lengths calculated for the 1- and 2-directions by the smeared crack model. As noted by Zhu et al, from a thermodynamic standpoint the anisotropic parameters in equation 6.5 of the viscoplastic model would change in accordance with the loading conditions (63). However establishing and implementing the anisotropic parameter relationships to the loading condition would lead to an untenable engineering solution. As such the anisotropic parameters for the viscoplastic model are considered to be constant for all loading conditions. Several researchers have performed Split Hopkinson Pressure Bar (SPHB) testing to verify whether the anisotropic parameters could be considered constant for increasing strain rates. Both Thiruppkuzhi et al and Ninan et al performed off-axis SPHB testing and verified for S2-Glass/8552 epoxy composites that the anisotropic parameters for the viscoplastic model can be considered constant up to a strain rate of 1000 per second (64) (27). Weeks et al performed SPHB testing to verify the anisotropic parameters for

AS4/PEEK composites up to strain rates of 1000 per second (29). Strain rates in excess of 2500 per second could occur in ballistic impact for the velocity regimes used in previous rounds of experimental testing (21). Thus for the present research it is necessary to assume that the anisotropic parameters are constants. Additionally it is assumed that the rate-dependent hardening rule in equation 6.9 can be extrapolated beyond the range of strain rates used to fit the dual power law. The coupled damage model divides the material behavior into elastic, plastic, and damage regimes as depicted in Figure 6.6.

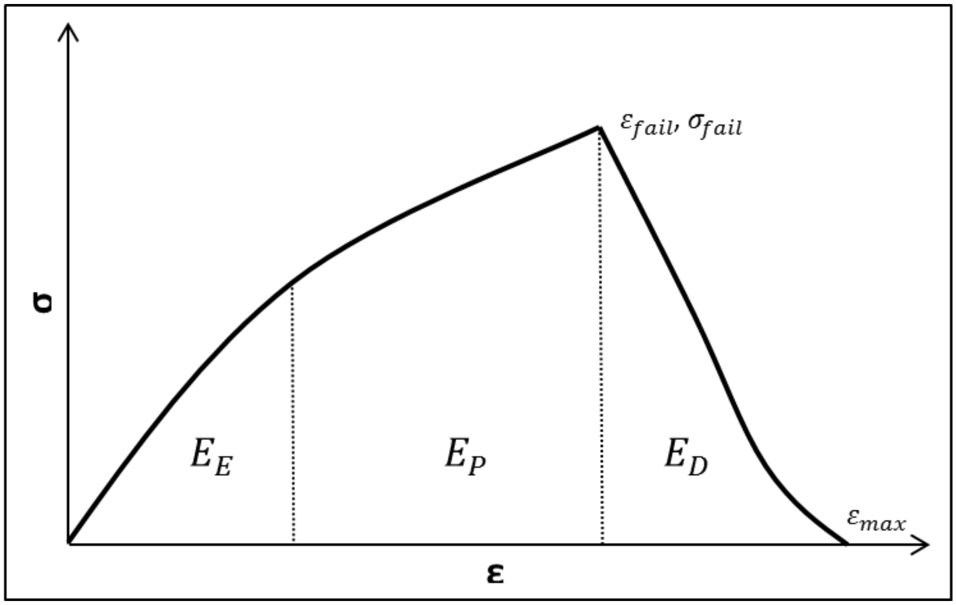

Figure 6.6: Material Model Energy Dissipation Due To Elastic, Plastic, And Damage Contributions

The energy dissipation attributed to the elastic, plastic, and damage contributions are E_E , E_P, and E_D, respectively. Iannucci et al and Donadon et al considered stress response to be a largely bilinear response as shown in Figures 6.1 and 6.2 where the damage is due to the elastic and damage contributions. Based on the bilinear response assumption, Iannucci et al approximated the area underneath the curve or the energy dissipation to be simply the area of a triangle as evidenced in equations 6.18 and 6.19. In order to simplify the implementation of the material model, the same bilinear response will be assumed. This saves computational effort by avoiding explicitly integrating the stress-strain relationship to determine the energy balance. It is assumed that there will be negligible error introduced in the energy balance for the damage model by the bilinear response assumption. Currently the material model is only derived for explicit solver FEM codes since they are more efficient for the anticipated strain rate regimes present in ballistic impact. The model could be readily implemented into implicit FEM solvers since the return mapping algorithm is unconditionally stable and also maintains the quadratic rate of convergence for the Newmark implicit integration (38). This would allow for use of the model in long duration quasi-static simulations. Derivation of the consistent tangent modulus tensor is necessary for the stiffness matrix calculations present in the implicit integration scheme.

6.7: LS-DYNA Implementation

The coupled viscoplastic progressive damage material model has been implemented into LS-DYNA as a user-defined material model. LS-DYNA allows for the user-defined material model (UMAT) through programming a Fortran subroutine which can be called using the user-defined material model interface (65). The LS-DYNA Fortran source code for the user defined interface is written using Fortran 77, 90, and 95 conventions. The UMAT can be written in either scalar or vectorized subroutines. The vectorized subroutines group the models' elements into blocks of up to 192 elements. Vectorized subroutines offer an efficiency advantage over scalar subroutines since fewer calls are made to the material subroutine during each time step (65). For the present research a vectorized UMAT will be implemented on the Auburn University High Performance Compute Cluster (AU HPCC) in order to exploit the computational power. The AU HPCC utilizes the MPICH Message Passing Interface running Redhat Linux on 512 processors over 4 nodes (66). LS-DYNA can utilize either Shared Memory Processing (SMP) or Massively Parallel Processing (MPP) for single and multiple processor computations (65). The UMAT was implemented in both SMP and MPP double precision versions of LS-DYNA release 7.0. For the cluster configuration and release of LS-DYNA, the Intel Fortran Compiler version 10.1 is required.

6.7.1 : LS-DYNA UMAT Overview

The overview of the coupled viscoplastic damage model algorithm is outlined in the flowchart in Figure 6.7. Before the simulation begins, LS-DYNA initializes the Cauchy stresses and history variables for each element. During the pre- simulation initialization the equivalent plastic strain and plastic strain rate also need to be defined to remain consistent with the dual power law. A result of using a power law is that upon loading the equivalent plastic strain and plastic strain rate will instantaneously progress (22). Based on the precision for the history variables, the equivalent plastic strain and plastic strain rate are both initialized to a value of $1.0E-16$. During the simulation, for each load cycle, LS-DYNA calls the UMAT and passes Cauchy stresses and the incremental strains in addition to the history variables which includes the equivalent stress, equivalent plastic strain and plastic strain rate, plastic strains, damage variables, and maximum strain from the previous time step for each element. The characteristic lengths are calculated using relations defined in the 3-D smeared crack model for the element. Next, the viscoplastic return mapping algorithm calculates the effective stresses, plastic strains and equivalent plastic strain and plastic strain rate using the present state of strain. The progressive damage model then calculates the current value for the damage variables. Using the damage variables, the Cauchy stresses can be calculated from the effective stresses. The values for the Cauchy stresses and the history variables are returned to the main LS-DYNA executable for use in the next time step calculations.

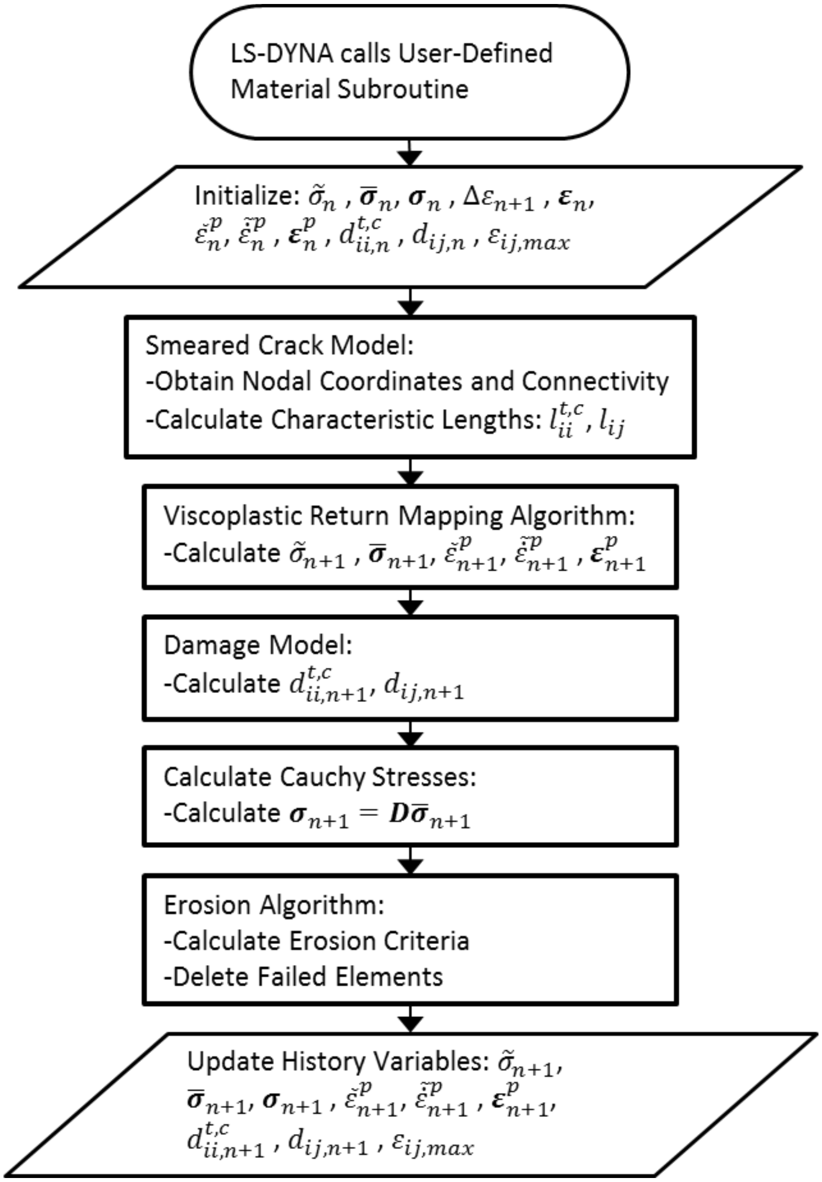

Figure 6.7: Coupled Viscoplastic Damage Material Model Flowchart

6.7.2 : Smeared Crack Model Algorithm

The smeared crack model algorithm is depicted in the flowchart shown in Figure 6.8. As with most finite element codes LS-DYNA renumbers the nodes and elements during the simulation to improve calculation efficiency. The node and element numbering used in the time step calculations are referred to as the internal ID while the numbering defined in the LS-DYNA model is the external ID. For each element during the current time step, the UMAT requests the external ID for the element. Then using the external element ID, the internal node IDs are obtained. LS-DYNA provides the internal node

IDs in the same order as defined in Figure 6.4 which is critical to ensure that a positive element Jacobian is obtained. Otherwise the simulation will terminate prematurely due to a negative element volume. Next the algorithm uses the internal node IDs to obtain the global x-y-z coordinates for the elements' nodes. For both the in-plane and out-of-plane virtual planes, as defined in Figures 6.4 and 6.5, associated with in-plane and out-of-plane failure modes, the global coordinates are calculated. The Q4 virtual nodes are calculated using the midpoint rule for the hexahedral element node pairs as defined in Table 6.3. The node associations defined in Table 6.3 are easily verified by Figures 6.4 and 6.5.

Virtual Midplane	Q4 Node ID	Hexahedral Element Node Pair	
		Node 1	Node 2
In-Plane	1	1	5
	2	2	6
	3	3	7
	4	4	8
Out-of-Plane	1	1	4
	2	2	3
	3	6	7
	4	5	8

Table 6.3: Virtual Mid-plane Q4 Element Node-Hexahedral Element Node Pair Associations

Using the calculated global coordinates for the virtual mid-planes, equations 6.30, 6.31, 6.33, and 6.34 are used to calculate the partial derivatives of the virtual Q4 mid-plane element isoparametric functions with respect to the global coordinates.

$$\left\{\boldsymbol{e}_f^0\right\} = \left\{\cos\theta_f^0, \sin\theta_f^0, 0\right\}^T \tag{6.38}$$

$$\left\{\boldsymbol{e}_f\right\} = \frac{\left[F^{DEF}\right]\left\{\boldsymbol{e}_f^0\right\}}{\left\|\left[F^{DEF}\right]\left\{\boldsymbol{e}_f^0\right\}\right\|} \tag{6.39}$$

$$\theta_f = \tan^{-1}\left(\frac{\boldsymbol{e}_f(2)}{\boldsymbol{e}_f(1)}\right) \tag{6.40}$$

Since it is anticipated that a significant amount of element deformation may occur during the simulation, the element deformation gradient, F^{DEF}, is used to calculate the current fiber angle, θ_f. LS-DYNA allows the UMAT to request the deformation gradient, F^{DEF}, from the main program. The deformation gradient is passed into the material model subroutine at the end of the history variable array. The initial fiber direction vector, $\boldsymbol{e}_f^0$, is defined in equation 6.38. The current fiber direction can then be calculated using the deformation gradient as defined in 6.39. The current fiber direction is then calculated using the inverse tangent of the x and y components of the fiber direction vector as defined in equation 6.40. Given the current state of strain, the current fiber angle and the relations defined in equations 6.28, 6.29, 6.32, and 6.35 are used to calculate the characteristic lengths for the element.

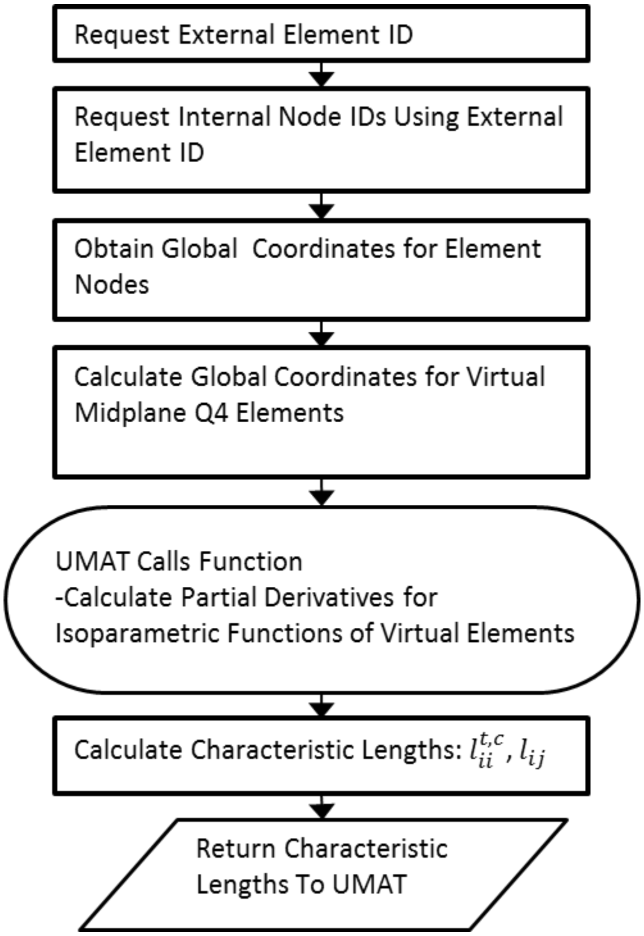

Figure 6.8: Smeared Crack Model Algorithm Flowchart

6.7.3 : Viscoplastic Return Mapping Algorithm

The viscoplastic damage model is coupled through the integration algorithm. The approach presented by Chen et al (49) will be utilized since it provides a simpler method than the thermodynamic framework of Zhu et al (63) to fully couple the viscoplastic and damage models. Since the material model will be only implemented for the explicit solver, the consistent tangent stiffness matrix does not need to be defined. Additionally since explicit solvers do not have the convergence issues due to strain softening and damage progression as implicit solvers, viscous regularization is not necessary for the present research.

As is typical for most finite element codes, LS-DYNA is based on an incremental strain driven solution. For each load cycle, the incremental strains, time increment, state variables, and stress state from the previous load step, n, are passed to the material model which returns the updated state variables and stress state for the current load step, n+1, for each element. Since the material model is intended for highly dynamic simulations where large strain increments can occur in a load cycle, the integration algorithm for viscoplastic model should be stable for all loading conditions. For the present research a return mapping algorithm will be utilized since it is unconditionally stable and reasonably efficient.

Return mapping algorithms transform the nonlinear problem from a system of ordinary differential equations into an algebraic constrained optimization problem (38). The algorithms are based on the split operator methodology which divides the material response into the elastic and plastic contributions (38) (39). Typically the response is decomposed into an elastic predictor and plastic corrector where the response is returned to the plastic yield surface. The integration scheme usually for the return mapping algorithms is either fully implicit or semi-implicit. Fully implicit integration schemes are desired where unconditional stability is required. Wang et al (42) proposed a fully implicit backward Euler return mapping algorithm that is applicable to the yield function presented in equation 6.10. The Wang return mapping algorithm was referred to as the ‘Consistency Model’ since the integration is constrained by the consistency condition. The consistency condition, equation 6.42, results from the Kuhn Tucker or loading/unloading conditions, equation 6.41.

$$\dot{\lambda} \geq 0,\ F \leq 0,\ \dot{\lambda} F \leq 0\ \ where\ \ F(\bar{\sigma}, \lambda, \dot{\lambda}) = 0 \qquad \textbf{6.41}$$

$$\dot{F}(\bar{\sigma}, \lambda, \dot{\lambda}) = \frac{\partial F}{\partial \bar{\sigma}} : \dot{\bar{\sigma}} + \frac{\partial F}{\partial \lambda} \dot{\lambda} + \frac{\partial F}{\partial \dot{\lambda}} \ddot{\lambda} = 0 \qquad \textbf{6.42}$$

```
Calculate Elastic Predictor
$\Delta\varepsilon_{n+1} \quad \bar{\sigma}_{tr} = \bar{\sigma}_n + C^E \Delta\varepsilon_{n+1}$
if $F\left(\bar{\sigma}_{tr}, \tilde{\varepsilon}^p_{n+1}, \dot{\tilde{\varepsilon}}^p_{n+1}\right) \geq 0$; plastic state
Initialize
$\Delta\tilde{\varepsilon}^{p,k=0}_{n+1} = 0 \quad \dot{\tilde{\varepsilon}}^{p,k=0}_{n+1} = \dot{\tilde{\varepsilon}}^p_n \quad \bar{\sigma}^{k=0} = \bar{\sigma}_{tr} \quad F^{k=0} = F\left(\bar{\sigma}_{tr}, \tilde{\varepsilon}^{p,k=0}_{n+1}, \dot{\tilde{\varepsilon}}^{p,k=0}_{n+1}\right)$
Begin $k^{th}$ iteration
$H^k = \left[ S^E + \Delta\tilde{\varepsilon}^{p,k} \frac{\partial^2 F}{\partial \bar{\sigma}^2} \right]^{-1}$
$\beta^k = \left( \frac{\partial F}{\partial \bar{\sigma}} \right)^T H^k \left[ \frac{\partial F}{\partial \bar{\sigma}} + \Delta\tilde{\varepsilon}^{p,k} \frac{\partial^2 F}{\partial \bar{\sigma} \partial \tilde{\varepsilon}^p} + \frac{\Delta\tilde{\varepsilon}^{p,k}}{\Delta t} \frac{\partial^2 F}{\partial \bar{\sigma} \partial \dot{\tilde{\varepsilon}}^p} \right] - \frac{\partial F}{\partial \tilde{\varepsilon}^p} - \frac{1}{\Delta t} \frac{\partial F}{\partial \dot{\lambda} \dot{\tilde{\varepsilon}}^p}$
$\Delta\tilde{\varepsilon}^{p,k+1} = \Delta\tilde{\varepsilon}^{p,k} + \frac{F^k}{\beta^k}$
$\bar{\sigma}^{k+1}_{n+1} = \bar{\sigma}_n + C^E \left( \Delta\varepsilon_{n+1} - \Delta\tilde{\varepsilon}^{p,k+1} \frac{\partial F}{\partial \bar{\sigma}} \right)$
$F^{k+1} = F\left( \bar{\sigma}_{tr}, \tilde{\varepsilon}^p_n + \Delta\tilde{\varepsilon}^{p,k+1}, \frac{\Delta\tilde{\varepsilon}^{p,k+1}}{\Delta t} \right)$
if $F^{k+1} > tol$, perform next iteration
else elastic state; $\bar{\sigma}_{n+1} = \bar{\sigma}_{tr}$
```

Figure 6.9: Viscoplastic Return Mapping Algorithm

Simplifying the general form presented by Wang et al, the return mapping algorithm can be summarized as in Figure 6.9. The partial derivatives for the plastic yield function defined by equation 6.10 are defined in equations 6.43 - 6.45. For each time step, Δt, the algorithm begins with the elastic predictor step to calculate the trial stresses, $\bar{\sigma}_{tr}$, from the strain increments, $\Delta\varepsilon_{n+1}$, using the elastic stiffness matrix, C^E. During the elastic predictor step plasticity is ‘frozen’ where the equivalent plastic strain is zero, $\Delta\tilde{\varepsilon}_{n+1}^{p,k=0} = 0$. If the material state predicted exceeds the yield surface, the material state is returned iteratively until yield function is within a predefined error tolerance.

$$\frac{\partial F}{\partial \tilde{\varepsilon}^{p}} = -\frac{1}{\tilde{\varepsilon}^{p} n}\left(\frac{\tilde{\varepsilon}^{p}}{\chi\left(\dot{\tilde{\varepsilon}}^{p}\right)^{m}}\right)^{1/n} \quad \frac{\partial F}{\partial \dot{\tilde{\varepsilon}}^{p}} = \frac{m}{\dot{\tilde{\varepsilon}}^{p} n}\left(\frac{\tilde{\varepsilon}^{p}}{\chi\left(\dot{\tilde{\varepsilon}}^{p}\right)^{m}}\right)^{1/n} \qquad \textbf{6.43}$$

$$\frac{\partial F}{\partial \bar{\sigma}} = \frac{3}{2\tilde{\sigma}}\left\{A\;B\;C\;D\;E\;F\right\}^{T}$$

$$\mathit{where}$$

$$\begin{aligned}
A &= \left(\mathrm{A}_{12} + \mathrm{A}_{31}\alpha_{31}^{2}\right)\bar{\sigma}_{11} - \mathrm{A}_{12}\alpha_{12}\bar{\sigma}_{22} - \mathrm{A}_{31}\alpha_{31}\bar{\sigma}_{33} \quad & D &= 2a_{66}\bar{\sigma}_{12} \\
B &= -\mathrm{A}_{12}\alpha_{12}\bar{\sigma}_{22} + \left(\mathrm{A}_{23} + \mathrm{A}_{12}\alpha_{12}^{2}\right)\bar{\sigma}_{22} - \mathrm{A}_{23}\alpha_{23}\bar{\sigma}_{33} \quad & E &= 2a_{44}\bar{\sigma}_{23} \\
C &= -\mathrm{A}_{31}\alpha_{31}\bar{\sigma}_{11} - \mathrm{A}_{23}\alpha_{23}\bar{\sigma}_{22} + \left(\mathrm{A}_{31} + \mathrm{A}_{23}\alpha_{23}^{2}\right)\bar{\sigma}_{33} \quad & F &= 2a_{55}\bar{\sigma}_{13}
\end{aligned} \qquad \textbf{6.44}$$

$$\frac{\partial^2 F}{\partial\bar{\sigma}^2}=\begin{bmatrix}
\frac{\partial^2 F}{\partial\bar{\sigma}_1^2} & \frac{\partial^2 F}{\partial\bar{\sigma}_2\partial\bar{\sigma}_1} & \frac{\partial^2 F}{\partial\bar{\sigma}_3\partial\bar{\sigma}_1} & \frac{\partial^2 F}{\partial\bar{\sigma}_{12}\partial\bar{\sigma}_1} & \frac{\partial^2 F}{\partial\bar{\sigma}_{23}\partial\bar{\sigma}_1} & \frac{\partial^2 F}{\partial\bar{\sigma}_{13}\partial\bar{\sigma}_1} \\
\frac{\partial^2 F}{\partial\bar{\sigma}_2\partial\bar{\sigma}_1} & \frac{\partial^2 F}{\partial\bar{\sigma}_2^2} & \frac{\partial^2 F}{\partial\bar{\sigma}_3\partial\bar{\sigma}_2} & \frac{\partial^2 F}{\partial\bar{\sigma}_{12}\partial\bar{\sigma}_2} & \frac{\partial^2 F}{\partial\bar{\sigma}_{23}\partial\bar{\sigma}_2} & \frac{\partial^2 F}{\partial\bar{\sigma}_{13}\partial\bar{\sigma}_2} \\
\frac{\partial^2 F}{\partial\bar{\sigma}_3\partial\bar{\sigma}_1} & \frac{\partial^2 F}{\partial\bar{\sigma}_3\partial\bar{\sigma}_2} & \frac{\partial^2 F}{\partial\bar{\sigma}_3^2} & \frac{\partial^2 F}{\partial\bar{\sigma}_{12}\partial\bar{\sigma}_3} & \frac{\partial^2 F}{\partial\bar{\sigma}_{23}\partial\bar{\sigma}_3} & \frac{\partial^2 F}{\partial\bar{\sigma}_{13}\partial\bar{\sigma}_3} \\
\frac{\partial^2 F}{\partial\bar{\sigma}_{12}\partial\bar{\sigma}_1} & \frac{\partial^2 F}{\partial\bar{\sigma}_{12}\partial\bar{\sigma}_2} & \frac{\partial^2 F}{\partial\bar{\sigma}_{12}\partial\bar{\sigma}_3} & \frac{\partial^2 F}{\partial\bar{\sigma}_{12}^2} & \frac{\partial^2 F}{\partial\bar{\sigma}_{23}\partial\bar{\sigma}_{12}} & \frac{\partial^2 F}{\partial\bar{\sigma}_{13}\partial\bar{\sigma}_{12}} \\
\frac{\partial^2 F}{\partial\bar{\sigma}_{23}\partial\bar{\sigma}_1} & \frac{\partial^2 F}{\partial\bar{\sigma}_{23}\partial\bar{\sigma}_2} & \frac{\partial^2 F}{\partial\bar{\sigma}_{23}\partial\bar{\sigma}_3} & \frac{\partial^2 F}{\partial\bar{\sigma}_{23}\partial\bar{\sigma}_{12}} & \frac{\partial^2 F}{\partial\bar{\sigma}_{23}^2} & \frac{\partial^2 F}{\partial\bar{\sigma}_{13}\partial\bar{\sigma}_{23}} \\
\frac{\partial^2 F}{\partial\bar{\sigma}_{13}\partial\bar{\sigma}_1} & \frac{\partial^2 F}{\partial\bar{\sigma}_{13}\partial\bar{\sigma}_2} & \frac{\partial^2 F}{\partial\bar{\sigma}_{13}\partial\bar{\sigma}_3} & \frac{\partial^2 F}{\partial\bar{\sigma}_{13}\partial\bar{\sigma}_{12}} & \frac{\partial^2 F}{\partial\bar{\sigma}_{13}\partial\bar{\sigma}_{23}} & \frac{\partial^2 F}{\partial\bar{\sigma}_{13}^2}
\end{bmatrix}$$

where

$$\begin{aligned}
&\frac{\partial^2 F}{\partial\bar{\sigma}_1^2}=\frac{3}{2\tilde{\sigma}^2}\left[\left(\mathrm{A}_{12}+\mathrm{A}_{31}\alpha_{31}^2\right)\tilde{\sigma}-A\frac{\partial F}{\partial\bar{\sigma}_1}\right] &&\frac{\partial^2 F}{\partial\bar{\sigma}_2\partial\bar{\sigma}_1}=\frac{3}{2\tilde{\sigma}^2}\left[-\mathrm{A}_{12}\alpha_{12}\tilde{\sigma}-A\frac{\partial F}{\partial\bar{\sigma}_2}\right]\\
&\frac{\partial^2 F}{\partial\bar{\sigma}_3\partial\bar{\sigma}_1}=\frac{3}{2\tilde{\sigma}^2}\left[-\mathrm{A}_{31}\alpha_{31}\tilde{\sigma}-A\frac{\partial F}{\partial\bar{\sigma}_3}\right] &&\frac{\partial^2 F}{\partial\bar{\sigma}_{12}\partial\bar{\sigma}_1}=\frac{3}{2\tilde{\sigma}^2}\left[-A\frac{\partial F}{\partial\bar{\sigma}_{12}}\right]\\
&\frac{\partial^2 F}{\partial\bar{\sigma}_{23}\partial\bar{\sigma}_1}=\frac{3}{2\tilde{\sigma}^2}\left[-A\frac{\partial F}{\partial\bar{\sigma}_{23}}\right] &&\frac{\partial^2 F}{\partial\bar{\sigma}_{13}\partial\bar{\sigma}_1}=\frac{3}{2\tilde{\sigma}^2}\left[-A\frac{\partial F}{\partial\bar{\sigma}_{13}}\right]\\
&\frac{\partial^2 F}{\partial\bar{\sigma}_2^2}=\frac{3}{2\tilde{\sigma}^2}\left[\left(\mathrm{A}_{23}+\mathrm{A}_{12}\alpha_{12}^2\right)\tilde{\sigma}-B\frac{\partial F}{\partial\bar{\sigma}_2}\right] &&\frac{\partial^2 F}{\partial\bar{\sigma}_3\partial\bar{\sigma}_2}=\frac{3}{2\tilde{\sigma}^2}\left[-\mathrm{A}_{23}\alpha_{23}\tilde{\sigma}-B\frac{\partial F}{\partial\bar{\sigma}_2}\right]\\
&\frac{\partial^2 F}{\partial\bar{\sigma}_{12}\partial\bar{\sigma}_2}=\frac{3}{2\tilde{\sigma}^2}\left[-B\frac{\partial F}{\partial\bar{\sigma}_{12}}\right] &&\frac{\partial^2 F}{\partial\bar{\sigma}_{23}\partial\bar{\sigma}_2}=\frac{3}{2\tilde{\sigma}^2}\left[-B\frac{\partial F}{\partial\bar{\sigma}_{23}}\right]\\
&\frac{\partial^2 F}{\partial\bar{\sigma}_{13}\partial\bar{\sigma}_2}=\frac{3}{2\tilde{\sigma}^2}\left[-B\frac{\partial F}{\partial\bar{\sigma}_{13}}\right] &&\frac{\partial^2 F}{\partial\bar{\sigma}_3^2}=\frac{3}{2\tilde{\sigma}^2}\left[\left(\mathrm{A}_{31}+\mathrm{A}_{23}\alpha_{23}^2\right)\tilde{\sigma}-C\frac{\partial F}{\partial\bar{\sigma}_3}\right]\\
&\frac{\partial^2 F}{\partial\bar{\sigma}_{12}\partial\bar{\sigma}_3}=\frac{3}{2\tilde{\sigma}^2}\left[-C\frac{\partial F}{\partial\bar{\sigma}_{12}}\right] &&\frac{\partial^2 F}{\partial\bar{\sigma}_{23}\partial\bar{\sigma}_3}=\frac{3}{2\tilde{\sigma}^2}\left[-C\frac{\partial F}{\partial\bar{\sigma}_{23}}\right]\\
&\frac{\partial^2 F}{\partial\bar{\sigma}_{13}\partial\bar{\sigma}_3}=\frac{3}{2\tilde{\sigma}^2}\left[-C\frac{\partial F}{\partial\bar{\sigma}_{13}}\right] &&\frac{\partial^2 F}{\partial\bar{\sigma}_{12}^2}=\frac{3}{2\tilde{\sigma}^2}\left[2a_{66}\left(\tilde{\sigma}-\bar{\sigma}_{12}\frac{\partial F}{\partial\bar{\sigma}_{12}}\right)\right]\\
&\frac{\partial^2 F}{\partial\bar{\sigma}_{23}\partial\bar{\sigma}_{12}}=\frac{3}{2\tilde{\sigma}^2}\left[-D\frac{\partial F}{\partial\bar{\sigma}_{23}}\right] &&\frac{\partial^2 F}{\partial\bar{\sigma}_{13}\partial\bar{\sigma}_{12}}=\frac{3}{2\tilde{\sigma}^2}\left[-D\frac{\partial F}{\partial\bar{\sigma}_{13}}\right]\\
&\frac{\partial^2 F}{\partial\bar{\sigma}_{23}^2}=\frac{3}{2\tilde{\sigma}^2}\left[2a_{44}\left(\tilde{\sigma}-\bar{\sigma}_{23}\frac{\partial F}{\partial\bar{\sigma}_{23}}\right)\right] &&\frac{\partial^2 F}{\partial\bar{\sigma}_{13}\partial\bar{\sigma}_{23}}=\frac{3}{2\tilde{\sigma}^2}\left[-E\frac{\partial F}{\partial\bar{\sigma}_{13}}\right]\\
&\frac{\partial^2 F}{\partial\sigma_{13}^2}=\frac{3}{2\tilde{\sigma}^2}\left[2a_{55}\left(\tilde{\sigma}-\bar{\sigma}_{13}\frac{\partial F}{\partial\bar{\sigma}_{13}}\right)\right]
\end{aligned}\tag{6.45}$$

6.7.4 : Damage Model Algorithm

The overall damage model algorithm is summarized in Figure 6.10. As established in Section 6.3, the maximum strain failure criteria will be used to determine damage initiation. In addition, different failure strains will be defined for the normal strains when the material is under either compressive or tensile loading. As such a total of nine damage variables will be tracked through the load time history: $d_{11}^t, d_{11}^c, d_{22}^t, d_{22}^c, d_{33}^t, d_{33}^c, d_{12}, d_{23}, d_{13}$. There are nine maximum strains, $\varepsilon_{\max}$, associated with each of the damage variables.

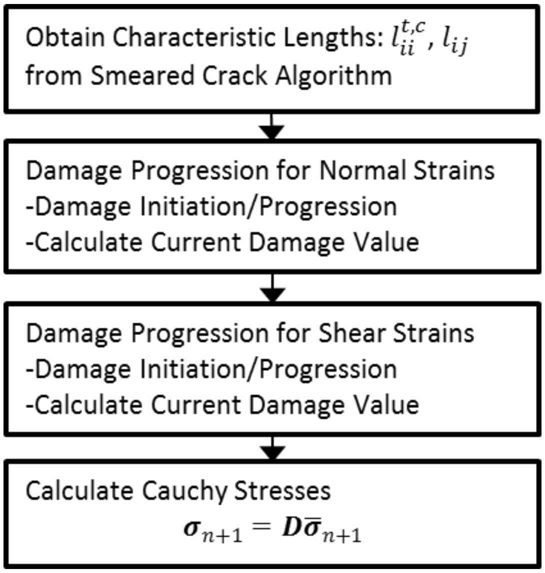

Figure 6.10: Damage Model Algorithm Flowchart

The damage progression for the normal strains is dependent on the current state of strain. The corresponding failure strain is selected and used to determine if failure has occurred. If failure is detected by the maximum strain criteria, damage has either initiated or progressed. At the time of damage initiation, $\varepsilon_{\max}$ is calculated using equation 6.20. In order to maintain the initial energy balance illustrated in Figure 6.1, the value of $\varepsilon_{\max}$ at damage initiation is stored as a history variable and used in the subsequent time steps to calculate the progression of damage. If full damage has not occurred yet, $d_{ii}^n < 1$, then the damage for the current time step, d_{ii}^{n+1}, is calculated using equation 6.23. Since damage is an irreversible process, damage may only progress in an increasing fashion. As such the calculated damage value for the current time step, d_{ii}^{n+1}, is compared to the previous time step value, d_{ii}^{n}, and if the value has not increased, the previous value is stored to preserve the damage accrued. The resulting damage variable from the above algorithm is then stored as a history variable and returned to the main LS-DYNA program. A summary of the damage progression logic for the normal strains is outlined in Figure 6.11.

```
if $\varepsilon_{ii} \geq 0$ then   (Tensile Strain)
  if $\varepsilon_{ii} \geq \left(\varepsilon_{fail}\right)_{ii}^{t}$ then
    if Damage Initiated then
      Calculate $\left(\varepsilon_{\max}\right)_{ii}^{t}$
    if $d_{ii}^{t,n} < 1$ then
      Calculate $d_{ii}^{t,n+1}$
    if $d_{ii}^{t,n+1} < d_{ii}^{t,n}$ then   (Ensure Damage Progression)
      $d_{ii}^{t,n+1} = d_{ii}^{t,n}$
  Update $d_{ii}^{t}$ history variable
else   (Comressive Strain)
  if $\left|\varepsilon_{ii}\right| \geq \left(\varepsilon_{fail}\right)_{ii}^{c}$ then
    if Damage Initiated then
      Calculate $\left(\varepsilon_{\max}\right)_{ii}^{c}$
    if $d_{ii}^{c,n} < 1$ then
      Calculate $d_{ii}^{c,n+1}$
    if $d_{ii}^{c,n+1} < d_{ii}^{c,n}$ then   (Ensure Damage Progression)
      $d_{ii}^{c,n+1} = d_{ii}^{c,n}$
  Update $d_{ii}^{c}$ history variable
```

Figure 6.11: Normal Strain Damage Progression Algorithm

The damage progression of the shear strains follows the same general logic as the normal strains. The algorithm is illustrated in Figure 6.12.

```
$if\ \varepsilon_{ij} \geq 0\ then$
  $if\ \varepsilon_{ij} \geq \left(\varepsilon_{fail}\right)_{ij}\ then$
    $if\ Damage\ Initiated\ then$
      $Calculate\ \left(\varepsilon_{\max}\right)_{ij}$
    $if\ d_{ij}^{n} < 1\ then$
      $Calculate\ d_{ij}^{n+1}$
    $if\ d_{ij}^{n+1} < d_{ij}^{n}\ then\quad (Ensure\ Damage\ \mathrm{Pr}ogression)$
      $d_{ij}^{n+1} = d_{ij}^{n}$
  $Update\ d_{ij}\ history\ \text{variable}$
```

Figure 6.12: Shear Strain Damage Progression Algorithm

After the effective stresses are calculated for the current time step using the viscoplastic return mapping integration scheme, is used to calculate the nominal Cauchy stresses with the relationship described by equation 6.2.

6.7.5 : Erosion Criteria Algorithm

LS-DYNA allows user-defined material models to access the erosion algorithm utilized by other material models natively implemented into the program. The erosion algorithm simply removes an element and its' mass from the simulation solution as a means to prevent severe element distortion. The UMAT must define the criteria for which determine when the erosion algorithm is called. A logical array, FAILELS, is passed between the main LS-DYNA program and the UMAT which maintains which elements have failed and been eroded or deleted from the simulation. The outline of the calculation of the erosion criteria is depicted in Figure 6.13.

```
$Calculate \quad V_{REL} = \frac{V_{el}}{V_{el}^{initial}} = \det\left(F^{DEF}\right)$
$if \ V_{REL} \geq EEXPN \ \ OR \ \ V_{REL} \leq ECRSH \ then$
  $FAILELS = TRUE$
$if \ Unidirectional \ then$
  $if \ \left|\varepsilon_{11}\right| \geq E\_LIMT \ then$
    $FAILELS = TRUE$
$elseif \ \ Plain\,Weave \ then$
  $if \ \left|\varepsilon_{11}\right| \geq E\_LIMT \ \ OR \ \ \left|\varepsilon_{22}\right| \geq E\_LIMT \ then$
    $FAILELS = TRUE$
$if \ \ FAILELS = TRUE \ then$
  $\sigma_{ij} = 0$
```

Figure 6.13: Erosion Criteria Algorithm

Using the erosion criteria from Yen highlighted in Section 6.5, ECRSH, EEXPN, and E_LIMT, the element failure can easily be determined. The relative element volume is calculated from the determinant of the deformation gradient. Next the relative element volume is compared to both the EEXPN and ECRSH criteria and the element is failed if the criteria are met. Depending on whether the composite panel considered is unidirectional or plain weave, either the absolute value of the total strain in the 1-direction or both the 1- and 2-directions are compared to the E_LIMT criteria. Finally if the element has failed, the Cauchy stresses can be set to zero.

6.8: LS-DYNA UMAT Model Validation

In order to validate the material model, published experimental data for IM7/8552 unidirectional composite was considered for several single element and coupon test cases. The simple test cases include the viscoplastic behavior under off-axis uniaxial tensile loading, mesh sensitivity for energy dissipation, and damage progression to cyclic loading.

6.8.1 : IM7/8552 Material Model Parameters

As mentioned previously, Koerber et al performed both quasi-static and SPHB off-axis compression testing for IM7/8552 unidirectional composites (44) (51). The off-axis loading was performed from 0° to 90° with increments of 15°. The quasi-static cases were performed on a hydraulic mechanical tester at a constant strain rate of 4.0E-4 per second. The SPHB strain rates ranged from ~100 to 400 per second depending on the off-axis angle. The IM7/8552 composite exhibited significant nonlinear behavior at the larger off-axis angles where the material behavior is matrix-dominated. At the shallower angles where the behavior is fiber-dominated the response is largely linear elastic. This behavior is expected due to the fact that carbon fiber has been reported to be rate-independent, linear elastic such as the case of T300 reported by Zhou et al (67). Also evident is that the IM7/8552 composite at larger off-axis angles is significantly rate-dependent in that the composite becomes stiffer at higher loading rates.

The elastic constants were either reported values (51) (68), calculated, or estimated under the assumption of transverse isotropy. The thermodynamic constraints presented by Jones were observed for the elastic constant estimations (69). The material constants are summarized in Table 6.4. LS-DYNA requires the density, elastic modulus, and bulk modulus be defined for time step, boundary condition, and contact calculations (65). It was observed during the research that for orthotropic models the simulation stability was highly dependent on the elastic and bulk moduli defined. A poor definition of the moduli caused negative element volume errors similar to the issue present in the simulation of soft materials such as foam (70). As such the moduli were increased to the maximum values calculated within 1-/2-plane with a rotation about the 3-axis. The exaggerated moduli values improved the element stability to varied loading conditions while having no effect on the stress response in the simulation.

Type	Constant	Value	Source
Density (ton/mm^3)	ρ	1.59E-09	Koerber
Modulus (GPa)	E	158.720	Calculated
Bulk Modulus (GPa)	K	64.931	Calculated
Moduli (GPa)	E_1	171.420	ASTM 3039
	E_2	9.080	ASTM 3039
	E_3	9.080	Estimated
	G_{12}	5.068	Calculated
	G_{23}	3.492	Calculated
	G_{13}	5.068	Calculated
Poisson Ratios	ν_{12}	0.32	ASTM 3039
	ν_{23}	0.30	Estimated
	ν_{13}	0.32	Estimated

Table 6.4: IM7/8552 Material Constants

From the optimization algorithm outlined in Sections 5.5 and 5.6 the anisotropic and hardening rule parameters can be determined. Using the relations in equations 5.8 and 5.9 with the results for the 1-D off-axis loading case considered by the optimization algorithm, the anisotropic parameters for the 3D UMAT can be expressed as shown in Table 6.5.

A_{12}	A_{23}	A_{31}	a_{44}	a_{55}	a_{66}	α_{12}	α_{23}	α_{31}
0.1	0.1	11.0174	2.0	48.0	48.0	10.4964	1.0000	0.0953

Table 6.5: IM7/8552 Anisotropic Parameters

The hardening rule parameters calculated by the optimization algorithm are reiterated in Table 6.6.

A, (MPa)$^{-n}$	n	χ, (MPa)$^{-n}$	m
4.9756E-17	4.3930861	1.0010E-17	-0.16103

Table 6.6: IM7/8552 Hardening Rule Parameters

The fracture energies utilized for the IM7/8552 composite were obtained from data presented by Camanho et al summarized in Table 6.7 (45). The fracture energies are related to intralaminar and interlaminar crack growth under Mode I and Mode II fracture.

Fracture Energy	N/mm^2
$G_{fr,1t}$	81.5
$G_{fr,1c}$	106.3
$G_{fr,2t}$	0.2774
$G_{fr,2c}$	0.7879
$G_{fr,3t/c,12,23,13}$	0.7879

Table 6.7: IM7/8552 Fracture Energies

Since the maximum strain failure criteria is the basis for the damage model, the failure strains are required. The failure strains, summarized in Table 6.8, were either obtained or estimated from the manufacturer supplied data (71) (18) (72) or based on the data presented by Koerber et al (44).

Failure Strain	Value	Source
$(\varepsilon_{fail})_{1t}$	1.6000E-02	Hexcell
$(\varepsilon_{fail})_{1c}$	1.2281E-02	Hexcell
$(\varepsilon_{fail})_{2t}$	1.2223E-02	Hexcell
$(\varepsilon_{fail})_{2c}$	4.2600E-02	Estimated - Koerber
$(\varepsilon_{fail})_{3t}$	1.2223E-02	Hexcell
$(\varepsilon_{fail})_{3c}$	4.2600E-02	Estimated - Koerber
$(\varepsilon_{fail})_{12}$	3.4361E-02	Estimated - Koerber
$(\varepsilon_{fail})_{23}$	3.4361E-02	Estimated - Hexcell
$(\varepsilon_{fail})_{13}$	3.4361E-02	Estimated - Hexcell

Table 6.8: IM7/8552 Failure Strains

Based on some preliminary single element simulations and the values determined for other carbon fiber based composites (73), the erosion criteria values established for the model validation simulations in the upcoming sections are summarized in Table 6.9.

Erosion Criteria	Value
ECRSH	0.15
EEXPN	2.00
E_LIMT	0.10

Table 6.9: IM7/8552 Erosion Criteria

In the LS-DYNA UMAT subroutine the material constants are obtained from the CM and CMA arrays (65). Each material constant is defined to a specific location within the two material constant arrays. For the current implementation the populated material keycard is shown in Figure 6.14. The anisotropic parameters α_{12}, α_{23}, and α_{31} can be calculated by the UMAT as shown in Figure 6.14 by leaving the values entered as zero or can also be overridden, if necessary, by explicitly entering values. This allows the analyst more flexibility in defining anisotropic plastic behavior mentioned previously. For the following simulations an error tolerance, ERRTOL, of 1.0E-3 is used for the viscoplastic return mapping algorithm. As noted in Figure 6.14, the consistent system of units are metric ton, millimeter, and seconds such that the derived units for force, pressure, and energy are newtons, megapascals, and kilojoules per squared millimeter, respectively.

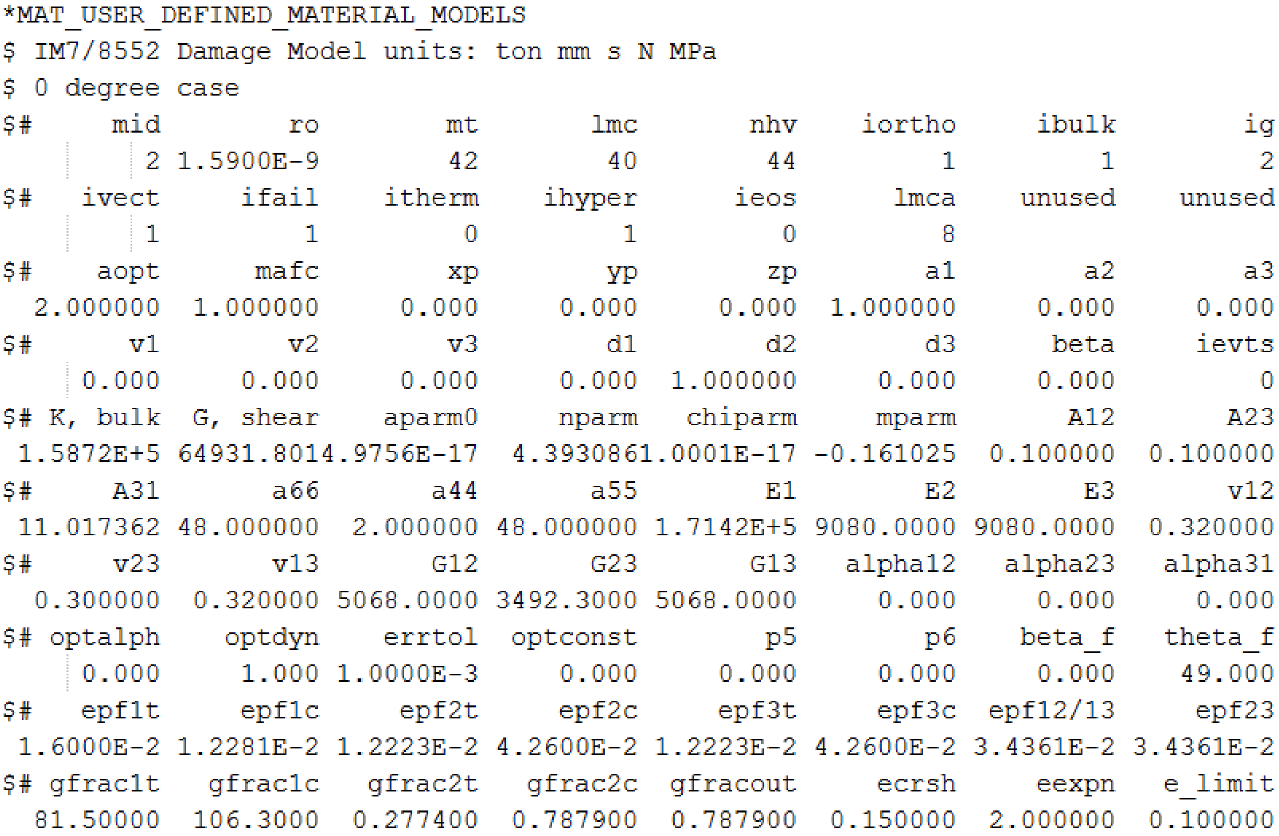

```
*MAT_USER_DEFINED_MATERIAL_MODELS
$ IM7/8552 Damage Model units: ton mm s N MPa
$ 0 degree case
$#     mid        ro        mt       lmc       nhv    iortho     ibulk        ig
         2 1.5900E-9        42        40        44         1         1         2
$#   ivect     ifail    itherm    ihyper      ieos      lmca    unused    unused
         1         1         0         1         0         8
$#    aopt      mafc        xp        yp        zp        a1        a2        a3
  2.000000  1.000000     0.000     0.000     0.000  1.000000     0.000     0.000
$#      v1        v2        v3        d1        d2        d3      beta     ievts
     0.000     0.000     0.000     0.000  1.000000     0.000     0.000         0
$# K, bulk  G, shear    aparm0     nparm   chiparm     mparm       A12       A23
 1.5872E+5 64931.8014.9756E-17  4.3930861.0001E-17 -0.161025  0.100000  0.100000
$#     A31       a66       a44       a55        E1        E2        E3       v12
 11.017362 48.000000  2.000000 48.000000 1.7142E+5 9080.0000 9080.0000  0.320000
$#     v23       v13       G12       G23       G13   alpha12   alpha23   alpha31
  0.300000  0.320000 5068.0000 3492.3000 5068.0000     0.000     0.000     0.000
$# optalph    optdyn    errtol  optconst        p5        p6    beta_f   theta_f
     0.000     1.000 1.0000E-3     0.000     0.000     0.000     0.000    49.000
$#   epf1t     epf1c     epf2t     epf2c     epf3t     epf3c  epf12/13     epf23
 1.6000E-2 1.2281E-2 1.2223E-2 4.2600E-2 1.2223E-2 4.2600E-2 3.4361E-2 3.4361E-2
$# gfrac1t   gfrac1c   gfrac2t   gfrac2c  gfracout     ecrsh     eexpn   e_limit
  81.50000  106.3000  0.277400  0.787900  0.787900  0.150000  2.000000  0.100000
```

Figure 6.14: Populated LS-DYNA Keycard For Coupled Viscoplastic Damage UMAT

In addition to the material parameters, LS-DYNA requires the material density, and the bulk and shear moduli for the critical time step calculation. Additionally the material orientation must be defined for orthotropic material models. The parameter selection $\mathrm{IORTHO} = 1$ denotes the directional behavior of the model and therefore definition of the material orientation is required. For the present work due to the geometry and layup pattern in the simulations, the material orientations were defined with respect to the global coordinate system, $\mathrm{AOPT} = 2$, through definition of the vectors $\bar{\mathrm{A}}$ and $\bar{\mathrm{D}}$ where the parameters $\mathrm{a}_1, \mathrm{a}_2, \mathrm{a}_3$ and $\mathrm{d}_1, \mathrm{d}_2, \mathrm{d}_3$ are the respective x, y, and z vector components. As noted previously the routine has been implemented in the vectorized form which is noted by $\mathrm{IVECT} = 1$. Since the element erosion algorithm will be utilized, the parameter IFAIL is set to one. The deformation gradient is requested from the main routine by setting $\mathrm{IHYPER} = 1$. The LS-DYNA main program provides the deformation gradient to the material model through the history variables. For the present implementation of the material model, forty four history variables are used by the routine and are requested by the parameter NHV. Currently no equation of state is implemented and thus the equation of state parameter, IEOS, is set to zero.

6.8.2 : LS-DYNA User Defined Material Implementation Validation

In order to verify that the Fortran subroutine is performing as intended, a series of single element simulations were performed to evaluate the viscoplastic model using the IM7/8552 data presented in previous sections. In order to isolate the viscoplastic model behavior, the simulations were performed without the evaluation of damage. Damage will also be considered in the upcoming section. Off-axis uniaxial tension was performed on a unit sized element for rotations about the Z- and X-axes as shown below in Figure 6.15 where the X-axis if the fiber direction as defined previously. Off-axis uniaxial tension load case was selected since it will demonstrate the nonlinear model behavior in various directions and the simulation results can be readily verified using the 1-D simplification of the load case with the 1-D return mapping integration scheme summarized in Figure 5.3. It should be noted that although the 1-D return mapping algorithm presented in Figure 5.3 has been derived explicitly for off-axis uniaxial tension/compression loading with a rotation about the Z-axis, a similar simplification can be easily obtained for rotations about the X-axis. The 1-D return mapping algorithms to solve the off-axis load cases have been programmed into MATLAB in order to compare the results calculated by the LS-DYNA implementation.

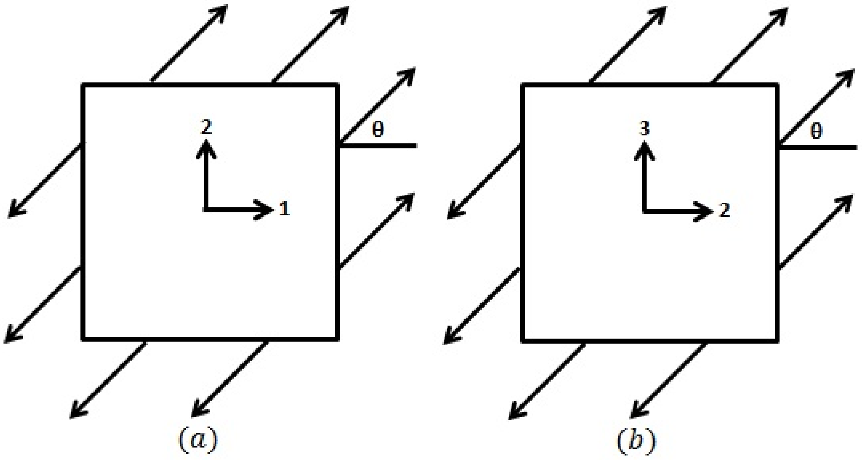

Figure 6.15: Off-Axis Tension Rotation About (a) Z-Axis (b) X-Axis

Rotation angles of 0°, 30°, 60°, and 90° about both the Z- and X- axes were simulated at an arbitrary constant strain rate of 100 per second. Tension at a constant strain rate was enforced through displacement at the element boundary as shown in Figure 6.16. The off-axis angles were defined through specification of the material orientation with respect to the global coordinate system. LS-DYNA internally performs the coordinate system transformations to obtain the correct material response. Due to the directional behavior of the model and to reduce the error due to element rotations, the *CONTROL_ACCURACY keyword was selected so that the second order terms will be utilized in the stress updates (65).

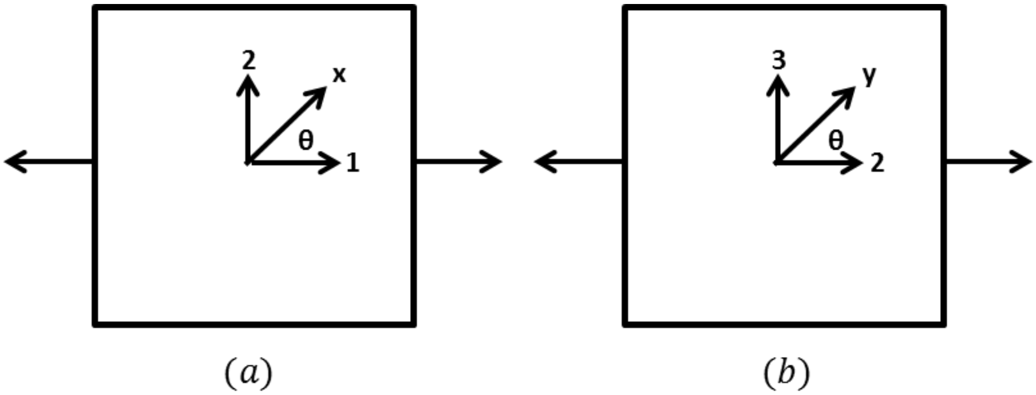

Figure 6.16: LS-DYNA Single Element Off-Axis Tension Boundary Conditions and Material Orientations for Rotations About: a) Z-Axis b) X-Axis

Figures 6.17, 6.18, 6.19, and 6.20 below compare the 1-D model calculations to the 3-D LS-DYNA user defined material subroutine output for the Z-axis off-axis cases. As can be seen from the plots, the simulation results match almost identically to the calculated 1-D simplification calculations. However the 30° case shows some difference at the larger strains. Most of the discrepancy in the results is due to element rotation that is present at higher strains in the simulations. As the element rotates the off-axis loading angle is affected. The reason for the element rotation is the highly directional behavior of the material considered. For the 30° load case the material behavior is largely fiber-dominated and in combination with the off-axis strain state which consists of normal and shear strains, the element has a tendency to rotate due to the shear contributions. IN order to reduce or eliminate the element rotation, additional nodal constraints would be necessary. However for the purposes of validating the LS-DYNA implementation, it is desired to have a minimal amount of nodal constraints in order to avoid over constraining the element and affecting the LS-DYNA calculations. Thus the minimal boundary constraints were only utilized.

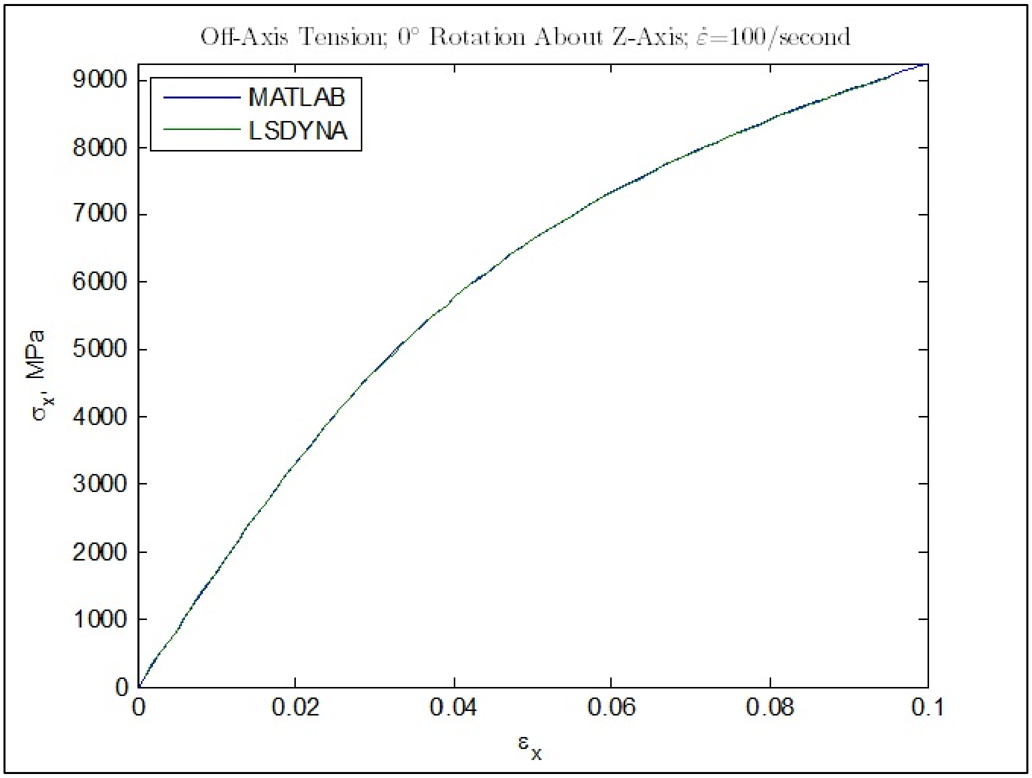

Figure 6.17: LS-DYNA Comparison; Off-Axis Tension 0° Rotation About Z-Axis

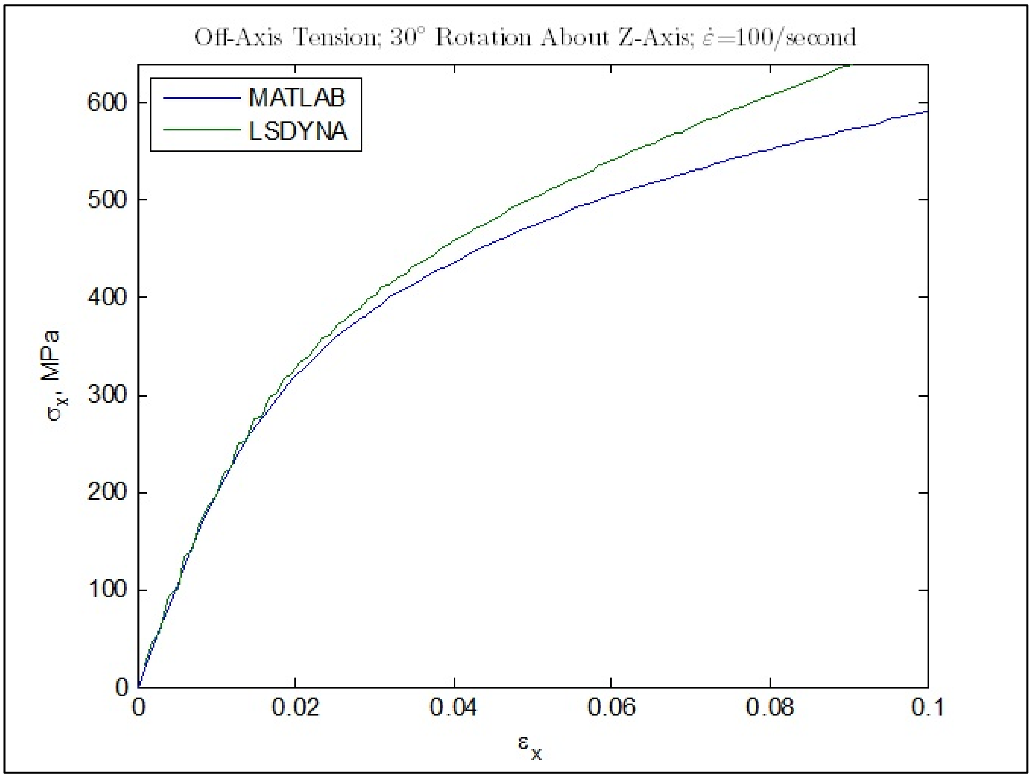

Figure 6.18: LS-DYNA Comparison; Off-Axis Tension 30° Rotation About Z-Axis

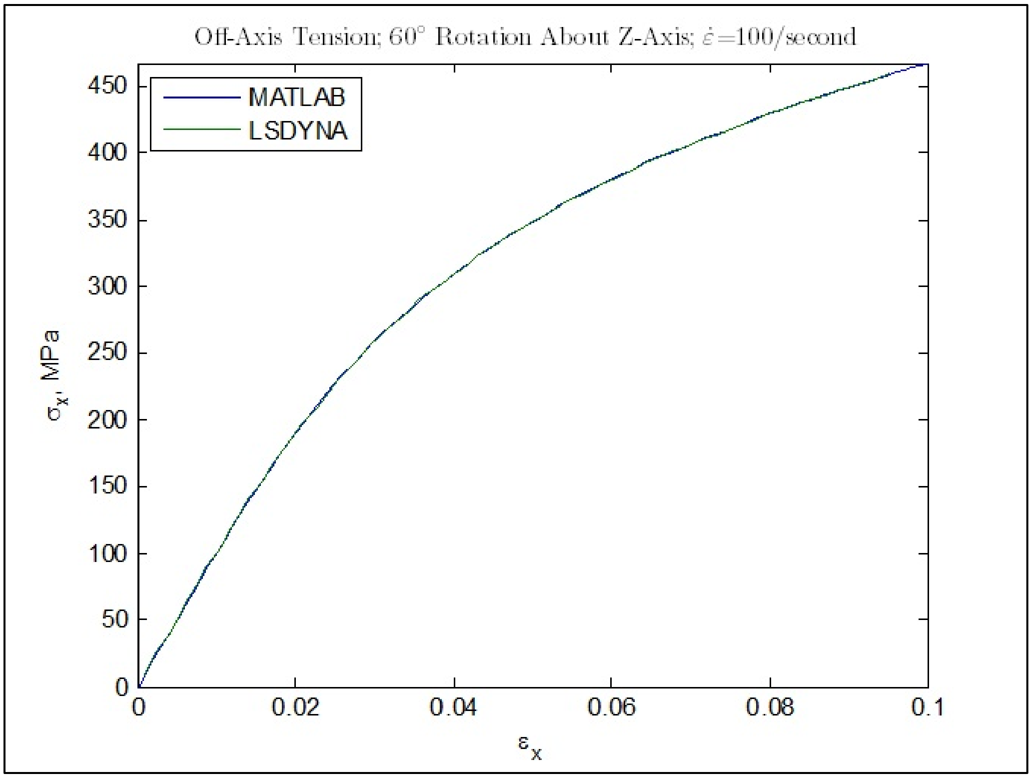

Figure 6.19: LS-DYNA Comparison; Off-Axis Tension 60° Rotation About Z-Axis

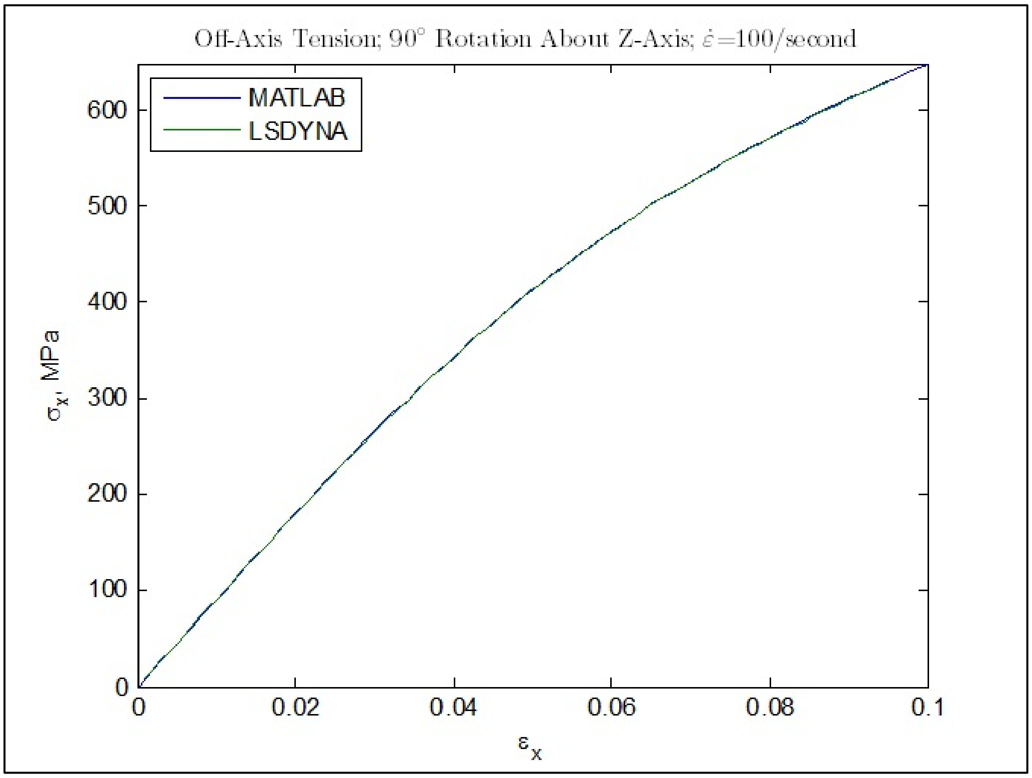

Figure 6.20: LS-DYNA Comparison; Off-Axis Tension 90° Rotation About Z-Axis

Figures 6.21, 6.22, 6.23, and 6.24 compare the 1-D calculations for the off-axis tensile load cases with a rotation about the X-axis. For all the angles considered, the results are nearly identical to the expected response calculated in MATLAB. Additionally, since the IM7/8552 unidirectional composite for the present case is considered to be transversely isotropic, the angles of 0° and 90°, and 30° and 60° are identical as well.

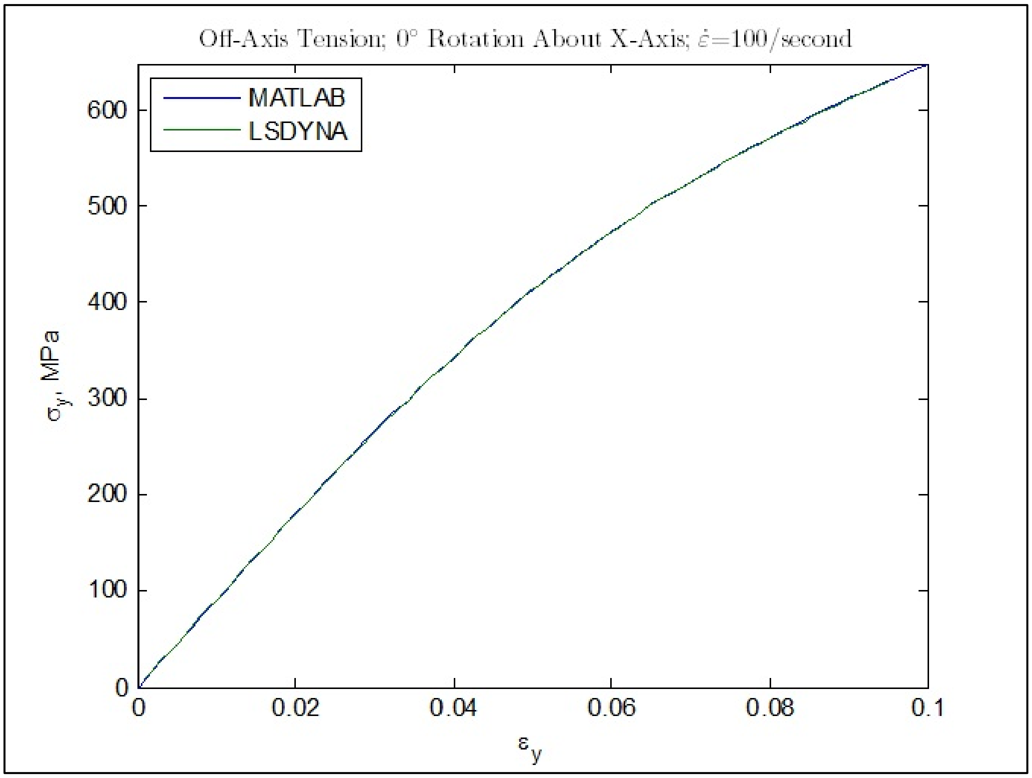

Figure 6.21: LS-DYNA Comparison; Off-Axis Tension 0° Rotation About X-Axis

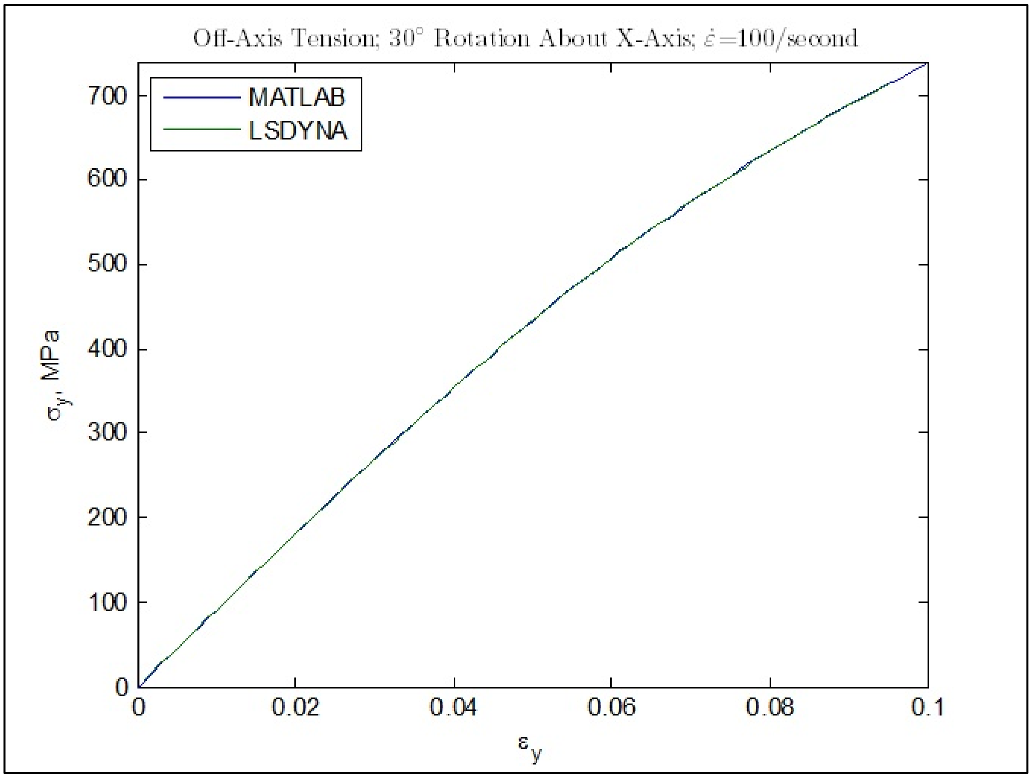

Figure 6.22: LS-DYNA Comparison; Off-Axis Tension 30° Rotation About X-Axis

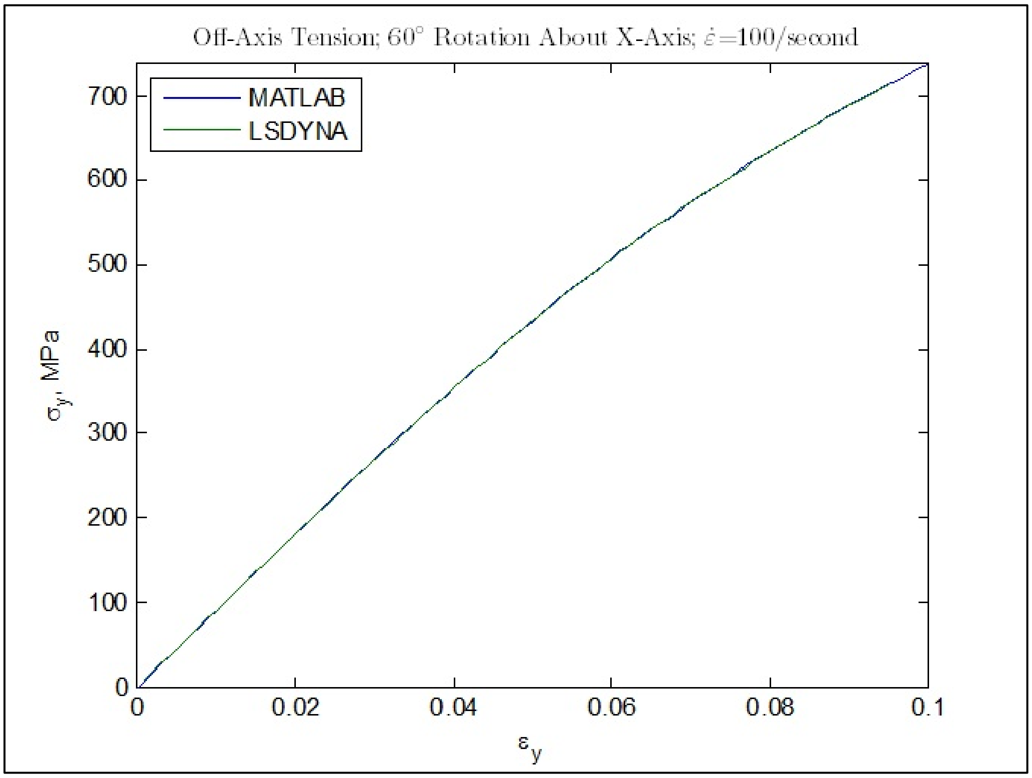

Figure 6.23: LS-DYNA Comparison; Off-Axis Tension 60° Rotation About X-Axis

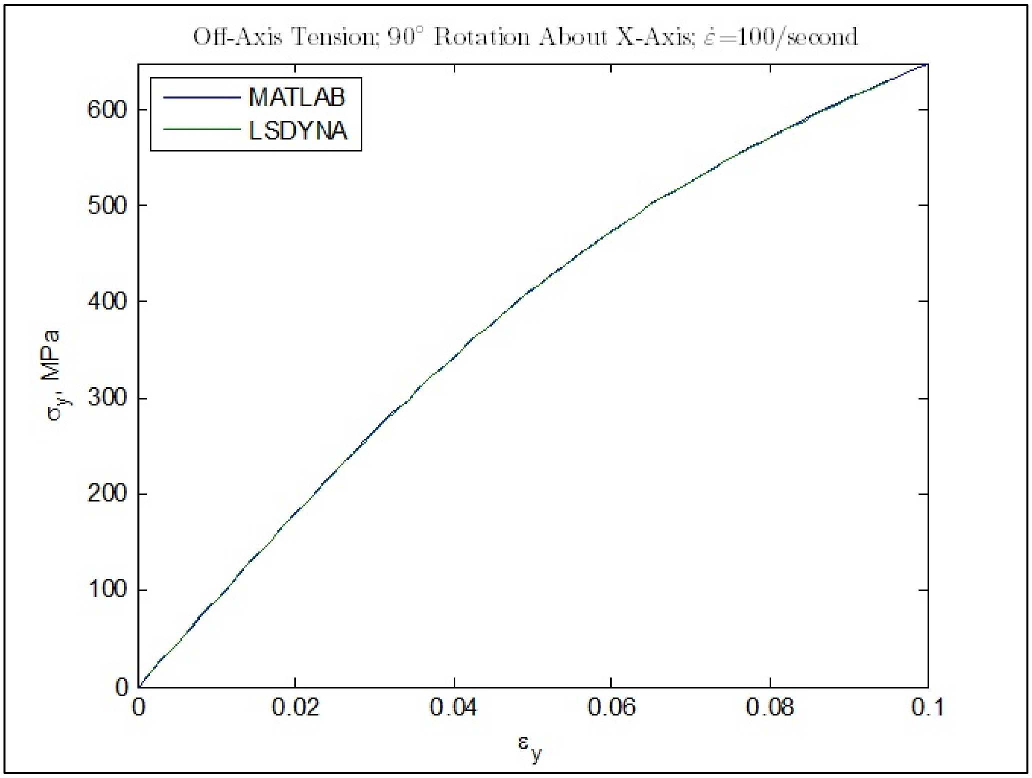

Figure 6.24: LS-DYNA Comparison; Off-Axis Tension 90° Rotation About X-Axis

6.8.3 : Off-Axis Loading With Damage Behavior

The off-axis behavior of the material model will be examined using a single element simulation including damage behavior. In LS-DYNA the material directions are defined in the global 1/2/3-coordinate system while the loading is occurring in the x-direction as illustrated previously in Figure 6.15(a). The damage model response will be compared to the SPHB data for IM7/8552 composite studied by Koerber et al.

Figures 6.25, 6.26, and 6.27 compare the single element simulation results for the 15°, 30°, and 60° off-axis loading cases to the experimental SPHB data, respectively. Since the SPHB experimental data is under uniaxial compression, the simulations are under the same loading conditions with the assumption of a constant strain rate. The constant strain rates assumed are as listed in Table 6.2. Since Koerber et al did not publish the strain-time histories for each of the experimental tests, the constant strain rate assumption was made out of necessity. The simulation results for the 15° case is within reasonable agreement with the experimental data in the failure strain. From Figure 6.25, large oscillations in the stress response are observed post-damage. These oscillations are due to the explicit solver and the damage model. In order to avoid the oscillating behavior, global damping could be added to the simulation without affecting the material stress response.

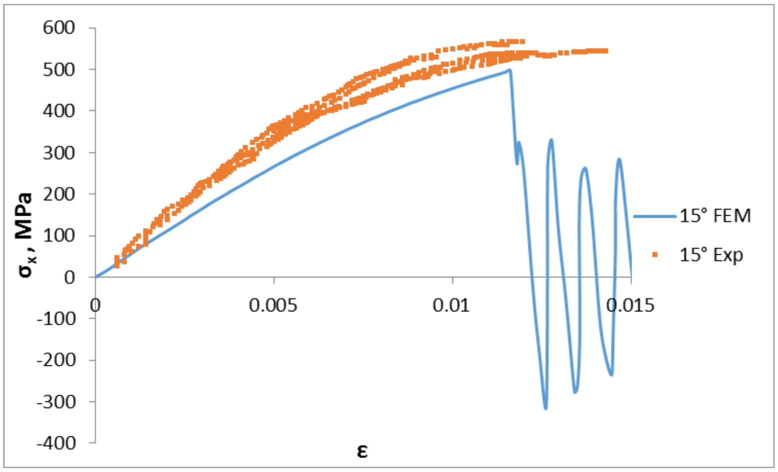

Figure 6.25: 15° Off-Axis Compressive Loading With Damage Model; Strain Rate 122 1/sec

The 30° case comparison presented in Figure 6.26 shows that the model does not predict the ultimate strain well. For the loading case the damage variable d_{12} is leading to the premature damage. Although the shear failure strain $\left(\varepsilon_{fail}\right)_{12}$ has been increased beyond what has been reported by the manufacturer of the composite, the maximum failure strain criteria does not predict the ultimate strain for the 30° case well.

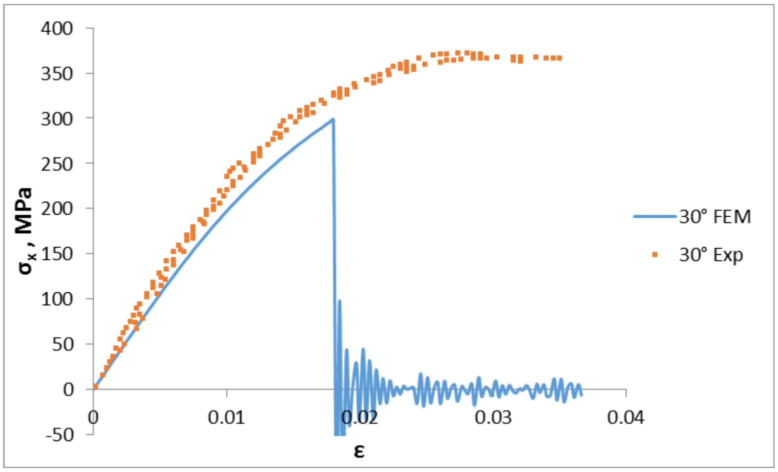

Figure 6.26: 30° Off-Axis Compressive Loading With Damage Model; Strain Rate 246 1/sec

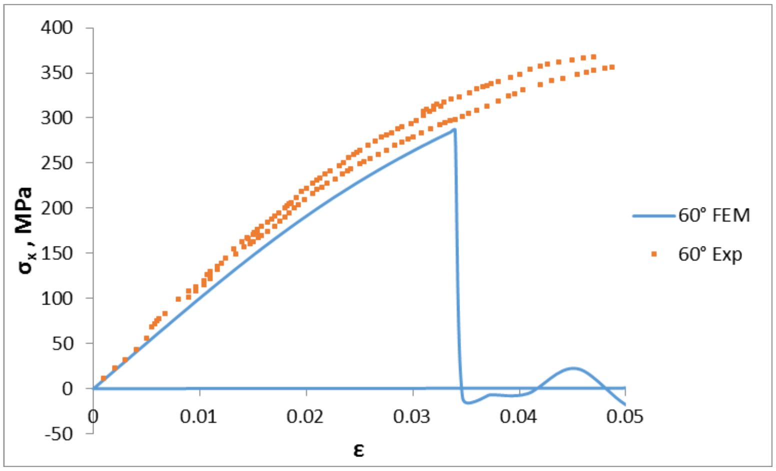

Figure 6.27: 60° Off-Axis Compressive Loading With Damage Model; Strain Rate 367 1/sec

Considering the 60° case in Figure 6.27, the model shows a discrepancy between the failure strain obtained experimentally. The model discrepancies between the predicted and the observed failure strains result from the underlying assumptions where the failure strains remain constant regardless of the strain rate and that all of the behavior pre-failure is plastic. However in reality the plastic and damage processes occur concurrently. As such in experimental testing the reported failure strains are at the onset of damage. The failure strains used in the simulations, Table 6.8, likely do not include all of the plasticity and damage. Despite this deficiency the model should still be suitable since the intended ballistic simulation uses a $\left[\left(0^{\circ}/90^{\circ}\right)_{7}\ 0^{\circ}\right]$ layup (74).

6.8.4 : Cyclic Loading

As damage accumulates the stiffness of the composite progressively degrades accordingly. This is also a physically based behavior present in cyclic loading of composite materials in experimental testing. As a means to demonstrate the progressive nature of the damage model, a cyclic tensile loading simulation was created. A single element simulation was used where the loading direction is aligned with 1-axis material direction along the fiber axis. The strain rate was held constant at 1 per second. For the simulation the element remained under tension and was cyclically loaded and unloaded until the element was fully damaged. Figure 6.28 demonstrates the progressive nature of the damage model. From the figure it is apparent that the modulus is progressively degrading. In addition plastic strain is accumulating as the damage progresses.

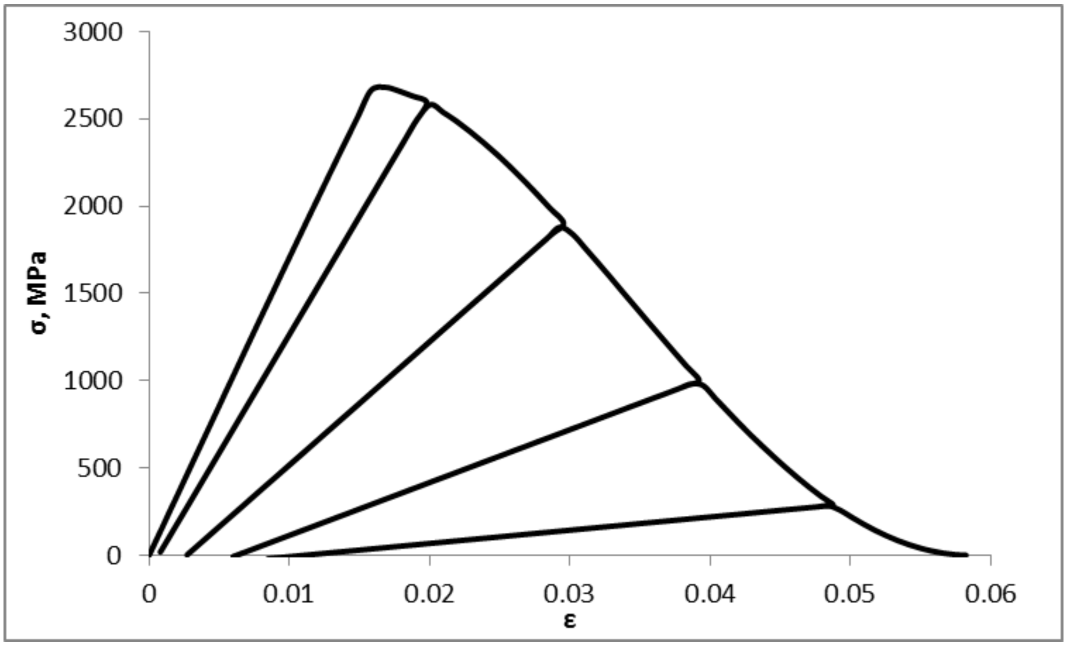

Figure 6.28: Progressive Damage Of Uniaxial Tensile Cyclic Loading Case

6.8.5 : Mesh Sensitivity Study

One of the key considerations of the material model is the damage model and the ability to dissipate energy due to fracture regardless of the specific mesh discretization. Similar to Oliver and Donadon et al, a coupon test comparison using solid hexahedral elements was performed at a strain rate of 1 per second with the dimensions of 10 x 5 x 1 mm (length, width, and depth) (53) (58). The coupons are under uniaxial tension along the length axis. The boundary conditions for the coupons are illustrated in Figure 6.29 where one side is fixed such that contraction due to Poisson effect can still occur and the other side is under constant displacement to approximate constant strain rate.

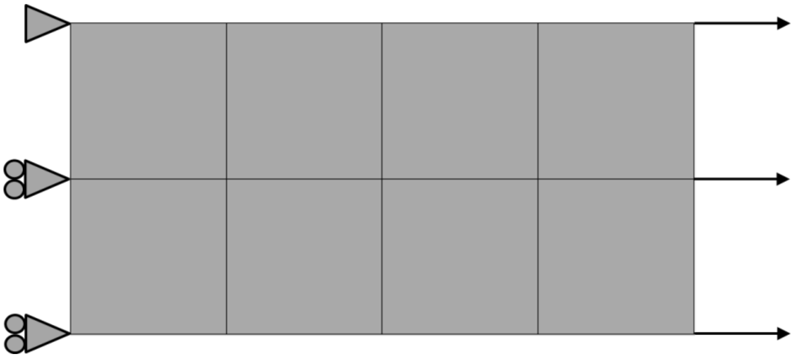

Figure 6.29: Mesh Sensitivity Coupon Boundary Conditions

The five coupons considered have different levels of mesh density and element distortion as shown in Figure 6.30.

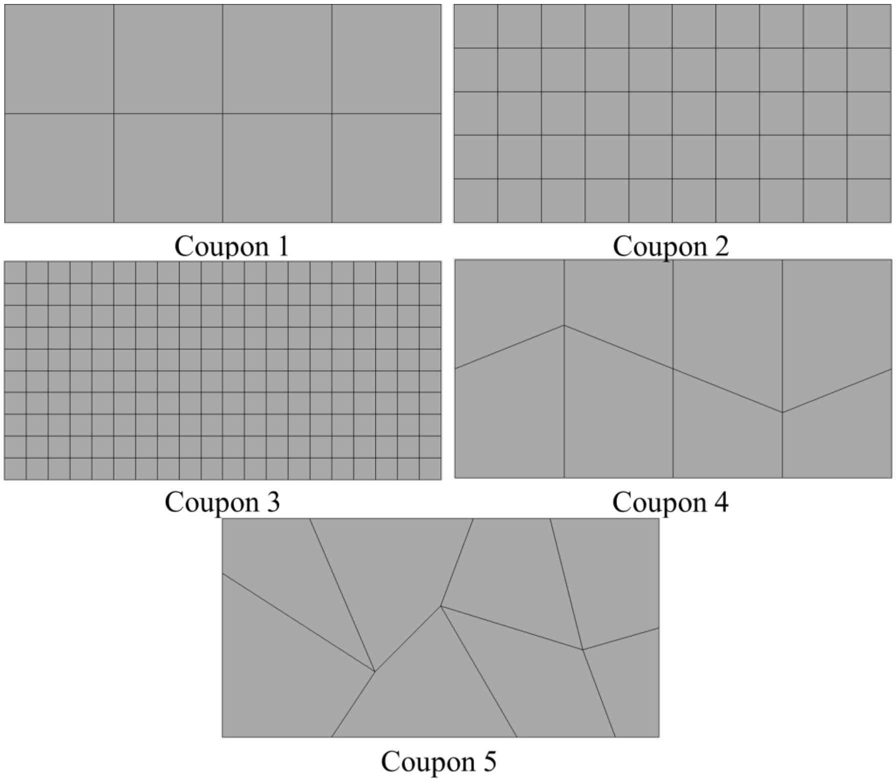

Figure 6.30: Mesh Sensitivity Coupon Comparison

The force exerted on the coupon and the resulting displacement for all of the coupons considered is summarized in Figure 6.31 where the area underneath the curve represents the energy dissipated by the coupon. From the figure it is apparent that the material model is largely mesh insensitive for the coupons considered. However there is still some variation present in the energy dissipated. This is largely due to the location of damage and its proximity to either the fixed or displacement boundary condition. As noted by Donadon et al, the damage location results from the rounding errors for the viscosity used to average the stress wave over the elements (58). Coupons 1, 4, and 5 have the greater level of damage at the fixed boundary condition while Coupons 2 and 3 occur on the constant displacement boundary condition. These results are corroborated by the disparity in the energy dissipated between the two Coupon groups shown in Figure 6.31.

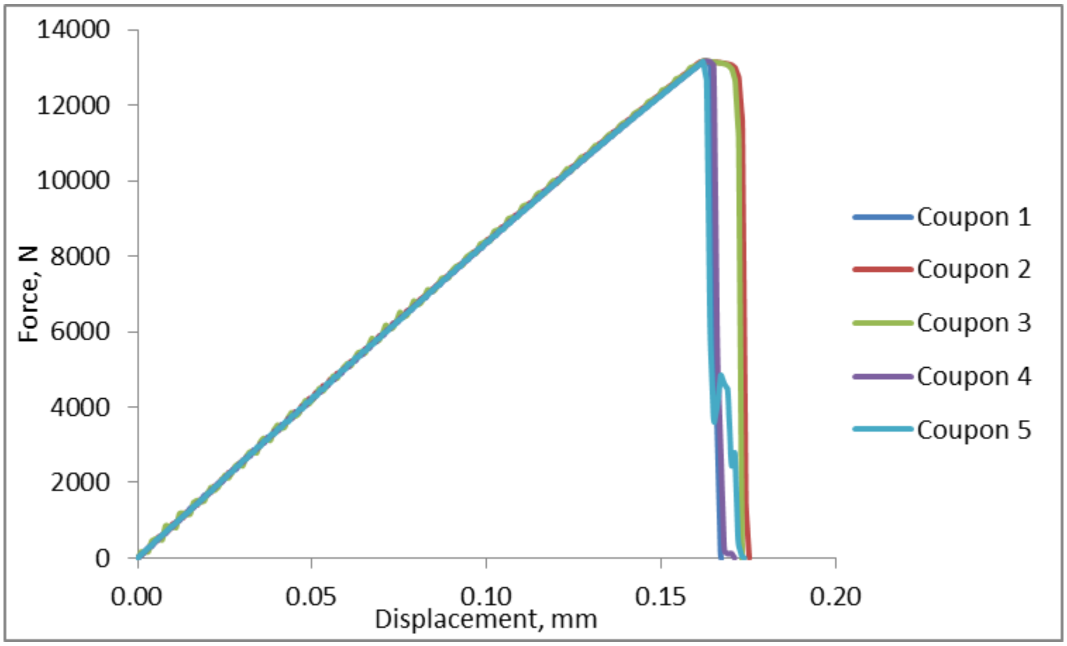

Figure 6.31: Fracture Energy Dissipation Comparison

In order to establish the rate of convergence with mesh refinement, the structured or mapped meshes of Coupons 1, 2, and 3 are compared with maximum force prior to full damage. Figure 6.32 shows that the smeared crack model allows for the solution to converge rapidly as the element number is increased from 8 to 200 for Coupons 1 and 3, respectively.

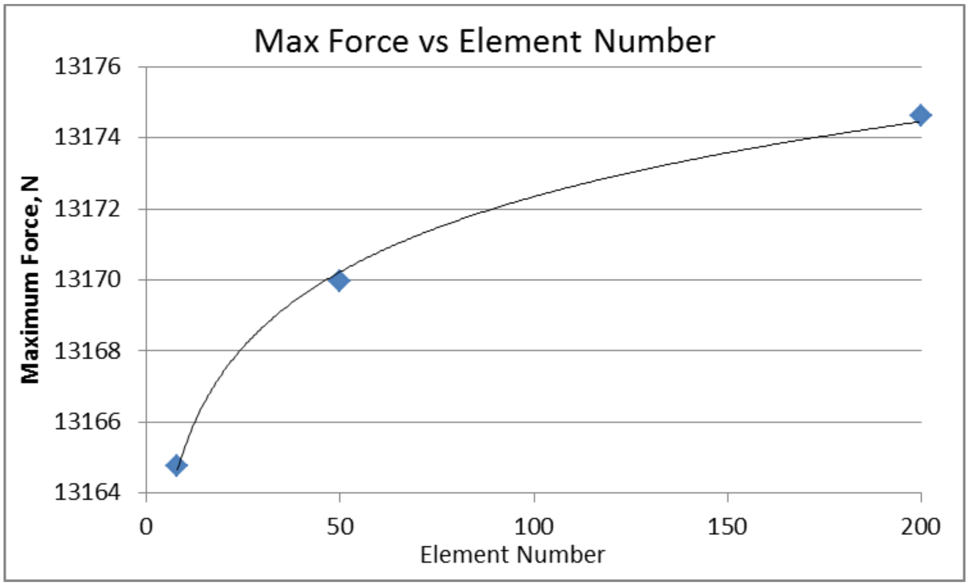

Figure 6.32: Smeared Crack Model Mesh Convergence; Maximum Force vs Element Number

Contour plots of the coupons at the time where one of the elements has reached full damage are provided in Figures 6.33 through 6.37 to show the location of maximum damage in the coupon.

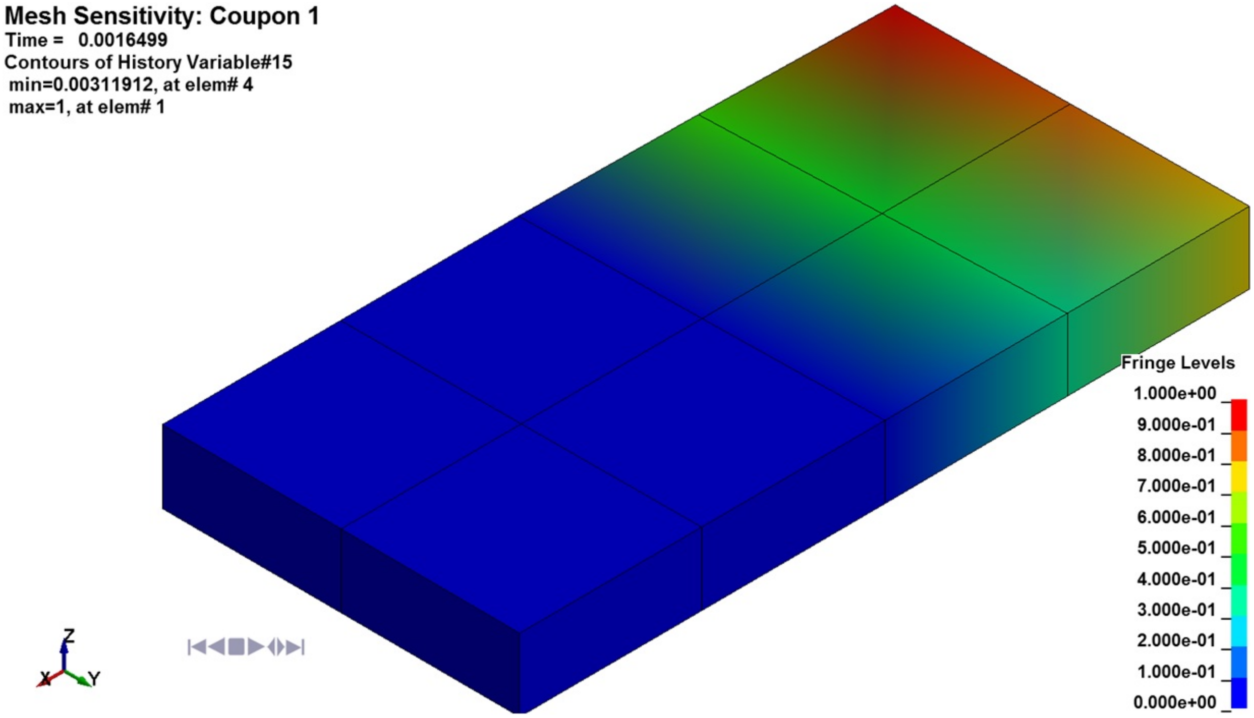

Figure 6.33: Mesh Sensitivity Damage Study Coupon 1

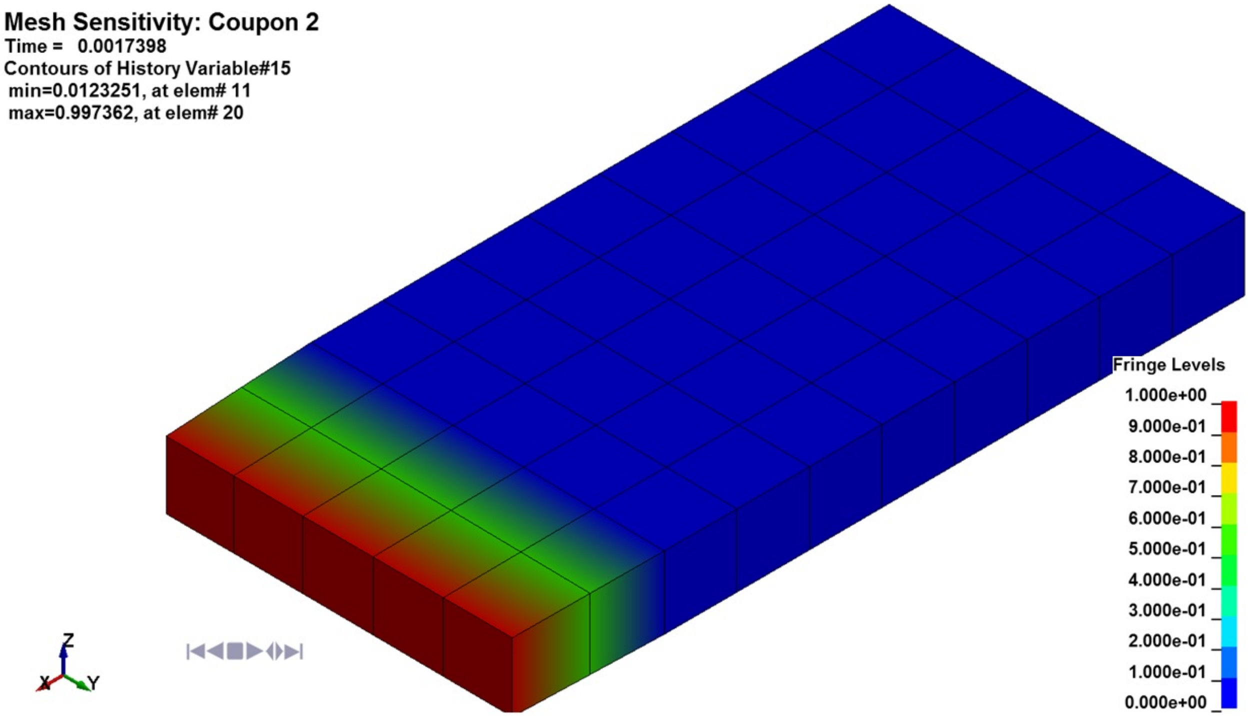

Figure 6.34: Mesh Sensitivity Damage Study Coupon 2

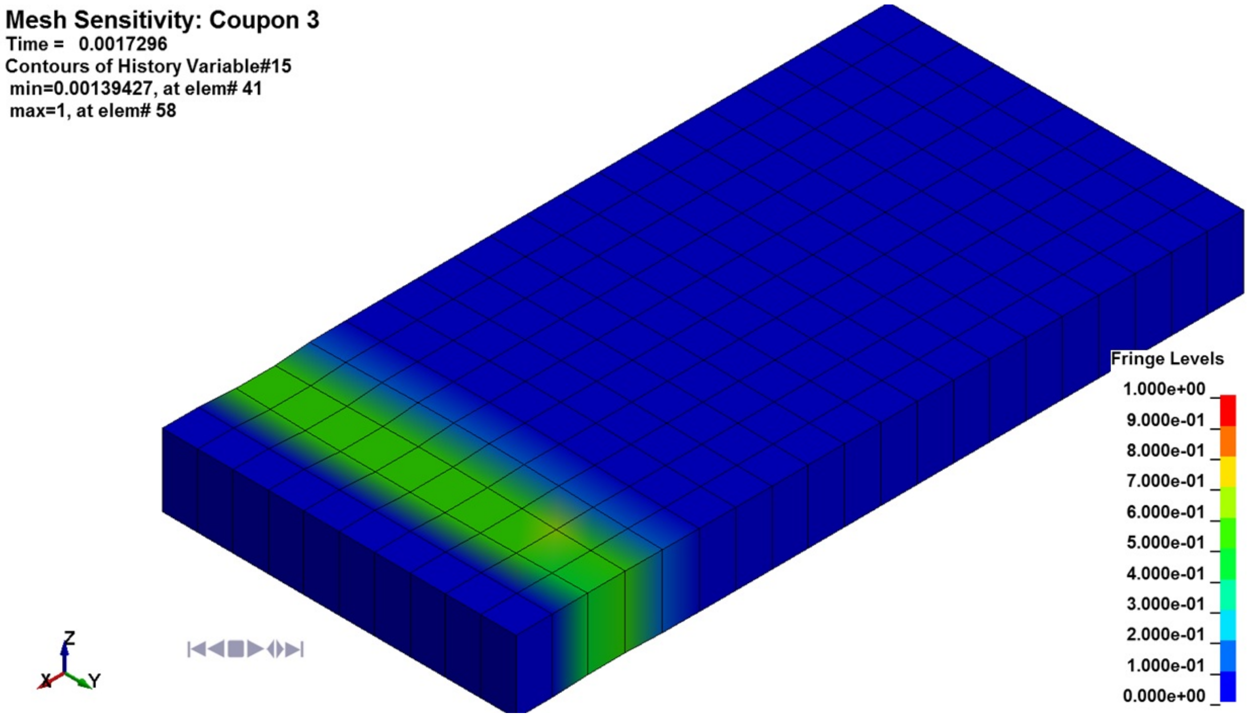

Figure 6.35: Mesh Sensitivity Damage Study Coupon 3

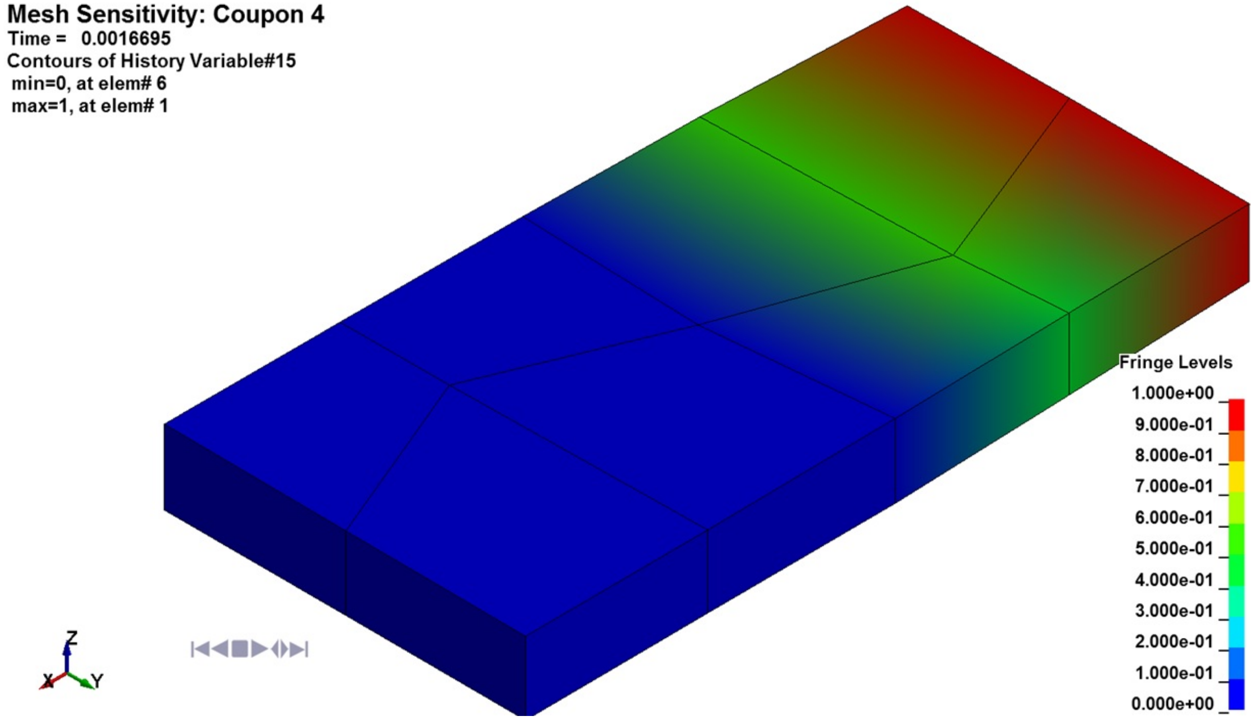

Figure 6.36: Mesh Sensitivity Damage Study Coupon 4

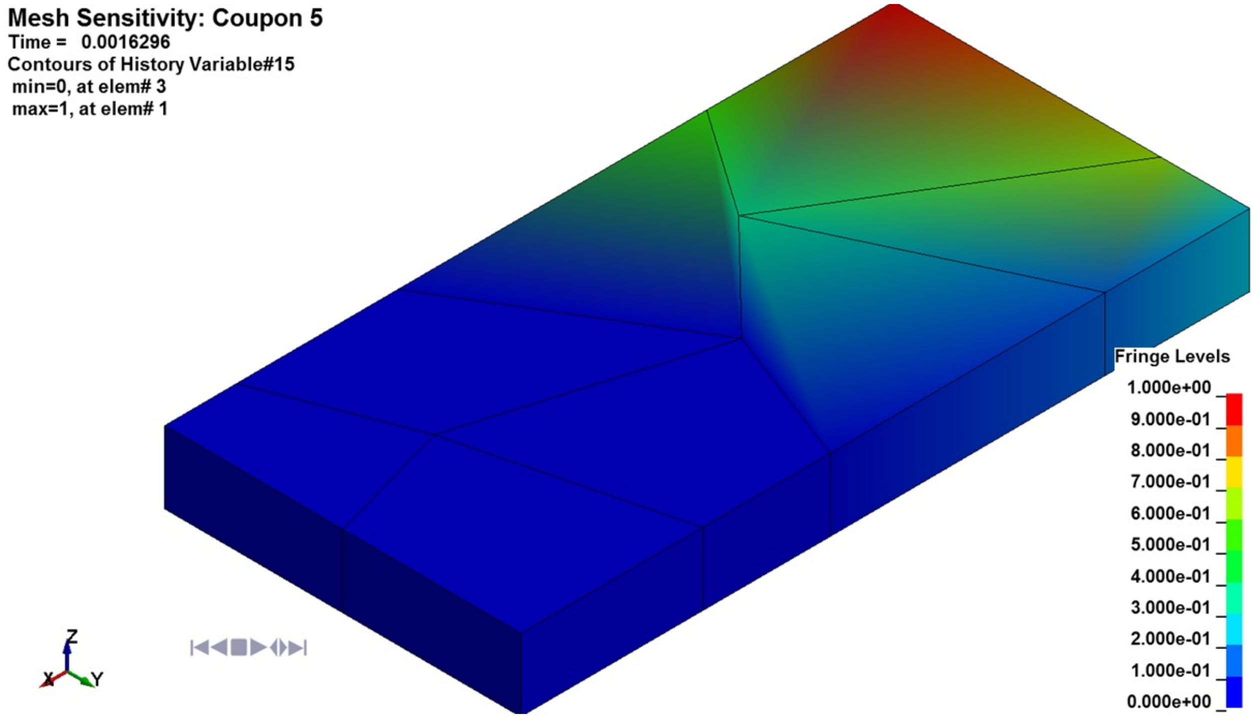

Figure 6.37: Mesh Sensitivity Damage Study Coupon 5

Chapter 7 : IM7/8552 Ballistic Impact Simulation Results

The material model response to ballistic impact will be considered using the same IM7/8552 unidirectional composite presented previously. Karthikeyan et al performed experimental testing comparing the ballistic response of IM7/8552 and Ultra High Molecular Weight Polyethylene (UHMWPE) composite laminate panels to monolithic 304 stainless steel plates subject to spherical steel projectiles (74). The steel plate was used as a reference to the composite panels. Additionally, Karthikeyan et al utilized a Moiré technique presented by Espinosa et al (75) to measure the backplane deflection of the composite panels. For the present research, it is assumed that the material behavior of the IM7/8552 composite plates reported by the multiple sources reported in the literature matches that used in the ballistic impact experiments and thus can be used in the ballistic simulation of the composite panels.

Since Karthikeyan et al anticipated that the isotropic material behavior of the 304 stainless steel would lead to circular Moiré fringe patterns, a circular clamped boundary condition with inner and outer diameters of 100 and 150 millimeters, respectively, was implemented in order to facilitate a more direct comparison of the composite and the steel reference plate impact responses. The clamped condition induces a similar radial fringe pattern on the composite panels as observed on the reference steel plate. The panels tested are 15 plies thick for a total 3.75 millimeters with a $\left[\left(0^{\circ}/90^{\circ}\right)_{7}\ 0^{\circ}\right]$ layup. The IM7/8552 carbon fiber composite panels were impacted by a 8.3 gram, 12.7 millimeter diameter spherical steel projectile normal to the composite panel face at initial velocities ranging from approximately 54 to 100 meters per second.

In order to reduce the computational requirements of the simulation, a quarter symmetry model was created as shown in Figure 7.1 where the boundary conditions are highlighted. On the perimeter of the clamped boundary condition, a no slip condition is assumed and as such the nodes are fully constrained in all six degrees of freedom.

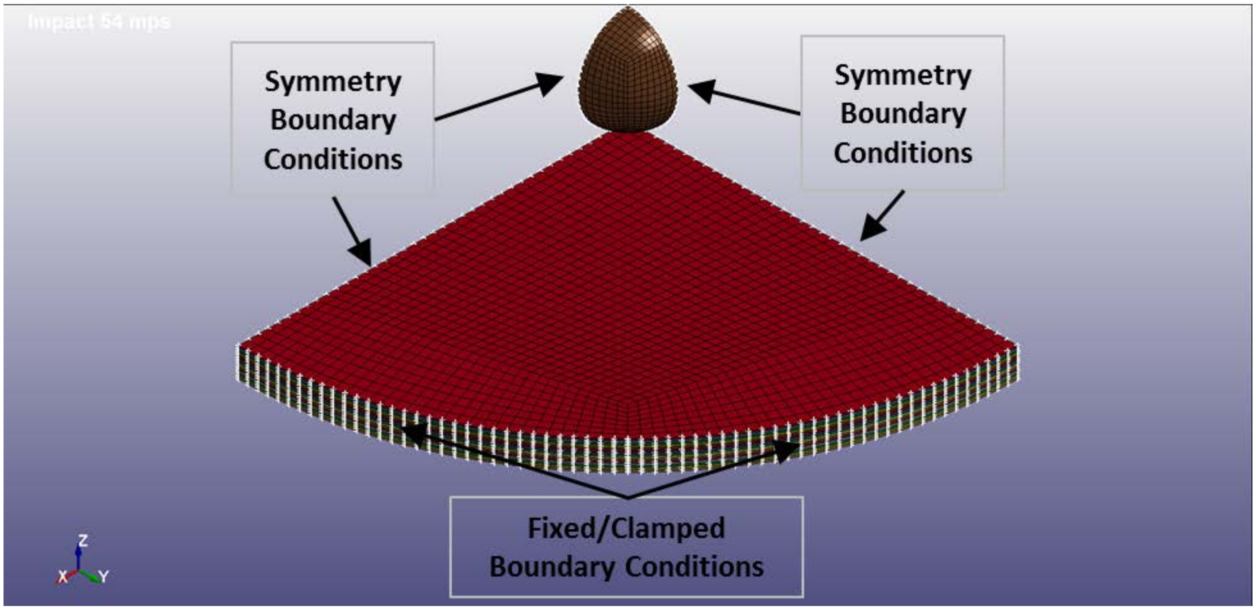

Figure 7.1: LS-DYNA Ballistic Impact Simulation Model Boundary Conditions

Along the symmetry planes, symmetry boundary conditions are enforced to prevent translation and rotation with respect to the plane. A mapped mesh consists of hexahedral solid elements created using the 2-D and block element meshers native to the LS-PrePost pre-/post-processor. The material orientations of the model are based on the layup pattern $\left[\left(0^\circ/90^\circ\right)_7 0^\circ\right]$ where the angle orientations are with respect to the X-axis. The ply definitions are defined in the model as highlighted in Figure 7.2.

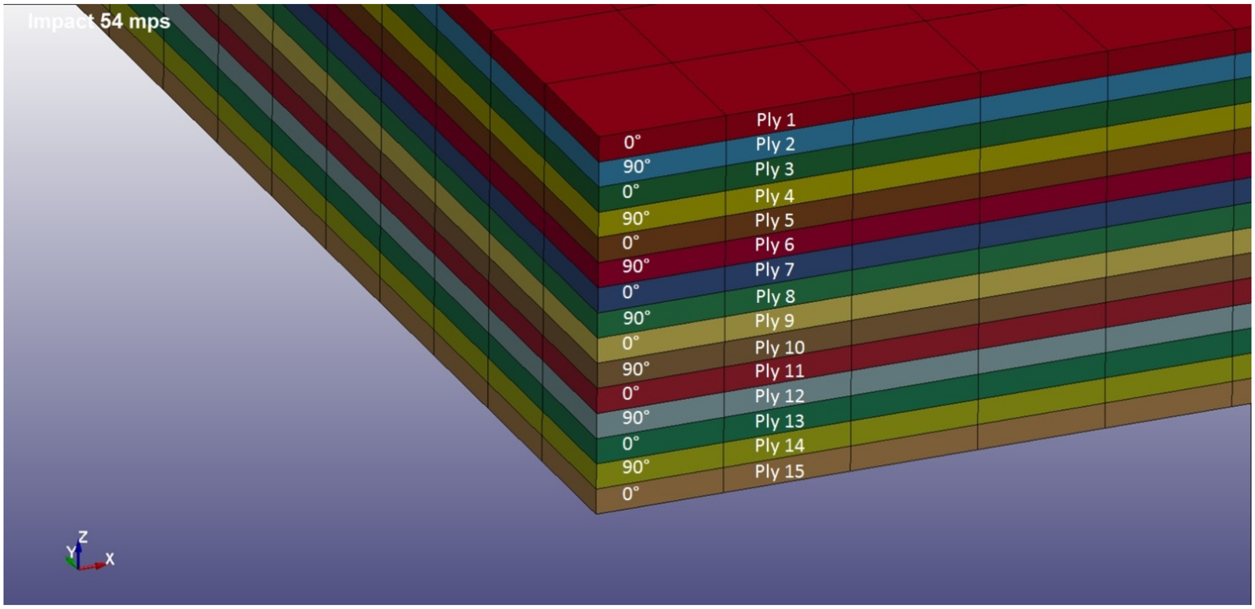

Figure 7.2: LS-DYNA Ballistic Model Composite Layup

During the initial development of the ballistic simulation, difficulty was encountered using underintegrated 'brick' elements with hourglass energy. A viscosity based hourglassing routine was used which still allowed for more than 30% of the total simulation energy be due to hourglassing. Since an appropriate hourglass setting could not be established, fully integrated hexahedral elements were selected for the simulation to avoid hourglassing or spurious modes associated with under-integrated elements. Since fully integrated elements with poor aspect ratios, such as those in the composite plies, can encounter transverse shear locking, a fully integrated element formulation developed for poor aspect ratio elements is utilized in the present analysis (65) (70) (76). LS-DYNA has two variations of the element available as presented by Borvall (76). The higher efficiency formulation is utilized for the present work through the selection of the element formulation option, $\mathrm{ELFORM} = -1$, in the keyword *SECTION_SOLID (65). In the model each of the 15 plies in the composite panel are represented individually.

Although LS-DYNA offers both cohesion and contact elements that can represent the adhesion between the plies, it is desired for the present research to evaluate only the performance of the material model without the influence due to the interaction of the material model and contact model. Therefore for this simulation adhesion will be assumed to be perfect and duplicate nodes from adjacent plies can be merged which allows for better evaluation of the material models' performance. However it should be noted that the material model does consider both intralaminar and interlaminar fracture energies. A penalty-based contact model between the projectile and the composite panel was defined. The static and dynamic coefficients of friction, 0.33 and 0.68, were obtained from the published data provided by Quitelier et al and Schön, respectively (77) (78). For orthotropic materials undergoing large deformations such as in ballistic impact, the material direction orientation can have a large influence on the accuracy of the material model response. LS-DYNA allows for the improved accuracy for such events by utilizing second order stress updates with the Jaumann rates when the *CONTROL_ACCURACY keyword is called (65) (70).

In early development of the ballistic impact simulation, a mesh convergence study was performed to determine the optimum level of mesh refinement. The center composite plate deflection at an impact velocity of 54 meters per second was used to determine mesh convergence. This impact velocity was chosen since, based on the published results from Karthikeyan et al, perforation is not expected to occur. The model response is plotted for various levels of mesh refinement in Figure 7.3. The model is trending towards convergence at the higher mesh refinement of 38000 elements. However the computational cost increases disproportionately from approximately three and half hours at the lowest number of elements to over 20 hours for the finest mesh case. In the interest of the development effort for the material model, the moderate mesh refinement will be selected as it offers a better balance of accuracy and computational efficiency.

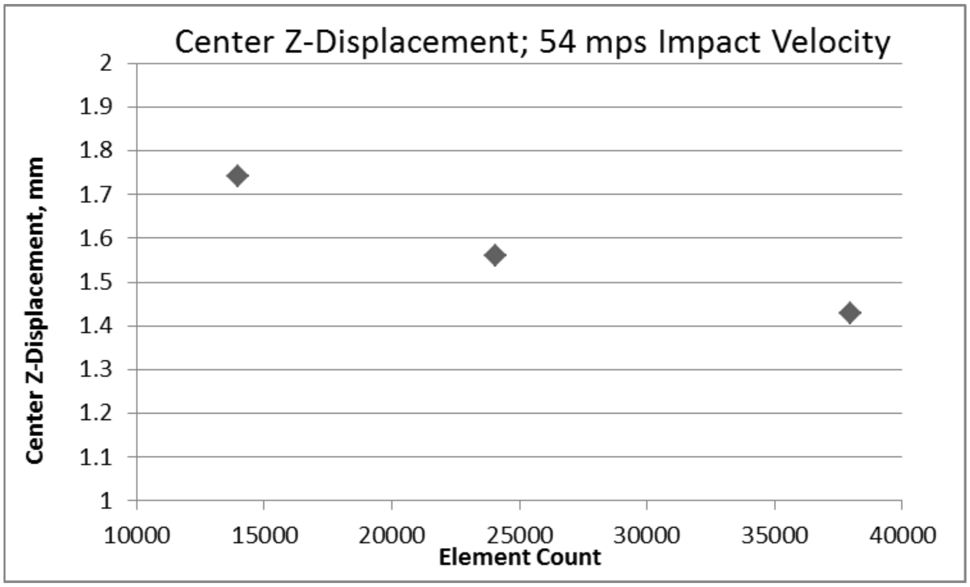

Figure 7.3: Mesh Convergence Study; Maximum Center Deflection at 54 mps Impact Velocity

Since the deformation of the steel projectile will be negligible in comparison to the composite panel during the ballistic event, the steel material behavior can be assumed to be perfectly rigid in order to reduce computational load in the simulation. *MAT_RIGID material model was used for the steel projectile where the material constants are defined in Table 7.1.

Density (kg/m^3)	7877
Elastic Modulus (GPa)	207
Poisson's Ratio	0.33

Table 7.1: Steel Projectile Material Model Parameters

7.1: Backplane Deflection

Ballistic simulations were created to simulate the impact velocities reported by Karthikeyan et al: 54, 70, and 100 meters per second. Additional simulations were performed at other velocities to determine the bsllistic limit velocity, or V_{50}, for the carbon fiber panels considered. The experimental Moiré fringe deflection data as a function of the radial location, r, and the time after impact for the initial velocity of 54 meters per second is summarized in Figure 7.4. In a similar fashion, the panel deflection predicted in the FEM simulation at various times after impact are illustrated in Figure 7.5. Comparison of the experimental data to the simulation data shows that the simulations under predict the backplane deflection throughout time after impact. The maximum deflection observed experimentally is approximately 2.9 millimeters compared to 1.75 predicted by the FEM simulation. For both the experimental results and FEM predictions, the maximum deflection occurs at approximately 107 microseconds after impact. The difference in deflection is largely due to two key contributors: the material characterization data used to determine the model's material parameters and the perfect bond simplification assumed in the model. In the ballistic impact event considered, in-plane tension towards the outer boundary condition plays a large role in the overall panel response. However, in the immediate vicinity of the impact, out of plane behavior such as through the thickness compression and bending have a larger impact. For the present simulation, the material model parameters have been determined using in-plane behavior under both tension and compression from the literature. As such an accurate description of the out of plane behavior is needed to further improve the material model response. Additionally the perfect bond simplification prevents delamination of the composite and the following translation between the delaminated plies. This simplification has a stiffening effect on the panel response which also leads to the reduce panel deflection observed in the simulations.

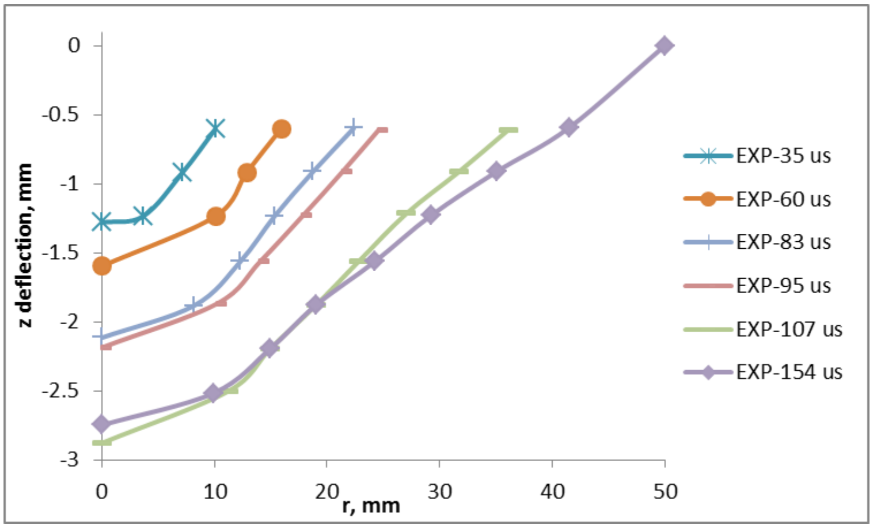

Figure 7.4: Moiré Fringe Experimental Data; 54 mps Impact Velocity

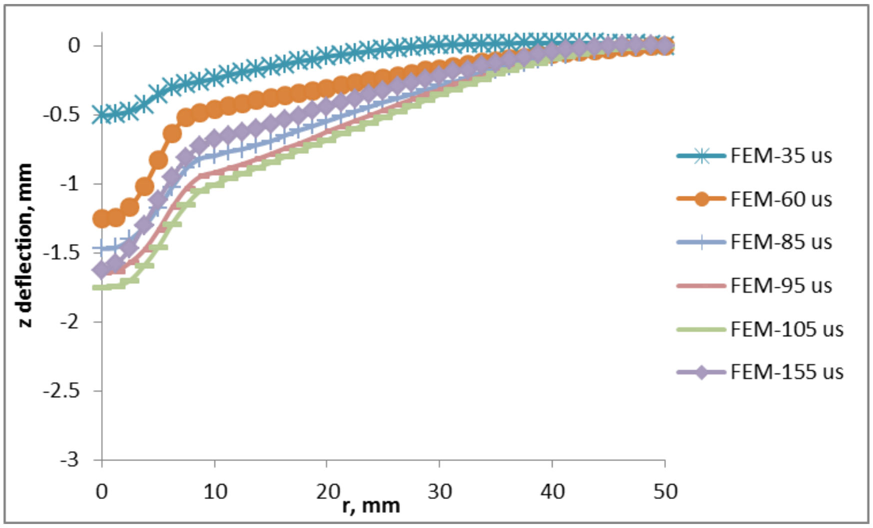

Figure 7.5: FEM Simulation Deflection Results; 54 mps Impact Velocity

7.2: Damage Progression

Ultrasonic analysis of composite panels post-impact oftentimes will show a 'figure-eight' or 'peanut' shaped pattern for the delamination between plies. Since for this particular model the interlaminar fracture energy is dissipated only through the material model, the damage variables related to the out-of-plane failure modes should also show this 'figure-eight' pattern. Considering the 54 meter per second case the damage for the shear in the 2/3 plane, d_{23}, the total damage accrued post-impact is compared among plies in Figure 7.6. As seen in the literature the same pattern is predicted by the LS-DYNA simulation for some of the plies. In addition the pattern varies in relation to the orientation of each individual ply. The layup of the plies is $\left[\left(0^{\circ}/90^{\circ}\right)_7\ 0^{\circ}\right]$ with the top ply being ply 1 in Figure 7.6.

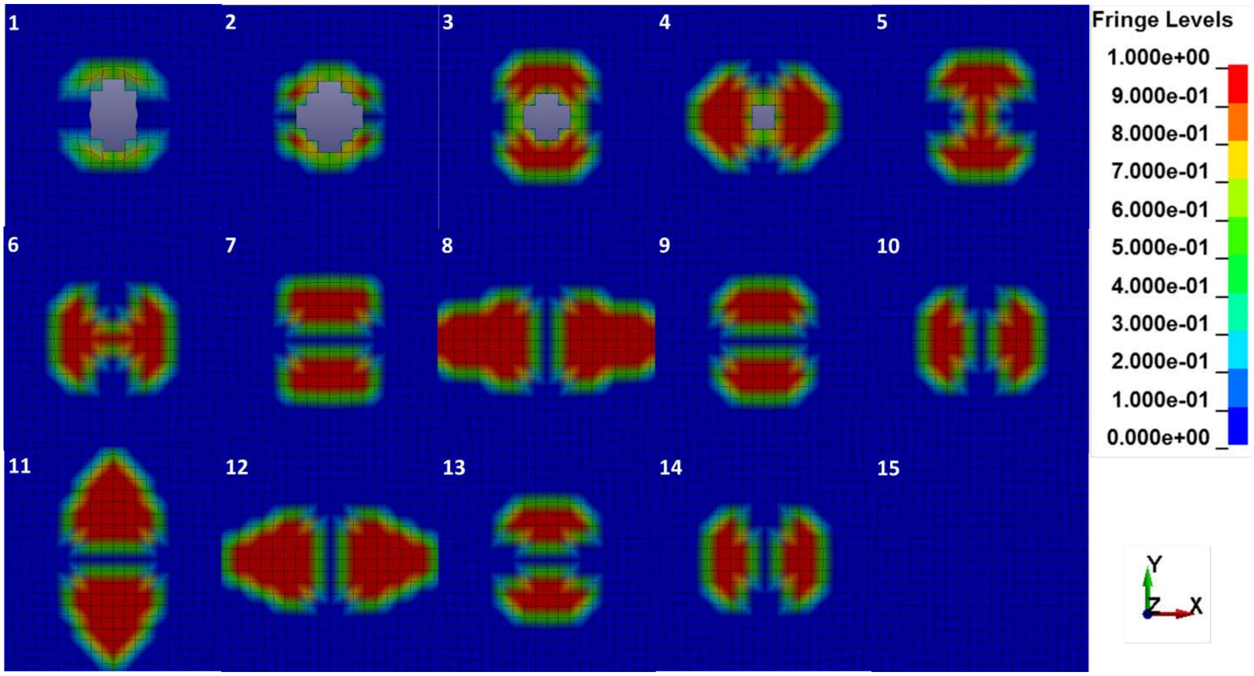

Figure 7.6: d_{23} Damage Variable Ply Comparison; 54 mps Case

7.3: Ballistic Limit Velocity

Figure 7.7 compares initial and residual velocities for all of the simulations considered in the ballistic limit study. The negative values denote a change in direction where the composite deflected the projectile. Similar to experimental testing, the bisection method was used to determine the ballistic limit or the root of the initial and residual velocity relationship. The model predicts that the ballistic limit will occur at around 87.06 meters per second which is a conservative estimation to the reported V_{50} of approximately 100 meters per second by Karthikeyan et al.

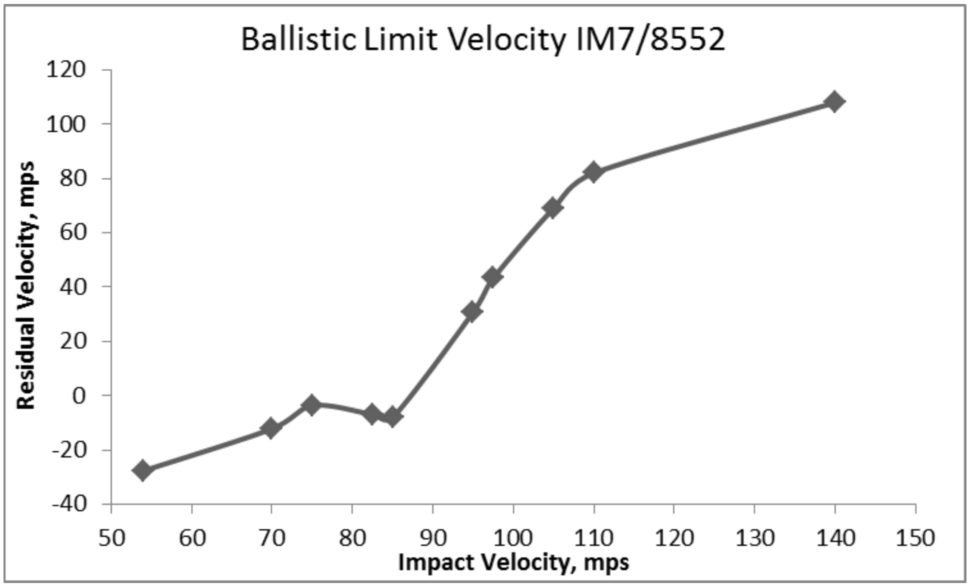

Figure 7.7: Comparison of Initial and Residual Velocities for IM7/8552 Ballistic Impact Simulations

Figure 7.8 shows the simulation where the composite stops the projectile at 165 microseconds after impact. It is apparent from the figure that while the erosion criteria are not causing premature deletion of elements, there is still potential for some elements to become overly distorted during the simulation. After the element is fully damaged for one of the particular failure modes, plasticity can still occur. Since none of the erosion criteria implemented directly control the progression of plasticity, the element can become highly distorted post-damage.

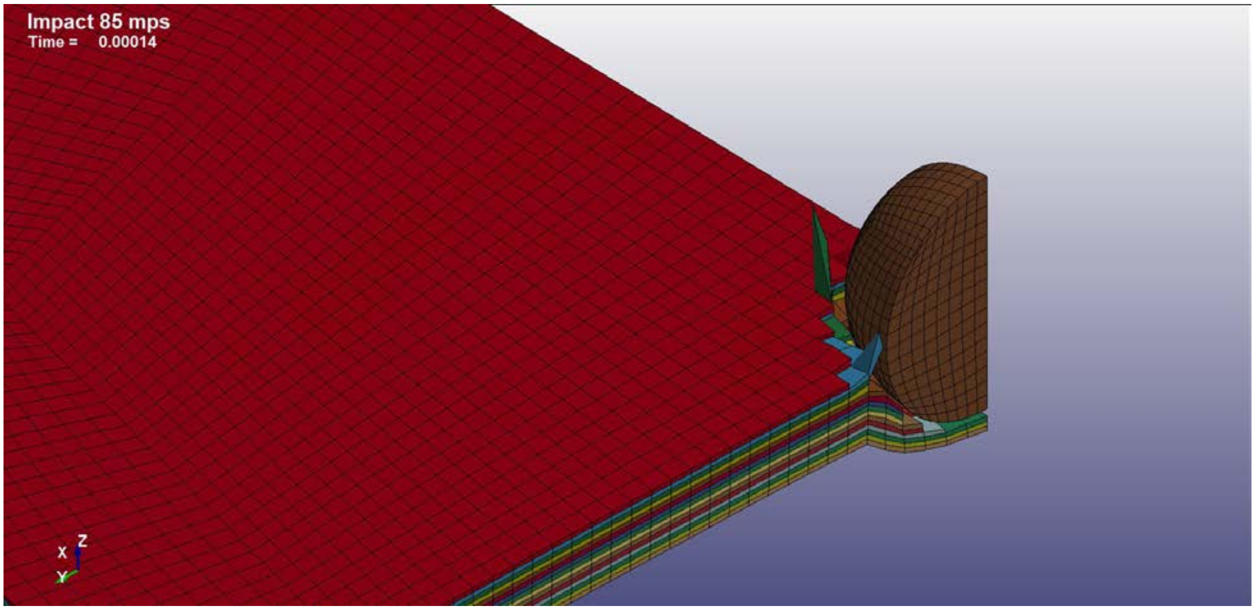

Figure 7.8: Element Distortion at 85 mps Impact Velocity; 140 µsec after impact

Chapter 8 : Polycarbonate Glazing Experimental Test Methodology

Experimental equipment to facilitate the requirements of the ISO 11839 standard for thrown saw teeth against operator enclosures used in forestry applications are proposed and outlined (79). Polycarbonate panels are tested under high velocity impact using a representative chain fragment that has been identified to be particularly hazardous. The results are compared to what has been observed in the field and other researchers.

8.1: Chainshot or Thrown Object Hazard

Polycarbonate glazing in forestry applications is an integral component in the protection of operators during operation. Polycarbonate is also known by its tradenames of Lexan and Makrolon. Polycarbonate has demonstrated an excellent impact resistance in comparison to other polymers and some metals (80). Currently low velocity methods are typically utilized by manufacturers to establish the energy absorption capabilities of polycarbonate glazing. Drop impact towers in ASTM D3763 are used to establish the puncture resistance of plastics (81). This is appropriate in establishing the impact resistance to obstructions such as tree branches but is not able to properly establish high speed impact resistance. The response of the polycarbonate panel is dependent on the rate of impact. As noted by Zukas, the overall response of a plate subject to impact is highly localized for high velocity impact (82). For low velocity impact the response becomes more global as the contact time is longer. A comparison of the general response of plates to low and high velocity impact is illustrated in Figure 8.1. As such, high velocity testing is necessary to fully establish the energy absorption capabilities of polycarbonate for glazing applications.

Figure 8.1: Plate Response To (a) Low And (b) High Velocity Impact

Recently ISO 11839 has been accepted to address the needs for a high velocity testing methodology for the chainshot impact hazard in forestry applications. Chainshot is defined as "the high velocity separation and ejection of a piece or pieces of cutting chain from the end of a broken chain in mechanized timber harvesting." (83) Chain failure and/or derailment often occurs due to either unsafe operating conditions or poor equipment maintenance. The sequence of events after chain failure is outlined in Figure 8.2 (84). Initially the chain fails and breaks which leads to some initial separation from the chain bar. In the absence of any guards to restrict the motion of the chain, the inertia of the chain leads to a whipping action which causes further separation from the chain bar. Eventually the whipping motion can lead to substantial dynamic energy to fragment the chain and eject a piece or pieces in the vicinity of the harvesting equipment. The chainshot event is highly unpredictable since it depends on the location of the chain failure, the chain speed at the time of failure, and the guard system implemented on the particular harvesting equipment. A particular danger is when the chainshot trajectory is towards the cab and operator of the harvester. Recently the Washington State Department of Labor & Industries reported an investigation of a chainshot incident that resulted in fatal injuries to the harvester operator (85). The glazing was 12 mm thick Lexan Margard MR5E which was struck by 0.404" pitch Carlton chain.

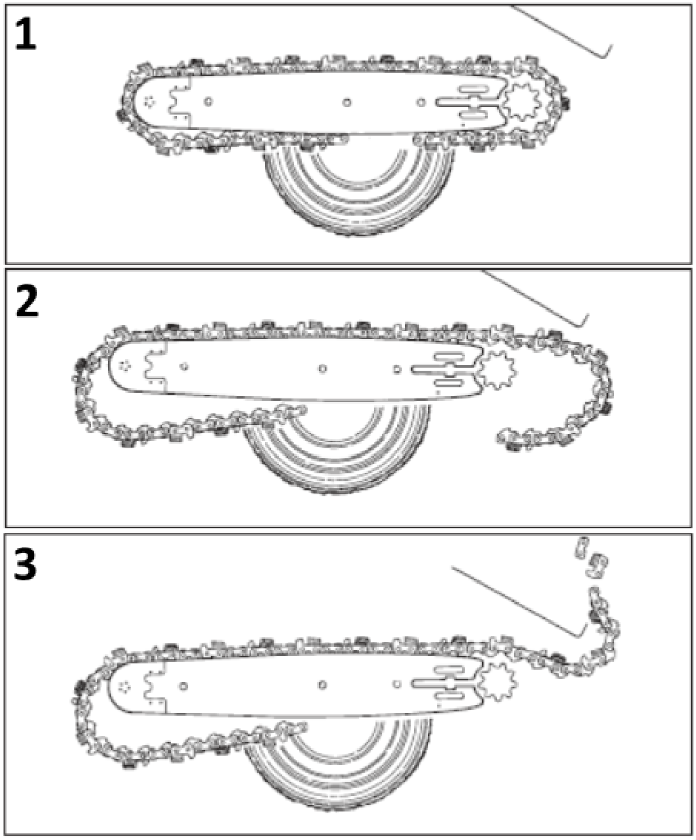

Figure 8.2: Chainshot Event Sequence (Oregon Mechanical Timber Harvesting Handbook, 2005)

The chainshot event has been analyzed through an experimental setup developed through collaboration between The Forestry Research Institute of Sweden (Skogforsk) and the Swedish Machinery Testing Institute (SMP) (86). An experimental test rig was created that was capable of rotating the chain at speeds between 20 and 50 meters per second. The experimental launcher consists of an Oregon chain bar, a 15 kW electric motor to drive the chain, and a chain arrestor mechanism to instantly stop the chain. The launcher mounted within a safety enclosure is shown in Figure 8.3 where the arresting mechanism is highlighted. The chain arrestor induces a chain failure to create the whipping action demonstrated in Figure 8.2.

Figure 8.3: Experimental Chainshot Launcher (Skogforsk, 2004)

High speed video stills of the chain whip and chainshot event recreated by the experimental launcher is shown in Figure 8.4. The chain fragment is highlighted in the video stills. The researchers found that at a normal operation chain speed of 40 meters per second, the chain fragment velocity ranged between 250 to 325 meters per second regardless of whether the fragment consisted of a rivet, tie strap, or multiple parts (86). This confirms reports made by Carlton Products of approximate chainshot velocities of 310 meters per second (85).

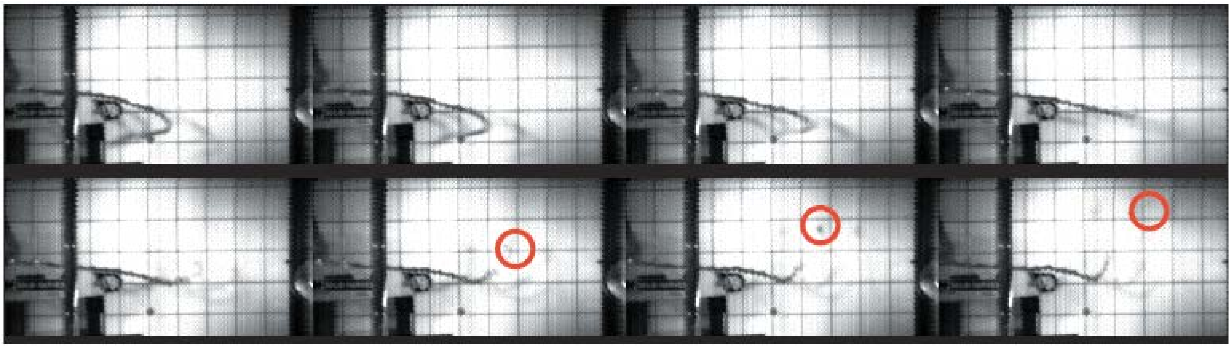

Figure 8.4: High Speed Video Stills of Chain Shot Event (Skogforsk, 2004)

The experimental launcher developed by Skogforsk is able to accurately recreate the chainshot event which is beneficial in the development of chain guard systems. However the inherent unpredictability in the resulting fragment and the chain fragment trajectory does not allow for a repeatable, accurate validation of polycarbonate panels to chainshot event. The response of a polycarbonate panel will be dependent on the impact surface geometries of the projectile and impacted material, the trajectory and attitude of the projectile, projectile mass and velocity, and ambient conditions. In order to quantify the energy absorption capabilities of the polycarbonate panels to chainshot, several measures are necessary. First a representative fragment must be selected so that a direct comparison between experimental tests can be made. Oftentimes the representative fragment is referred to as a fragment simulating projectile (FSP) in the ballistic literature. Secondly the experimental launcher must be able to accelerate the projectile in a controlled, repeatable trajectory with minimal attitude (pitch, yaw, and roll) and a high level of control of the energy delivered to the panel (projectile velocity). In order to meet these requirements an experimental launcher is proposed. Experimental testing is performed based on the reported fatality incident. A LS-DYNA Finite Element simulation is performed to reconfirm the experimental findings.

8.2 : Chainshot Fragment Simulating Projectile

Due to the chaotic and unpredictable nature of the chainshot event, various chain fragments may be ejected from the harvester and impact the operator cabin. In the interest of creating a repeatable experiment that allows for replication where statistical confidence levels are desired, a FSP for the chainshot event is needed. As noted by the incident report from Washington State various chain fragments impacted the operator cabin (85). Skogforsk researchers observed similar chain fragmentation in their experimental launcher (86). As illustrated in Figure 8.5, typical harvester chains consist of the following main components: tie straps, rivets, driving links, and cutters (84).

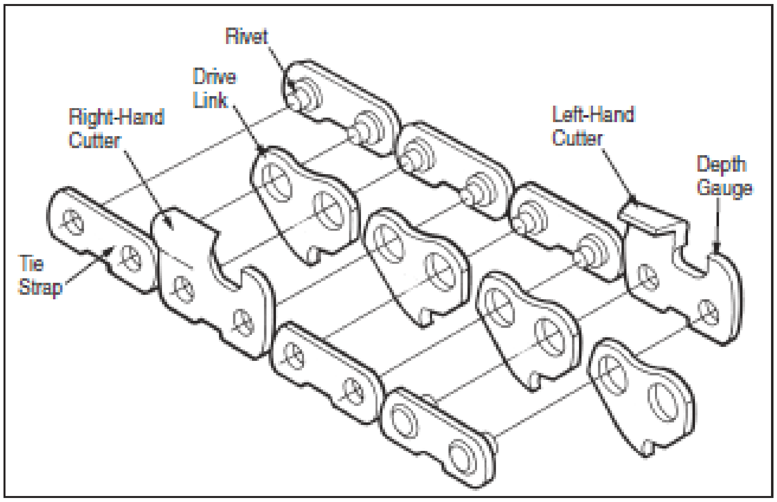

Figure 8.5: Harvester Chain Components (Oregon Mechanical Timber Harvesting Handbook, 2005)

Oregon Products, a harvester chain manufacturer, has suggested that some of the more potentially dangerous combination of chain fragments and combinations are shown in Figure 8.6 (83).

Figure 8.6: Highest Potentially Hazardous Chainshot Fragments (Oregon, 2013)

Based on the harvester chain involved in the incident, Oregon 0.404” pitch chain was selected for the experimental testing. In order to maximize the mass and proportionately the energy delivered to the polycarbonate panels, the chain fragment consisting of the tie straps, rivets, and driving link was selected. The selected fragment simulating projectile, FSP, has a nominal weight of 6.1 grams. A CAD representation of the chainshot FSP is illustrated in Figure 8.7 and based on measurements made from the considered Oregon 0.404” harvester chain. The FSPs used in the experimental testing were created by segmenting the chain using disassembly techniques outlined in the Oregon Timber Harvesting Handbook.

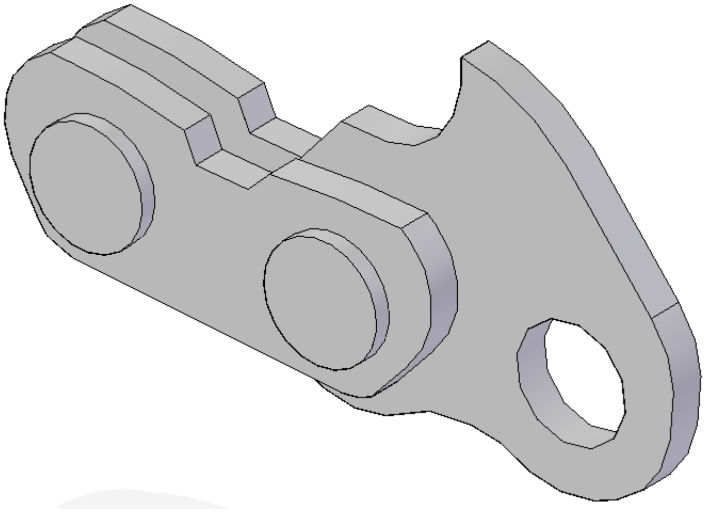

Figure 8.7: CAD Representation Of Chainshot FSP

8.3: Test Setup

An existing single-stage gas gun was utilized to accelerate the chain fragment. The gun consists of a gas reservoir, a fast-acting solenoid valve, and 10’ long barrel with a bore diameter of 5/8” as shown in Figure 8.8.

Figure 8.8: Experimental Single-Stage Gas Gun System

Compressed air and helium were utilized as the driving gases to accelerate the projectile. Depending on the desired velocity for the particular test, air or helium can be used to pressurize the gun system. Since the speed of sound for helium in considerably higher than air, 1107 and 345 meters per second at standard temperature and pressure respectively, the use of helium results in significantly higher velocities. The projectile velocity was controlled through the initial pressure of the gas reservoir and the choice of driving gas. The ballistic limit velocity of the polycarbonate panels was measured using a NAC 512sc high speed video camera. The velocity measurements were calculated by using the camera pixel coordinates and the video framerate. Since the gun barrel bore diameter was undersized for the chainshot FSP, the driving links on the FSPs were trimmed slightly to facilitate testing with the gas gun as shown in Figure 8.9.

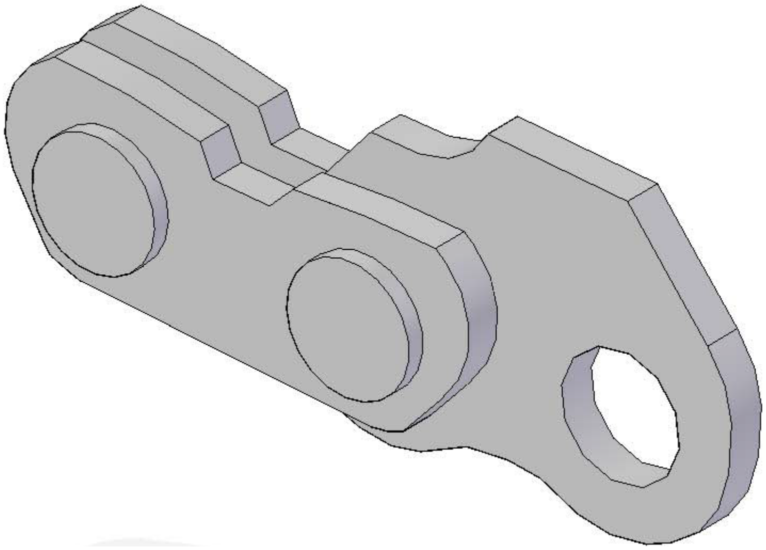

Figure 8.9: Trimmed Driving Link Chainshot FSP

A sabot or projectile carrier is critical in ensuring the projectile trajectory and attitude in addition to the overall performance of the gun in terms of projectile velocity. A three piece sabot design has been previously developed to facilitate ballistic testing with the aforementioned gun. The sabots are machined from a standard grade acetal plastic. The general sabot design is illustrated in the CAD representation of the sabot with a spherical projectile in Figure 8.10.

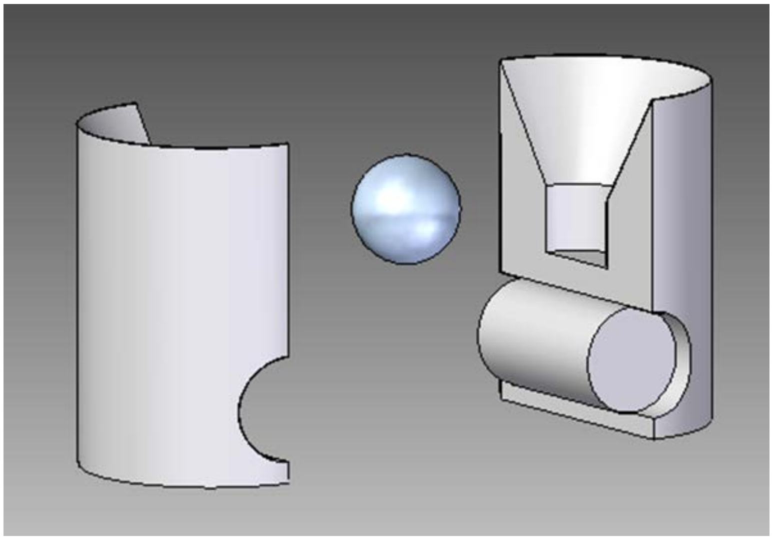

Figure 8.10: CAD Representation Of General Sabot Design With Spherical Projectile

The general sabot design was modified to support the chainshot FSP. Figure 8.11 shows the finished sabot. The sabot has been lengthened and on the interior an oblong profile secures the FSP preflight. A closer examination of the interior profile is shown in Figure 8.12.

Figure 8.11: Assembled Chainshot FSP Sabot

Figure 8.12: Unassembled Chainshot FSP Sabot

It is anticipated that the FSP due to geometry and the moment of inertia will be susceptible to a significant amount of pitch, roll, and yaw. During the development of the sabot design, 1/4” diameter, 1” long cylindrical rods were used to verify the amount of projectile attitude during flight. The rods were fired at a velocity of approximately 200 meters per second. The high speed video camera was used to document the behavior of the projectile and sabot. From the video stills in Figure 8.13, the sabot is shown to readily separate from the projectile without inducing any attitude. As the sabot further separates, the projectile maintains its’ trajectory path. The video stills were further analyzed and in all of the validation performed no more than 5° of pitch were observed where the sabot had a tight fit in the barrel bore. Thus it was expected that the proposed design would yield similar results for the chainshot FSP.

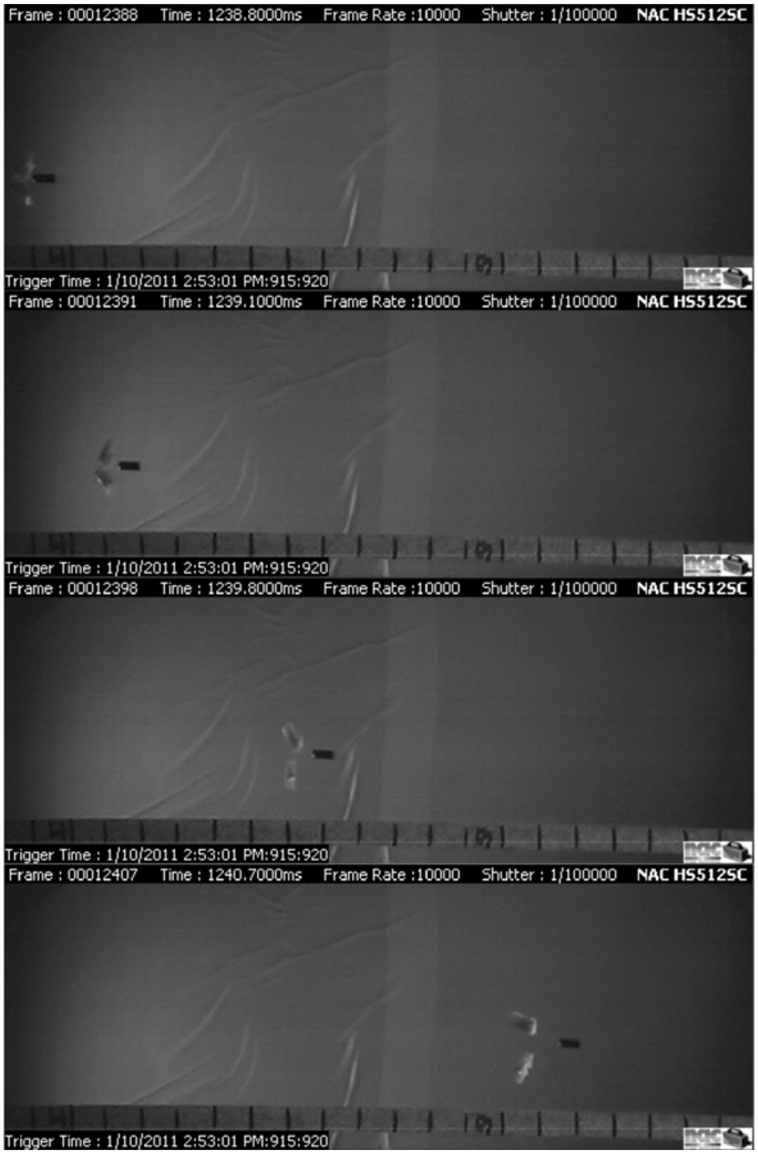

Figure 8.13: Sabot Design Validation High Speed Video Stills

8.4: Experimental Test Results

8.4.1 : 0.5” Monolithic Lexan Impact

Monolithic Lexan panels measuring 6” x 6” x 0.5” (LWD) were impacted with the aforementioned chainshot FSP using the gas gun. The Lexan panels were clamped around the perimeter with 0.5” overlap. The FSPs impacted in a trajectory path normal to the panel surface. For the panels considered, air was used as the driving gas since it yielded sufficient gun performance. The panels were tested at a room temperature of approximately 70° F. A summary of the tests performed are highlighted in Table 8.1

Test Number	Initial Weight (grams)		Residual Weight (grams)		Velocity (meters/sec)		Comments
	Panel	Projectile	Panel	Projectile	Impact	Residual	
1	345.8	6.35	N/A	N/A	291.1999	0	Projectile Stuck
2	342.15	6.15	341.55	6.15	294.17	128.083	Full Perforation
3	343.55	6.2	N/A	N/A	281.669	0	Projectile Stuck
4	344.15	6.15	343.85	6.25	291.33	83.09	Full Perforation
5	344.15	6	343.9	6.05	309.203	143.77	Full Perforation
6	340.85	6.05	340.55	6.05	305.689	127.316	Full Perforation

Table 8.1: 0.5" Monolithic Lexan Chainshot FSP Impact Testing Summary

Based on the testing it is estimated that for the particular testing conditions the ballistic limit velocity of the monolithic Lexan panel is approximately 282 meters per second. The damage modes observed for the monolithic Lexan impact testing was plastic deformation and crazing or the generation of microcracks. The crazing was denoted by a slight discoloration or whitening of the Lexan.

From Test 1 the isometric view of the post-impact damage is presented in Figure 8.14. The FSP in this case has almost fully perforated the panel. From the damage it is apparent that after the projectile initial penetrates the Lexan panel, a plastic deformation front forms and progresses through the thickness of the panel as the projectile moves forward. The plastic deformation front in this case has taken a mushroom or plug shape. This is similar to the plug formation that occurs in metals under high velocity impact (9). Wright et al reported the same plugging behavior for thick polycarbonate panels under impact from cylindrical projectiles (87).

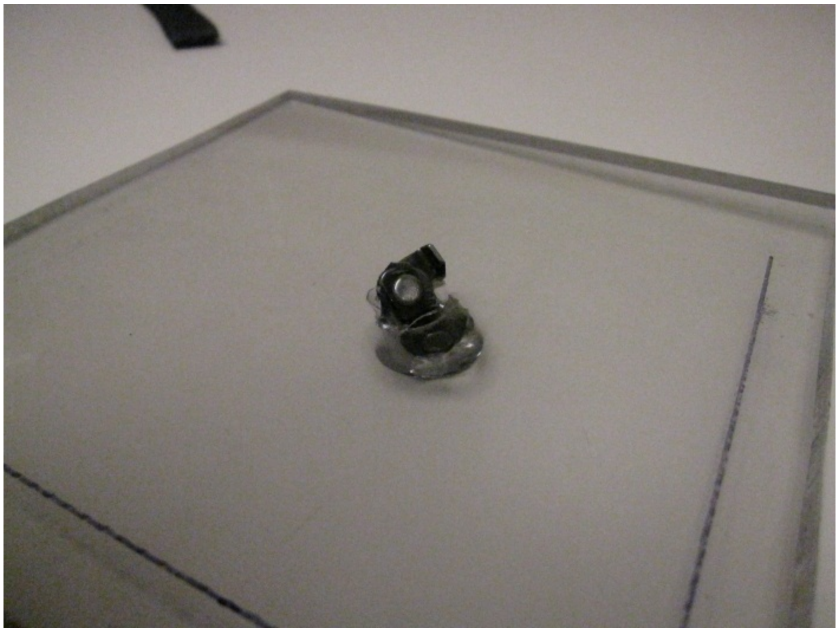

Figure 8.14: 0.5" Monolithic Lexan Post-Impact Damage For Test 1; Isometric View

From Test 4 post-impact damage is shown in Figures 8.15 and 8.16. The predominant damage mode is plastic deformation. Slight crazing was observed in the direct vicinity of the impact.

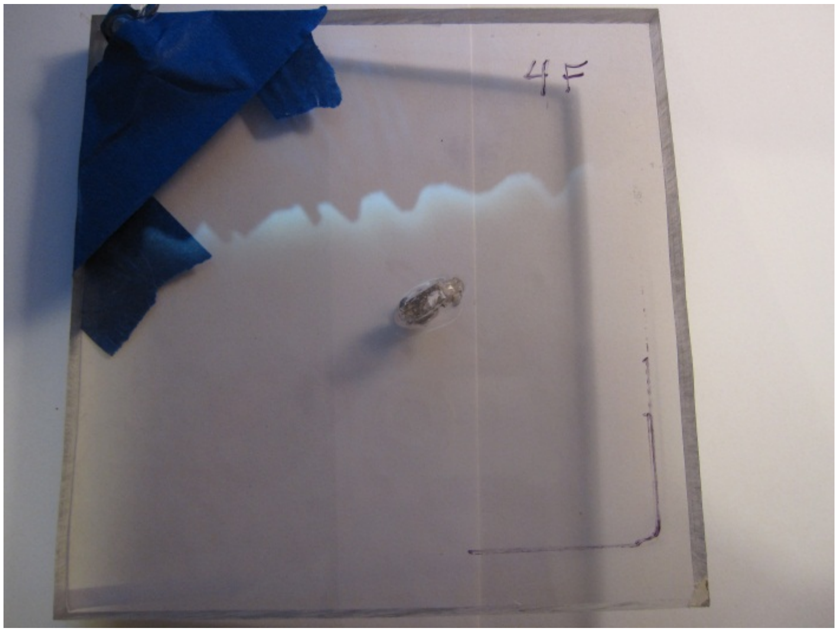

Figure 8.15: 0.5" Monolithic Lexan Post-Impact Damage For Test 4; Front Face

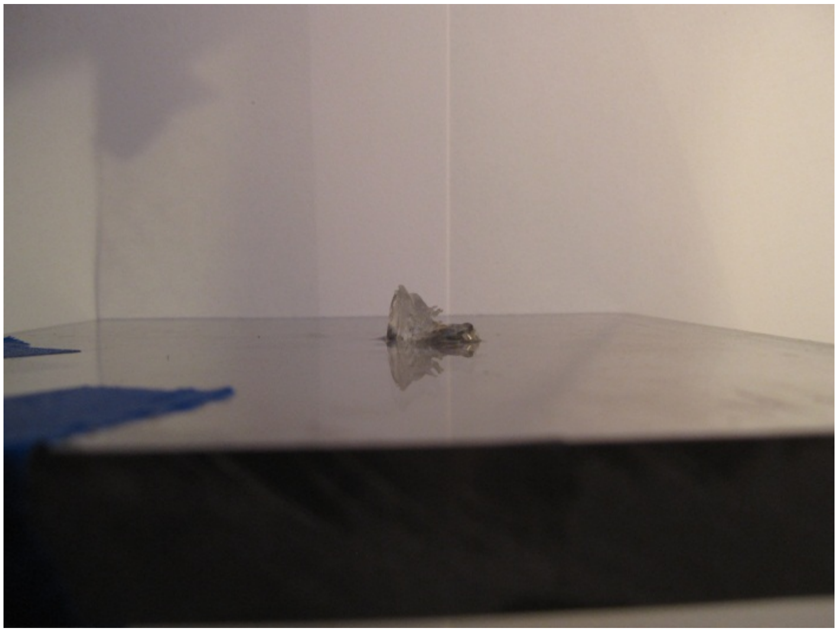

Figure 8.16: 0.5" Monolithic Lexan Post-Impact Damage For Test 4; Side View

The video stills from Test 5 show that the progression of the pre-impact projectile trajectory. Minimal attitude is present. In the fifth frame there is a noticeable amount of plastic flow. As the FSP progresses the plastically deformed plug is driven from the panel and ejected into a small particulate cloud. After impact the projectile perforates the Lexan panel at an upwards angle. The high speed video corroborates the progression of the plug formation observed post-impact in Figures 8.14, 8.15, and 8.16.

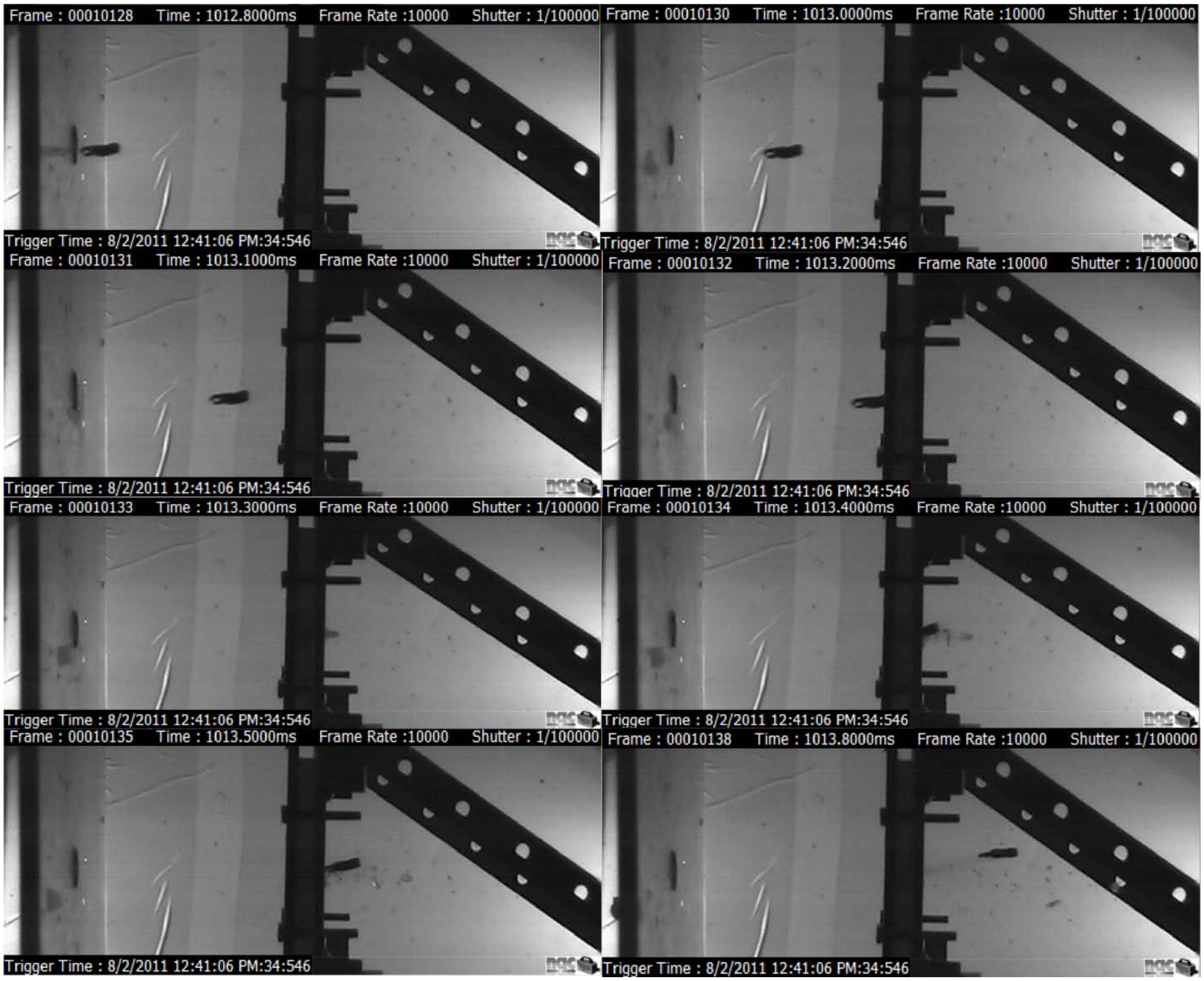

Figure 8.17: 0.5" Monolithic Lexan Impact – Test 5 High Speed Video Stills

8.4.2: 0.75" Laminated Lexan Impact

Laminated Lexan panels measuring 6" x 6" x 0.75" (LWD) were impacted using the chainshot FSP with a normal trajectory path. The laminates Lexan consisted of a central 0.5" thick panel with 0.125" thick panels adhered to each side. Due to the thickness of the panels, helium was necessary to be able to fully perforate the panels. The summary of the impact test results for the 0.75" laminated Lexan panels is shown in Table 8.2.

Test Number	Initial Weight (grams)		Residual Weight (grams)		Velocity (meters/sec)		Comments
	Panel	Projectile	Panel	Projectile	Impact	Residual	
1	520.05	6.15	N/A	N/A	303.66	0	Projectile Stuck
2	539.25	6.15	N/A	N/A	425.09	0	Projectile Stuck
3	540.25	6.05	537.95		464.79	179.27	Full Perforation
4	532.55	6.2	532.33		454.18	105.2	Full Perforation
5	530.05	6.1			472.98	234.28	Full Perforation
6	546.05	6.05	546.1		452	191.81	Full Perforation

Table 8.2: 0.75" Laminated Lexan Chainshot FSP Impact Testing Summary

Based on the test results it is estimated that the ballistic limit velocity of the laminated Lexan panels is approximately 425 meters per second. Due to the construction of the laminated panels, the damage modes present are more complex than in the monolithic case. It was observed that at velocities significantly lower than the ballistic limit that a substantial amount of delamination, cracking, and plastic flow occurred. While velocities at or beyond the ballistic limit, plastic flow was the predominant damage mode.

In Figure 8.18 post-impact damage of Test 1 is shown. The bubble shown is the delamination of the laminates from the central monolithic panel. Several radial cracks have formed from the center of the impact point. Also crazing is present on the central monolithic panel as shown in Figure 8.19.

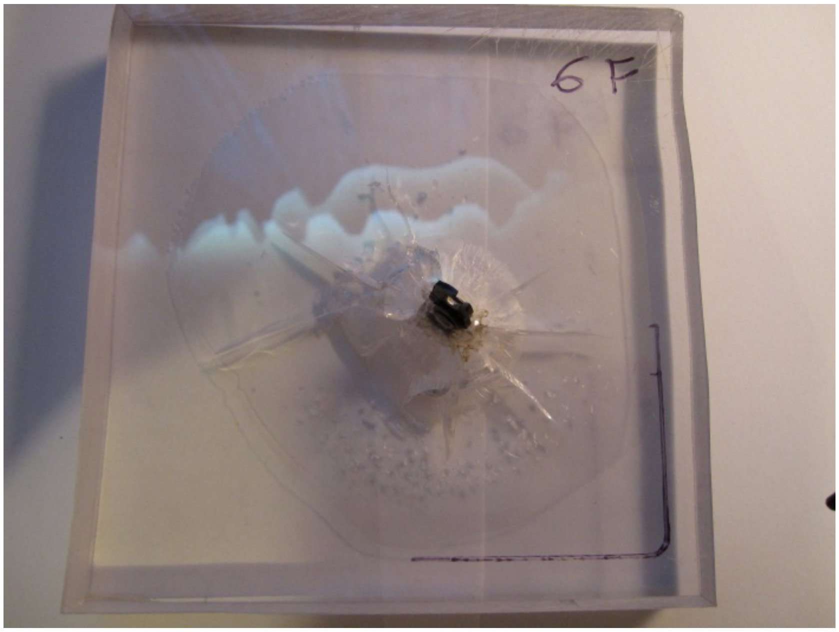

Figure 8.18: 0.75" Laminated Lexan Post-Impact Damage For Test 1; Front Face

Figure 8.19: 0.75" Laminated Lexan Post-Impact Damage For Test 1; Front Close Up

At velocities above the ballistic limit, the damage accrued includes plastic deformation and delamination. From Test 3 the delamination of the front and back 0.125" thick plies as shown in Figure 8.20. The amount of delamination for the back ply is significantly greater than the front. The plastic deformation is very similar to the 0.5" monolithic panels. The Lexan panel response differs greatly dependent on the incident velocity due to the speed of the wave propagation and the length of the contact time. As mentioned previously, the response of the panel will be largely global at low velocities and will become more localized as the incident velocity increases (82).

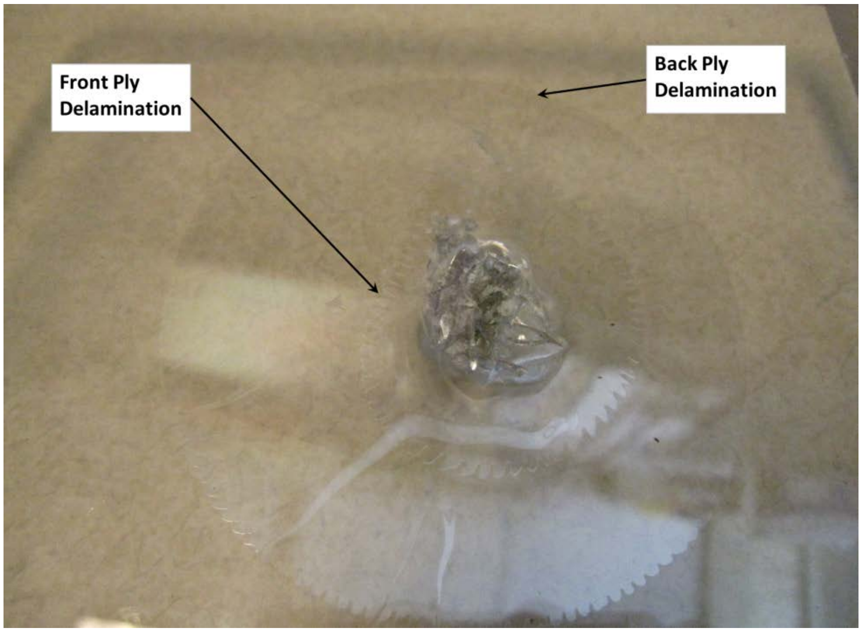

Figure 8.20: 0.75" Laminated Lexan Post-Impact Damage For Test 3; Front Close Up

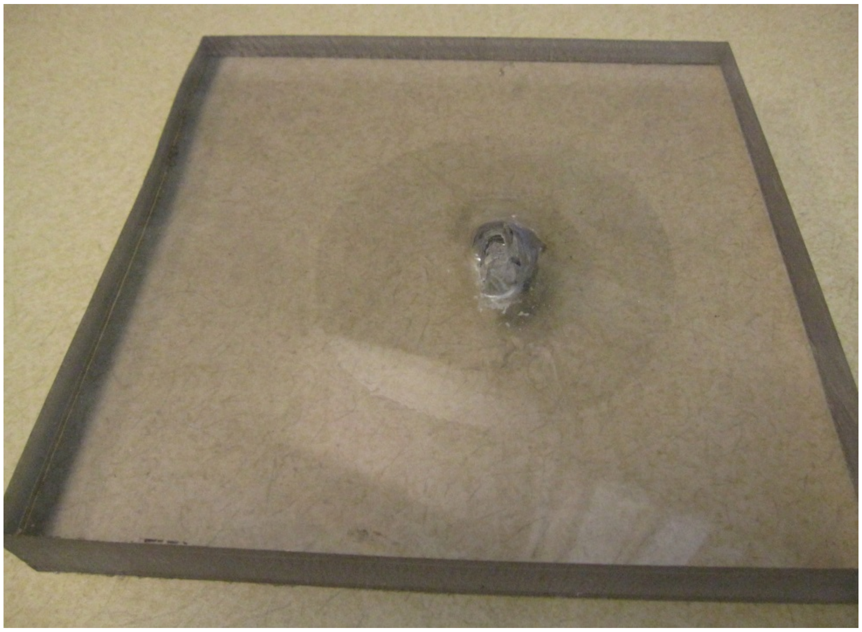

Figure 8.21: 0.75" Laminated Lexan Post-Impact Damage For Test 3; Back

Chapter 9 : Polycarbonate Glazing Ballistic Impact Simulations

Finite simulations were developed in LS-DYNA to further explore the chainshot experiments performed for the Lexan panels. Since many different trajectories and projectile fragments can occur in chainshot events, there can be a substantial savings for the analyst to develop Finite Element simulations that can accurately reflect the ballistic impact event. Towards this end, the monolithic case presented in Section 8.4.1 will be considered. A suitable material model in LS-DYNA to represent the polycarbonate is explored. Experimental characterization for polycarbonate presented in the literature is analyzed to develop the material parameters necessary for the ballistic impact simulation. The results obtained from the simulation are compared to the observations made during testing.

9.1: Polycarbonate Material Behavior

Polycarbonate behavior is rate-dependent in addition to being affected by the loading conditions such as loading direction and ambient temperature. Moy et al performed SPHB testing comparing the response of Lexan 9034 to increasing strain rates under compressive loads (88). From Figure 9.1, it is apparent that polycarbonate is rate-dependent exhibits linear elastic, yielding, strain softening, and strain hardening behavior (88).

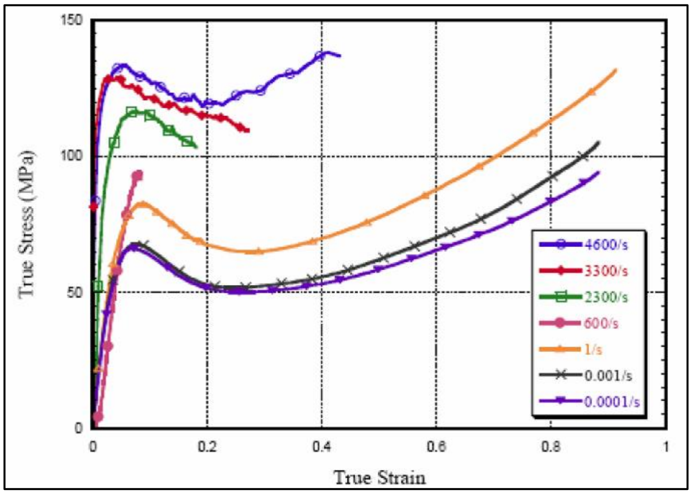

Figure 9.1: Polycarbonate Stress-Strain Relationship at Various Strain Rates (Moy et al)

Additionally the elastic modulus increases with the strain rate. Li et al studied the strain rate effect of polycarbonate under compressive dynamic loading conditions using a SPHB setup. The strain rate effects reported by Li et al are summarized in Table 9.1. It is clear from Figure 9.1 and Table 9.1 the modulus can be divided by strain rate regime.

Strain Rate (1/second)	Yield Stress (MPa)	Elastic Modulus (GPa)
4.00E-05	25.2	2.4
4.00E-02	35	2.4
1200	47.5	5.4
1700	54.1	5.4
2200	68.9	5.4

Table 9.1: Polycarbonate Strain Rate Effects On Yield Stress And Elastic Modulus (Li et al)

Polycarbonate exhibits a strength differential depending on whether it under compressive or tensile loading conditions. In Figure 9.2 Boyce et al compared the polycarbonate response under uniaxial compressive and tensile quasi-static loading (89). There is a clear difference in the stress magnitude depending on the loading direction.

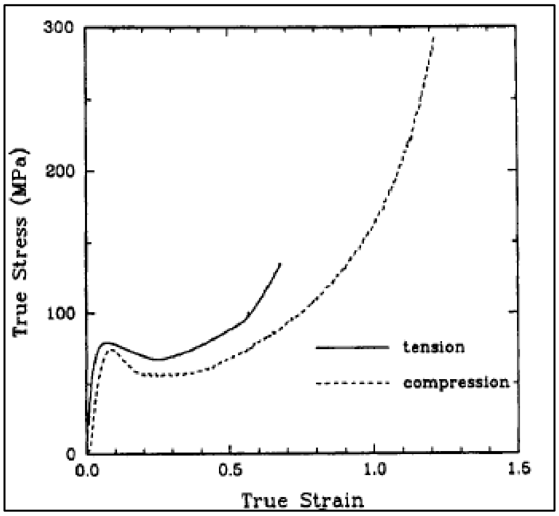

Figure 9.2: Strength Differential of Polycarbonate (Boyce et al)

Additionally, polycarbonate is also temperature dependent. Richeton et al compared the response under compressive loads for a range of temperatures as illustrated in Figure 9.3 (90). Comparing Figures

9.1 and 9.3, increasing strain rates and decreasing sample temperature both increase the magnitude of the stress response of polycarbonate.

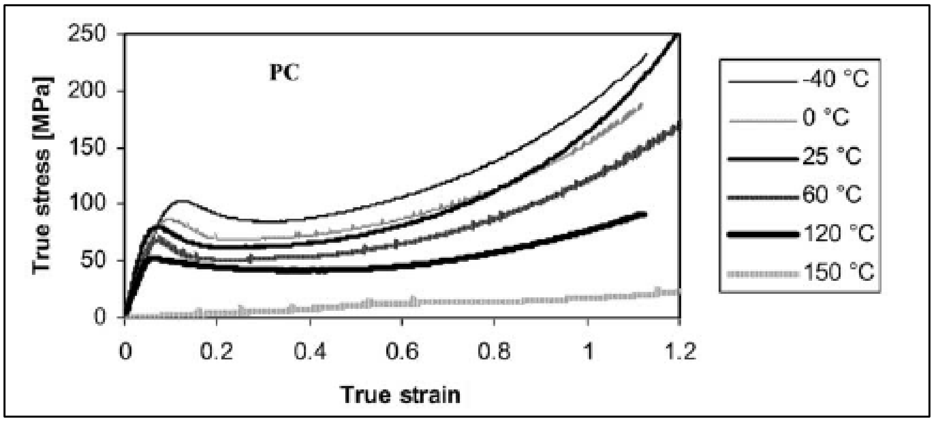

Figure 9.3: Polycarbonate Stress-Strain Relationship at Various Temperatures at 0.01 / second Strain Rate (Richeton et al)

As a result the yield stress follows the same increasing trend for increasing strain rates and decreasing temperatures. From Moy et al, Figure 9.4 shows the yield stress increasing to the increasing strain rates (88). Richeton et al considered yield stress in relation to strain rate and temperature (91). In Figure 9.5 both increasing trends related to strain rate and temperature are observed in the yield stress (91).

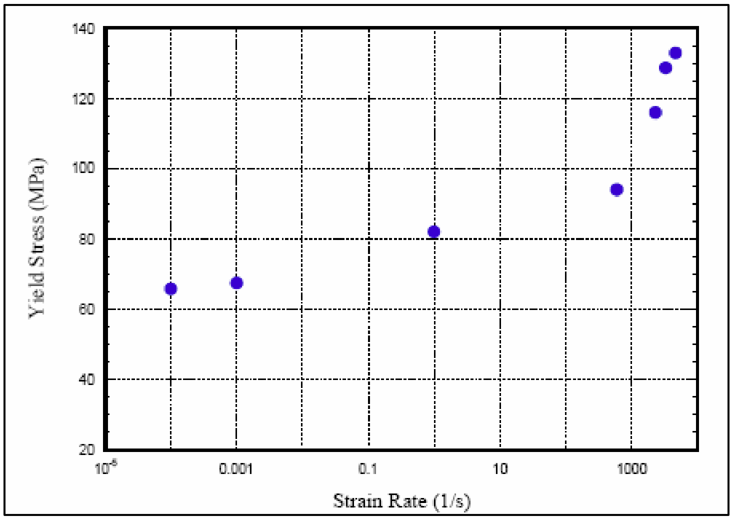

Figure 9.4: Polycarbonate Yield Stress As Function of Strain Rate (Moy et al)

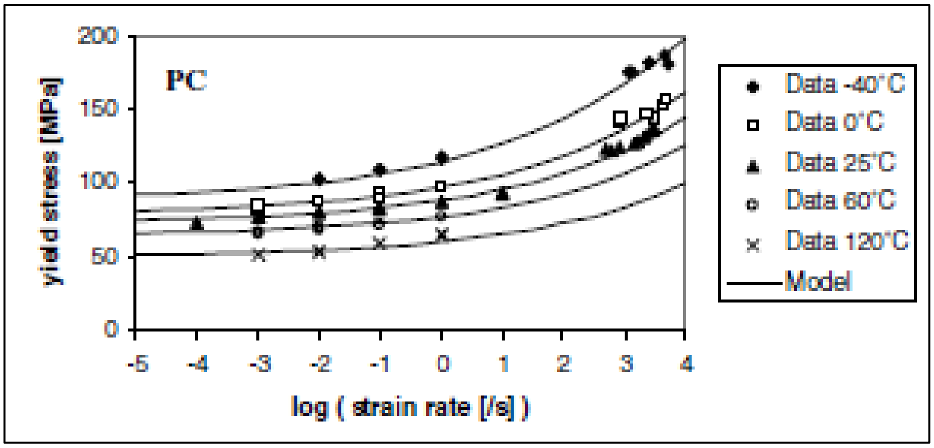

Figure 9.5: Polycarbonate Yield Stress As Function of Strain Rate and Temperature (Richeton et al)

9.2: LS-DYNA Polycarbonate Ballistic Impact Model

Based on the experimental testing outlined in Chapter 8, the LS-DYNA Finite Element model was created. Figure 9.6 shows the model before impact. Since it was observed in the experimental testing that the post-impact trajectory of the chain fragment could be unpredictable, symmetry could not be used to reduce the number of elements in the simulation. A mapped hexahedral mesh for the polycarbonate panel was created using LS-Prepost. The element size was biased towards the center of the panel where a finer resolution is needed to capture the highly localized response of the ballistic impact.

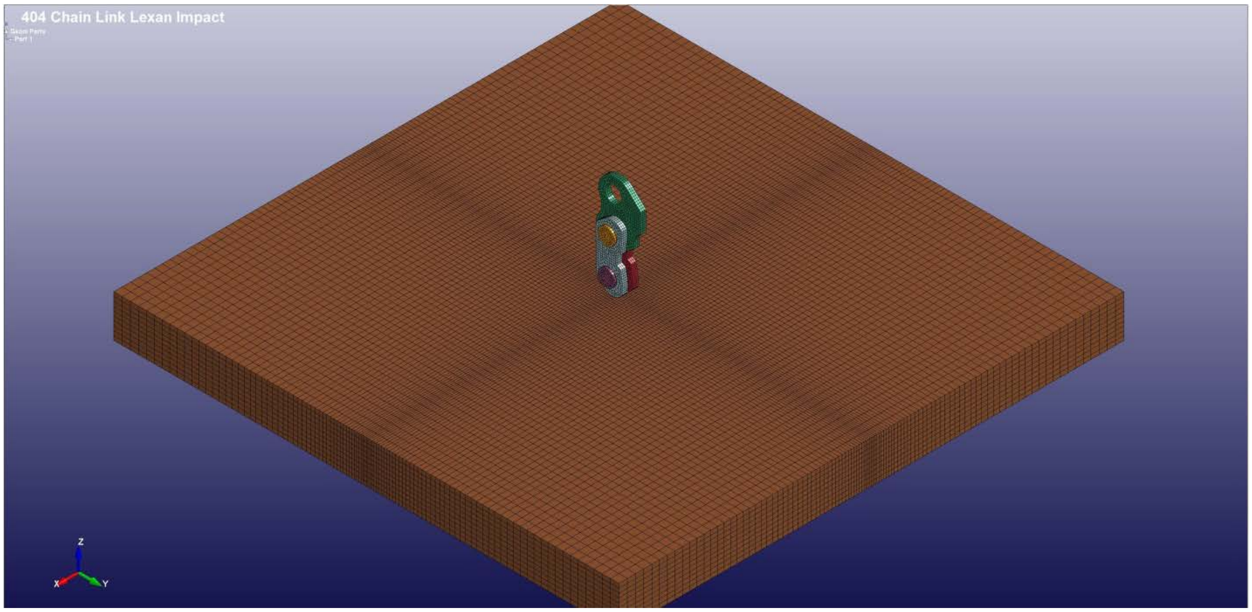

Figure 9.6: LS-DYNA FEM Model For Chainshot Impact

The chain fragment consisted of the assembly of five parts: rivets, chain, tie straps, and the driving link. Due to the geometry of the chain fragment assembly, a mixed mesh of tetrahedral and hexahedral elements was used. A close-up of the resulting chain fragment assembly mesh is shown in Figure 9.7. Between each of the individual parts, contact elements are defined to form the assembly. The *CONTACT_AUTOMATIC_SURFACE_TO SURFACE contact model was defined between each of the chain fragment components using the standard penalty-based method. For the present model, friction between the chain components was ignored. As a result of the contact element definitions, the driving link is able to rotate freely in relation to the assembly. Contact elements were also defined between the Lexan panel and the chain fragment assembly using *CONTACT_ERODING_SURFACE_TO_SURFACE. The contact model is also based on the penetration methodology. Additionally it allows for the erosion or deletion of distorted elements due to the contact model. The static and dynamic friction coefficients were defined as 0.38 for each (92).

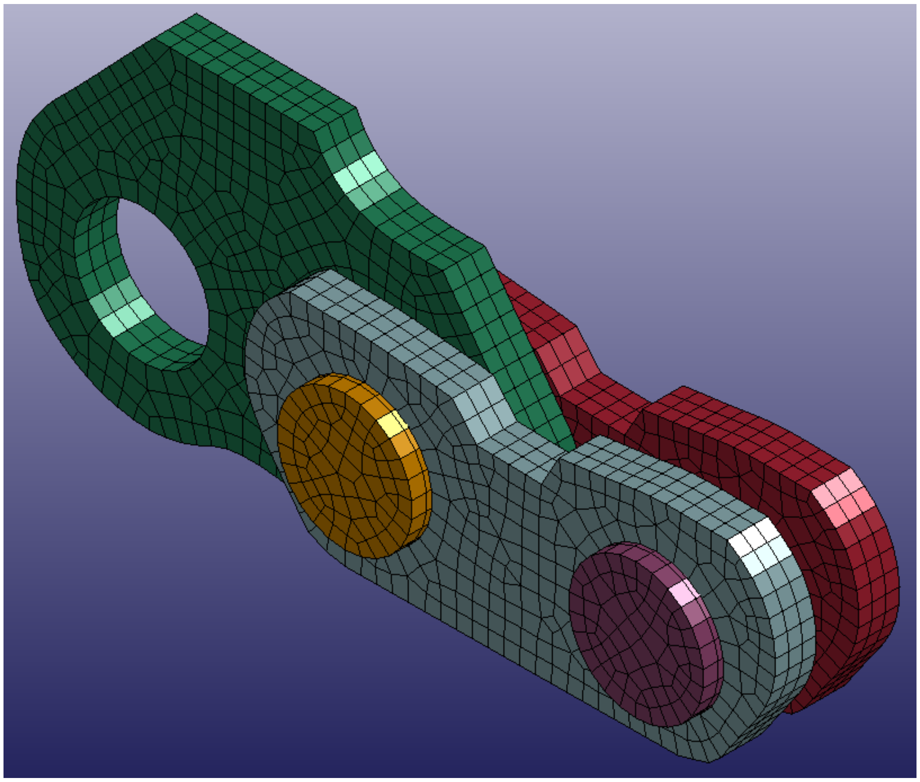

Figure 9.7: Chain Fragment Assembly Finite Element Mesh

Under-integrated elements are used in the simulation to reduce the computational cost of the simulations. As such hourglass control was enabled though the keyword *CONTROL_HOURGLASS to prevent the non-physical modes that can result when using under-integrated elements.

9.2.1 : Chain Fragment Steel Material Model

In the experimental testing no noticeable permanent deformation or damage was observed in the chain fragments therefore it is assumed that the majority of deformation will be elastic. Additionally since there is a large difference in modulus between steel and polycarbonate, the chain fragment deformation will be considered to be largely negligible. Based on the aforementioned assumptions, a bilinear elasto-plastic material model, *MAT_PLASTIC_KINEMATIC, was used to model the behavior of the steel chain fragment. The material model parameters for the chain fragment are summarized in Table 9.2.

Density (kg/m^3)	8000
Elastic Modulus (GPa)	193.00
Poisson's Ratio	0.30
Yield Stress (GPa)	1.03
Tangent Modulus (GPa)	6.90
β, Hardening Parameter	1
FS, Effective Plastic Strain At Failure (%)	1.20

Table 9.2: Steel Chain Fragment Material Parameters

The parameters are based on common values for 316 stainless steel. The model allows the analyst to select the hardening behavior using the β parameter. Values can vary from 0 to 1 for kinematic and isotropic hardening. It was observed that kinematic hardening led to the erosion of elements in the chain fragment that was not observed experimentally. As such purely isotropic hardening was selected for the simulations; $\beta = 1$. The model also allow for failure through the definition of the FS parameter which is the effective plastic strain at failure. The effective plastic strain, $\bar{\varepsilon}^{p}$, can be defined in terms of the true stress and strain as shown in equation 9.1.

$$\bar{\varepsilon}^{p} = \varepsilon^{tr} - \frac{\sigma^{tr}}{E} \qquad \textbf{9.1}$$

The bilinear response for the resulting steel material model can be represented as shown in Figure 9.8.

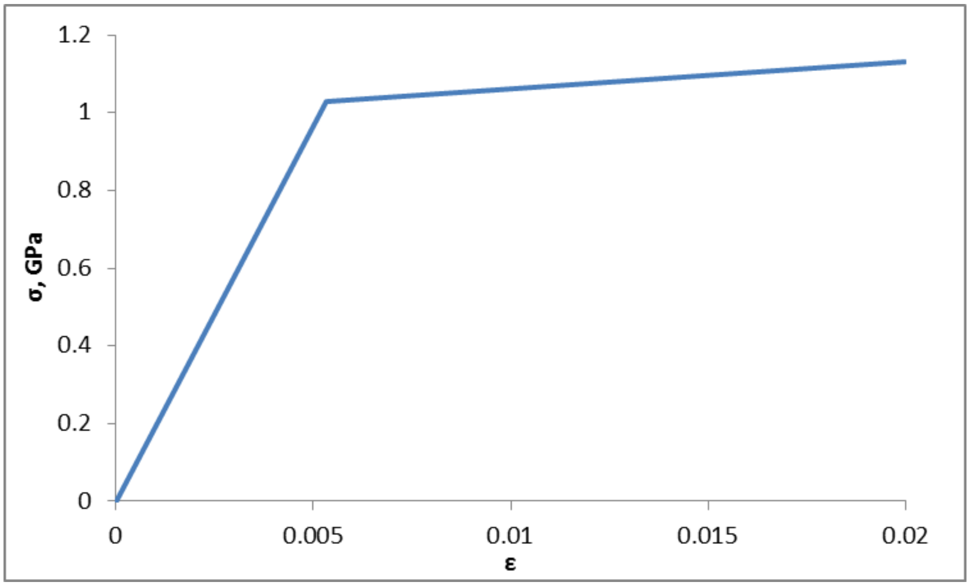

Figure 9.8: Steel Material Model Bilinear Response

9.2.2 : Polycarbonate Material Model

Given the material behavior observed in the literature summarized in Section 9.1, the strain rate dependent material model *MAT_STRAIN_RATE_DEPENDENT_PLASTICITY was selected since it can model the majority of the behavior observed experimentally in Section 9.1. The model is capable of capturing the rate-dependent behavior but does not include the thermal effects or strength differential. For the present research, it is assumed that the chainshot impact is an isothermal process so thermal effects are ignored. Additionally it is assumed that the impact of the strength differential will be negligible in the overall response.

The model allows for the analyst to define curves to describe the relationship of yield strength, elastic modulus, and tangent modulus in terms of the effective strain rate (65). The effective strain rate, $\bar{\dot{\varepsilon}}$, can be defined in terms of the deviatoric strain rates, $\dot{\varepsilon}'$, as defined in equation 9.2 (65).

$$\bar{\dot{\varepsilon}} = \left(\frac{2}{3} \dot{\varepsilon}'_{ij} \dot{\varepsilon}'_{ij} \right)^{1/2} \qquad \textbf{9.2}$$

The yield stress in terms of the yield strength, σ_0, elastic modulus, E, tangent modulus, E_t, and effective plastic strain can be defined as in equation 9.3.

$$\begin{gathered} \sigma_y = \sigma_0\left(\bar{\dot{\varepsilon}}\right) + E_p \bar{\varepsilon}^p \\ where \\ E_p = \frac{E\,E_t}{E - E_t} \end{gathered} \qquad \textbf{9.3}$$

Additionally the model has a simple material failure option by allowing the analyst to define a failure curve in relation to the effective strain rate. The failure curve can be defined in terms of either the effective or Von-Mises stress , effective plastic strain, maximum and absolute value of the principal stresses, or the maximum principal stresses at failure (65). The effective stress and effective plastic strain can be defined as shown in equations 9.4 (5) and 9.5 (70), respectively. The effective plastic strain is in terms of the true stress and strain for a uniaxial load.

$$\bar{\sigma} = \left(\frac{1}{2}\left[\left(\sigma_{11} - \sigma_{22}\right)^2 + \left(\sigma_{22} - \sigma_{33}\right)^2 + \left(\sigma_{33} - \sigma_{11}\right)^2 + 3\left(\sigma_{12}^2 + \sigma_{23}^2 + \sigma_{31}^2\right) \right] \right)^{1/2} \tag{9.4}$$

$$\bar{\varepsilon}^p = \varepsilon_{tr} - \frac{\sigma_{tr}}{E} \tag{9.5}$$

The material parameters for the polycarbonate are summarized in Table 9.3. The density and poisson's ratio were obtained from the manufacturer datasheet for Lexan 9034 (93). As mentioned earlier a curve relating the elastic modulus with the effective strain rate can be defined. However this option is not recommended in LS-DYNA (65). As such a constant elastic modulus is defined. Since high strain rates are expected during the ballistic impact event, the elastic modulus is based on the values reported by Li et al for high strain rates.

Density (kg/m^3)	1200
Elastic Modulus (GPa)	5.00
Poisson's Ratio	0.37

Table 9.3: Polycarbonate Material Constants

In order to define the curves relating yield strength and tangent modulus to effective strain rate, the data from Richeton et al (90) was considered. The material model takes the discrete curve data and interpolates for intermediate values. In order to reduce the amount of interpolation required, a curve fit was used for the dataset in order to provide a continuous and smooth representation of the relationships. In Figures 9.9 and 9.10, the strain rate effects for the yield stress and tangent modulus are plotted. The nonlinear regression was performed on the experimental data using power law relationships for strain rates ranging from 1E-3 to 3000 per second. The model fit obtained for the curve was excellent. Since it is unknown whether the strain rate relationships will follow the same relationships as shown in Figures 9.9 and 9.10, the last calculated datapoint was used for strain rates above 3000 per second to form a piecewise function. Curve data was generated for strain rates ranging from 1E-3 to 1E+7 per second.

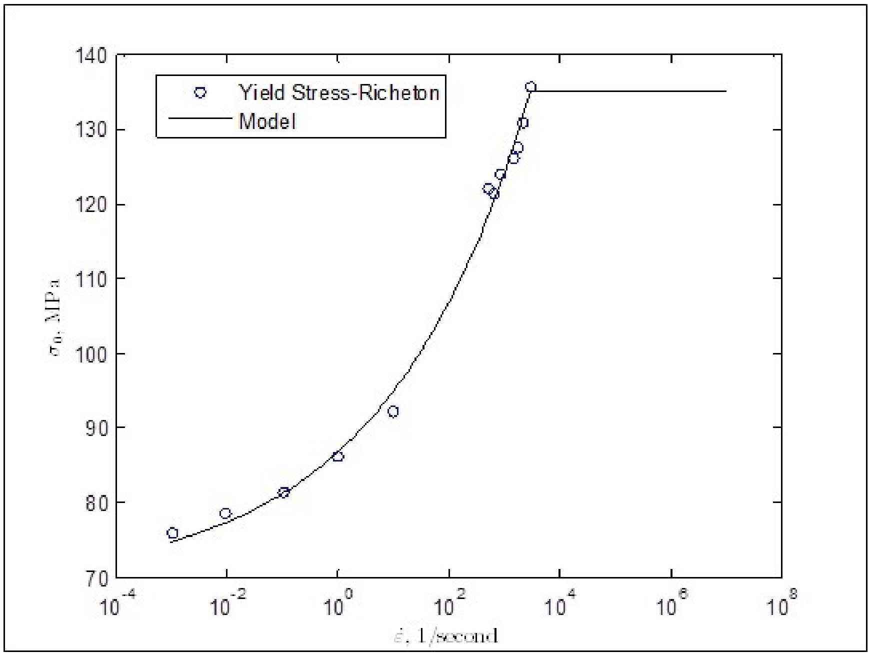

Figure 9.9: Polycarbonate Yield Stress As A Function of Strain Rate

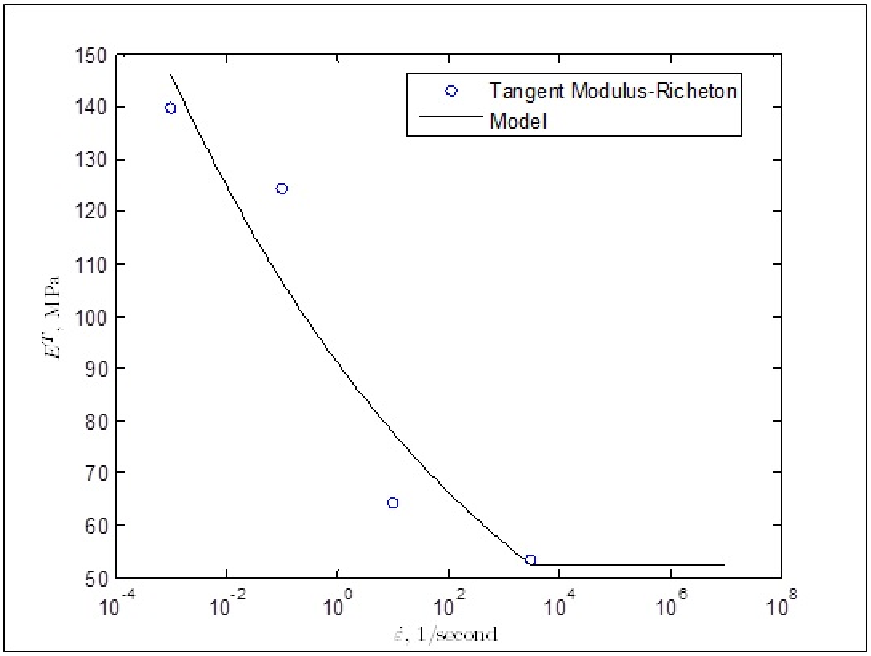

Figure 9.10: Polycarbonate Tangent Modulus As A Function of Strain Rate

As mentioned earlier, the model allows for the analyst to define material failure through several different options. For the current research failure was defined in terms of the effective plastic strain in relations to the corresponding strain rate. The failure strains are calculated by determining the plastic strain using the uniaxial data from Richeton et al (90) and Moy et al (88). After converting the failure strains back to engineering strain from true strain, the relationship based on strain rate can be summarized as in Table 9.4. Due to the difficulty of developing a smooth curve through a regression model fit, a piecewise step function was defined for the material model using the experimental data.

Strain Rate	Failure Strain
1.00E-03	1.80
1.00E-01	1.70
10	1.40
3000	0.65
4600	0.50

Table 9.4: Polycarbonate Effective Plastic Strain at Failure Versus Strain Rate

9.3: LS-DYNA Simulation Results

The simulations were performed at the impact velocities for each of the experimental tests outlined in Section 8.4.1. The relationship between the impact and residual velocities are summarized in Figure 9.11 for both the experimental and simulation results. As shown in the plot, the LS-DYNA simulations are in good agreement with the experimental test for impact velocities above 290 meters per second. As the model approaches closer to the ballistic limit velocity, a larger discrepancy in the residual projectile velocity is observed. The FEM model predicts a ballistic limit of approximately260 meters per second compared to 281.67 determined experimentally. The 7.7% percent difference for the ballistic limit is a good first estimation since limited experimental data was available for the yield stress, tangent modulus, and failure strain curves.

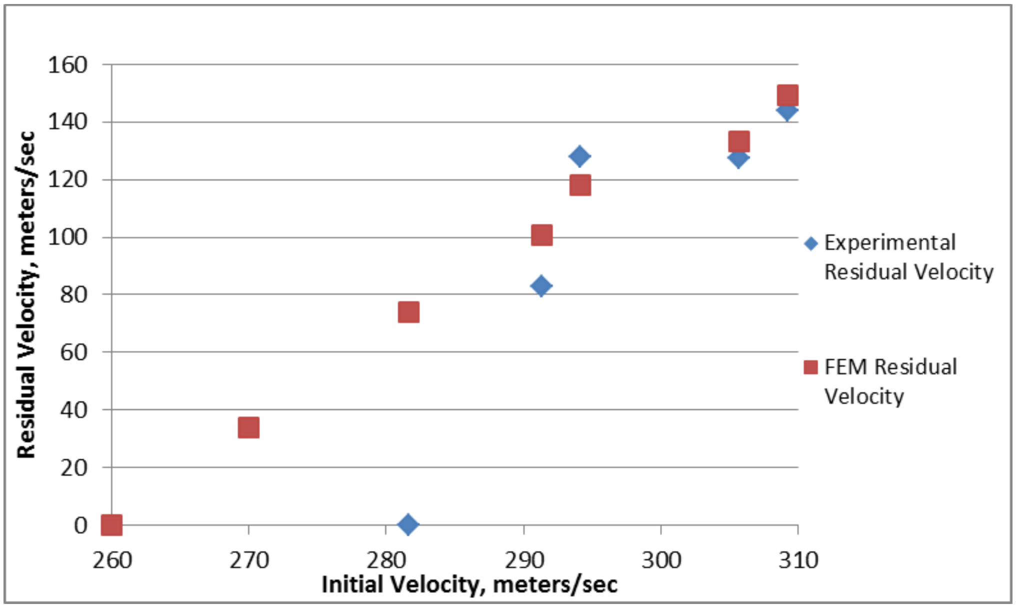

Figure 9.11: 0.5" Monolithic Lexan Ballistic Impact Experimental Vs. FEM Comparison

In the simulations, the plugging behavior observed experimentally during the impact event was recreated. A comparison of the high speed video stills to the corresponding simulation output is depicted in Figure 9.12 for Test 5 of the monolithic testing matrix. After impact plastic deformation initiates and progresses as the chain fragment continues to penetrate the panel. As more plastic deformation occurs, the plug size continues to increase. After perforation the plug is ejected from the panel. Figure 9.13 shows the progression of the effective plastic strain for the cross-section of the Lexan panel. Simulation stills 1 and 2 clearly show the plastic plug formation observed experimentally in Figure 8.14. The remaining stills show the ejection of the plastic plug and the plastic zone evolution as the chain fragment further perforates the panel.

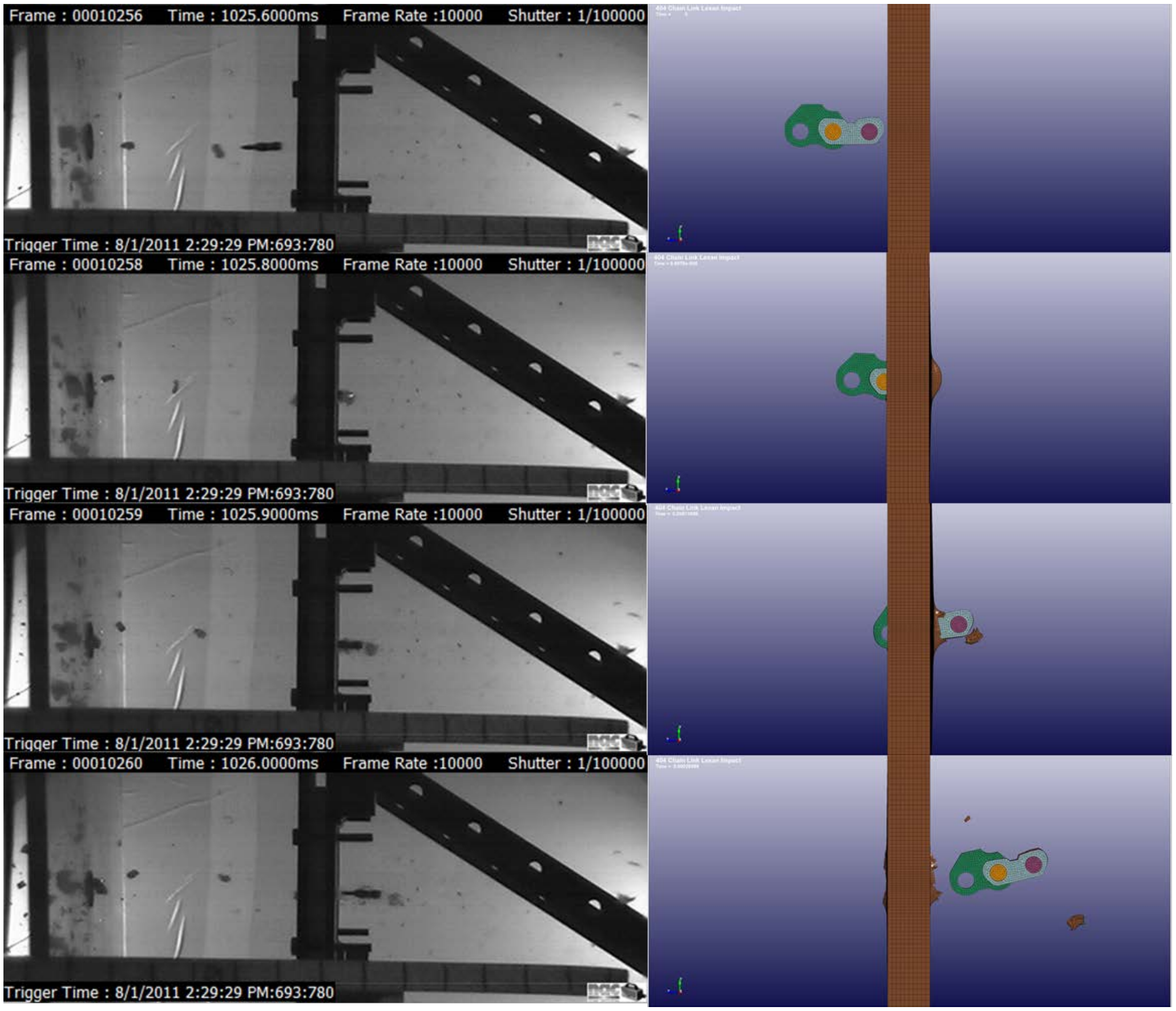

Figure 9.12: Comparison Of Experimental And LS-DYNA Ballistic Event for Test 5 of Monolithic Testing

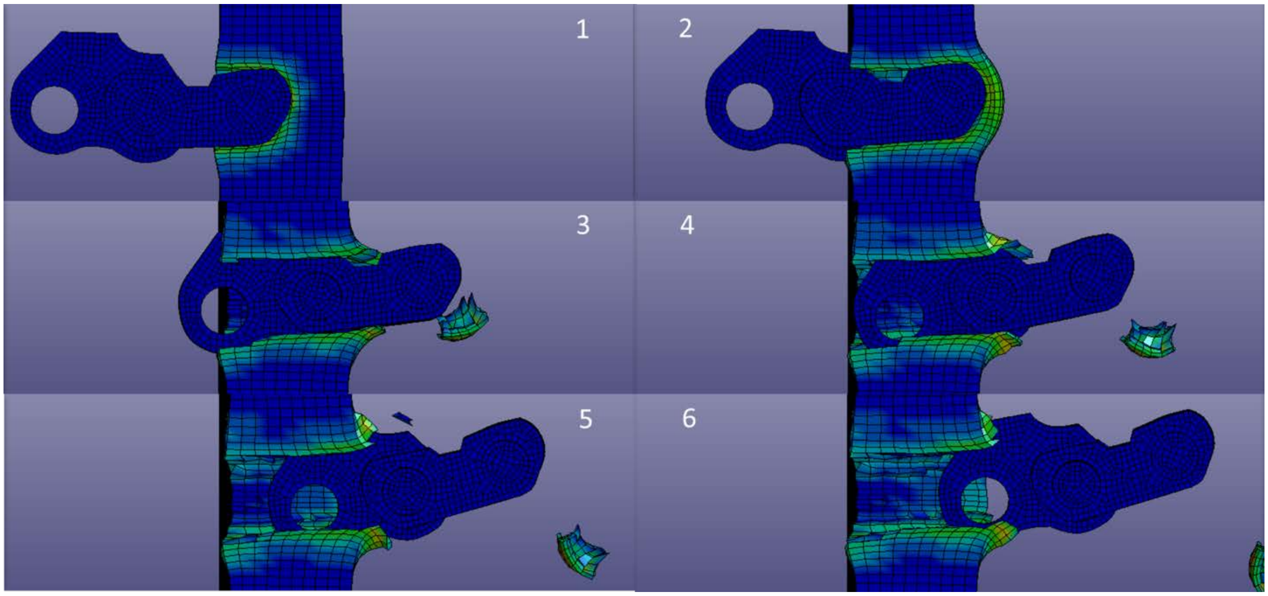

Figure 9.13: Progression of Effective Plastic Strain for Test 5 of Monolithic Testing

Chapter 10 : Conclusions

The preceding chapters have covered the experimental and numerical methods developed and utilized throughout the course of the research studying ballistic impact of polymeric composites and polymers. The experimental portion of the research included the development of the ballistic impact test equipment and procedures, comparison between thermoplastic and epoxy based composites for ballistic performance, development of the falling object hazard test, and 'chainshot' polycarbonate impact. The numerical analysis included the derivation of a coupled viscoplastic progressive damage composite material model, development of an optimization algorithm to determine the composite model parameters, implementation of the aforementioned model into the explicit integration FEM solver LS-DYNA, and validation of the LS-DYNA implementation for various loading conditions.

A single stage gas gun system has been developed and utilized for several test programs. Through continuous improvement activities, the gun is capable of accelerating 1/4" diameter steel spherical projectiles consistently within a velocity range of 100 to 800 meters per second at a high level of target accuracy. By maintaining a modular system design, the gun is capable of accommodating a wide range of projectile sizes through the standard and upsized barrel configurations. Due to the simplicity of both the sabot design and corresponding manufacturing processes, asymmetrical projectile geometries can also be accelerated with a true trajectory and minimal attitude. The velocity calculation GUI for the high speed camera video data demonstrated that it can readily handle the video files typically produced during the different ballistic impact testing programs. The current implementation utilizes very simple image preprocessing techniques for identification of the projectile. Future works should consider more advanced routines which can also predict the trajectory path based on previous data and subdivide the pixel data for a quicker grid search of the projectile. This would help minimize the amount of preprocessing necessary while also allowing for the tracking of multiple objects simultaneously.

It was observed in the thermoplastic comparison that there is a significant performance advantage for thermoplastic based composites over the epoxy based subject to high velocity impact. Since, in the present research, replication was not utilized, a significant difference within the thermoplastic and epoxy matrix classes could not be established. A larger sample size would be necessary to quantify the difference. The upsized gun configuration developed for the large object falling hazard test program was capable of accelerating the 1-3/8” diameter steel sphere to a velocity of 150 feet per second at an acceptable level of accuracy. Prior to future testing programs, the target fixture and safety enclosure will both need to be further stiffened to eliminate or significantly reduce the amount of deflection observed during the initial testing. The gas gun was also used for the ‘chainshot’ impact against monolithic and laminated polycarbonate panels. The experimentally-determined ballistic limit velocity of 282 meters per second for the considered monolithic case is in agreement with the reports made by the chain manufacturer. Using published experimental material characterization data for polycarbonate, the ‘chainshot’ event for 0.5” thick monolithic Lexan panel was simulated using a strain rate dependent plasticity model. The simulation results were able to recreate the plastic plug formation observed experimentally in the polycarbonate panels. Additionally the model predicted a ballistic limit velocity of approximately 260 meters per second. This is a reasonable estimate of the ballistic limit for monolithic polycarbonate panels.

A 3-D coupled viscoplastic progressive damage material model suitable for simulation of the ballistic response of composite materials was developed with the intent of implementation into the Finite Element software, LS-DYNA. The model describes the nonlinear behavior exhibited by composites through both the plasticity and progressive damage models. The composite material model algorithmically couples the plastic and damage models through a return mapping integration scheme where the viscoplastic model response is corrected by the damage model. Based on literature recommendations and published experimental data for a common aerospace-grade composite material, the maximum strain criteria was selected for determining the onset of damage. The damage model uses a bilinear energy balance approach for the dissipation of the intralaminar and interlaminar fracture energies of the composite material. In order to couple the fracture mechanics and the continuum damage mechanics frameworks, a 3-D smeared crack model was utilized. The smeared crack model represents the microcracks with the composite by a characteristic length relative to the element size. A benefit to the smeared crack model is that the energy dissipation of a composite structure predicted by the model will not be as sensitive due to the level discretization in the Finite Element simulation.

The composite material model was implemented into the commercial FEM software, LS-DYNA, for model validation and ballistic simulation. A common aerospace-grade composite, IM7/8552 carbon fiber/epoxy, was presented as an example for model validation. Since the viscoplastic model is generalized to accommodate a wider range of composite constituents, there are more material parameters to determine. In order to ease the use of the model, a simple optimization algorithm was developed to determine the viscoplastic model parameters. The example case was then validated through a series of simulations to examine the behavior of the viscoplastic, progressive damage, and smeared crack algorithms within the composite material model. The simulations demonstrated that for the IM7/8552 example the model was able to reproduce the majority of the nonlinear behavior demonstrated in the published characterization data. However for off-axis loading, the maximum strain criteria did not predict the amount of damage observed experimentally for the larger angles. This limitation is mainly attributed to the estimation of the failure shear strain since it was desired to avoid the use of exaggerated shear strain values. For future research efforts, further development is necessary for the failure criteria utilized. Also the model demonstrated minimal variation in the fracture energy dissipation when comparing the sensitivity to different levels of mesh refinement and distortion.

Based on the validation of the material model for the considered IM7/8552 case, ballistic testing published in the literature was simulated for the prediction of both the ballistic limit velocity and center panel deflection. The simulation result was within a reasonable margin with the experimentally determined ballistic limit velocity. The model predicted velocity of 87.06 meters per second compared with approximately 97 meters per second reported in the literature. However the model under-predicted the central panel deflection predicted with a value of 1.75 millimeters at 107 microseconds after impact. This discrepancy in the predicted panel deflection is largely attributed to the perfect bond assumption made between each of the plies made for computational efficiency and that the material model parameters were developed with only in-plane behavior. The damage associated with shear in the 2-/3-plane for the 54 meters per second case simulation exhibited a similar pattern to what is observed experimentally in ultrasonic testing. As anticipated, for each of the plies the orientation of the damage coincided with the ply orientation.

References

1. **Stilp, A. J. and Hohler, V.** Experimental Methods for Terminal Ballistics and Impact Physics. [book auth.] Jonas A. Zukas. *High Velocity Impact Dynamics.* s.l. : John Wiley & Sons, Inc., 1990, pp. 515-592.

2. *Development of a three-stage, ligh-gas gun at the University of Dayton Research Institute.* **Piekutowski, A.J., Poorman, K.L.** s.l. : International Journal of Impact Engineering, 2006, Vol. 33.

3. **Fox, Robert W. and McDonald, Alan T.** *Introduction to Fluid Mechanics.* s.l. : John Wiley & Sons, Inc., 1998. ISBN 0-471-12464-8.

4. **Seigel, Arnold E.** *The Theory of High Speed Guns.* s.l. : United States Naval Ordinance Laboratory, 1965.

5. **Ugural, Ansel C. and Fenster, Saul K.** *Advanced Strength And Applied Elasticity.* s.l. : Prentice Hall, 2009.

6. **NAC Image Technology.** *NAC HotShot 512sc User's Manual.* 2010.

7. *Hypervelocity impact daamge prediction in composites: Part I-material model and characterisation.* **Clegg, R.A., White, D.M., Riedel, W., Harwick, W.** s.l. : International Journal of Impact Engineering, 2006, Vol. 33.

8. *Hypervelocity impact daamge prediction in composites: Part II-experimental investigations and simulations.* **Riedel, W., Nahme, H., White, D.M., Clegg, R.A.** s.l. : International Journal of Impact Engineering, 2006, Vol. 33.

9. **Nicholas, Theodore and Recht, Rodney F.** Introduction to Impact Phenomena. [book auth.] Jonas A. Zukas. *High Velocity Impact Dynamics.* s.l. : John Wiley & Sons, Inc., 1990.

10. **Zukas, Jonas A.** Introduction to Penetration Mechanics. *High Velocity Impact Dynamics.* s.l. : John Wiley & Sons, Inc., 1990.

11. **Recht, Rodney F.** High Velocity Impact Dynamics: Analytical Modeling of Plate Penetration Dynamics. [book auth.] Jonas A. Zukas. *High Velocity Impact Dynamics.* s.l. : John Wiley & Sons, Inc., 1990.

12. *Ballistic Perforation Dynamics.* **Recht, R.F. and Ipson, T.W.** s.l. : Journal of Applied Mechanics, 1963, Vol. 30.

13. **Lambert, J. P. and Jonas, G. H.** *Towards Standardization in Terminal Ballistics Testing: Velocity Represention.* Aberdeen Proving Grounds, MD : Ballistic Research Laboratories, 1975.

14. *On the Lambert-Jonas approximation for ballistic impact.* **Ben-Dor, G., Dubinsky, A. and Elperin, T.** 29, s.l. : Elsevier Science Ltd., 2002, Vol. Mechanics Research Communications.

15. **Ferriter, E. Andrew, McCulloh, Ian A. and DeRosset, William.** *Techniques Used to Estimate Limit Velocity in Ballistics Testing with Small Sample Size.* s.l. : U.S. Army Aviation School.

16. **Silsby, G.** *Penetration Mechanics of Anti-Armor Kinetic Energy Penetrators.* s.l. : LAB-R-GFS871, 1987.

17. **Renegade Materials Corporation.** *RM-2005 Toughned Epoxy (Product Data Sheet).* 2012.

18. **Hexcell.** *HexPly 8552 Epoxy Matrix Product Data.* 2014.

19. **Tencate.** *Datasheet Tencate Cetex PPS.*

20. —. *Datasheet Tencate Cetex PEI.*

21. *Terminal Ballisitics Of Composite Panels and Verfication of Finite Element Analysis; Masters Thesis.* **Grupp, J.S.** Auburn : Auburn University, 2011.

22. *A Simple Flow Rule for Characterizing Nonlinear Behavior of Fiber Composites.* **Sun, C. T. and Chen, J. L.** 10, s.l. : Journal Composite Materials, 1989, Vol. 23.

23. **Srinivasa, Arun R. and Srinivasan, Sivakumar M.** *Inelasticity Of Materials: An Engineering Approach and a Practical Guide.* s.l. : World Scientific, 2009. ISSN: 1793-0901.

24. *A theory of the yielding and plastic flow of anisotropic metals.* **Hill, R.** 1033, s.l. : Proceedings Of The Royal Society London A, 1948, Vol. 193.

25. *A Quadratic Yield Function for Fiber-Reinforced Composites.* **Chen, J. K., Allahdadi, F. A. and Sun, C. T.** 8, s.l. : Journal Of Composite Materials, 1997, Vol. 31.

26. *Model for the strain-rate-dependent behavior of polymer composites.* **Thiruppukuzhi, Srikanth V. and Sun, C. T.** s.l. : Composites Science and Technology, 2001, Vol. 61.

27. *Use of split Hopkinson pressure bar testing off-axis composites.* **Ninan, Lal, Tsai, J. and Sun, C. T.** s.l. : International Journal Of Impact Engineering, 2001, Vol. 25.

28. *Constitutive model for high strain rate response of polymeric composites.* **Tsai, J. and Sun, C. T.** s.l. : Composites Science and Technology, 2002, Vol. 62.

29. *Modeling Non-Linear Rate-Dependent Behavior In Fiber-Reinforced Composites.* **Weeks, C. A. and Sun, C. T.** 3-4, s.l. : Composites Science and Technology, 1998, Vol. 58.

30. *Crash energy absorption of braided composite tubes.* **Flesher, Nathan D.** s.l. : Thesis, Stanford University, 2005.

31. *A dynamic crash model for energy absorption in braided composite materials. Part I: Viscoplastic material model.* **Flesher, Nathan D., Chang, Fu-Kuo and Janapala, Nageswara R.** 8, s.l. : Journal Of Composites Materials, 2011, Vol. 45.

32. *A dynamic crash model for energy absorption in braided composite materials - Part II: Implementation and verification.* **Flesher, Nathan D., Chang, Fu-Kuo and Janapala, Nageswara R.** 8, s.l. : Journal Of Composite Materials, 2011, Vol. 45.

33. *Crashworthiness of Composite Structures with Various Fiber Architectures.* **Janapala, Nageswara R., et al., et al.** Detroit : 11th International LS-DYNA Users Conference, 2010.

34. *The effects of strain rate on the mechanical behaviour of kevlar fibre bundles: an experimental and theoretical study.* **Wang, Yang and Xia, Yuanming.** s.l. : Composites Part A, 1998, Vol. 29 A.

35. *A Plastic Potential Function Suitable for Anisotropic Fiber Composites.* **Chen, J.L. and Sun, C.T.** 14, s.l. : Journal Of Composite Materials, 1993, Vol. 27.

36. *Micro-mechanical Model with Strain-Rate Dependency and Damage for Impact Simulation of Woven Fabric Composites.* **Tabiei, Ala and Ivanov, Ivelin.** s.l. : Mechanics of Advanced Materials and Structures, 2007, Vol. 14.

37. **Hyer, Michael W.** *Stress Analysis Of Fiber-Reinforced Composite Materials.* s.l. : McGraw-Hill, 1998. 0-07-016700-1.

38. **Simo, J.C. and Hughes, T.J.R.** *Computational Inelasticity.* New York : Springer-Verlag, 1998. 0-387-97520-9.

39. **Belytschko, Ted, Liu, Wing Kam and Moran, Brian.** *Nonlinear Finite Elements for Continua and Structures.* West Sussex : John Wiley & Sons Ltd., 2000. 0-471-98773-5.

40. *A Universal Integration Algorithm For Rate-Dependent Elastoplasticity.* **Fotiu, P.A. and Nemat-Nasser, S.** 6, s.l. : Computers & Structures, 1996, Vol. 59.

41. *An Analysis Of A New Class Of Integration Algorithms For Elastoplastic Constitutive Relations.* **Ortiz, M and Simo, J.C.** s.l. : International Journal For Numerical Methods In Engineering, 1986, Vol. 23.

42. *Viscoplasticty For Instabilities Due To Strain Softening And Strain-Rate Softening.* **Wang, W.M., Sluys, L.J. and De Borst, R.** s.l. : International Journal For Numerical Methods In Engineering, 1997, Vol. 40.

43. **Ramsey, Fred and Schafer, Daniel.** *The Statistical Sleuth: A Course In Methods Of Data Analysis.* s.l. : Cengage Learning, 2002. 978-0534386702.

44. *High strain rate characterisation of unidirectional carbon-epoxy IM7-8552 in transverse compression and in-plane shear using digital image correlation.* **Koerber, H, Xavier, J. and Camanho, P.P.** s.l. : Mechanics Of Materials, 2010, Vol. 42.

45. *Prediction of size effects in notched laminates using continuum damage mechanics.* **Camanho, P.P., Maimi, P. and Davila, C.G.** s.l. : Composites Science and Technology, 2007, Vol. 67.

46. *An energy based damage mechanics approach to modelling impact onto woven composite materials: Part I. Numerical models.* **Iannucci, L., Willows, M.L.** s.l. : Composites: Part A, 2006, Vol. 37.

47. *A Three-Dimensional Ply Failure Model for Composite Structures.* **Donadon, M.V., Almeida, S.F.M., Arbelo, M.A., Faria, A.R.** s.l. : International Journal of Aerospace Engineering, 2009, Vol. 2009.

48. **Kachanov, L.M.** *Introduction to Continuum Damage Mechanics.* Brookline, MA : Martinus Nijhoff Publishers, 1986. 90-247-3319-7.

49. *A combined elastoplastic damage model for progressive failure analysis of composite materials and structures.* **Chen, J.F., Morozov, E.V., Shankar, K.** s.l. : Composite Structures, 2012, Vol. 94.

50. *LS-DYNA Implementation of Polymer Matrix Composite Model Uner High Strain Rate Impact.* **Zheng, X., Goldberg, R.K., Binienda, W.K., Roberts, G.D.** s.l. : NASA 2003-212583, 2003.

51. *High strain rate characterisation of unidirectional carbon-epoxy IM7-8552 in longitudinal compression.* **Koerber, H., Camanho, P.P.** s.l. : Composites: Part A, 2011, Vol. 42.

52. *Crack Band theory for fracture of concrete.* **Bazant, Z.P., Oh, B.H.** s.l. : Materials and Structures, 1983, Vol. 16.

53. *A Consistent Characteristic Length For Smeared Cracking Models.* **Oliver, J.** s.l. : International Journal For Numerical Methods In Engineering, 1989, Vol. 28.

54. *A continuum damage model for composite laminates: Part I - Constitutive model.* **Maimí, P., Camanho, P.P., Mayugo, J.A., Dávila, C.G.** s.l. : Mechanics of Materials, 2007, Vol. 39.

55. *A continuum damage model for composite laminates: Part II - Computational implementation and vaildation.* **Maimí, P., Camanho, P.P., Mayugo, J.A., Dávila, C.G.** s.l. : Mechanics of Materials, 2007, Vol. 39.

56. *Progressive damage modeling in fiber-reinforced materials.* **Lapczyk, I., Hurtado, J.A.** s.l. : Composites: Part A, 2007, Vol. 38.

57. *An Objectivity Algorithm for Strain Softening Material Models.* **Donadon, M.V., Iannucci, L.** Dearborn, MI : 9th International LS-DYNA Users Conference, 2006.

58. *A progressive failure model for composite laminates subjected to low velocity impact damage.* **Donadon, M.V., Iannucci, L., Falzon, B.G., Hodgkinson, J.M., de Almeida, S.F.M.** s.l. : Computers and Structures, 2008, Vol. 86.

59. *Ballisitic Impact Modeling of Composite Materials.* **Yen, Chian-Fong.** 7th International LS-DYNA Users Conference.

60. *A ballisitc material model for continuous-fiber reinforced composites.* **Yen, Chian-Fong.** s.l. : Internation Journal of Impact Engineering, 2012, Vol. 46.

61. **Lai, Michael W., Rubin, David and Krempl, Edward.** *Introduction To Continuum Mechanics.* s.l. : Butterwortk-Heinemann;Elsevier, 2010. 978-07506-8560-3.

62. *CDPM2: A damage-plasticity approach to modelling the failure of concrete.* **Grassl, Peter, et al., et al.** s.l. : International Journal Of Solids And Structures, 2013, Vol. 50.

63. *A Fully Coupled Elasto-Viscoplastic Damage Theory For Anisotropic Materials.* **Zhu, Y.Y., Cescotto,S.** 11, s.l. : International Journal of Solids and Structures, 1994, Vol. 32.

64. *Testing and modeling high strain rate behavior of polymeric composites.* **Thiruppukuzhi, S.V and Sun, C.T.** s.l. : Composites Part B, 1998, Vol. 29B.

65. **(LSTC), Livermore Software Technology Corporation.** *LS-DYNA Keyword User's Manual Version 971.* s.l. : (LSTC), Livermore Software Technology Corporation, 2007.

66. **Auburn University College of Engineering.** vSMP HPCC - Virtual Symmetric Multiprocessing High Performance Compute Cluster description. *Auburn University College of Engineering.* [Online] February 9, 2011. [Cited: July 21, 2014.] http://www.eng.auburn.edu/admin/ens/hpcc/hpcc-description.html.

67. *Tensile mechanical behavior of T300 and M40J fiber bundles at different strain rate.* **Zhou, Yuanxin, Jiang, Dazhi and Xia, Yuanming.** s.l. : Journal Of Materials Science, 2001, Vol. 36.

68. **American Society for Testing and Materials (ASTM).** ASTM D3039/D3039M-00 Standard test method for tensile properties of polymer matrix composite materials.

69. **Jones, Robert M.** *Mechanics Of Composite Materials.* s.l. : Taylor & Francis, 1999. ISBN: 1-56032-712-X.

70. **(LSTC), Livermore Software Technology Corporation.** *LS-DYNA Theory Manual.* s.l. : (LSTC), Livermore Software Technology Corporation, 2006.

71. **Hexcell.** *HexTow IM7 Product Data.* 2014.

72. —. *HexTow Carbon Fiber.* 2014.

73. **Material Sciences Corporation (MSC).** *MAT 162 Material Model Users Manual V1.0.* 2010.

74. *The effect of shear strength on the ballisitic response of laminated composite plates.* **Karthikeyan, K., Russell, B.P., Fleck, N.A., Wadley, H.N.G., Deshpande, V.S.** s.l. : European Journal of Mechanics A/Solids, 2013, Vol. 42.

75. *A Novel Fluid Structure Interaction Experiment to Investigate Deformation of Structural Elements Subjected to Impulsive Loading.* **Espinosa, H.D., Lee, S., Moldovan, N.** s.l. : Experimental Mechanics, 2006, Vol. 46.

76. *A heuristic attempt to reduce transverse shear locking in fully integrated hexahedra with poor aspect ratio.* **Borvall, T.** s.l. : 7th European LS-DYNA Conference, 2009.

77. *Wear of Steel Against Carbon Fibre Reinforced PPS.* **Quintelier, Samyn, P., De Baets, Ost, W., Van Paepegem, W.** 3 & 4, s.l. : Tribology In Industry, 2005, Vol. 27.

78. *Coefficient of friction for aluminum in contact with a carbon fiber epoxy composite.* **Schön, Joakim.** s.l. : Tribology International, 2004, Vol. 37.

79. *Machinery for forestry - Glazing and panel materials used in operator enclosures for protection against thrown sawteeth - Test Method and performance criteria.* **International Organization for Standardization (ISO).** Vol. ISO 11839:2010.

80. *Normal missile penetration and perforation of layered plates.* **Radin, J and Goldsmith, W.** s.l. : International Journal of Impact Engineering, 1988, Vol. 7.

81. *D3763-10: Standard Test Method for High Speed Puncture Properties of Plastics Using Load and Displacement Sensors.* **American Society for Testing and Materials (ASTM).** 2010.

82. **Zukas, Jonas A.** *Introduction to Hydrocodes.* s.l. : Elsevier Science, 2004. ISBN: 0-08-044348-6.

83. **Oregon Products North America.** Chain Shot. *Oregon Products North America.* [Online] 2013. [Cited: July 31, 2014.] http://www.oregonproducts.com/harvester/service/chain_shot.htm.

84. **Oregon Products.** *Oregon Mechanical Timber Harvesting Handbook.* Portland, Oregon : s.n., 2005.

85. **Washington State Department of Labor Industries.** *Timber Harvester Operator Killed Following a Chain Shot Incident.* 2014. Investigation # 10WA04801; SHARP Report # 52-30-2014.

86. **Johansson, Louise, Hallonborg, Ulf and Granlund, Paul.** *Chain shot - clear road ahead for development and testing of shot guards.* s.l. : Skogforsk, The Forestry Institute of Sweden, 2004.

87. *Ballisitic Impact Of Polycarbonate - An Experimental Investigation.* **Wright, S.C., Fleck, N.A. and Stronge, W.J.** 1, s.l. : International Journal of Impact Engineering, 1993, Vol. 13.

88. *Strain Rate Response Of A Polycarbonate Under Uniaxial Compression.* **Moy, P., et al., et al.** Charlotte, NC : Proceedings of SEM Annual Conference on Experimental Mechanics, 2003.

89. *An experimental and analytical investigation of the large strain compressice and tensile response of glassy polymers.* **Boyce, M.C. and Arruda, E.M.** 20, s.l. : Polymer Engineering & Science, 1990, Vol. 30.

90. *Influence of temperature and strain rate on the mechanical behavior of three amorphous polymers: Characterization and modeling of the compressive yield stress.* **Richeton, J., et al., et al.** s.l. : International Journal of Solids And Structures, 2006, Vol. 43.

91. *Constitutive modeling of polymer matierials at impact loading rates.* **Richeton, J., et al., et al.** s.l. : J. Phys. IV France, 2006, Vol. 134.

92. **American Society for Metals (ASM).** Appendix: Static and Kinetic Friction Coefficients for Selected Materials. [book auth.] American Society for Metals (ASM). *ASM Handbook.* 1992.

93. **General Electric Structured Products.** *Lexan 9034 Sheet Product Data Sheet.* 1998.